

**UCLA**

**UCLA Electronic Theses and Dissertations**

**Title**

Neural Circuit-Specialized Astrocytes

**Permalink**

<https://escholarship.org/uc/item/3sb5v1h8>

**Author**

Chai, Hua Chai

**Publication Date**

2017

**Supplemental Material**

<https://escholarship.org/uc/item/3sb5v1h8#supplemental>

Peer reviewed|Thesis/dissertation

UNIVERSITY OF CALIFORNIA

Los Angeles

Neural Circuit-Specialized Astrocytes

A dissertation submitted in partial satisfaction of the  
requirements for the degree of Doctor of Philosophy  
in Neuroscience

by

Hua Chai

2017

© Copyright by  
Hua Chai  
2017

# ABSTRACT OF THE DISSERTATION

Neural Circuit-Specialized Astrocytes

by

Hua Chai

Doctor of Philosophy in Neuroscience

University of California, Los Angeles, 2017

Professor Baljit S. Khakh, Chair

Astrocytes are one of the major types of glia ubiquitously found in the brain and are widely held to be largely identical. However, this view has not been fully tested and the possibility that astrocytes are neural circuit-specialized remains largely unexplored. We deployed integrated optical, anatomical, electrophysiological, transcriptomic and proteomic approaches to explore astrocyte similarities and differences in two adult neural circuits under identical conditions. To overcome the paucity of tools permitting astrocyte selective genetic manipulations, we generated *Aldh111-Cre/ERT2* transgenic mice and adeno-associated viruses to selectively target astrocytes *in vivo*. Crosses with RiboTag mice allowed sequencing of actively translated mRNAs and determination of the adult cortical, striatal, and hippocampal astrocyte transcriptomes. Unbiased evaluation of actively translated RNA and proteomic data found significant astrocyte diversity between hippocampal and striatal circuits. Significant differences between striatal and hippocampal astrocytes were also found in electrophysiological

properties, Ca<sup>2+</sup> signaling, morphology and astrocyte-synapse proximity. Our data provide strong, direct evidence for neural circuit-specialized astrocytes in the adult brain and provide new, integrated database resources and approaches to explore astrocyte diversity and function throughout the adult brain.

### **Supplemental Materials** (attached separately)

**Supplemental movie 1:** GCaMP6f expression in example brain areas of a representative sagittal brain section resulting from tamoxifen induced gene expression in mice that were made by crossing *Aldh111-Cre/ERT2* and Ai95 mice.

**Supplemental movie 2:** eGFP expression in the striatum of *Aldh111-eGFP* mice assessed with confocal microscopy and ScaleS tissue clearing.

**Supplemental movie 3:** eGFP expression in the hippocampus of *Aldh111-eGFP* mice assessed with confocal microscopy and ScaleS tissue clearing.

**Supplemental movie 4:** Representative movie of striatal and hippocampal astrocyte morphology based on LY dye filling.

**Supplemental movie 5:** Representative movie of striatal and hippocampal astrocyte process proximity to excitatory synapses from serial block-face scanning electron microscopy.

### **Supplemental Excel file 1**

Table 1: Astrocyte enriched genes by percentile from cortical RNA-Seq data.

Table 2: 2818 differentially expressed genes in striatal and hippocampal RNA-Seq data.

Table 3: Transmembrane Ca<sup>2+</sup> flux pathways in striatal and hippocampal astrocytes.

Table 4: Ca<sup>2+</sup> binding protein expression in striatal and hippocampal astrocytes.

## Supplemental Excel file 2

Table 1: Low-stringency proteomic data for striatal and hippocampal astrocytes.

Table 2: High-stringency proteomic data for striatal and hippocampal astrocytes.

Table 3: Common striatal and hippocampal astrocyte enriched proteins.

Table 4: Striatal astrocyte enriched proteins.

Table 5: Hippocampal astrocyte enriched proteins.

The dissertation of Hua Chai is approved.

S. Thomas Carmichael

Peyman Golshani

Thomas M. Vondriska

Baljit S. Khakh, Committee Chair

University of California, Los Angeles

2017

## TABLE OF CONTENTS

List of Figures.....	x-xv
List of Tables.....	xvi
List of Acronyms.....	xvii-xviii
Acknowledgements.....	xix-xxi
<i>Vita</i> .....	xxii-xxiii
<b>Chapter 1: Introduction</b> .....	1-16
1.1: Astrocytes play functionally important roles in the central nervous system.....	1
1.2: Historical understanding of neuroglia and astrocyte diversity.....	3
1.3: Physiological regional astrocyte diversity in the brain remains relatively unexplored.....	5
1.4: Understanding cell diversity: an interneuron perspective.....	7
1.5: Hypothesis and rationale.....	8
1.6: Two exemplar neural circuits.....	11
1.7: Summary.....	15
<b>Chapter 2: Methods</b> .....	17-49
2.1: Experimental design.....	17
2.2: AAV.....	17
2.3: Mouse models.....	18
2.4: Tamoxifen administration to adult mice.....	21
2.5: Stereotaxic microinjections of AAVs .....	21
2.6: <i>In vivo</i> calcium imaging.....	22
2.7: Immunohistochemistry.....	24
2.8: Acute brain slice preparation for imaging and electrophysiology.....	28
2.9: Electrophysiological recording and assessment of dye coupling <i>ex vivo</i> .....	29

2.10: Astrocyte intracellular Ca <sup>2+</sup> and cell surface glutamate imaging with confocal microscopy <i>ex vivo</i> .....	30
2.11: Calcium imaging analysis.....	31
2.12: Glutamate imaging analysis.....	34
2.13: <i>In vivo</i> activation of HM4D.....	35
2.14: Brain tissue clearing using ScaleS.....	35
2.15: Astrocyte intracellular Lucifer yellow iontophoresis.....	36
2.16: Electron microscopy.....	37
2.17: Adult astrocyte transcriptomes.....	39
2.18: RNA and protein extraction from astrocytes isolated by FACS.....	41
2.19: Microarrays of FACS astrocyte.....	42
2.20: Mass spectrometry based proteomics.....	43
2.21: Mass spectrometry data analysis.....	46
2.22: qPCR experiments.....	47
2.23: Western blot analyses.....	47
2.24: Statistical analysis.....	48
<b>Chapter 3: New transgenic mouse line for selectively targeting astrocytes.....</b>	<b>50-90</b>
3.1: Introduction.....	50
3.2: Creating the <i>Aldh111</i> -Cre/ERT2 BAC line.....	51
3.3: Comparison to existing astrocyte targeting mouse lines.....	52
3.4: <i>Ex vivo</i> and <i>in vivo</i> validation of the <i>Aldh111</i> -Cre/ERT2 BAC line.....	61
3.5: Establishing the adult cortical astrocyte transcriptome.....	69
3.6: Summary and discussion.....	78
<b>Chapter 4: Exploration of molecular astrocyte diversity between adult neural circuits.....</b>	<b>91-126</b>

4.1: Introduction.....	91
4.2: Generating striatal and hippocampal astrocyte transcriptomes.....	91
4.3: Comparing striatal and hippocampal astrocyte transcriptomes.....	92
4.4: Generating striatal and hippocampal astrocyte proteomes.....	107
4.5: Comparing striatal and hippocampal astrocyte proteomes.....	107
4.6: Validating the top striatal and hippocampal astrocyte enriched genes .....	116
4.7: Summary and discussion.....	125
<b>Chapter 5: Astrocyte morphological diversity between adult neural circuits.....</b>	<b>127-143</b>
5.1: Introduction.....	127
5.2: Astrocyte density assessed with cleared brain tissue.....	129
5.3: Astrocyte morphology assessed with light microscopy.....	132
5.4: Astrocyte-synapse proximity assessed with SBF-SEM.....	133
5.5: Summary and discussion.....	134
<b>Chapter 6: Exploring diversity of astrocyte intrinsic properties.....</b>	<b>144-155</b>
6.1: Introduction.....	144
6.2: Astrocyte membrane properties in d.l. striatum and hippocampus CA1 s.r.....	145
6.3: Astrocyte network size in striatum and hippocampus.....	146
6.4: Summary and discussion.....	146
<b>Chapter 7: Exploring functional diversity of astrocyte calcium signaling.....</b>	<b>156-182</b>
7.1: Introduction.....	156
7.2: Astrocyte spontaneous Ca <sup>2+</sup> signaling in d.l. striatum and CA1 s.r.....	158
7.3: Astrocyte Ca <sup>2+</sup> homeostasis in d.l. striatum and CA1 s.r.....	161
7.4: Astrocyte evoked Ca <sup>2+</sup> signaling in d.l. striatum and CA1 s.r.....	166
7.5: Astrocyte GPCR mediated Ca <sup>2+</sup> signaling in d.l. striatum and CA1 s.r.....	166

7.6: Summary and discussion.....	171
<b>Chapter 8: Glutamate Exocytosis.....</b>	<b>183-195</b>
8.1: Introduction.....	183
8.2: Lack of molecular or morphological evidence for glutamate exocytosis.....	185
8.3: Astrocyte cell surface glutamate imaging.....	186
8.4: Neuronal extrasynaptic NMDA receptor mediated slow inward current.....	187
8.5: Summary and discussion.....	187
<b>Chapter 9: Discussion.....</b>	<b>196-203</b>
9.1: Summary of data.....	196
9.2: Hippocampal astrocytes are better responders to neuronal glutamate release.....	197
9.3: $\mu$ -Crystallin is specific to striatal astrocytes.....	201
9.4: Implications for brain function in disease.....	202
9.5: Overall conclusion.....	203
<b>Chapter 10: Bibliography.....</b>	<b>204-229</b>

## LIST OF FIGURES

<u>Figure 1.1:</u> Multiple dimensions of interneuron diversity.....	9
<u>Figure 1.2:</u> Schematic showing the integrated approaches used in this dissertation.....	10
<u>Figure 1.3:</u> Illustration showing the location of the hippocampus and striatum.....	12
<u>Figure 1.4:</u> Cartoon of coronal slice view of mouse hippocampus and striatum.....	13
<u>Figure 2.1:</u> Schematic drawings showing the workflow for <i>in vivo</i> 2PLSM in head-fixed, awake mice.....	25
<u>Figure 2.2:</u> Schematic of the workflow for imaging of astrocyte calcium or glutamate signals in coronal brain slices.....	33
<u>Figure 2.3:</u> Schematic of tissue dissociation and FACS purification of astrocytes.....	45
<u>Figure 3.1:</u> <i>Aldh111</i> -Cre/ERT2 BAC construct.....	54
<u>Figure 3.2:</u> Construction of <i>Aldh111</i> -Cre/ERT2 transgenic mice.....	55
<u>Figure 3.3:</u> Characterizing <i>Aldh111</i> -Cre/ERT2 and existing BAC transgenic mice using AAV FLEX-GFP virus.....	57
<u>Figure 3.4:</u> Comparing transgenic lines following AAV FLEX-GFP injection.....	58
<u>Figure 3.5:</u> <i>Aldh111</i> -Cre/ERT2 BAC transgenic mice using AAV FLEX-GCaMP6f.....	59
<u>Figure 3.6:</u> High magnification images of CA1 s.r. astrocytes in <i>Aldh111</i> -Cre/ERT2 mice.....	60
<u>Figure 3.7:</u> <i>Aldh111</i> -eGFP astrocytes colocalize with S100 $\beta$ .....	63
<u>Figure 3.8:</u> Characterization of Lck-GCaMP6 <sup>fllox</sup> x <i>Aldh111</i> -Cre/ERT2 double transgenic mice.....	64
<u>Figure 3.9:</u> Characterization of Lck-GCaMP6 <sup>fllox</sup> x <i>Aldh111</i> -Cre/ERT2 double transgenic mice.....	65
<u>Figure 3.10:</u> Comparison of <i>Slc1a3</i> -Cre/ERT and <i>Aldh111</i> -Cre/ERT2 transgenic mice. ....	66

<u>Figure 3.11</u> : No expression of cyto-GCaMP6f in NeuN positive cells when driven by <i>Aldh111</i> -Cre/ERT2 in Ai95 mice at ~P80.....	67
<u>Figure 3.12</u> : No expression of cyto-GCaMP6f in the absence of tamoxifen when driven by <i>Aldh111</i> -Cre/ERT2 in Ai95 mice at ~P80.....	70
<u>Figure 3.13</u> : Cyto-GCaMP6f expression when driven by <i>Aldh111</i> -Cre/ERT2 in ~P66 Ai95 mice varied depending on tamoxifen dose administered <i>in vivo</i> .....	71
<u>Figure 3.14</u> : Cyto-GCaMP6f expression when driven by <i>Aldh111</i> -Cre/ERT2 in Ai95 mice at ~P66 was dependent on the tamoxifen dose administered <i>in vivo</i> .....	72
<u>Figure 3.15</u> : Visual cortex astrocytes from Ai95 x <i>Aldh111</i> -Cre/ERT2 double transgenic mice display spontaneous and PE-evoked calcium signals.....	73
<u>Figure 3.16</u> : <i>In vivo</i> astrocyte calcium signals measured with cyto-GCaMP6f driven by <i>Aldh111</i> -Cre/ERT2 mice.....	74
<u>Figure 3.17</u> : <i>Aldh111</i> -Cre/ERT2 x RiboTag mice and the determination of the cortical astrocyte transcriptome at P80.....	75
<u>Figure 3.18</u> : Immunoprecipitation of cortex from P80 <i>Aldh111</i> -Cre/ERT2 x RiboTag mice to purify astrocyte mRNA.....	76
<u>Figure 3.19</u> : P80 cortical astrocyte transcriptome are enriched for P7 astrocyte genes.....	82
<u>Figure 3.20</u> : P80 cortical astrocyte transcriptome are depleted of P7 neuronal genes.....	83
<u>Figure 3.21</u> : <i>Aldh111</i> -Cre/ERT2 x RiboTag mice and the determination of the cortical astrocyte transcriptome at P80.....	84
<u>Figure 3.22</u> : Comparison of cortical astrocyte transcriptome at P80 vs P7.....	85
<u>Figure 4.1</u> : <i>Aldh111</i> -Cre/ERT2 drives expression of Rpl22HA exclusively in astrocytes to enable purification of striatal and hippocampal astrocyte mRNA.....	93

<u>Figure 4.2</u> : Representative montages of the striatum and hippocampus from <i>Aldh1l1</i> -Cre/ERT2 x RiboTag mice.....	94
<u>Figure 4.3</u> : Schematic of immunoprecipitation to isolate astrocyte RNA.....	95
<u>Figure 4.4</u> : Validation of adult striatal and hippocampal astrocyte transcriptomes.....	97
<u>Figure 4.5</u> : Principal component analysis of adult striatal and hippocampal astrocyte transcriptomes.....	98
<u>Figure 4.6</u> : Gene Set Enrichment Analysis (GSEA) of adult striatal and hippocampal astrocyte transcriptomes.....	99
<u>Figure 4.7</u> : Adult striatal and hippocampal astrocyte transcriptomes differ by ~15%.....	104
<u>Figure 4.8</u> : FPKM heatmaps of the top 40 astrocyte genes that were not differentially expressed.....	105
<u>Figure 4.9</u> : FPKM heatmaps of the 40 most differentially expressed astrocyte genes.....	106
<u>Figure 4.10</u> : Purification of striatal and hippocampal astrocytes.....	109
<u>Figure 4.11</u> : Microarray validation of FACS astrocyte purification.....	110
<u>Figure 4.12</u> : Example spectra for proteomics peptide detection and labeling.....	111
<u>Figure 4.13</u> : High-stringency identified 692 unique proteins across 4 replicates.....	112
<u>Figure 4.14</u> : Striatal and hippocampal astrocyte protein expression largely correlate with gene expression but with clear exceptions. ....	113
<u>Figure 4.15</u> : Comparison of striatal and hippocampal astrocyte proteomes.....	114
<u>Figure 4.16</u> : Top 20 most abundant common astrocyte proteins.....	115
<u>Figure 4.17</u> : Differentially expressed proteins in striatal and hippocampal astrocytes.....	118
<u>Figure 4.18</u> : Further validation of sorted eGFP positive cells as strongly astrocyte enriched.....	119

<u>Figure 4.19</u> : Validating GFAP and $\mu$ -crystallin expression in striatal and hippocampal astrocytes.....	120
<u>Figure 4.20</u> : Validating GFAP and $\mu$ -crystallin expression in striatal and hippocampal astrocytes.....	121
<u>Figure 4.21</u> : $\mu$ -crystallin expression displays a gradient in striatal astrocytes.....	122
<u>Figure 4.22</u> : $\mu$ -crystallin expression in striatal and hippocampal astrocytes.....	123
<u>Figure 4.23</u> : $\mu$ -Crystallin expression in striatal and hippocampal astrocytes.....	124
<u>Figure 5.1</u> : Evaluating astrocyte density in d.l. striatum and hippocampal CA1 s.r.....	130
<u>Figure 5.2</u> : Astrocyte neuron ratio in d.l. striatum and CA1 s.r.....	131
<u>Figure 5.3</u> : Comparison of striatal and hippocampal astrocyte morphology.....	135
<u>Figure 5.4</u> : Striatal astrocytes with large territory volume have large striatal volumes.....	136
<u>Figure 5.5</u> : Comparison of striatal and hippocampal astrocyte primary branches.....	137
<u>Figure 5.6</u> : Striatal astrocytes are less elongated compared to hippocampal astrocytes. ....	138
<u>Figure 5.7</u> : Comparison of striatal and hippocampal astrocyte proximity to synapses.....	139
<u>Figure 5.8</u> : Comparison of striatal and hippocampal astrocyte proximity to synapses.....	140
<u>Figure 5.9</u> : Comparison of striatal and hippocampal astrocyte contact with and coverage of synapses.....	141
<u>Figure 6.1</u> : Evaluating astrocyte physiological properties in striatal and hippocampal circuits.....	149
<u>Figure 6.2</u> : Hippocampal astrocytes have larger $Ba^{2+}$ -sensitive currents.....	150
<u>Figure 6.3</u> : Evaluating astrocyte gap-junction coupled networks.....	152
<u>Figure 6.4</u> : Hippocampal CA1 s.r. astrocyte membrane conductance is less sensitive to CBX.....	153

<u>Figure 6.5</u> : Evaluating astrocyte physiological similarities and differences in striatal and hippocampal circuits.....	154
<u>Figure 6.6</u> : RNA-Seq analyses of K <sup>+</sup> channels in striatal and hippocampal astrocytes.....	155
<u>Figure 7.1</u> : The canonical Gq-coupled GPCR mediated intracellular calcium increase.....	159
<u>Figure 7.2</u> : Intracranial injection of AAV2/5 GfaABC <sub>1</sub> D-GCaMP6f into striatum and hippocampus robustly expresses GCaMP6f in astrocytes with no overt reactivity.....	160
<u>Figure 7.3</u> : Spontaneous Ca <sup>2+</sup> signals in striatal and hippocampal astrocytes.....	162
<u>Figure 7.4</u> : Properties of Ca <sup>2+</sup> signals in striatal and hippocampal astrocytes.....	163
<u>Figure 7.5</u> : Characterization of somatic events.....	165
<u>Figure 7.6</u> : Average GCaMP6f dF/F trace with s.e.m. of striatal and hippocampal astrocytes.....	167
<u>Figure 7.7</u> : The drop in baseline Ca <sup>2+</sup> levels from normal Ca <sup>2+</sup> to Ca <sup>2+</sup> -free conditions for both regions.....	168
<u>Figure 7.8</u> : Action potential-dependent evoked astrocyte Ca <sup>2+</sup> signals.....	169
<u>Figure 7.9</u> : Striatal and hippocampal astrocytes differ in GPCR mediated Ca <sup>2+</sup> responses.....	172
<u>Figure 7.10</u> : Astrocyte Ca <sup>2+</sup> responses to activation of different G-protein coupled GPCRs.....	173
<u>Figure 7.11</u> : Striatal and hippocampal astrocytes differ in GPCR mediated Ca <sup>2+</sup> responses.....	174
<u>Figure 7.12</u> : Activation of HM4D in astrocytes causes increase in expression of immediate early gene <i>c-Fos</i> .....	175
<u>Figure 7.13</u> : Endogenous GPCR mediated Ca <sup>2+</sup> responses in astrocytes.....	176

<u>Figure 7.14</u> : GPCR mediated somatic Ca <sup>2+</sup> responses.....	177
<u>Figure 7.15</u> : GPCR mediated Ca <sup>2+</sup> responses in major processes .....	178
<u>Figure 7.16</u> : Striatal and hippocampal astrocytes differ in GPCR mediated Ca <sup>2+</sup> responses.....	179
<u>Figure 8.1</u> : Lack of molecular evidence for astrocyte Ca <sup>2+</sup> -evoked glutamate exocytosis.....	189
<u>Figure 8.2</u> : Assessing astrocyte Ca <sup>2+</sup> -evoked increase in extracellular glutamate.....	190
<u>Figure 8.3</u> : Quantification of astrocyte Ca <sup>2+</sup> -evoked iGluSnFR signals.....	191
<u>Figure 8.4</u> : iGluSnFR signals increase in response to exogenous glutamate application.....	192
<u>Figure 8.5</u> : iGluSnFR signals increase in response to synaptic glutamate release.....	193
<u>Figure 8.6</u> : Assessing extrasynaptic glutamate mediated neuronal SICs with striatal and hippocampal astrocyte Ca <sup>2+</sup> increase.....	194
<u>Figure 8.7</u> : Quantification of neuronal SICs.....	195
<u>Figure 9.1</u> : Adult Astrocyte RNA-Seq Explorer.....	199

## LIST OF TABLES

<u>Table 1.1:</u> Astrocyte derived factors involved in synapse development and maintenance.....	2
<u>Table 2.1:</u> Pharmacological agents used in acute brain slice experiments.....	32
<u>Table 2.2:</u> qPCR primer sets.....	49
<u>Table 3.1:</u> Summary of the Cre mice.....	53
<u>Table 3.2:</u> The quantity and quality of the cortical RNA samples.....	79
<u>Table 3.3:</u> Gene ontology analysis of astrocyte genes with differential expression (P7 vs P80) .....	81
<u>Table 3.4:</u> 34 cortical astrocyte genes that were differentially expressed between P80 and P7.....	82
<u>Table 3.5:</u> Representative astrocyte genes compared between P7 and P80.....	86
<u>Table 3.6:</u> Expression of genes related to vesicular transport compared between P7 and P80.....	87
<u>Table 4.1:</u> The quantity and quality of the striatal and hippocampal RNA samples.....	96
<u>Table 4.2:</u> 21 striatal enriched gene sets.....	100
<u>Table 4.3:</u> 4 hippocampal enriched gene sets.....	101
<u>Table 4.4:</u> Genes related to synapse formation and removal.....	103
<u>Table 6.1:</u> Basic electrophysiological properties of astrocytes.....	151
<u>Table 7.1:</u> Spontaneous astrocyte Ca <sup>2+</sup> signals are not dependent on action potentials.....	164
<u>Table 9.1:</u> Genes related to glutamate uptake and recycling.....	198

## LIST OF ACRONYMS

3D: three-dimensional

AAV: adeno-associated virus

aCSF: artificial cerebral spinal fluid

ATP: adenosine 5' triphosphate

Ca<sup>2+</sup>: calcium ions

CBX: carbenoxolone

CNO: clozapine N-oxide

CNQX: 6-cyano-2,3-dihydroxy-7-nitroquinoxaline

CPA: cyclopiazonic acid

Cre: Cre recombinase

cyto-GCaMP6f: cytosolic GCaMP6f

DE: differentially expressed

DHPG: (S)-3,5-Dihydroxyphenylglycine

DMSO: dimethyl sulfoxide

DREADD: designer receptor exclusively activated by designer drug

FACS: fluorescence-activated cell sorting

FC: enrichment fold-change

FDR: false discovery rate

FPKM: fragments per kilobase of transcript per million mapped reads

GFP: green fluorescent protein

GPCR: G-protein coupled receptor

GSEA: gene set enrichment analysis

IHC: immunohistochemistry

IP: immunoprecipitated

K<sup>+</sup>: potassium ions

LC-MS/MS: liquid chromatography-tandem mass spectrometry

LTP: long-term potentiation

mGluR: metabolic glutamate receptor

MSN: medium spiny neuron

NA: numerical aperture

NMDA: N-methyl-D-aspartate

P: postnatal day

PSD: postsynaptic density

RIN: RNA integrity number

ROI: region of interest

RNA-Seq: ribonucleic acid sequencing

SBF-SEM: serial block-face scanning electron microscopy

TBOA: (3S)-3-[[3-[[4-(Trifluoromethyl)benzoyl]amino]phenyl]methoxy]-L-aspartic acid

TTX: tetrodotoxin

vGlut: vesicular glutamate transporter

## ACKNOWLEDGEMENTS

The work described in this doctoral dissertation could be completed due to the efforts of many. I would like to first and foremost thank my mentor Dr. Baljit Khakh for his guidance during these four years and for his patience and dedication to my scientific and career training. I am grateful to my committee members, Dr. Tom Carmichael, Dr. Peyman Golshani, and Dr. Thomas Vondriska, who provided valuable feedback on my work. I also want to thank Khakh lab members present and past for their technical training and intellectual engagement. Many excellent scientists made intellectual and data contributions to this work as detailed below. My training was possible due to financial support from the UCLA Department of Physiology, the UCLA Medical-Scientist Training Program, the UCLA Neuroscience Interdepartmental PhD program, and the National Institute of Mental Healthy NRSA F30 Training Fellowship (MH106197). The project was supported by Dr. Khakh's grants from the National Institute of Mental Health (MH099559 and MH104069) and by the NINDS Informatics Center for Neurogenetics and Neurogenomics at UCLA (P30 NS062691).

The work described in **Chapter 3** is modified from published work: Srinivasan, R., Lu, T.-Y., Chai, H., Xu, J., Huang, B.S., Golshani, P., Coppola, G., and Khakh, B.S. (2016). New Transgenic Mouse Lines for Selectively Targeting Astrocytes and Studying Calcium Signals in Astrocyte Processes In Situ and In Vivo. *Neuron* 92, 1181-1195 (co-first authors). Dr. Rahul Srinivasan and Dr. Ji Xu performed molecular biology for the BAC mice (*Aldh111-Cre/ERT2* and *Slc6a11-Cre/ERT2*, respectively). Data for **Figures 3.1-15** were generated by Dr. Rahul Srinivasan with help from Dr. Amy Gleichman for **Figure 3.13**. Data for **Figures 3.16** were generated by Dr. Tsai-Yi Lu with help from Dr. Ben Huang. Data for **Figure 3.17B,C** were generated by Dr. Tsai-Yi Lu. Dr. Giovanni Coppola contributed to the design of RNA-Seq experiment. Dr. Amy Gleichman trained me to perform RiboTag immunoprecipitation. Dr. Giovanni Coppola and Dr. Fuying Gao helped with analysis of RNA-Seq data.

**Chapters 4-8** are modified from an accepted manuscript in press: Hua Chai, Blanca Diaz-Castro, Eiji Shigetomi, Emma Monte, J. Christopher Oceau, Xinzhu Yu, Whitaker Cohn, Pradeep S. Rajendran, Thomas M. Vondriska, Julian P. Whitelegge, Giovanni Coppola & Baljit S. Khakh. Neural circuit-specialized astrocytes: genomic, proteomic, morphological and functional evidence. *Neuron* (*accepted*), (co-first authors). This portion of my dissertation was done in close collaboration with Dr. Blanca Diaz-Castro. In **Chapter 4**, we generated data for **Figures 4.10, 4.19, and 4.20** together. Dr. Blanca Diaz-Castro generated the data for **Figures 4.11-18, 4.21-23** with help from Emma Monte, Whitaker Cohn, Thomas M. Vondriska, and Dr. Julian P. Whitelegge. Dr. Giovanni Coppola and Chen Cheng contributed to the design of RNA-Seq experiment. Dr. Giovanni Coppola, Dr. Fuying Gao, Chen Cheng, and Dr. Blanca Diaz-Castro helped with analysis of RNA-Seq and microarray data. For **Chapter 5**, brain clearing was performed by Pradeep S. Rajendran, and images were acquired at the Gradinaru Laboratory at Caltech. Electron microscopy sample staining and imaging were done by Emily Benson and Dr. Grahame Kidd at Renovo Neural Inc. They also provided training for tracing electron microscopy structures. Dr. Baljit Khakh did the electrophysiology for **Chapter 6**, generating data for **Figures 6.1-2 and 6.4**. Dye-coupling experiments were done by Dr. Baljit Khakh and me to generate **Figures 6.3 and 6.5**. Dr. Blanca Diaz-Castro performed RNA-Seq analysis for **Figure 6.6**. In **Chapters 7 and 8**, I used DREADD viruses generated by Dr. J. Christopher Oceau, Alexander Reeves, and Dr. Xinzhu Yu. EFS-evoked calcium imaging in **Figure 7.8** and EFS-evoked glutamate imaging in **Figure 8.5** were performed by Dr. Eiji Shigetomi. Some of the electrophysiology for **Figure 8.7** were performed by Dr. Baljit Khakh. Dr. Blanca Diaz-Castro performed RNA-Seq analysis for **Figure 8.1**.

Dr. Sandeep Deverasetty developed the searchable website for our RNA-Seq and proteomic data (<http://astrocyternaseq.org/>) with help with Dr. Giovanni Coppola, Dr. Blanca Diaz-Castro, Dr. Baljit Khakh, and myself. Additionally, Dr. Blanca Diaz-Castro created hand-

drawn cartoons used in **Figures 2.1 and 6.1**. RNA-Seq and microarrays were performed at the UCLA Clinical Microarray Core and the UCLA Neuroscience Genomic Core. Flow cytometry was performed in the UCLA Jonsson Comprehensive Cancer Center (JCCC) and Center for AIDS Research Flow Cytometry Core Facility.

My graduate training has been incredibly exciting, and like many things worth doing in life, it had its challenges. Therefore, I want to thank Dr. Baljit Khakh, Khakh lab members and the Department of Physiology administration for their encouragement during this process. Dr. Daguang Wang, Dr. Stephen George, Dr. Bjoern Schwer, Dr. Kelsey Martin, and Dr. Carlos Portera-Cailliau have all provided support and valuable advice. I am grateful for my wonderful friends and family near and far. Finally, none of this would be possible without my mother who taught me how to stand up after falling down, and whose unwavering love and support I never take for granted.

## VITA

### Education

2005-2009 B.A. in Neuroscience from **Amherst College**, Amherst, MA

### Publications

1. Vilariño-Güell C, Soto AI, Lincoln SJ, Yahmed SB, Kefi M, Heckman MG, Hulihan MM, **Chai H**, Diehl NN, Amouri R, Rajput A, Mash DC, Dickson DW, Middleton LT, Gibson RA, Hentati F, Farrer MJ (2009). *ATP13A2* variability in Parkinson's disease. ***Human Mutation***, 30(3): 406-10. PMID: PMC2650009.
2. Vilariño-Güell C, **Chai H**, Keeling BH, Young JE, Rajput A, Lynch T, Aasly JO, Uitti RJ, Wszolek ZK, Farrer MJ, Lin SC (2009). MEIS1 p.R272H in familial restless legs syndrome. ***Neurology***, 73(3): 243-5. PMID: PMC2715576.
3. Schwer B, Schumacher B, Lombard DB, Xiao C, Kurtev MV, Gao J, Schneider JI, **Chai H**, Bronson RT, Tsai LH, Deng CX, Alt FW (2010). Neural sirtuin 6 (Sirt6) ablation attenuates somatic growth and causes obesity. ***Proc Natl Acad Sci USA***, 107(50): 21790-4. PMID: PMC3003110.
4. Boboila C, Oksenyich V, Gostissa M, Wang JH, Zha S, Zhang Y, **Chai H**, Lee CS, Jankovic M, Saez LM, Nussenzweig MC, McKinnon PJ, Alt FW, Schwer B (2012). Robust chromosomal DNA repair via alternative end-joining in the absence of X-ray repair cross-complementing protein 1 (XRCC1). ***Proc Natl Acad Sci USA***, 109(7): 2473-8. PMID: PMC3289296.
5. Shi W, Bain AL, Schwer B, Al-Ejeh F, Smith C, Wong L, **Chai H**, Miranda MS, Ho U, Kawaguchi M, Miura Y, Finnie JW, Wall M, Heierhorst J, Wicking C, Spring KJ, Alt FW, Khanna KK (2013). Essential developmental, genomic stability, and tumour suppressor

functions of the mouse orthologue of hSSB1/NABP2. **PLoS Genet**, Feb; 9(2):e1003298.

PMCID: PMC3567186.

6. Xu J, **Chai H**, Ehinger K, Egan TM, Srinivasan, R, Frick M, Khakh BS (2014). Imaging P2X4 receptor subcellular distribution, trafficking and regulation using P2X4-pHluorin. **Journal of General Physiology**, 144(1): 81-104. PMCID: PMC4076521.
7. Srinivasan R\*, Huang B\*, Venugopal S, Johnston A, **Chai H**, Zeng H, Golshani P, Khakh BS (2015). Ca<sup>2+</sup> signaling in astrocytes from IP3R2<sup>-/-</sup> mice in brain slices and during startle responses in vivo. **Nature Neuroscience**, 18(5): 708-717. PMCID: PMC4429056. \*co-first authors
8. Srinivasan R\*, Lu TY\*, **Chai H\***, Xu J, Huang BS, Golshani P, Coppola G, Khakh BS (2016). New transgenic mouse lines for selectively targeting astrocytes and studying calcium signals in astrocyte processes in situ and in vivo. **Neuron**, 92(6): 1181-1195. \*co-first authors
9. **Chai H\***, Diaz-Castro B\*, Shigetomi E, Monte E, Oceau JC, Yu X, Cohn W, Rajendran PS, Vondriska TM, Whitelegge JP, Coppola G, Khakh BS. Neural circuit-specialized astrocytes: genomic, proteomic, morphological and functional evidence. **Neuron**, (*accepted for publication*) \*co-first authors
10. Oceau JC, **Chai H**, Jiang R, Bonanno S, Martin KC, Khakh BS. Neuron-astrocyte proximity assay (NAPA) at synaptic scales. (*being prepared for submission*)

### Honors and Awards

2007-2009	Barry M. Goldwater Excellence in Education Scholarship
2013-2015	Jennifer S. Buchwald Graduate Fellowship in Physiology
2015-2019	Ruth L. Kirschstein National Research Service Award (F30)
2017	Eva Mary Kavan Prize for Excellence in Research on the Brain

## CHAPTER 1: INTRODUCTION

### Section 1.1: Astrocytes play functionally important roles in the central nervous system

Astrocytes are one of the major types of glia, which make up roughly half of the cells in the adult human brain, and serve active and homeostatic roles within neural circuits (Barres, 2008; Herculano-Houzel, 2014; Li et al., 2014). These ubiquitous cells are remarkably complex with thousands of processes that create characteristically “bushy” astrocytes (Shigetomi et al., 2013; Tong et al., 2013). The finest processes impinge on synapses, where they regulate synapse formation, removal, and function (Allen, 2014; Chung et al., 2015b). In the last decade or so, a number of astrocyte secreted and membrane-bound factors have been identified and shown to be involved in modulating synapse development and maintenance (**Table 1.1**).

The endfeet of astrocytes also wrap around blood vessels, and are thought to modulate blood flow and contribute to the blood brain barrier (Bazargani and Attwell, 2015; Li et al., 2014; Otsu et al., 2014). Thus astrocytes are physically poised to be involved in brain metabolism. Consistent with this, astrocytes are the only cells in the brain to store glycogen, which in fact is a defining feature of astrocytes (Lundgaard et al., 2014; Ventura and Harris, 1999). Furthermore, astrocytes also produce cholesterol and other lipoproteins, which are key components of cell and organelle membranes with defects linked to a variety of neuropsychiatric disorders (Dietschy and Turley, 2004; Vitali et al., 2014).

In addition to their metabolic functions, astrocytes modulate neuronal excitability and facilitate fast repetitive neurotransmission through uptake of potassium ions ( $K^+$ ) and neurotransmitters (Waltz 2000, Oliet 2001). Astrocytes may also act as sensors of other extracellular ions to modulate neuronal network activity. For example, some retrotrapezoid nucleus astrocytes respond to extracellular pH ( $CO_2/H^+$ ) and modulate local network activity to influence respiratory drive (Mulkey and Wenker, 2011). Astrocytes function as individual cells and as a network to potentially integrate and modulate signaling in a local neuronal circuit.

<b>Factors</b>	<b>Function and mechanism</b>	<b>Levels of evidence</b>	<b>References</b>
Thrombospondins	Secreted and induce formation of excitatory synapses via neuronal gabapentin receptor $\alpha 2\delta 1$	-mRNA expression, synapse counting and function with electrophysiology (cell culture and mouse)	(Cahoy et al., 2008; Christopherson et al., 2005; Eroglu, 2009; Eroglu et al., 2009)
Hevin	Secreted and promotes formation of excitatory synapses by bridging neurexins and neuroligins.	- synapse function with electrophysiology (cell culture) - mRNA expression, synapse counting (cell culture and mouse) - circuit function (mouse)	(Cahoy et al., 2008; Kucukdereli et al., 2011; Singh et al., 2016)
SPARC	Secreted to antagonize hevin and inhibits formation of excitatory synapses	- synapse function with electrophysiology (cell culture) - mRNA expression, synapse counting (cell culture and mouse)	(Cahoy et al., 2008; Kucukdereli et al., 2011)
Glypicans 4/6	Secreted and induce formation of functional excitatory synapses via increased recruitment of GluA1 AMPA receptors to neuron cell surface	- synapse function with electrophysiology, synapse counting (cell culture and mouse) - mRNA expression (mouse)	(Allen et al., 2012)
Megf10 and Mertk	Membrane receptors that recognize engulfment signals to eliminate synapses during development	- synapse counting (cell culture) - circuit function with electrophysiology, mRNA expression, protein expression and engulfed structures (mouse)	(Chung et al., 2013)
ApoE	Synapse elimination	- protein expression and engulfed structures (cell culture and mouse)	(Chung et al., 2016; Zhu et al., 2012)

**Table 1.1: Astrocyte derived factors involved in synapse development and maintenance.**

Astrocytes couple to one another through gap-junctions composed of Connexins (Cxn43 and Cxn 30) (Oberheim et al., 2012; Pannasch et al., 2011) and exhibit intracellular and intercellular calcium ion ( $\text{Ca}^{2+}$ ) elevations in response to local excitatory and inhibitory neuronal activity (Charles et al., 1991; Cornell-Bell et al., 1990a; Dani et al., 1992; Kang et al., 1998). Astrocytes also respond with intracellular  $\text{Ca}^{2+}$  elevations during distinct responses *in vivo* such as locomotion and startle (Otsu et al., 2014; Paukert et al., 2014; Shigetomi et al., 2016; Srinivasan et al., 2015; Wang et al., 2006) and they are implicated in the regulation of complex mouse behaviors (Halassa and Haydon, 2010). The mechanisms of how astrocyte calcium signals regulate circuit activity and animal behavior remain an open question.

## **Section 1.2: Historical understanding of neuroglia and astrocyte diversity**

Although the functional importance of astrocytes is increasingly valued by today's neuroscience community, these cells have not been historically viewed as such. In fact, glial cells (referring collectively to the non-neuronal cells in the brain) were considered structural support cells for many years. Neuroglia was first termed in 1856 by Rudolf Virchow as the substance which "lies between the proper nervous parts" of the nervous system acting as a connective element with few cellular components (Kettenmann and Verkhratsky, 2008). Neuroscientists' ideas about glia, and indeed neurons, were changing rapidly due to the creation of Golgi's silver nitrate staining method in 1886, which revealed individual cell morphology at a hitherto unknown resolution (Andriezen, 1893). Nearly 40 years later after Virchow described neuroglia, Michael von Lenhossek coined the term astrocyte for protoplasmic stellate glia (Kettenmann and Verkhratsky, 2008). Around the turn of the 20<sup>th</sup> century, Santiago Ramón y Cajal advanced our understanding of glia by creating a gold chloride-sublimate staining method that we now know visualizes GFAP intermediate filaments, found in many astrocytes (Roqué, 1966; Şovrea and Boşca, 2013).

In the late 19<sup>th</sup> century when the term astrocytes was first coined also came the first recognition of glial diversity with the division of glia into fibrous and protoplasmic glia (Andriezen, 1893; Kettenmann and Verkhratsky, 2008). Ramón y Cajal's drawings clearly highlighted morphological diversity of protoplasmic glia, and astrocytes in particular, although they were not referred to as such until later (Ramón y Cajal and DeFelipe, 1988). Over the years, genetic targeting approaches have become increasingly powerful tools to study cell function and cell subtype differences. However, the inability to specifically target astrocytes has caused the astrocyte field to lag behind in these areas. Moreover, understanding of the functional heterogeneity of astrocytes had been slowed by the fact that these cells are electrically unexcitable and thus not easily explored by traditional electrophysiological approaches, which were used to describe neuronal firing patterns in the classification neurons (Ascoli et al., 2008; Cauli et al., 1997; Kepecs and Fishell, 2014; Klausberger et al., 2003).

Although the focus of this dissertation is on regional, physiological heterogeneity of protoplasmic astrocytes, one cannot ignore the longest standing classification of astrocytes. The earliest observation of astrocyte heterogeneity was the difference between fibrous astrocytes found in white matter and protoplasmic astrocytes found in grey matter. These cells exist in very different environments as white matter is heavily myelinated but synaptically sparse whereas grey matter is the opposite. The morphological differences between fibrous and protoplasmic astrocytes were noted as early as the 1890s (Andriezen, 1893; Kettenmann and Verkhratsky, 2008). Fibrous astrocytes have an elongated shape as their processes align with myelinated fibers whereas protoplasmic astrocyte processes are distributed more spherically with more complex branching (Lundgaard et al., 2014). However, whether these morphological differences have any function and molecular relevance eluded scientists for nearly a century (Lundgaard et al., 2014). More recently, white matter and grey matter astrocytes have been shown to exhibit molecular differences: protoplasmic astrocytes have lower expression of filamentous proteins

such as GFAP and vimentin (Lundgaard et al., 2014), which could contribute to fibrous astrocyte branch morphology. Cultured astrocytes and *ex vivo* experiments have provided evidence suggesting that fibrous astrocytes are functionally different and more tightly regulate extracellular levels of glutamate (Goursaud et al., 2009; Hassel et al., 2003). These are some examples of the evidence for morphological, molecular, and functional differences between protoplasmic and fibrous astrocytes. However, the possibility that the morphological differences between protoplasmic astrocytes first documented by Ramón y Cajal have functional and molecular relevance was largely unexplored. This was likely due to the lack of available tools and approaches needed to tackle this issue.

### **Section 1.3: Physiological regional astrocyte diversity in the brain remains relatively unexplored**

Astrocytes were considered to be a homogenous population even into the new millennium, in part due to the lack of tools to study their functions and molecular machinery. Studies of astrocyte biology began to take off in the 1970s with the ability to create primary astrocyte cultures (Kimelberg, 1983). The standard approach was to prepare astrocyte cultures from “cerebral cortices or hemispheres, and sometimes other regions,” of the brain of P1-3 rodents (Kimelberg, 1983). In a 1983 review of astrocyte function, the concept of regional astrocyte heterogeneity and its potential confound was disregarded; however, the evidence for astrocyte heterogeneity was starting to emerge. In 1984, Hansson showed that primary astrocytes cultured from the hippocampus had higher levels of catechol-O-methyltransferase, one of several enzymes that degrade catecholamines, when compared to cortex and striatum (Hansson, 1984). Using cultured astrocytes prepared from various embryonic day 13-16 mouse brain regions, Barbin and colleagues found that extracellular matrix glycoprotein gp190 was expressed at higher levels in cerebellum and midbrain derived astrocytes as compared with

cortical ones (Barbin et al., 1988; Prochiantz and Mallat, 1988). In low-density astrocyte cultures from various postnatal day (P) 1 mouse brain regions, more cortical and hippocampal astrocytes expressed  $\mu$ -opioid receptors as compared to striatal and cerebellar ones (Stiene-Martin et al., 1998). Striatal astrocytes in particular also had low expression of  $\delta$ -opioid receptors (Stiene-Martin et al., 1998). Therefore, astrocytes cultured from distinct brain regions exhibited differences in proteins with functional importance although direct functional roles were not shown.

Many of these early pieces of evidence for astrocyte heterogeneity relied on astrocyte cultures. However, gene expression profiling shows that cultured astrocytes are molecularly distinct from freshly dissociated astrocytes (Cahoy et al., 2008) and exhibit differences in  $\text{Ca}^{2+}$  signaling (Kimmelberg et al., 1997). These *in vitro* studies provided valuable insight into astrocyte biology, but the issue remains whether these findings reflected *in vivo* astrocyte biology. As discussed earlier, some of earliest evidence of *in vivo* astrocyte diversity came from morphological studies using GFAP staining. Expanding on documentation of morphological heterogeneity first begun by Ramón y Cajal, more recent studies have described several instances of regional astrocyte diversity in terms of shape. Olfactory bulb astrocytes can be categorized morphologically with GFAP staining and the distribution of astrocyte morphologies depended on the laminar layer (Bailey and Shipley, 1993). For example, the authors define astrocytes with a wedge shaped territory that was unique to the glomerular layer (Bailey and Shipley, 1993). Whether the regional diversity in astrocyte morphology reflects functional differences is still an open question.

The advent of astrocyte targeted transgenic (fluorescent protein reporters and Cre) mouse lines (Garcia et al., 2004; Yang and Gong, 2005; Zhuo et al., 1997; Zhuo et al., 2001) has led to increased understanding of astrocyte biology and appreciation for their complexity. Regional heterogeneity of astrocytes have been shown to be functionally relevant in spinal cord

development (Molofsky et al., 2014). Molofsky and colleagues performed transcriptomic analysis of sorted astrocytes from dorsal and ventral spinal cord of P7 mice and found *Sema3a*, a member of the semaphoring family that is critical for normal neuronal pattern development, to be preferentially expressed in ventral spinal cord astrocytes. They showed that *Sema3a* in ventral horn astrocytes was necessary for correct orientation of axon initial segment of nearby motor neurons and for repelling axons from dorsal sensory neurons during late prenatal development (Molofsky et al., 2014). Deletion of *Sema3a* in astrocytes but not motor neurons resulted in decreased motor neuron survival by P30 (Molofsky et al., 2014). Although not yet directly tested, there is emerging evidence supporting astrocyte heterogeneity in the brain. Soreq and colleagues examined gene expression in hundreds of post-mortem human brain samples spanning 10 brain regions from 20 to 100 years olds (Soreq et al., 2017) and found that astrocyte gene expression modules from different brain regions have appreciable spread in gene expression.

It is important to the study of regional astrocyte heterogeneity to first address what parameters cell type diversity should be based on. To frame this issue properly, we turn to the demonstration of interneuron subtypes and the lessons that have been learned from those studies.

#### **Section 1.4: Understanding cell type diversity: an interneuron perspective**

In the past few decades, there has been a great effort to understand the diversity of interneurons and classify them into subtypes. Initial efforts separately classified interneurons by cell morphology and connections, by protein expression and surface cell markers, and by electrophysiological properties (Ascoli et al., 2008). However, interneuron subtypes classified using different parameters could not be easily reconciled with each other. For example, Cre mouse lines driven by different molecular markers have failed to target homogenous cell

populations, indicating that molecular marker alone cannot classify interneurons (Kepecs and Fishell, 2014). Firing pattern is one electrophysiological property used to classify neurons and especially interneurons. However, interneurons in the same cortical layer can have similar firing patterns despite having localized versus projected axonal arborization (Ascoli et al., 2008). Instead of classifying interneurons based on one parameter, the consensus in the field is to instead classify based on morphology, connectivity, molecular markers, and intrinsic properties, such as firing pattern (**Figure 1.1**; (Ascoli et al., 2008; Cauli et al., 1997; Kepecs and Fishell, 2014). For example, Martinotti cells of the neocortex are defined based on branching pattern, connectivity to layers 1 and 5, firing pattern, and expression of somatostatin marker protein (Ascoli et al., 2008). Astrocytes, like interneurons, are multifaceted entities as evidenced by the multitude of functions attributed to these glial cells. Therefore, astrocyte heterogeneity and region-specific properties must also be assessed with multiple approaches rather than based on a single modality. This is a central theme of this dissertation.

### **Section 1.5: Hypothesis and rationale**

We sought to determine whether astrocytes from two distinct, mature brain neural circuits display physiological diversity in morphology, functions, and molecularly machinery using multiple approaches (**Figure 1.2**). We chose two exemplar neural circuits to test the hypothesis: the dorsal lateral (d.l.) striatum and hippocampus CA1 stratum radiatum (s.r.). The d.l. striatum and hippocampus CA1 s.r. are two brain regions that differ in cellular composition, connectivity, and are involved in distinct physiological behavior. Therefore, if astrocytes have neural circuit-specialized properties, then we would expect striatal and hippocampal astrocytes to differ in shape, cell intrinsic properties, and gene and protein expression.

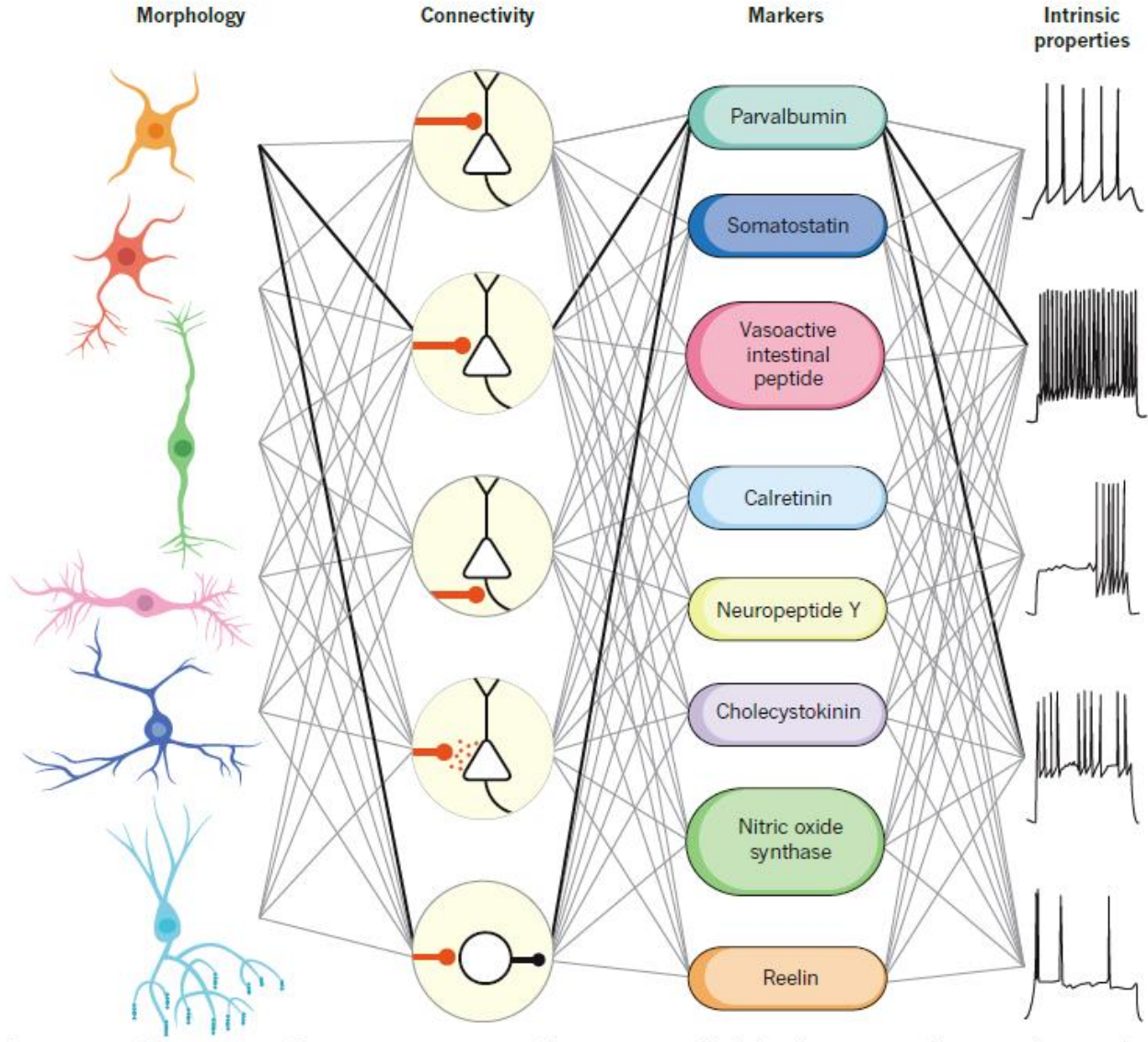


**Figure 1.1: Multiple dimensions of interneuron diversity.** Interneuron cell types are usually defined using a combination of criteria based on morphology, connectivity pattern, synaptic properties, marker expression and intrinsic firing properties. The highlighted connections define fast-spiking cortical basket cells. Reprinted with permission from Macmillan Publishers Ltd: *Nature*, Kepecs and Fishell, copyright 2014.

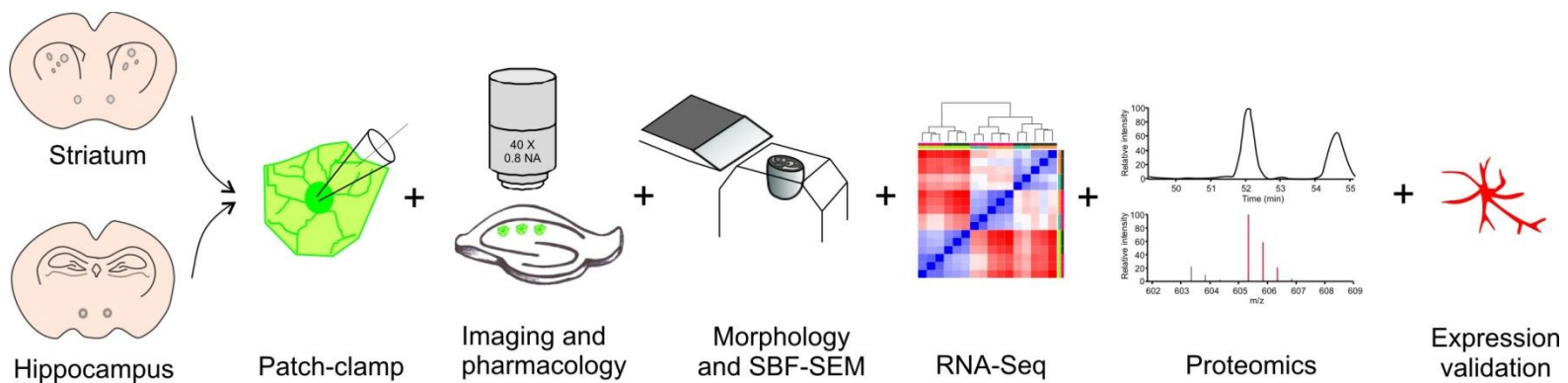


**Figure 1.2:** Schematic showing the integrated approaches used in this dissertation to evaluate striatal and hippocampal astrocytes for similarities and differences in molecular, morphological, and physiological features.

## Section 1.6: Two exemplar neural circuits

The hippocampus (**Figure 1.3**) comprises mainly excitatory glutamatergic neurons (Spruston and McBain, 2007). The hippocampal CA1 region is the site of the majority of hippocampal output and is necessary, among other things, for establishing long-term explicit memory (Morris, 2007). The hippocampus exhibits a highly stratified cytoarchitecture in both primate and rodent brains (**Figure 1.4**) (Amaral and Lavenex, 2006). The s.r. region is where glutamatergic Schaffer collateral axonal projections from the CA3 field synapse onto apical dendrites of the CA1 pyramidal neurons (Amaral and Lavenex, 2006). The excitatory glutamatergic neurons of the CA fields are located in the pyramidal cell layer, leaving the CA1 s.r. filled with axons, dendrites, and glia, with only sparse interneurons (Amaral and Lavenex, 2006).

In the hippocampus, work in *ex vivo* brain slices found that intracellular  $\text{Ca}^{2+}$  elevation have been shown to increase synaptic efficacy (Perea and Araque, 2007). This affects long-term potentiation (LTP) required for encoding hippocampal-mediated memory. Hippocampal LTP depends on astrocyte glutamate and D-serine release mediated by intracellular  $\text{Ca}^{2+}$  elevation (Henneberger et al., 2010; Perea and Araque, 2007). Furthermore, defects in astrocyte intercellular coupling have been shown to reduce LTP and contextual fear memory (Pannasch et al., 2014). Thus, hippocampal astrocytes appear to have functional significance on local neuronal circuits and behavior.

The striatum (**Figure 1.3**) is the major nucleus of the basal ganglia: it integrates converging excitatory and inhibitory signals from numerous parts of the brain and is involved in action selection, habit formation and motor function (Graybiel, 2008). The striatum consists mainly of inhibitory GABAergic medium spiny neurons (MSNs) (Graybiel, 2008). Unlike the hippocampus, the striatum does not have stratified cytoarchitecture (**Figure 1.4**), although complex labyrinth-like compartments of matrisomes and striosomes defined by neurochemical

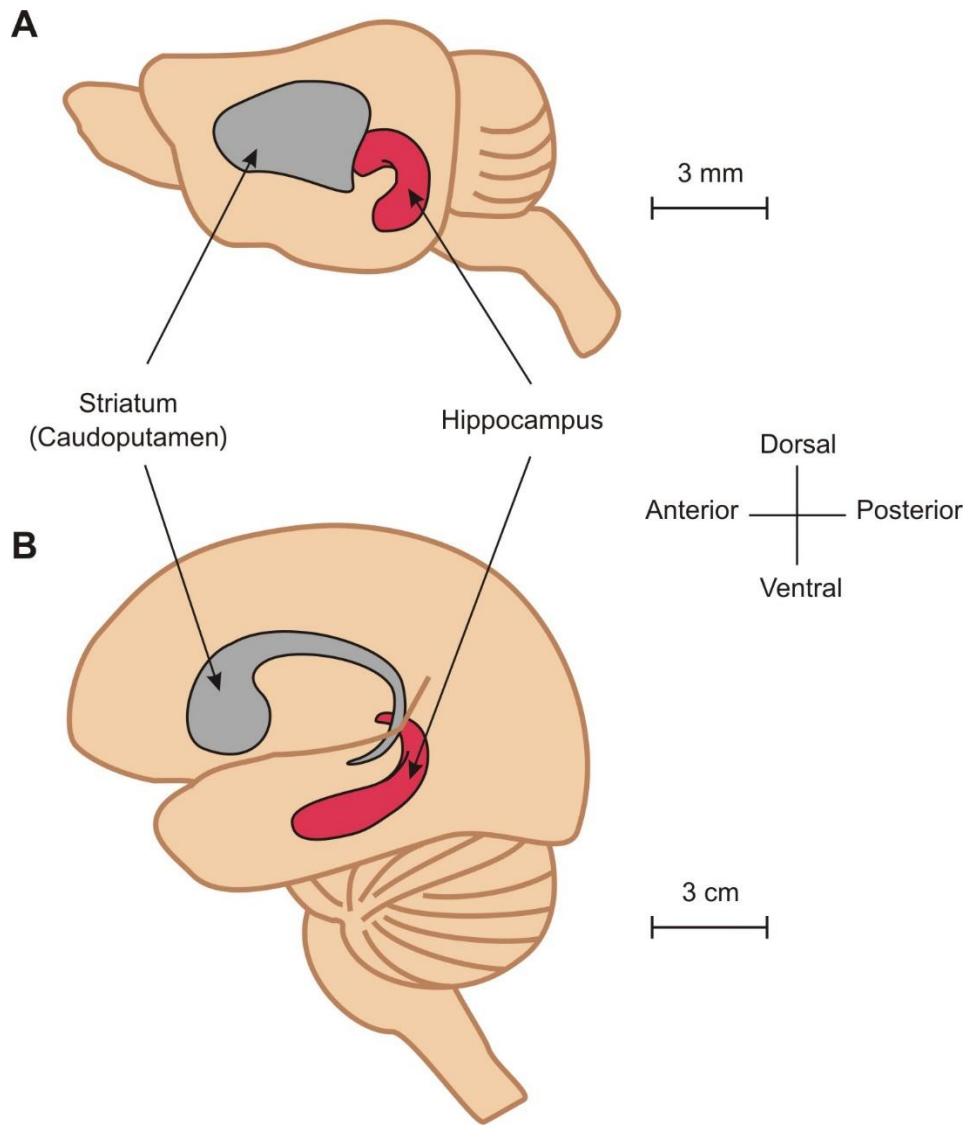


**Figure 1.3:** Illustration showing the location of the hippocampus and striatum in the rodent (**A**) and human (**B**) brain.

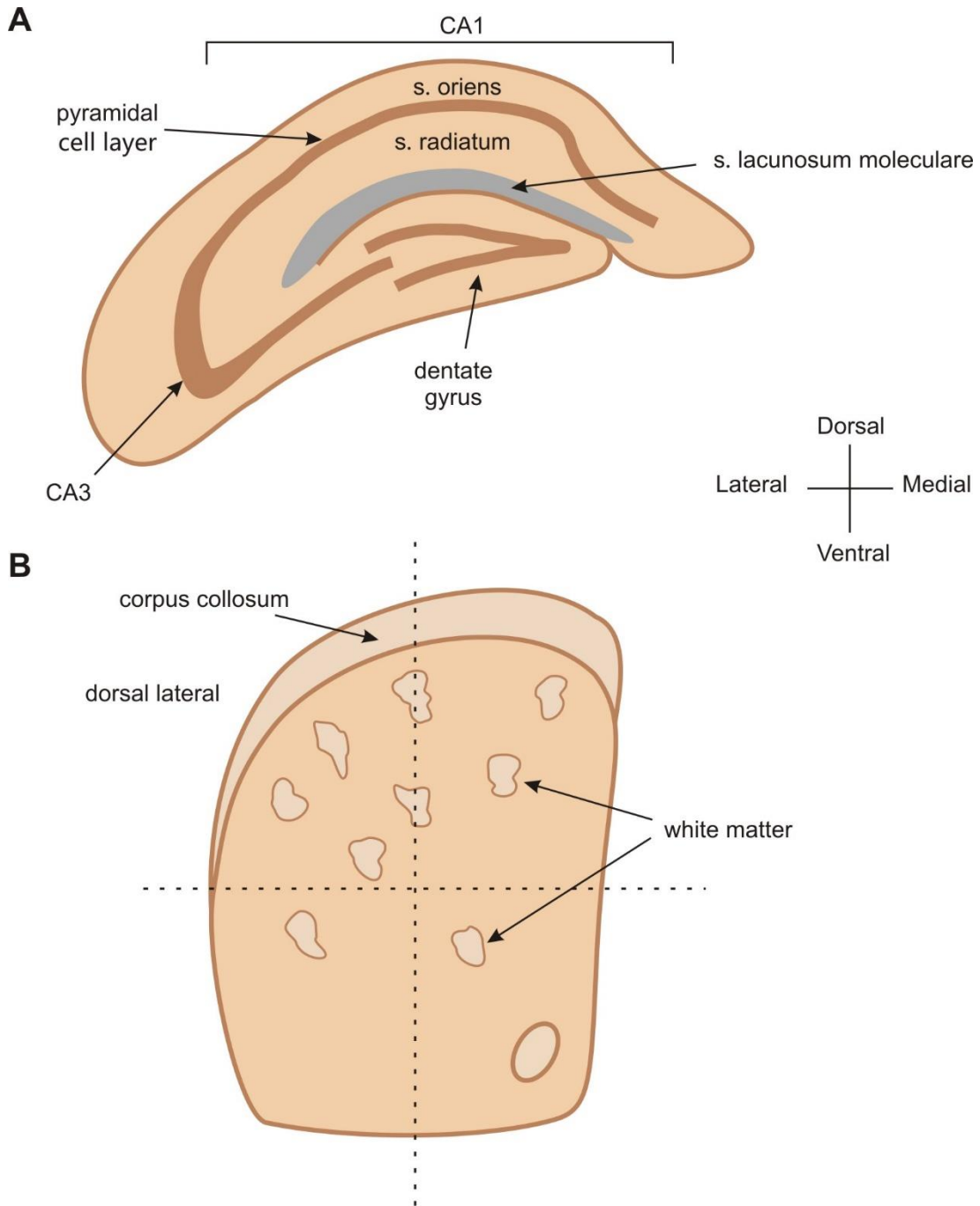


**Figure 1.4: Cartoon of coronal slice view of mouse hippocampus and striatum. A.** The layers of the murine hippocampus CA1 region: from dorsal to ventral: stratum oriens, pyramidal cell layer, stratum radiatum, stratum lacunosum moleculare. **B.** The nonstratified striatum described in quadrants imposed by scientists. Note: Matrisomes and striosomes classification are separate from white matter bundles coursing through the striatum.

expression and connectivity exist (Brown et al., 2002; Malach and Graybiel, 1986; Pert et al., 1976). The striatum as a whole receives significant dopaminergic innervations from the midbrain (namely substantia nigra pars compacta and ventral tegmental area) (Graybiel, 2008). The d.l. striatum specifically receives dopaminergic input from substantia nigra pars compacta (nigrostriatal pathway) and glutamatergic inputs from the sensorimotor cortex (corticostriatal pathway) and thalamus (thalamostriatal pathway) (Berendse and Groenewegen, 1990; Graybiel, 2008; Palmiter, 2008). The d.l. striatum mediates repetitive innate behaviors and consolidation of stimulus-reward association into habitual actions less sensitive to outcome (Balleine et al., 2007; Everitt and Robbins, 2013; Palmiter, 2008). Defects in the nigrostriatal pathway either due to lesions or pathology (such as Parkinson's disease) have been shown to cause significant motor impairment (Papp and Bal, 1987; Pioli et al., 2008).

Huntington's disease is a neurodegenerative disorder characterized by preferential dysfunction of striatal MSNs. Our lab has reported that striatal astrocytes show decreased Kir4.1 K<sup>+</sup> channel functional expression in mouse models of Huntington's disease (Tong et al., 2014). This leads to elevated levels of striatal extracellular K<sup>+</sup>, which increased MSN excitability. Viral delivery of Kir4.1 channels to striatal astrocytes restored Kir4.1 function and recovered aspects of MSN dysfunction, showing that astrocyte-mediated disturbances of K<sup>+</sup> homeostasis contributed to pathogenesis of Huntington's disease (Tong et al., 2014). Therefore, striatal astrocytes, much like hippocampal astrocytes, also have functional significance on local neuronal circuit and behavior.

Important to the discussion of regional astrocyte heterogeneity, it was observed that astrocytes from the striatum displayed larger Kir4.1 currents and marked Kir4.1 deficits in HD mice, whereas those from the hippocampus did not (Tong et al., 2014). This functional evidence for region specific differences in astrocytes in pathology raised the larger question of whether striatal and hippocampal astrocytes differ in the healthy brain. However, this issue was not

directly explored. For these reasons, we chose to study whether astrocytes in the d.l. striatum and CA1 s.r. have neural circuit-specialized properties.

## **Section 1.7: Summary**

Despite important progress, astrocytes remain an understudied cell population and much remains to be explored. Unlike neurons, which are extremely diverse and distinct within neural circuits, astrocytes have been viewed as a largely homogeneous population of cells. This raises a fundamental question: how can astrocytes be largely interchangeable and yet mediate their myriad separable responses? One hypothesis that has been recently advanced to explain this quandary is the possibility that astrocytes are not in fact a homogeneous population of glue-like cells throughout the brain (Haim and Rowitch, 2017; Khakh and Sofroniew, 2015; Zhang and Barres, 2010).

We sought to determine if astrocytes within two distinct, mature brain neural circuits were largely similar or distinct when assessed using a range of integrated state-of-the-art approaches that would permit candid assessment of diversity at multiple biological levels. In designing our study, we benefitted from the demonstration of interneuron diversity, which emphasizes evaluations using physiology, morphology, as well as gene, protein and cell marker expression (Kepecs and Fishell, 2014). Critical functions have been ascribed to astrocytes in both the hippocampus and striatum [for reviews see (Allen, 2014; Araque et al., 2014; Khakh and Sofroniew, 2015)], but like for other brain areas it is unclear how potentially interchangeable cells serve such diverse roles in hippocampal and striatal neural circuits, which themselves operate by utilizing distinct neuronal populations. Thus, the necessity to address astrocyte diversity at a basic biology level, the relevance to disease and neural circuit function, and the availability of new reagents/tools (see **Chapter 3**) presented a unique opportunity to determine if

astrocytes in the striatum and hippocampus were largely similar or if they displayed neural circuit-specificity.

## CHAPTER 2: METHODS

### Section 2.1: Experimental design

All animal experiments were conducted in accordance with the National Institute of Health Guide for the Care and Use of Laboratory Animals and were approved by the Chancellor's Animal Research Committee at the University of California, Los Angeles. Sample sizes were not calculated *a priori*. Data from every experiment represent a minimum of three animals.

For **Chapters 4 to 7**, data from every experiment represent a minimum of three animals using a balanced number of male and female mice. For adeno-associated virus (AAV) injections, mice were randomly assigned to striatal or hippocampal groups. In calcium imaging experiments where endogenous G-protein coupled receptor (GPCR) agonists were applied sequentially, the sequence of drug application was randomized and each slice received at most three different agonists. For RNA-Seq (ribonucleic acid sequencing), the dissection and homogenization order of striatum and hippocampus alternated with every animal. For fluorescence-activated cell sorting (FACS), the sorting order of striatum and hippocampal cells alternated with every run.

### Section 2.2: AAV

In order to generate an AAV 2/5 capable of expressing Cre recombinase (Cre) or muscarinic receptor based Designer Receptors Exclusively Activated by Designer Drugs (DREADDs) in astrocytes, we modified plasmid "pZac2.1final" (Penn Vector Core). We removed the CMV promoter flanked by *Bgl*II and *Hind*III sites and replaced it with the minimal (~700 bp) *GfaABC<sub>1</sub>D* astrocyte-specific promoter, which was amplified by PCR from Addgene plasmid 19974. We then cloned Cre into this modified pZac2.1 vector between *Eco*RI and *Xba*I sites, to

generate plasmids we called “pZac2.1 GfaABC<sub>1</sub>D Cre”. The fully sequenced “pZac2.1” plasmids were sent to the Penn Vector Core, which used them to generate AAV 2/5 for each construct at a concentration of  $\sim 2 \times 10^{13}$  genome copies/ml (gc/ml). Our virus constructs have been deposited at Addgene in the Khakh lab repository ([http://www.addgene.org/Baljit\\_Khakh](http://www.addgene.org/Baljit_Khakh)). The AAVs are also available for purchase from the UPenn Vector Core (<http://www.med.upenn.edu/gtp/vectorcore>). The AAV2/5 GfaABC<sub>1</sub>D Cre has recently been reported by us (Anderson et al., 2016). The AAV FLEX-GFP was originally made in the Sternson laboratory (Atasoy et al., 2008) and was purchased from the UPenn Vector Core.

### **Section 2.3: Mouse models**

All mice were housed with food and water available *ad libitum* in a 12 h light/dark environment. All animals were healthy with no obvious behavioral phenotype, were not involved in previous studies, and were used during the light cycle. Data for experiments were collected from adult mice (8-11 weeks old for most experiments, 3-4 weeks old for electrophysiology, and 4-5 weeks old for proteomics and microarrays). Both male and female mice were used.

### **Generation of *Aldh111*-Cre/ERT2 and *Slc6a11*-Cre/ERT2 transgenic mice**

BAC transgenic mice expressing Cre/ERT2 from the *Aldh111* and *Slc6a11* locus were made using published methods (Yang and Gong, 2005). A 228 kb mouse BAC (RP23-7M9) containing the 48 kb mouse *Aldh111* coding region, a  $\sim 48$  kb 5' flanking region and  $\sim 130$  kb 3' flanking region was identified through a database search and obtained from the BACPAC Resource Center (Oakland Children's Hospital, Oakland, CA). Benefitting from an established protocol (Yang and Gong, 2005), the Cre/ERT2 cDNA (from Addgene plasmid #14797) was inserted into exon 1 of the *Aldh111* gene immediately preceding the translation initiation codon.

Cloning steps for construction of the modified *Aldh111* BAC targeting construct were essentially as described (Yang and Gong, 2005). Once completed, BAC purification, pronuclear injections and transgenic mouse generation was done at the University of California, Davis Mouse Biology Program (UC Davis MBP). Briefly, the modified *Aldh111* BAC construct was purified and then injected into the pronucleus of fertilized oocytes. Injected oocytes were implanted into female FVB mice to generate pups. Founder pups were identified by PCR amplification of the Cre/ERT2 cassette. All founder pups were created in an FVB background and then backcrossed to C57/Bl6N mice until a 100% congenic C57/Bl6N strain expressing *Aldh111*-Cre/ERT2 was achieved. The *Aldh111*-Cre/ERT2 mice were backcrossed with C57/Bl6N mice for > 5 generations, i.e. to ~97% C57/Bl6N. The mice that are to be deposited at JAX have been backcrossed for 8 generations (i.e. to ~99% C57/Bl6N).

Our mouse lines are available from The Jackson Laboratory: JAX Stock No. 029655: B6N.FVB-Tg(*Aldh111*-Cre/ERT2)1Khakh/J with a common name of “*Aldh111*-Cre/ERT2 BAC transgenic” and JAX Stock No. 029656: B6N.FVB-Tg(*Slc6a11*-Cre/ERT2)#Khakh/J with a common name of “*Slc6a11*-Cre/ERT2 BAC transgenic”.

### **Wild-type, other transgenic and knock-in mice**

B6;129S-*Gt(ROSA)26Sor<sup>tm95.1(CAG-GCaMP6f)Hze</sup>*/J (JAX# 024105; Ai95), Tg(*Slc1a3*-Cre/ERT)1Nat/J (JAX# 012586) and B6N.129-*Rpl22<sup>tm1.1Psam</sup>*/J (JAX# 011029; RiboTag) were acquired from the Jackson Laboratory. mGFAP-Cre 77.6 mice were available from past work (Gregorian et al., 2009). *Gjb6*-Cre/ERT2 mice were obtained from Dr. Frank Pfrieder (Institute of Cellular and Integrative Neurosciences, Strasbourg France). These mouse lines and *Aldh111*-Cre/ERT2 and *Slc6a11*-Cre/ERT2 BAC transgenic mice reported here were maintained by breeding with C57BL6/N mice (from Taconic), and hemizygous transgenic mice were used for experiments.

*Aldh111*-eGFP BAC transgenic mice (MMRRC #3843271) on a Swiss-Webster background were acquired from MMRRC and maintained by breeding with Swiss-Webster mice (from Taconic) to maintain outbred colony. The *Aldh111*-eGFP line labels essentially all astrocytes in the central nervous system with minimal expression in neurons (Cahoy et al., 2008). Hemizygous transgenic mice and wild-type littermates were used for experiments.

### **Generation of Ai95 x *Aldh111*-Cre/ERT2 double transgenic mice**

To generate double transgenic mice, heterozygous Ai95 mice were crossed with hemizygous *Aldh111*-Cre/ERT2 BAC mice. The Ai95 and Lck-GCaMP6<sup>flox</sup> knock-in mice respectively possess a floxed knock-in of cyto-GCaMP6f and Lck-GCaMP6f in the ROSA26 locus, while *Aldh111*-Cre/ERT2 BAC mice possesses promoter and enhancer elements of the *Aldh111* gene driving expression of Cre/ERT2. Double transgenic pups were identified by genotyping for GCaMP6f at the ROSA26 locus (forward primer 5'–AGCTCGCCTACCACTACCAGCA–3'; reverse primer 5'–TTGAAGAAGATGGTGCCTCCTG–3') and Cre/ERT2 (forward primer 5'–AGACCAATCATCAGGATCTCTAGCC–3'; reverse primer 5'–CATGCAAGCTGGTGGCTGG–3') in two separate PCR reactions for each pup. Double transgenic progeny used for experiments are heterozygous for cyto-GCaMP6f at the ROSA26 locus and hemizygous for the *Aldh111*-Cre/ERT2 insert.

### **Generation of RiboTag x *Aldh111*-Cre/ERT2 double transgenic mice**

To generate double transgenic mice for astrocyte RNA extraction, B6N.129-*Rpl22*<sup>tm1.1P<sup>sam</sup></sup>/J (JAX# 011029) were acquired from the Jackson Laboratory and bred with *Aldh111*-Cre/ERT2 mice (N8 backcrossed to C57BL6/N for Chapter 3; N3 backcrossed to

C57BL6/N for Chapter 4) from an in-house colony; hemizygous transgenic heterozygous knock-in mice were used for RNA-Seq experiments.

#### **Section 2.4: Tamoxifen administration to adult mice**

Tamoxifen (Sigma) was freshly prepared at a concentration of 20 mg/ml in corn oil (Crisco) and dissolved overnight with continuous agitation. To induce gene expression, tamoxifen was administered intraperitoneally 75 mg/kg per mouse for five consecutive days, using a 1 ml syringe and a 25 G 5/8-inch needle (BD Biosciences). Experiments were performed two weeks after the last tamoxifen injection. For **Figure 3.13** and **3.14**, single dose of tamoxifen at 25 mg/kg, 75 mg/kg, or 225 mg/kg was administered intraperitoneally.

#### **Section 2.5: Stereotaxic microinjections of AAVs**

Stereotaxic injections into the mouse hippocampus and striatum were performed as previously described (Jiang et al., 2016; Jiang et al., 2014; Shigetomi et al., 2013; Tong et al., 2013). Mice (P42-56) were used in all surgeries in accordance with institutional guidelines. All surgical procedures were conducted under general anesthesia using continuous isoflurane (induction at 5%, maintenance at 1–2.5% vol/vol). Depth of anesthesia was monitored continuously and adjusted when necessary. Following induction of anesthesia, the mice were fitted into a stereotaxic frame with their heads secured by blunt ear bars and their noses placed into an anesthesia and ventilation system (David Kopf Instruments). Mice were administered 0.1 mg/kg of buprenorphine (Buprenex, 0.1 mg/ml) subcutaneously before surgery. The surgical incision site was then cleaned three times with 10% povidone iodine and 70% ethanol (vol/vol). Skin incisions were made, followed by craniotomies of 2–3 mm in diameter above the left frontal or parietal cortex using a small steel burr (Fine Science Tools) powered by a high-speed drill

(K.1070, Foredom). Saline (0.9%) was applied onto the skull to reduce heating caused by drilling. Unilateral viral injections were carried out by using a stereotaxic apparatus (David Kopf Instruments) to guide the placement of beveled glass pipettes (1B100-4, World Precision Instruments). For the left hippocampus: the coordinates were 2 mm posterior to bregma, 1.5 mm lateral to midline, and 1.6 mm from the pial surface. For the left striatum: the coordinates were 0.8 mm anterior to bregma, 2 mm lateral to midline, and 2.4 mm from the pial surface. AAV was injected by using a syringe pump (Pump11 PicoPlus Elite, Harvard Apparatus). Glass pipettes were left in place for at least 10 min prior to slow withdraw. Surgical wounds were closed with external 5-0 nylon sutures. Following surgery, animals were allowed to recover overnight in cages placed partially on a low-voltage heating pad. Buprenorphine (0.1 mg/kg) was administered two times per day for up to 2 days after surgery. In addition, trimethoprim sulfamethoxazole was provided in food to the mice for 1 week. Virus injected mice were euthanized two to three weeks post surgery for live slice imaging or perfused for immunohistochemistry. Viruses used were: 1  $\mu$ l of AAV2/5 CAG-FLEX-GFP virus ( $\sim 10^{10}$  genome copies), 1  $\mu$ l of AAV2/5 GfaABC<sub>1</sub>D-Cre (Anderson et al., 2016), 1.3  $\mu$ l of AAV2/5 GfaABC<sub>1</sub>D-cyto-GCaMP6f virus ( $3 \times 10^{10}$  genome copies); 1.3  $\mu$ l of AAV2/5 GfaABC<sub>1</sub>D-HM3D-mCherry, HM4D-mCherry, or RM3D-mCherry virus ( $\sim 10^{10}$  genome copies); 1.3  $\mu$ l of AAV2/5 GfaABC<sub>1</sub>D-iGluSnFr virus ( $6 \times 10^9$  genome copies). Two viruses were co-injected for DREADD calcium and glutamate imaging; the injections in those cases were as follows: 1.3  $\mu$ l of AAV2/5 GfaABC<sub>1</sub>D-cyto-GCaMP6f virus with AAV2/5 GfaABC<sub>1</sub>D-HM3D-mCherry, HM4D-mCherry, or RM3D-mCherry virus ( $\sim 10^{10}$  genome copies each); 1.3  $\mu$ l of AAV2/5 GfaABC<sub>1</sub>D-iGluSnFr with AAV2/5 GfaABC<sub>1</sub>D-HM3D-mCherry virus ( $4 \times 10^9$  genome copies each).

## **Section 2.6: *In vivo* calcium imaging**

### **Head bar installation and cranial window surgery**

Five days after tamoxifen injections (see **Section 2.3**), adult (> 8 weeks) male and female mice of the relevant genotypes were anesthetized with isoflurane and placed in a stereotaxic frame (Kopf). Dexamethasone (0.2 mg/kg) was administered subcutaneously before surgery began. Surgery was performed under standard and sterile conditions. After hair removal and lidocaine application (2%, Akorn), the mouse's skull was exposed from the frontal to the intraparietal bone, and the connective tissue was carefully removed from the skull for the custom-made head bar to be glued on using cyanoacrylate (Krazy Glue). Vetbond (3M) was used to close the incision site. A small chamber then was made surrounding the incision site with black dental cement (Ortho-Jet, Lang Dental) to hold water for the water-immersion objective lens during imaging. A 3 mm diameter circular craniotomy was performed carefully using a dental drill bit with the center located at 2.5 mm lateral to lambda (**Figure 2.1**). The cranial window was then sealed with a 3 mm diameter round #1 coverslip using Vetbond. The animal was given carprofen (5 mg/kg) and amoxicillin (BIOMOX, Virbac Animal Health) post-surgery for at least a week to recover from the surgery before subjecting to imaging.

### ***In vivo* two-photon laser scanning microscopy (2PLSM) and air puff startle**

Two-photon laser-scanning microscopy was performed with a Moveable Objective Microscope (Sutter MOM) using a Ti-Sapphire laser (Coherent Ultra II) at 920 nm, through a 40X 0.8 NA water-immersion objective (Olympus). The objective was mounted at a tilt of 30 degrees to the vertical axis in order to image with the light path perpendicular to the cranial window and the cortical surface. Images were acquired using the *ScanImage* software (Vidrio Technologies) and processed with *ImageJ* software (NIH). Fully awake mice, without any

anesthesia, were mounted on top of a spherical treadmill by securing the head-bar onto a custom-made head-bar holder under the microscope. The treadmill consisted of an 8-inch diameter Styrofoam ball resting inside another Styrofoam hollow half-sphere (Graham Sweet Studios) into which a constant stream of compressed air was blown to keep the ball afloat, allowing mice to freely run or rest on top. Images were acquired every 750 ms (1.33 Hz). To track the mouse's locomotion, the treadmill motion was measured every 25 ms (40 Hz) by a custom-designed optical sensor whose signals were converted into two servo pulse analog signals (front-back and left-right) using an external PIC microcontroller. The locomotion data were acquired simultaneously with the calcium imaging data and synchronized through the scanning mirror signals. These analog signals were digitized with a NIDAQ board (National Instruments) and acquired with the WinEDR software (Strathclyde). The microscope and treadmill were encased in a light-tight box, and the animals were kept in darkness without visible visual stimuli during the imaging sessions. Before experiments, mice were acclimated to the head fixation and to resting and running on the spherical treadmill, as previously described (Polack et al., 2013; Srinivasan et al., 2015).

Startle was induced by presenting a brief air puff to the face of the mice while the mice were resting on top of the spherical treadmill during the imaging sessions. The air puff was delivered by pressing a hand-pump air compressor (28 x 5 cm) attached to a ¼-inch PVC tubing with its opening positioned ~1 cm away from the nostril of the mice (**Figure 2.1**). One press of the hand pump generated a ~3 s long gentle air puff. Behavioral startle was confirmed by the locomotion induced immediately after presenting the air puff.

## **Section 2.7: Immunohistochemistry (IHC)**

For transcardial perfusion, mice were euthanized with barbiturate overdose and perfused with 10% buffered formalin (Fisher #SF100-20). Briefly, once all reflexes subsided, the

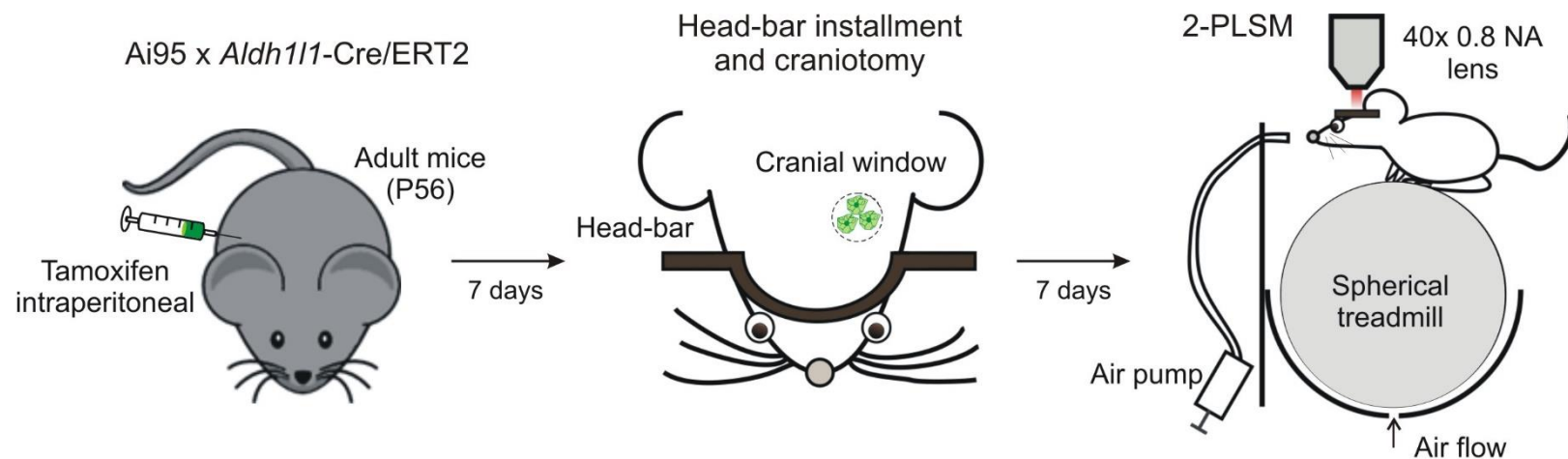


**Figure 2.1: Schematic drawings showing the workflow for *in vivo* 2PLSM in head-fixed, awake mice.** In brief, 7 days after the mice were injected with tamoxifen, a lightweight metal head bar was glued to their skull and a 3 mm cranial window was made above the visual cortex. After another 7 days, mice were then head-fixed onto a spherical treadmill where they were free to rest or run. A 40 x objective lens as part of a 2-photon laser scanning imaging microscope was positioned above the cranial window. An air pump outside the microscope enclosure was used to generate an unexpected air puff, which evoked startle responses.

abdominal cavity was opened and heparin (50 units) was injected into the heart to prevent blood clotting. The animal was perfused with 20 ml ice cold 0.1 M phosphate buffered saline (PBS) followed by 60 ml 10% buffered formalin. After gentle removal from the skull, the brain was postfixed in 10% buffered formalin overnight at 4°C. The tissue was cryoprotected in 30% sucrose PBS solution the following day for at least 48 h at 4°C until use. 40 µm coronal sections were prepared using a cryostat microtome (Leica) and processed for immunohistochemistry. For staining of acute slices, 300 µm slices were placed into 10% buffered formalin overnight at 4°C and processed as follows for IHC.

### **Diaminobenzidine (DAB) staining for brightfield microscopy**

To stain cyto-GCaMP6f for brightfield microscopy, sections were washed in 0.1 M tris buffered saline (TBS) and treated with 1% H<sub>2</sub>O<sub>2</sub> for 20 min to block endogenous peroxidase activity. The sections were incubated with 10% normal goat serum (NGS) and 0.5% Triton-X 100 in 0.1 M TBS at room temperature for 60 min. Sections were then incubated with a chicken anti-GFP antibody (1:1000; Abcam ab13970) in 0.1 M TBS overnight at 4°C. After three 10 min washes in 0.1 M TBS, followed by incubation with biotinylated goat anti-chicken antibody (1:400; Vector ABC Standard kit) in 0.1 M TBS with 10% NGS for 1 h at room temperature. After another three 10 min washes in 0.1 M TBS, the sections were incubated for 1 h at room temperature in an avidin–biotin complex, which was made by mixing one drop each of A and B solutions from the Vector ABC Standard Kit. Staining was visualized by incubation with a mixture of developing buffer from the ABC Standard Kit, diaminobenzidine (DAB, Sigma) as the developing agent and H<sub>2</sub>O<sub>2</sub> in ddH<sub>2</sub>O, which causes dark brown staining in areas with cyto-GCaMP6f expression. Brain sections were subsequently dehydrated and mounted with Eukitt (Calibrated Instruments).

## **Antibody staining for confocal microscopy**

Sections were washed 3 times in 0.1 M PBS for 10 min each, and then incubated in a blocking solution containing 10% NGS in 0.1 M PBS with 0.5% Triton-X 100 for 1 h at room temperature with agitation. Sections were then incubated with agitation in primary antibodies diluted in 0.1 M PBS with 0.5% Triton-X 100 overnight at 4°C. The following primary antibodies were used: chicken anti-GFP (1:1000; Abcam ab13970), rabbit anti-GFP (1:1000; Molecular Probes A11122), mouse anti-NeuN (1:1000; Millipore MAB377 or Abcam ab104225), rabbit anti-NeuN (1:1000; Cell Signaling D3531), mouse anti-mCherry (1:1000; Saint John's STJ97087), rabbit anti-S100 $\beta$  (1:1000; Abcam ab41548), chicken anti-GFAP (1:1000; Abcam ab4674), Guinea pig anti-GLT1 (1:2500; Millipore AB1783), rabbit anti-KIR4.1 (1:1500; Alomone APC-035), and mouse anti- $\mu$ -crystallin (1:250; Santa Cruz sc-376687). The next day the sections were washed 3 times in 0.1 M PBS for 10 min each before incubation at room temperature for 2 h with secondary antibodies diluted in 0.1 M PBS. The following Alexa conjugated secondary antibodies (Molecular Probes) were used: goat anti-chicken 488 (1:1000), goat anti-rabbit 488 (1:1000), streptavidin conjugated 488 (1:250), streptavidin conjugated 555 (1:250), goat anti-rabbit 546 (1:1000), goat anti-mouse 546 (1:1000), goat anti-guinea pig 546 (1:1000), and goat anti-rabbit 647 (1:1000). The sections were rinsed 3 times in 0.1 M PBS for 10 min each before being mounted on microscope slides in fluoromount-G.

## **IHC confocal microscopy imaging**

Fluorescence images were taken using UplanSApo 20X 0.85 numerical aperture (NA) and UplanFL 40X 1.30 NA oil immersion objective lens on a confocal laser-scanning microscope (Fluoview 1000; Olympus). We used the 488 nm line of an Argon laser to excite Alexa 488, with the intensity adjusted to 4% of the maximum output (10 mW). The emitted light pathway consisted of an emission high pass filter (505-525 nm) before the photomultiplier tube.

Alexa 546 was excited by the 543 nm laser line of the HeNeG laser at 20-25% of the maximum output (1 mW). The emitted light pathway consisted of a dichroic mirror (SDM560) and a 560–600 nm emission filter. Laser settings were kept the same within each experiment. Images represent maximum intensity projections of optical sections with a step size of 1.0  $\mu\text{m}$ . The data shown in **Figure 3.13** were gathered using an automated Nikon C2 confocal microscope and a 20X oil immersion lens.

### **IHC image analyses**

To generate coronal hippocampal and striatal montages such as those in **Figures 3.3, 3.5, 3.8, 3.12, 4.1, and 4.2**, images were obtained from 40  $\mu\text{m}$  thick coronal brain sections using a Fluoview 1000 confocal microscope equipped with a 20X 0.85 NA oil immersion lens (Olympus). Images were acquired at 1X digital zoom, such that immediately adjacent images had ~150 to 200  $\mu\text{m}$  of overlapping cellular features. Individual images obtained in this way were manually stitched on a black canvas in Microsoft PowerPoint or in Paint.net software and then exported as a single TIFF montage. During export of the TIFF image, dark boxes appear at the edges of the final images that are reported. These boxes do not represent areas of imaged fluorescence with zero pixel values, but they are areas for which no images were collected.

Images were processed with ImageJ software version 1.3 (NIH) and Imaris software version 7.6.5 (Bitplane). Cell counting was done on maximum intensity projections using the Cell Counter plugin; only cells with somata completely within the region of interest (ROI) were counted. In AAV injected hippocampal montages, numbers for GFP positive astrocytes and neurons were acquired by manually counting cells. Total numbers of astrocytes or neurons were obtained by counting the number of cells in the montage with S100 $\beta$  or NeuN staining, respectively. For signal area and intensity measurements of c-Fos (**Figure 7.13**), ROIs were created using the same intensity threshold in experimental and control images.

## Section 2.8: Acute brain slice preparation for imaging and electrophysiology

Slice procedures have been described previously (Jiang et al., 2016; Shigetomi et al., 2013). Coronal striatal or hippocampal slices were prepared from 8-11 week old Swiss-Webster mice with AAV injection and Ai95 x *Aldh111*-Cre/ERT2 mice with tamoxifen for imaging or from 3-4 week old *Aldh111*-eGFP and WT littermates for electrophysiology. Briefly, animals were deeply anesthetized with isoflurane and decapitated. The brains were placed and sliced in ice-cold modified artificial cerebral spinal fluid (aCSF) containing the following (in mM): 194 sucrose, 30 NaCl, 4.5 KCl, 1 MgCl<sub>2</sub>, 26 NaHCO<sub>3</sub>, 1.2 NaH<sub>2</sub>PO<sub>4</sub>, and 10 D-glucose, saturated with 95% O<sub>2</sub> and 5% CO<sub>2</sub>. A vibratome (DSK-Zero1, Ted Pella, Inc.) was used to cut 300 μm brain slices. The slices were allowed to equilibrate for 30 min at 32-34°C in normal aCSF containing (in mM); 124 NaCl, 4.5 KCl, 2 CaCl<sub>2</sub>, 1 MgCl<sub>2</sub>, 26 NaHCO<sub>3</sub>, 1.2 NaH<sub>2</sub>PO<sub>4</sub>, and 10 D-glucose continuously bubbled with 95% O<sub>2</sub> and 5% CO<sub>2</sub>. Slices were then stored at 21–23°C in the same buffer. All data were collected within 4-6 h of slicing.

We are aware that neurons and astrocytes can change in brain slices under some circumstances (Takano et al., 2014). However, our procedures were standardized, all relevant experiments were performed within 4-6 h of slicing, and the conditions were identical for hippocampus and striatum. Also, our procedures are identical to those routinely used for several decades to study both astrocytes and neurons. Finally, we have previously discussed the similarity between astrocyte calcium signaling in slices and *in vivo* under our experimental conditions (Khakh and Sofroniew, 2015; Shigetomi et al., 2016). Hence, we do not think slice procedures contribute markedly to our conclusions, but nonetheless our findings should be interpreted with these considerations in mind.

## Section 2.9: Electrophysiological recording and assessment of dye coupling *ex vivo*

Brain slices were placed in the recording chamber and continuously perfused with 95% O<sub>2</sub> and 5% CO<sub>2</sub> bubbled normal aCSF. Cells were visualized with infrared optics (700 nm) on an upright microscope (BX51WI, Olympus). pCLAMP10 software and a Multi-Clamp 700B amplifier was used for electrophysiology (Molecular Devices).

For recording from striatal medium spiny neurons and hippocampal CA1 pyramidal neurons, currents were measured in whole-cell mode using pipettes with a typical resistance of 5–6 MΩ when filled a K<sup>+</sup> intracellular solution consisting of the following (in mM): 135 potassium gluconate, 5 KCl, 0.5 CaCl<sub>2</sub>, 5 HEPES, 5 EGTA, 2 Mg-ATP and 0.3 Na-GTP, pH 7.3 adjusted with KOH. In some cases, 2 mg/ml biocytin was added to the intracellular solution to subsequently visualize patched neuron. Neurons were voltage-clamped at -70 mV unless otherwise stated. Extrasynaptic N-methyl-D-aspartate (NMDA)-mediated slow inward currents were recorded in low-Mg<sup>2+</sup> buffer (0.1 mM) in the presence of bicuculline (10 μM), tetrodotoxin (TTX; 250 nM), and 6-cyano-2,3-dihydroxy-7-nitroquinoxaline (CNQX; 10 μM). See **Table 2.1** for all pharmacological agents used. ClampFit 10.5 software was used to analyze traces from neuronal recordings.

For recording from astrocytes and dye coupling experiments, current were measured in whole-cell mode using pipettes with a typical resistance of 5.5 MΩ when filled with internal solution containing the following (in mM): 130 K-gluconate, 2 MgCl<sub>2</sub>, 10 HEPES, 5 EGTA, 2 Na-ATP, 0.5 CaCl<sub>2</sub>, with pH set to 7.3. 2 mg/ml biocytin was added to the intracellular solution to examine gap junction coupling. Astrocytes were held in whole-cell mode for 30 min to allow biocytin to diffuse from the patched cell to other cells connected by gap junctions. In some cases carbenoxolone (CBX; 100 μM) was added to the extracellular solution to block gap junctions. Brain slices were then rescued from the recording chamber for IHC.

## **Section 2.10: Astrocyte intracellular Ca<sup>2+</sup> and cell surface glutamate imaging with confocal microscopy *ex vivo***

Brain slice preparation was performed as in **Section 2.8**. Cells for all the experiments were imaged using a confocal microscope (Fluoview 1000; Olympus) with a 40X water-immersion objective lens with 0.8 NA at digital zoom of two to three (**Figure 2.2**). For EFS-evoked signals in **Chapters 7 and 8**, zoom of 1.5 was used. We used the 488 nm line of an Argon laser, with the intensity adjusted to 10-14% of the maximum output of 10 mW. The emitted light pathway consisted of an emission high pass filter (505-525 nm) before the photomultiplier tube. For animals that received DREADD viruses, the 543 nm line of the HeNeG laser with intensity adjusted to 20% of the maximum output of 1 mW was used. Astrocytes were typically ~25  $\mu\text{m}$  below the slice surface and scanned at 1 frame per second for imaging sessions (CPA Ca<sup>2+</sup>-free experiments were scanned at 1 frame per 5 seconds). For EFS-evoked signals, stimulus electrode was placed at CA1 s.r. and corpus callosum for hippocampal and striatal astrocytes, respectively. Ca<sup>2+</sup> and glutamate imaging were performed at 150-300  $\mu\text{m}$  away from the electrode. For pharmacological activation of DREADDs and endogenous GPCRs, agonists (see **Table 2.1**) were dissolved in either water or dimethyl sulfoxide (DMSO) to make 1000X stock solutions. Stock solutions were diluted in aCSF immediately prior to acute bath application.

## **Section 2.11: Calcium imaging analysis**

Analyses of time-lapse image series were performed using ImageJ. X-y drift was corrected using ImageJ; cells with z drift were excluded from analyses. The data were analyzed essentially as previously reported (Haustein et al., 2014; Srinivasan et al., 2015; Srinivasan et al., 2016). Using ImageJ and GEClquant plugin (Srinivasan et al., 2015), time traces of fluorescence intensity were extracted from the ROIs and converted to dF/F values.

PHARMACOLOGICAL AGENTS	CONCENTRATION USED ( $\mu\text{M}$ )	SOURCE	IDENTIFIER
Biocytin	2684.7 (i.e. 2 mg/ml)	Tocris	Cat#3349
TTX	0.25	Cayman Chemical Company	Cat#14964
Bicuculline	10	Sigma-Aldrich	Cat#14340
CNQX disodium salt	10	Abcam	Cat#ab120044
Carbenoxolone (CBX)	100	Tocris	Cat#3096
Cyclopiazonic acid (CPA)	20	Tocris	Cat#1235
TBOA	1	Tocris	Cat#2532
Clozapine N-oxide (CNO)	1	Tocris	Cat#4936
Phenylephrine	10	Tocris	Cat#2838
DHPG	100	Tocris	Cat#0342
ATP	100	Sigma	Cat#A2383
A77636	10	Tocris	Cat#1701
LY354740	100	Tocris	Cat#3246
Sumanitrole	10	Tocris	Cat#2773
PD128907	50	Tocris	Cat#1243
R-baclofen	50	Tocris	Cat#0796

**Table 2.1: Pharmacological agents used in acute brain slice experiments.**

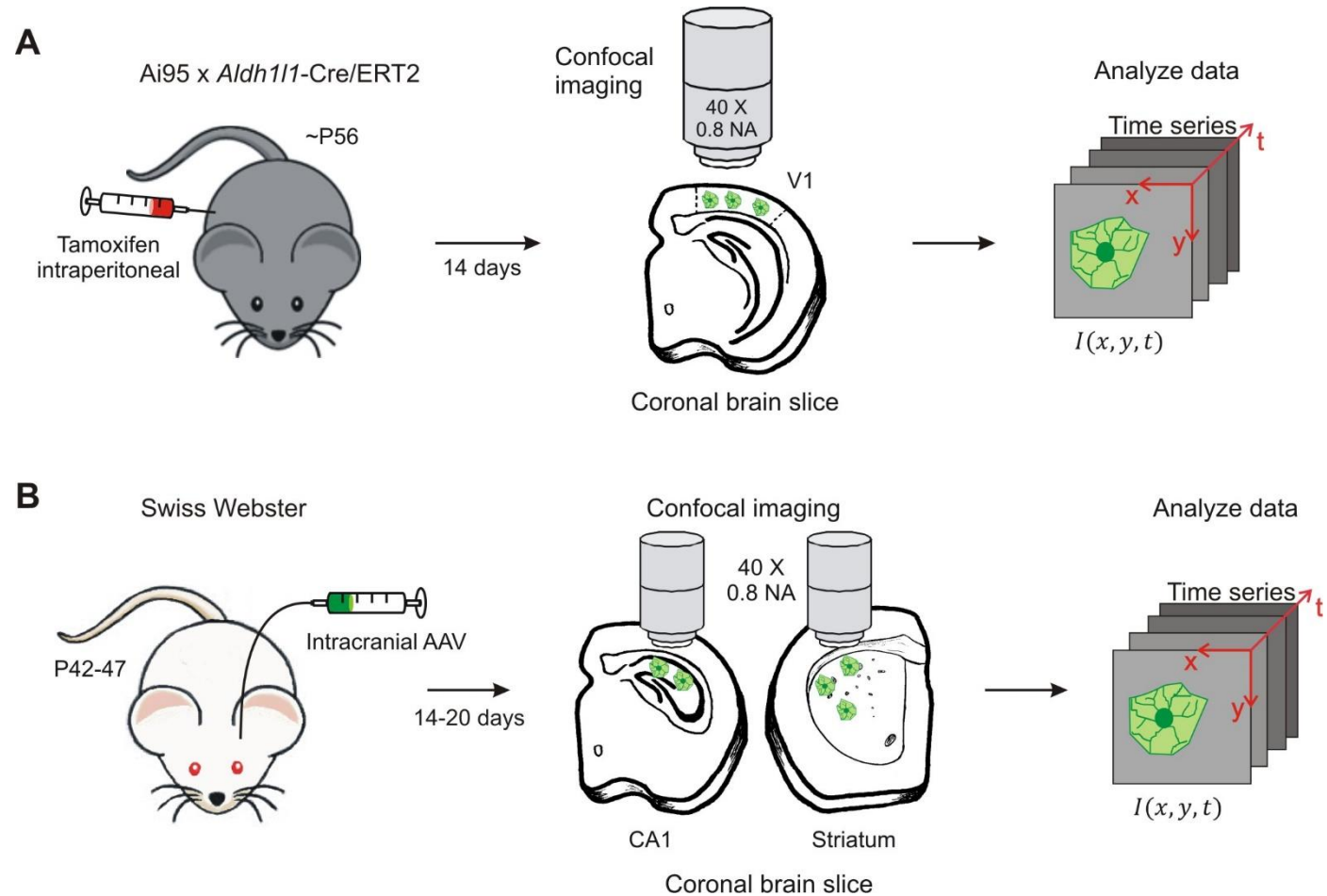


**Figure 2.2: Schematic of the workflow for imaging of astrocyte calcium or glutamate signals in coronal brain slices. A.** V1 cortex from double transgenic mice used in **Chapter 3**. **B.** Dorsal lateral striatum and hippocampus CA1 s.r. from AAV injected Swiss Webster mice used in **Chapters 7 and 8**.

For analyzing spontaneous  $\text{Ca}^{2+}$  signaling of hippocampal and striatal astrocytes, regions of interest (ROIs) were defined in normal aCSF (control) and the same ROIs were used to analyze the effect of TTX. Separately, to analyze the effect of removal of extracellular  $\text{Ca}^{2+}$ , ROIs were defined in TTX and the same ROIs were used to analyze the effect of TTX  $\text{Ca}^{2+}$ -free buffer. To compare between striatal and hippocampal astrocytes, ROIs were generated for control, TTX, and TTX  $\text{Ca}^{2+}$ -free conditions individually. Using MiniAnalysis 6.0.07 (Synaptosoft), spontaneous events were manually marked. Event amplitudes, half-width and event frequency per ROI per min was measured. Events were identified based on amplitudes that were at least 2-fold above the baseline noise of the  $\text{dF}/\text{F}$  trace.

For all other calcium imaging experiments, extracted calcium signals were analyzed using OriginPro 8.5/2015 (OriginLab). *In vivo* and acute brain slice data for cortical PE-evoked responses were acquired from square  $10\ \mu\text{m}^2$  ROIs drawn within individual astrocyte territories. We analyzed spontaneous events that occurred in the first 250 s before agonist application. For EFS-evoked signals, whole astrocyte territories were selected as ROIs. For  $\text{Ca}^{2+}$  homeostasis experiments, only the somatic fluorescence intensity was extracted. For DREADD experiments, time traces of fluorescence intensity were extracted from somata and processes. Using OriginPro, the integrated area-under-the-curve (AUC) of  $\text{dF}/\text{F}$  traces was analyzed. AUC per minute in baseline condition *versus* the first two minutes of CNO application was used for paired comparisons per cell. Two minutes of CNO was chosen to capture the peak response that was clearly visible from the traces. For endogenous GPCR experiments, somata AUC per minute during baseline condition *versus* during the two minutes after agonist hits the slice chamber were compared. As elevation of  $\text{Ca}^{2+}$  in processes lasted a shorter amount of time, processes' AUC per minute during baseline condition *versus* during the one minute after agonist hits the slice chamber was compared. Fold-change was used to compare agonist responses between regions, and was defined as the ratio of agonist *versus* baseline AUC per minute.

## **Section 2.12: Glutamate imaging analysis**

Glutamate signals were extracted in ImageJ using GEClquant soma function thresholded to encompass the whole astrocyte territory and then analyzed in OriginPro 8.5. Peaks in dF/F traces with twice the change as baseline noise were deemed iGluSnFR flashes.

## **Section 2.13: *In vivo* activation of HM4D**

Two weeks after unilateral injection of hM4D-mCherry AAV into the striatum and hippocampus of *Aldh1l1*-eGFP mice, CNO was administered to animals with intraperitoneal injection (1 mg/kg; dissolved in saline). One hour after CNO administration, animals were sacrificed and used for immunohistochemistry.

## **Section 2.14: Brain tissue clearing using ScaleS**

ScaleS tissue clearing was performed on *Aldh1l1*-eGFP mice as previously described (Hama et al., 2015) to allow for deeper imaging of endogenous fluorescence while preserving the three-dimensional architecture. P70-80 mice were given 100 units of heparin with intraperitoneal injection to prevent blood clotting and then euthanized with barbiturate overdose prior to transcardial perfusion with 50 ml of ice-cold 0.1 M PBS, followed by 50 ml of ice-cold 4% paraformaldehyde (EMS #19202). Brains were gently removed from the skull and post-fixed overnight at 4°C. One millimeter-thick coronal sections of striatum and hippocampus were cut using Pelco Vibrotome 3000. Brain sections were then cleared using the ScaleSQ(5) protocol. Briefly, sections were incubated in ScaleSQ(5) (22.5% D-(-)-sorbitol [w/v], 9.1 M urea and 5% triton X-100 [w/v] in distilled water; pH 8.2) for 2 h at 37°C under gentle agitation. Samples were then mounted overnight in ScaleS4(0) (40% D-(-)-sorbitol [w/v], 10% glycerol [w/v], 4 M urea and 15% dimethylsulfoxide [v/v] in distilled water; pH 8.1; refractive index 1.437). Cleared

sections were imaged using a Zeiss LSM 780 confocal microscope, and semi-automated cell counting of astrocytes was performed using Imaris version 7.6.5 (Bitplane). The volumes of the brain regions counted were measured using Imaris's surface function.

### **Section 2.15: Astrocyte intracellular Lucifer yellow iontophoresis**

This method for filling cells in fixed tissue was modified from published methods (Bushong et al., 2002). Swiss-Webster wild-type mice (P44-58) were euthanized with barbiturate overdose and transcardially perfused with 10 ml of 35°C Ringer's Solution with 0.02% lidocaine. Ringer's Solution contains the following (in mM): 135 NaCl, 14.7 NaHCO<sub>3</sub>, 5 KCl, 1.25 Na<sub>2</sub>HPO<sub>4</sub>, 2 CaCl<sub>2</sub>, 1 MgCl<sub>2</sub>, and 11 D-glucose, saturated with 95% O<sub>2</sub> and 5% CO<sub>2</sub>. Brains were lightly post-fixed at room temperature for 1.5 hrs and then washed three times in ice cold 0.1 M PBS for 10 min. 100 µm coronal sections were cut using Pelco Vibratome 3000 and then placed in ice-cold PBS for the duration of the experiment. 10 mg Lucifer yellow CH di-Lithium salt (Sigma) was dissolved in 1 ml 5 mM KCl solution and filtered prior to use. Sharp (~200 MΩ) glass electrodes were pulled from Borosilicate glass capillary with filament (O.D. 1.0 mm, I.D. 0.58 mm). Electrodes were gravity filled. Sections were transferred to a solution of room temperature PBS for filling. Astrocytes were identified using IR-DIC on Olympus microscope with 40X 0.8 NA water immersion objective lens and then impaled with a sharp electrode. Lucifer yellow was ejected into the cell by passing current (~2 µA) for ~20 s: three times with 15-20 s pauses in between. Sections were post-fixed completely with 4% PFA at 4°C prior to mounting on glass slides. In some cases, sections were processed for IHC co-staining with NeuN. Cells were imaged using a Zeiss LSM 780 confocal microscope with UplanFL 40X 1.30 NA oil immersion objective lens with 0.25 µm z-steps and 2.5-3.5x zoom.

Three-dimensional (3D) quantitative volumes were generated using Imaris's surface function. The astrocyte cell volume was segmented by raw intensity to create faithful

representation of the extremely bright soma and primary branches, as well as the finer astrocyte processes. For the soma, surface smoothing was set at the *x-y* plane resolution limit (0.25  $\mu\text{m}$ ) and minimum seed object diameter was set to 3.0  $\mu\text{m}$ . The reconstruction of soma was used to mask the raw confocal volume and the masked intensity was used to reconstruct the major processes. For major branches, surface smoothing and minimum seed object diameter were set to *z* plane step size (0.25  $\mu\text{m}$ ). The reconstruction of major branches was used to further mask the confocal signal, leaving the fluorescent intensity from only the fine processes. For the fine astrocyte processes, surface smoothing was set at the *x-y* plane resolution limit (0.18  $\mu\text{m}$ ) and minimum seed object diameter was set to *z* plane step size (0.25  $\mu\text{m}$ ). Summation of the soma, branches, and processes reconstruction volumes provided the astrocyte cell volume. The astrocyte territory volume was measured from a low-intensity threshold reconstruction (surface smoothing 0.75  $\mu\text{m}$ ) encompassing the cell volume and the space between its processes. NeuN co-staining was reconstructed as low threshold surfaces, and the number of neuronal cell bodies that intersect with the astrocyte territory was counted. The number of primary branches was counted visually.

## **Section 2.16: Electron microscopy**

Swiss-Webster wild-type mice (P59-64, 2 males and 1 female) were euthanized with barbiturate overdose and transcardially perfused with the following solution at 6 ml/min for 10 minutes: 4% paraformaldehyde (EMS #19202) and 2.5% glutaraldehyde (Polysciences #1909) in a 0.1 M sodium cacodylate (EMS #12300) buffer (pH 7.2). Brains were sliced into 1 mm coronal sections and then further dissected to the regions of interest: d.l. striatum and hippocampus CA1. Tissues were post-fixed in perfusion solution for 48 h at 4°C. Fixed tissues were prestained with 0.1% tannic acid, and then stained with osmium-ferrocyanide, followed by tetracarbohydrazide treatment, and then further stained with 2% aqueous osmium tetroxide.

Samples were then incubated overnight in saturated aqueous uranyl acetate, followed by Walton's lead aspartate stain. Next, samples were dehydrated through a series of alcohol, followed by propylene oxide then a 50/50 propylene oxide and resin mixture. Finally, samples were embedded in Epon 812-substitute resin. The resin blocks were then trimmed and mounted on an aluminium pin, coated with colloidal silver paste around the block edges, and then examined in a Zeiss Sigma VP system equipped with a Gatan 3View in-chamber ultramicrotome stage with low-kV backscattered electron detectors optimized for 3View systems. Samples were routinely imaged at 2.25kV, at 6.8nm/pixel resolution, with field sizes between 40-50  $\mu\text{m}$  in  $x$ - $y$  and slice thickness of 80 nm. The acquisition of the electron microscopy data was performed by Renovo Neural (Cleveland, Ohio). Image series were registered and then analyzed using Reconstruct software version 1.1 (Fiala, 2005); <https://synapseweb.clm.utexas.edu/software-0>).

Striatal MSN spines and hippocampal CA1 pyramidal neuron spines in the s.r. were traced. Striatal MSNs have aspiny primary dendrites that become spiny upon branching. Only dendrites whose aspiny primary and spiny secondary or tertiary portions were found in the image series were analyzed. Hippocampal CA1 pyramidal neurons have apical dendrites that run largely orthogonal to the pyramidal cell layer. A low magnification block-face image was used to orient hippocampal image series. At least three dendrites were analyzed per region per mouse. All spines on selected dendrites were traced along with their corresponding presynaptic axon bouton and nearby astrocyte processes. Astrocyte processes were identified by their persistent irregular shape through multiple sections, the presence of glycogen granules, bundles of intermediate filaments, and a relatively clear cytoplasm (Ventura and Harris, 1999). The postsynaptic density (PSD) of each spine was traced and the estimated center of the PSD marked. Spine types were defined as previously described (Harris et al., 1992) into mushroom, thin, and other (stubby and branched) using 3D rendering of the traces. Mushroom spines have spine head diameter much greater than neck diameter; thin spines have spine head diameter

similar to neck diameter and spine length much greater than neck diameter. Stubby spines have spine length similar to neck diameter; branched spines have more than one spine head. The shortest distance (straight line) between the center of the PSD and nearby astrocyte processes was measured for each traced synapse using the “Distance” function in Reconstruct software.

### **Section 2.17: Adult astrocyte transcriptomes**

*Aldh1l1*-Cre/ERT2 x RiboTag mice received intraperitoneal tamoxifen (Sigma, 20 mg/ml) for five consecutive days at 75 mg/kg. Experiments were performed two weeks after the last tamoxifen injection. RNA was collected from microdissected brain regions of *Aldh1l1*-Cre/ERT2 x RiboTag mice based on a published protocol (Sanz et al., 2009).

### **RNA-Seq of adult cortical astrocyte transcriptome**

Freshly dissected cortices were collected from four animals (P78-82, 3 males and 1 female) and homogenized. RNA was extracted from 15% of cleared lysate as input. The remaining lysate was incubated with mouse anti-HA antibody (Covance #MMS-101R) with rocking for 4 h at 4°C followed by addition of magnetic beads (Invitrogen Dynabeads #100.04D) and overnight incubation with rocking at 4°C. The beads were washed three times in high salt solution. The bound ribosomes and RNA were separated from the beads with 30 s of vortexing in RLT lysis buffer as the immunoprecipitated (IP) samples. RNA was purified from the IP and corresponding input samples (Qiagen RNeasy Plus Micro #74034). RNA concentration and quality were assessed with nanodrop and Agilent 2100 Bioanalyzer. RNA samples with RNA integrity number (RIN) greater than nine (mean RIN 9.6; range 9.2-9.9) were used for multiplexed library prep with KAPA Stranded RNA-Seq Kit with mRNA enrichment (#KK8401). Sequencing was performed on Illumina NextSeq 500 for 2x75. Data quality check was done on

Illumina SAV. Demultiplexing was performed with Illumina Bcl2fastq2 v 2.17 program. Reads were aligned to the latest mouse mm10 reference genome using the STAR spliced read aligner (~84% reads mapped uniquely). Fragment counts were derived using HTS-seq program (Anders et al., 2015). Differentially expressed (DE) genes between input and IP samples were identified using Bioconductor packages (<http://www.bioconductor.org>) and Limma-Voom with adjustment for difference between animals, which were then considered and ranked based on adjusted *P*-values (FDR) of < 0.05.

To determine the P80 astrocyte enriched genes, the IP enriched gene list at FDR < 0.05 was filtered for enrichment fold-change (FC) > 2 versus input. Genes that had FPKM (Fragments Per Kilobase of transcript per Million mapped reads) values of 0 for either input or IP were also filtered out to exclude genes with exaggerated FC values. The P7 astrocyte-enriched genes were determined with FC > 2 for astrocyte FPKM versus average FPKM of all cell types. Transcripts that were enriched at P80 and/or P7 constituted the master list of 4727 astrocyte enriched transcripts used to look for developmental changes in gene expression. To compare P80 and P7 datasets, transcript expression was normalized as percentile of highest FPKM transcript (percentile FPKM; from 0 to 1) in IP and Zhang *et al.* astrocyte samples, respectively. *ApoE* (P80 highest) and *Fos* (P7 highest) were both in the list of 4727 astrocyte enriched transcripts. The Rank-Rank Hypergeometric Overlap algorithm (Plaisier et al., 2010) was used to assess similarity between datasets. We focused on transcripts with a change in percentile (delta percentile) of at least 0.1 to highlight transcripts with different expression between P90 and P7 datasets.

### **RNA-Seq of striatal and hippocampal astrocyte transcriptomes**

Adult *Aldh111-Cre/ERT2* x RiboTag mice (P63, 2 males and 2 females) were used to purify RNA from astrocytes. RNA was collected from whole hippocampi and striata of *Aldh111-*

Cre/ERT2 x RiboTag mice based on a published protocol (Sanz et al., 2009). Briefly, freshly dissected tissue were collected from four animals and individually homogenized. RNA was extracted from 20% of cleared lysate as input. The remaining lysate was incubated with mouse anti-HA antibody (1:250; Covance #MMS-101R) with rocking for 4 h at 4°C followed by addition of magnetic beads (Invitrogen Dynabeads #110.04D) and overnight incubation with rocking at 4°C. The beads were washed three times in high salt solution. RNA was purified from the IP and corresponding input samples (Qiagen Rneasy Plus Micro #74034). RNA concentration and quality were assessed with nanodrop and Agilent 2100 Bioanalyzer. RNA samples with RNA integrity number (RIN) greater than eight (mean RIN 8.6; range 8.1-9.3) were used for multiplexed library prep with Nugen Ovation RNA-Seq System V2. Sequencing was performed on Illumina NextSeq 500 for 2x75. Data quality check was done on Illumina SAV. Demultiplexing was performed with Illumina Bcl2fastq2 v 2.17 program. Reads were aligned to the latest mouse mm10 reference genome using the STAR spliced read aligner (~88% reads mapped uniquely). Fragment counts were derived using HTS-seq program (Anders et al., 2015). Principal component analysis was performed using R v3.3.2 (RCoreTeam, 2016) using the 2000 most variable genes across all samples. Analysis of differential expression was performed using the Bioconductor LIMMA package (Law et al., 2014). The list of genes sequenced in striatal and/or hippocampal IP samples were ranked by LimmaVoom log ratio with no false discovery rate (FDR) threshold and used for Gene Set Enrichment Analysis (GSEA) (<https://software.broadinstitute.org/gsea/index.jsp>). DE genes were identified using Bioconductor packages and Limma-Voom with adjustment for difference between animals using FDR threshold < 0.05 for all comparisons.

## **Section 2.18: RNA and protein extraction from astrocytes isolated by FACS**

*Aldh1l1*-eGFP mice were used to purify astrocytes by FACS. Whole hippocampi or striata from heterozygous P30 mice were dissociated following published guidelines (Foo, 2013) with slight modifications (**Figure 2.3**). Briefly, the hippocampi and striata from four mice (P30, 2 males and 2 females) were dissected and pooled by region. Tissues were then digested for 45 min at 36°C in a 35 mm Petri dish with 2.5 ml of papain solution (1x EBSS, 0.46% D-glucose, 26 mM NaHCO<sub>3</sub>, 50 mM EDTA, 75 U/ml DNase1, 200 units of papain for hippocampal or 300 units of papain for striatal tissue, and 2 mM L-cysteine) while bubbling with 95% O<sub>2</sub> and 5% CO<sub>2</sub>. After digestion, the tissue was washed four times with ovomucoid solution (1x EBSS, 0.46% D-glucose, 26 mM NaHCO<sub>3</sub>, 1 mg/ml ovomucoid, 1 mg/ml BSA, and 60 U/ml DNase1) and gently mechanically dissociated with two fire-polished borosilicate glass pipettes with different bore sizes. A bottom layer of concentrated ovomucoid solution (1x EBSS, 0.46% D-glucose, 26 mM NaHCO<sub>3</sub>, 5. mg/ml ovomucoid, 5.5 mg/ml BSA, and 25 U/ml DNase1) was added to the cell suspension. The tubes were centrifuged at room temperature at 300 g for 10 min. The resultant pellet was re-suspended in D-PBS with 0.02% BSA and 13 U/ml of DNase1, and filtered with a 20 µm mesh. FACS was performed in a FACSAria II (BD Bioscience) with a 70 µm nozzle using standard methods at the University of California, Los Angeles (UCLA) Cell Sorting Core. For RNA extraction, sorted cells were collected in D-PBS with 0.1% BSA and centrifuged for 10 min at 4°C and 2000 g. The RNA was extracted from the pelleted cells using RNeasy Plus Micro Kit (QIAGEN). For protein extraction, cells were collected in D-PBS and, right after FACS, cells were incubated with lysis buffer (150 mM NaCl, 1% Triton X-100, 12 mM Na-Deoxycholate, 3.5 mM sodium dodecyl sulfate, 50 mM Tris pH8, and 1:100 Halt Protease Inhibitor cocktail (Thermo Scientific)) at 4°C for 40 min. The extracted protein was subsequently precipitated with trifluoroacetic acid and acetone. Protein pellet was dried and resuspended in a proteomics compatible buffer (0.5% Na-Deoxycholate, 12 mM N-Lauroylsarcosine sodium salt, and 50 mM triethylammonium bicarbonate), boiled at 95 °C for 10 min, and stored at -80°C.

### **Section 2.19: Microarrays of FACS astrocyte**

RNA was extracted from eGFP-negative, eGFP-positive and unsorted cells (i.e. cells that went through FACS but were not separated based on the GFP fluorescence). eGFP-negative and eGFP-positive cells obtained from three separate sorts (2 males and 2 females each), and unsorted cells from two, were used for microarray hybridization. RNA from both striatum and hippocampus were extracted from each pooled sample. RNA quantity was assessed with Nanodrop (Thermo Fisher Scientific Inc.), and quality with a bioanalyzer (Agilent Technologies). Samples were processed by the UCLA Neuroscience Genomics Core. 3 ng of RNA per sample with RIN greater than 7 were amplified using Ovation PicoSL WTA System v2 (Nugen) and 750 ng of biotin-cDNA were used to hybridize with Illumina MouseRef-8 v2.0 expression BeadChip (Illumina). Slides were scanned using BeadStation and signal extracted using Illumina BeadStudio software (Illumina). Quality assessment was performed by inter-array Pearson correlation, and clustering based on top variant genes was used to assess overall data coherence. Contrast analysis of differential expression was performed using Bioconductor packages and LIMMA (Law et al., 2014). After linear model fitting, a Bayesian estimate of differential expression was calculated. Differences in expression were considered statistically significant at a FDR < 0.05. Principal component analysis was performed using R v3.3.2 (RCoreTeam, 2016) using the 1000 most variable transcripts across all samples.

### **Section 2.20: Mass spectrometry based proteomics**

To be able to quantitatively compare the protein expression in striatal and hippocampal astrocytes, we labeled the tryptic peptides produced from proteins originating in each brain region with two isotopically different dimethyl tags, mixed the samples and ran them together in the same liquid chromatography-tandem mass spectrometry (LC-MS/MS) session. Four LC-MS/MS experiments were performed for a total of four biological replicates. For one LC-MS/MS

experiment, protein from hippocampal or striatal eGFP-positive cells from three cell sorting sessions (12 mice total, 6 females and 6 males; both hippocampal and striatal proteins were obtained from each mouse) were quantified using Pierce BCA protein assay kit (Thermo Scientific) and Nanodrop 2000 (Thermo Scientific). The 11-14  $\mu\text{g}$  of protein obtained per striatal or hippocampal sample were reduced with 5 mM tris(2- carboxyethyl) phosphine for 30 min at RT, and alkylated with 10 mM iodoacetamide for 30 min at RT in the dark. Samples then were diluted 1:5 (vol/vol) with 50 mM triethylammonium bicarbonate, and trypsin was added to each sample (0.1  $\mu\text{g}$  of trypsin per  $\mu\text{g}$  of protein) and incubated at 37°C. After 4 h of incubation, the same amount of trypsin was again added followed by incubation at 37°C overnight. The following day, detergent was precipitated out of solution with 0.5% trifluoroacetic acid (final concentration), phase transferred in 1:1 (vol/vol) ethyl acetate, and centrifuged at 16,000  $g$ . The organic phase was aspirated and the peptides were lyophilized.

Next, stable-isotopic dimethyl labeling was performed. “Light” (+28.0313 Da) or “intermediate” (+32.0564 Da) labels, that are added to the N-terminus and the  $\epsilon$ -amino group of Lysine residues via reductive amination, were used to tag either striatal or hippocampal samples. The label-brain region combination was shuffled between different LC-MS/MS experiments. Briefly, 0.16%  $\text{CH}_2\text{O}$  and 24 mM  $\text{NaBH}_3\text{CN}$  (for light label) or 0.16%  $\text{CD}_2\text{O}$  and 24 mM  $\text{NaBH}_3\text{CN}$  (for intermediate label) were mixed with each sample at RT for 1 h. Reaction was quenched with 0.15% ammonia hydroxide acidified with and 0.32% of formic acid, and vacuum dried. Labeled peptides were combined 1:1 (Str:Hip) and fractionated into 10 fractions by strong cationic exchange using Empore™ cation extraction disks (Empore 2251). Each fraction was desalted with a C18 column and loaded into the LC-MS/MS. The fractionated samples were analyzed with and Eksigent 2D nanoLC attached to a Thermo Orbitrap LTQ XL (Thermo Scientific). Peptides were injected onto a laser-pulled nanobore 20 cm x 75  $\mu\text{m}$  C18 column (Acutech Scientific) in buffer A (0.1% formic acid) and resolved using a 2 h gradient: from

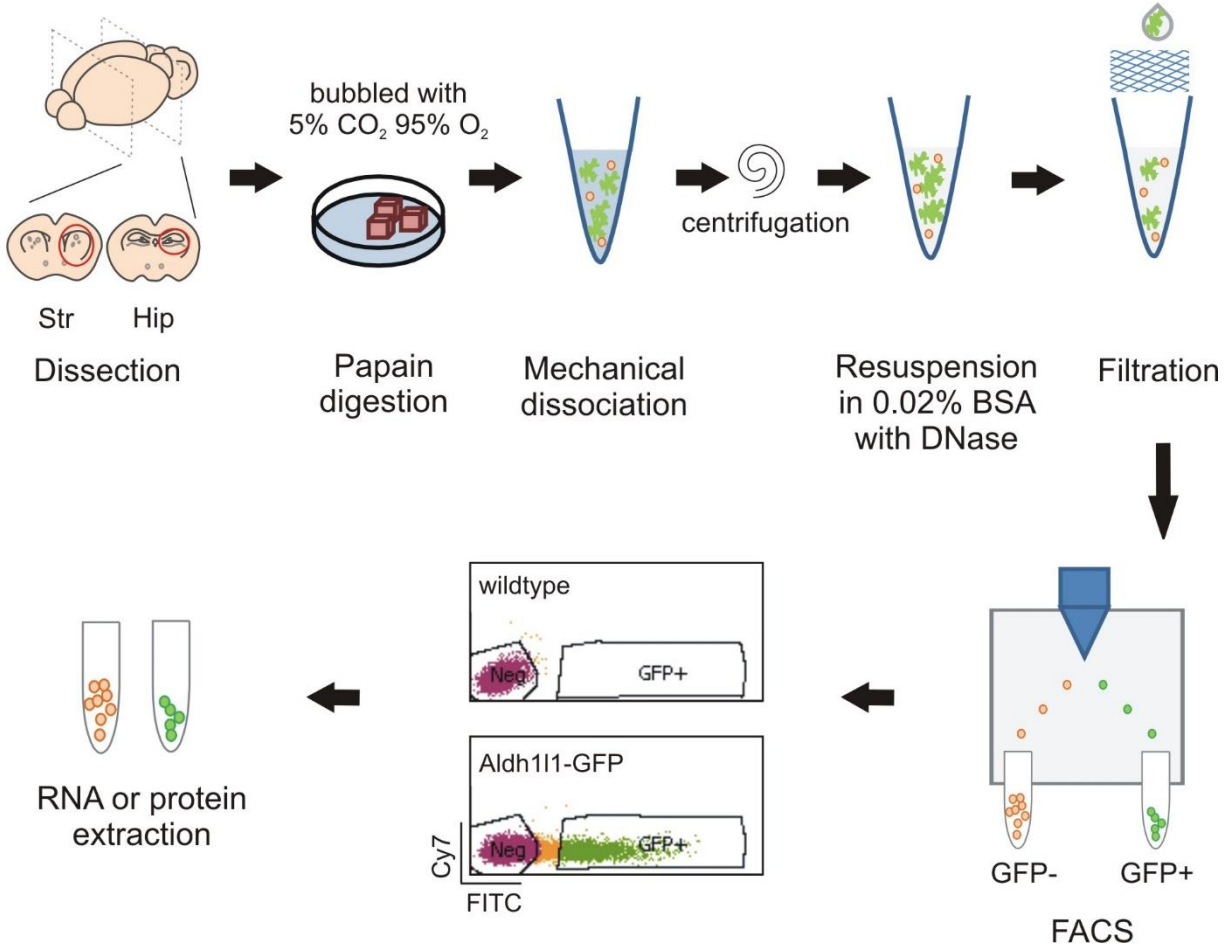


**Figure 2.3: Schematic of tissue dissociation and FACS purification of astrocytes.** Whole striata and hippocampi from four *Aldh111*-eGFP P30 mice were dissected, pooled by region, and digested in papain containing solution. Digested tissue was mechanically dissociated and the cells were filtered through a 20 µm mesh. FACS was performed to separate GFP positive cells from non-fluorescent cells. Purified cells were later used to extract protein or RNA.

0-9% buffer B (80% acetonitrile, 20% H<sub>2</sub>O with 0.1% formic acid) in 5 min, from 9% to 27% in 90 min, from 27% to 33% in 5 min, and from 33% to 50% in 10 min. The Orbitrap XL was operated in data-dependent mode with 60,000 resolution and target autogain control at 5e6 for parent scan. The top 12 ions (by parent ion abundance) above a charge of +1 were subjected to collision-induced dissociation set to a value of 35 with target autogain control of 5,000. Dynamic exclusion was set to 30 s.

### **Section 2.21: Mass spectrometry data analysis**

Raw data were processed and quantified using Sequest and Thermo Proteome Discoverer version 1.4. The 10 fractions were analyzed together. The Uniprot mouse database was searched with variable modifications of methionine oxidation, fixed modification of cysteine carbamidomethylation, N-terminus dimethyl (+28.0313 Da or +32.0564 Da), and lysine dimethyl (+28.0313 Da or +32.0564 Da). Two missed cleavages by trypsin were allowed on the full mass spectrometry; 10 ppm and 0.6 Da mass error were allowed for tandem mass spectrometry. Peptides and proteins were filtered using Percolator with a 1% FDR and maximum delta Cn of 0.05 (Minimum-stringency in the figures and tables). High-stringency protein lists were obtained applying peptide filters (Charge state 2-4; score 2.2 for charge state 2, 3.75 for charge state 3, and 5.0 for charge state 4; peptide confidence of FDR < 1%) and protein filters (2 unique peptides per protein required; Sequest score threshold of 10). Ratios between light and intermediate dimethyl labels were calculated per protein and normalized to the ratio of the total protein median. The average area of the three unique peptides with the largest peak area was considered as measurement of abundance of each protein per region. Abundance values were used to perform paired t-test to define striatum or hippocampus enriched proteins. At  $P < 0.05$  differences were considered significant. In these analyses we assume the two populations

contained normally distributed data. Gene ontology analyses were performed using Enrichr (Kuleshov et al., 2016).

### **Section 2.22: qPCR experiments**

Amplified cDNA from RNA samples (RiboTag and FACS) was generated using Ovation PicoSL WTA System V2 (Nugen). The cDNA was then purified with a QIAquick PCR Purification Kit (Qiagen) and quantified with Nanodrop 2000. qPCR was performed in a LightCycler 96 Real-Time PCR System (Roche). Ten nanograms of each sample was loaded per well, and gene specific amplification was performed using primers listed in **Table 2.2**. Expression levels were calculated based on Ct values of the genes of interest relative to Arbp using the following formula:  $2^{-\Delta Ct}$  (Gene of interest - Arbp).

### **Section 2.23: Western blot analyses**

Standard SDS-PAGE was performed. Each blot contained extracted protein from one FACS experiment. We probed for GFP, GFAP,  $\mu$ -crystallin and  $\beta$ -actin using rabbit anti-GFP (Invitrogen A11122), mouse anti-GFAP (Abcam ab4674), mouse anti- $\mu$ -Crystallin (Santa Cruz sc-376687) and rabbit anti- $\beta$ -actin (Abcam ab8227) primary antibodies at 1:1000 dilution. The secondary antibodies IRDye 680RD anti-mouse (Li-Cor 926-68170) and IRDye 800CW anti-rabbit (Li-Cor 827-08365) were added to visualize the proteins using a Li-Cor Odyssey imager. Signal intensities were quantified with Image Studio Lite software (Li-Cor, Inc.), and GFP, GFAP and  $\mu$ -crystallin signals were normalized to  $\beta$ -actin.

### **Section 2.24: Statistical analysis**

Statistical tests were run in OriginPro 8.5/9/2015 or GraphPad InStat 3. Summary data are presented as mean  $\pm$  s.e.m, with medians shown as a horizontal line where appropriate. Note that in some of the graphs, the bars representing the s.e.m. are smaller than the symbols used to represent the mean. For each set of data compared, we determined within GraphPad InStat or OriginPro whether the data were normally distributed or not. If they were normally distributed, we used parametric tests. If the data were not normally distributed, we used non-parametric tests. Paired and unpaired Student's two-tailed  $t$  tests (as appropriate) and two-tailed Mann-Whitney tests were used for most statistical analyses with significance declared at  $P < 0.05$ , but stated in each case with a precise  $P$  value. When the  $P$  value was less than 0.0001, it is stated as such to save space on the figure panels and text.  $N$  is defined as the numbers of cells, processes, or mice throughout on a case-by-case basis depending on the particular experiment; the unit of analysis is stated in each figure or figure legend. When a statistical test was employed that was not a Student's  $t$  test or a Mann-Whitney test, then it is stated as such in the text and figure. Throughout the manuscript, the results of statistical tests ( $P$  values and  $n$  numbers) are reported in full on the figure panels to save space in the main body of the manuscript. However, where appropriate key statistics are also reported in the text.

Gene	Primer sequence	Amplicon (bp)
<i>Crym</i>	F 5' TGCAAGGAGATGTTTCGGGTC 3'	177
	R 5' CATCCAGTTCTCGCCAGTCA 3'	
<i>Gfap</i>	F 5' AGAACAACCTGGCTGCGTAT 3'	188
	R 5' CTTGGCCACATCCATCTCCA 3'	
<i>Arbp</i>	F 5' TCCAGGCTTTGGGCATCA 3'	76
	R 5' AGTCTTTATCAGCTGCACATCAC 3'	

**Table 2.2: qPCR primer sets.**

## CHAPTER 3: NEW TRANSGENIC MOUSE LINE FOR SELECTIVELY TARGETING ASTROCYTES

### Section 3.1: Introduction

A key necessity to studying astrocytes *in vivo* is the ability to manipulate them selectively without concomitantly impacting other cells. From this perspective much attention has focused on genetic methods to selectively target astrocytes (Davila et al., 2013; Xie et al., 2015). Cell type specific expression of Cre recombinase (Cre) is frequently used to achieve gene expression and deletion by exploiting the Cre-loxP system (Sauer, 1994; Tsien, 2016). However, existing mouse lines expressing Cre under the control of astrocyte promoters are neither selective for astrocytes, nor are they pan-astrocytic (Khakh and Sofroniew, 2015; Xie et al., 2015; Zhang and Barres, 2010). Furthermore, several of the commonly used mouse lines express Cre from birth, which vitiates inducible gene expression/deletion in adult mice and complicates analyses of complex behaviors and disease mechanisms. In addition, several available Cre lines are known to target neural stem cells, thus compromising interpretation of behavior in adults. Overall, existing astrocyte Cre lines display some or all of these shortcomings, and thus fall short of minimal experimental requirements for cell specificity (Xie et al., 2015). For example, widely used *hGfap*-Cre lines target large populations of neurons (Sun et al., 2016; Zhuo et al., 2001) and several *mGfap*-Cre and *Slc1a3*-Cre/ERT lines target neural progenitors that give rise to neurons in the olfactory bulb and hippocampus (Garcia et al., 2004; Gregorian et al., 2009; Niu et al., 2013; Slezak et al., 2007) and smaller populations of neurons elsewhere (Xie et al., 2015). This problem is shared with mice constitutively expressing Cre under the control of the aldehyde dehydrogenase 1 family member L1 (*Aldh1l1*) promoter as *Aldh1l1* is expressed in neuroprogenitor cells at ~E13 (Foo and Dougherty, 2013; Molofsky et al., 2014; Tien et al., 2012). ~10% of Cre expressing cells in spinal cord of *Aldh1l1*-Cre animals are mature neurons and 15% are oligodendrocytes (Tien et al., 2012). In the brain, neuronal

expression of Cre was seen in the rostral migratory stream, olfactory bulb, hippocampus dentate gyrus, and cortex (Foo and Dougherty, 2013). Hence, the field lacks a reliable method to achieve pan-astrocytic, specific and inducible genetic manipulations in order to explore astrocyte physiology *in vivo*. The limitations of *Gfap* based mouse lines have been discussed (Sloan and Barres, 2014; Su et al., 2004).

The GENSAT project (Gong et al., 2003) found that the *Aldh111* gene marked astrocytes throughout the central nervous system, a finding confirmed by subsequent RNA (Cahoy et al., 2008; Molofsky and Deneen, 2015; Zhang et al., 2014; Zhang et al., 2016), lineage (Molofsky et al., 2013) and expression analyses (Cahoy et al., 2008; Foo and Dougherty, 2013). This raised the possibility that *Aldh111* could be used as a genetic locus to express tamoxifen inducible Cre/ERT2 and thus achieve temporally specific pan-astrocytic genetic manipulations. Using BAC transgenesis (Yang and Gong, 2005), we explored this possibility in this chapter. In order to characterize the *Aldh111*-Cre/ERT2 mice, we used IHC and Cre-dependent FLEX-GFP AAVs (Atasoy et al., 2008). We also crossed the *Aldh111*-Cre/ERT2 mice with Ai95 mice that express cytosolic GCaMP6f (cyto-GcaMP6f) in a Cre-dependent manner (Chen et al., 2013; Madisen et al., 2015) for *ex vivo* and *in vivo* imaging. Finally, we crossed the *Aldh111*-Cre/ERT2 mice with RiboTag mice that express the ribosomal protein Rpl22HA in a Cre-dependent manner (Sanz et al., 2009). We used this strategy to determine the cortical astrocyte transcriptome in adult mice, which we compared to data from P7 mice (Zhang et al., 2014). Our studies provide well characterized, much needed, and easy-to-use resources, which we exploited in to explore astrocyte diversity between striatal and hippocampal regions in the next chapter.

### **Section 3.2: Creating the *Aldh111*-Cre/ERT2 BAC line**

The Cre lines used are named according to the gene (**Table 3.1**). Cre/ERT2 was inserted at the *Aldh111* gene (*Aldh111*) start codon within the BAC DNA (**Figure 3.1**). Insertion

was confirmed by PCR using flanking and insert specific primers and with restriction analyses. The Cre/ERT2 sequence harbors a rare *AsiS1* restriction site and cutting with *AsiS1* linearized the modified BAC (**Figure 3.2**). The modified *Aldh111*-Cre/ERT2 BAC clone was used for pronuclear injections after detailed characterization with PCR over regions of *Aldh111* and Cre/ERT2. Following injection of ~200 embryos, two founder lines of transgenic mice were generated (*Aldh111*-Cre/ERT2; lines 1 and 2). Both resulted in germ-line transmission and were identical in initial experiments that are described in this chapter for line 1. The insertion of Cre/ERT2 was confirmed by PCR of tail biopsy genomic DNA and by characterization with PCR over regions of *Aldh111* (**Figure 3.2B**). Identical methods were used to make *Slc6a11*-Cre/ERT2 mice at the GABA transporter type 3 (GAT3) locus. Both the *Aldh111*- and *Slc6a11*-Cre/ERT2 mice reproduced, provided offspring in expected numbers, and displayed no obvious behavioral alterations. This was expected because the BAC method leaves both copies of the endogenous genes intact while achieving expression from the full length locus within the BAC (Yang and Gong, 2005).

### **Section 3.3: Comparison to existing astrocyte targeting mouse lines**

We initially tested for Cre/ERT2 mediated expression of GFP within adult *Aldh111*-Cre/ERT2 mice (i.e. at ~P80) using IHC 14-21 days after microinjections of Cre-dependent AAV FLEX-GFP, followed by tamoxifen induction (Atasoy et al., 2008). With this strategy, GFP is expressed in cells that express Cre. As a control, we injected AAV FLEX-GFP into the hippocampus of *Aldh111*-Cre/ERT2 mice, and in the absence of tamoxifen we detected no GFP expression in astrocytes based on cell morphology or colocalization with the astrocyte marker S100 $\beta$  in 40  $\mu$ m hippocampal sections (**Figure 3.3A**; n = 4 mice). However, we did detect GFP expression in a small number of neurons (~50), which represents leaky expression from the AAV FLEX-GFP (**Figures 3.3A, 3.4**; n = 4 mice). Later, we report no detectable leakiness from

<b>Gene name</b>	<b>Protein name</b>	<b>Cre type</b>	<b>Tamoxifen inducible</b>	<b>Expression in astrocytes</b>	<b>Expression in neurons</b>
<i>Gfap</i>	GFAP	Cre	No	High	High
<i>Slc1a3</i>	GLAST	Cre/ERT	Yes	Moderate	Very high
<i>Gjb6</i>	Cx30	Cre/ERT2	Yes	Very high	Moderate
<i>Slc6a11</i>	GAT3	Cre/ERT2	Yes	Moderate	Moderate
<i>Aldh111</i>	Aldh111	Cre/ERT2	Yes	Very high	Not detected

**Table 3.1: Summary of the Cre mice** (with regards to astrocyte and neuronal expression of GFP from AAV FLEX-GFP microinjections).

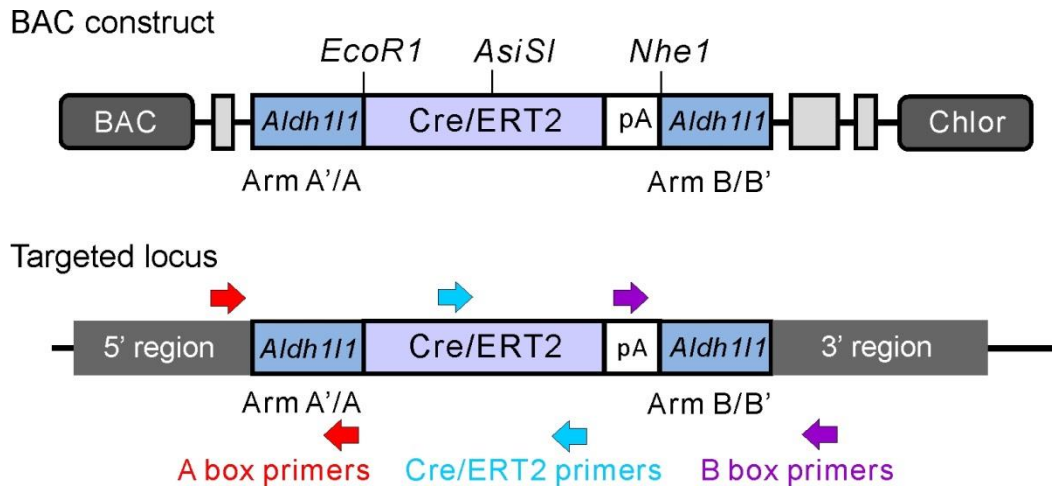


**Figure 3.1: *Aldh111*-Cre/ERT2 BAC construct.** Schematic showing the BAC targeting construct used to create the *Aldh111*-Cre/ERT2 transgenic mice (key primer locations are also shown).

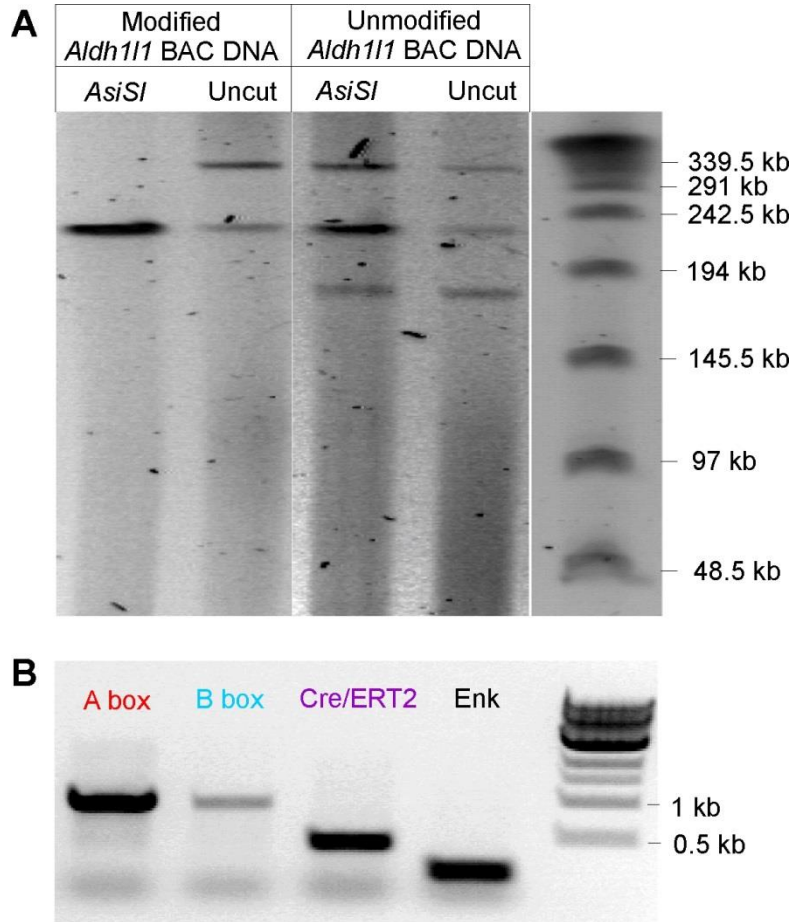


**Figure 3.2: Construction of *Aldh111*-Cre/ERT2 transgenic mice. A.** Pulse field gel electrophoresis of modified and unmodified *Aldh111* BAC DNA cut with *AsiS1*. *AsiS1* linearizes the modified *Aldh111*-Cre/ERT2 BAC, but fails to cut the unmodified *Aldh111* BAC. **B.** Genotyping of the *Aldh111*-Cre/ERT2 BAC transgenic mouse with primers flanking the A box, B box, and Cre/ERT2 cassette. Proenkephalin (Enk) primers were used as a positive control.

the *Aldh111*-Cre/ERT2 mouse line itself. However, with the AAV FLEX-GFP controls, we microinjected AAV FLEX-GFP into the hippocampi of *mGfap*-Cre 77.6 mice (Gregorian et al., 2009) that constitutively express Cre in GFAP positive cells. We observed expression of GFP in  $306 \pm 27$  astrocytes, but also in a substantial population of neurons ( $123 \pm 12$ ) throughout the hippocampus (arrows in **Figures 3.3C, 3.4**;  $n = 4$  mice). We repeated these experiments with *Slc1a3*-Cre/ERT mice at the GLAST glutamate transporter locus (Slezak et al., 2007), and again noted clear GFP expression in astrocytes ( $148 \pm 21$ ) and large numbers of neurons ( $207 \pm 61$ ; arrows in **Figures 3.3D, 3.4**;  $n = 4$  mice). Similar experiments were performed for *Gjb6*-Cre/ERT2 (Slezak et al., 2007) and *Slc6a11*-Cre/ERT2 mice (**Figures 3.3E-F, 3.4**;  $n = 4$  mice) the numbers of labeled astrocytes and neurons were  $374 \pm 14$  and  $81 \pm 14$ , and  $104 \pm 14$  and  $104 \pm 19$  for *Gjb6*-Cre/ERT2 and *Slc6a11*-Cre/ERT2 mice, respectively. Thus in the case of *mGfap*-Cre, *Slc1a3*-Cre/ERT, *Gjb6*-Cre/ERT2, and *Slc6a11*-Cre/ERT2, the number of GFP expressing neurons as a percentage of GFP expressing astrocytes in the hippocampus was 40, 140, 21 and 101%, respectively ( $n = 4$  mice of each genotype). In contrast, with *Aldh111*-Cre/ERT2 mice we detected GFP expression in large numbers of astrocytes ( $360 \pm 73$ ) and in essentially no neurons ( $36 \pm 2$  versus the AAV control of  $50 \pm 9$ ; **Figures 3.3, 3.4; Table 3.1**;  $n = 4$  mice). We emphasize that the comparison of different Cre lines shown in **Figures 3.3-3.5** and **Table 3.1** relates to the hippocampus at P80. We do not rule out judicious use of existing Cre lines or the need for further controls for the *Aldh111*-Cre/ERT2 mice when used in other settings.

The astrocytes labeled with GFP from AAV FLEX-GFP in the *Aldh111*-Cre/ERT2 mice displayed typical, unambiguous, complex bushy astrocyte morphologies and colocalized with S100 $\beta$ , GFAP and Glt1, but not with NeuN (**Figure 3.5, 3.6**;  $n = 4$  mice each). A single pan-astrocyte antibody marker does not exist, but the bushy morphologies and colocalization with S100 $\beta$ , GFAP and Glt1 provides strong evidence that the GFP expressing cells were astrocytes. S100 $\beta$  was chosen as a marker for astrocytes based on *Aldh111*-eGFP mice, which showed >90+%

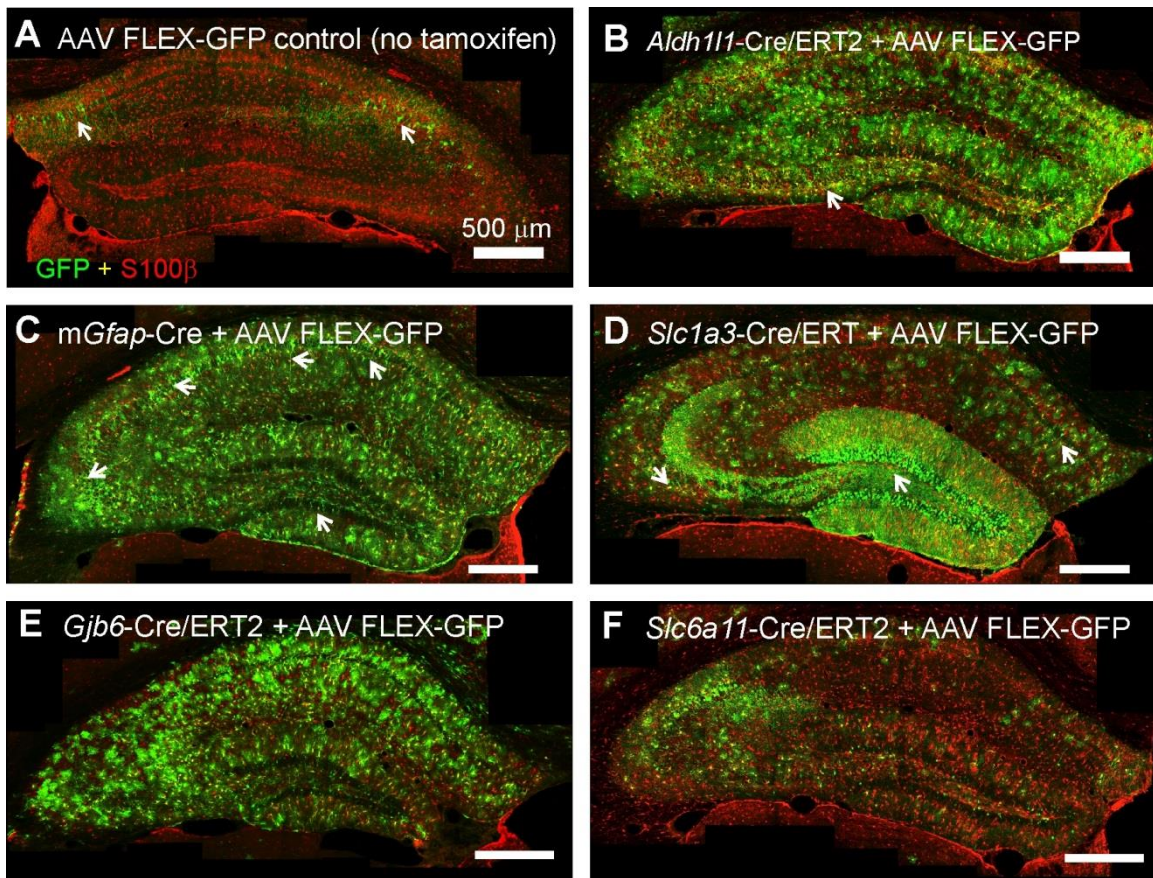


**Figure 3.3: Characterizing *Aldh11-Cre/ERT2* and existing BAC transgenic mice using AAV FLEX-GFP virus.** **A.** Representative montage of the hippocampus from *Aldh11-Cre/ERT2* transgenic mice injected with AAV FLEX-GFP with no tamoxifen injection. The white arrows show leaky expression of GFP in neurons. **B.** Representative montage of the hippocampus from an *Aldh11-Cre/ERT2* transgenic mice injected with AAV FLEX-GFP, followed by 75 mg/kg i.p. tamoxifen for 5 days. There was abundant, widespread expression in astrocytes; the white arrow shows GFP expression in one neuron. **C.** Representative montage of the hippocampus from *mGfap-Cre* transgenic mice injected with AAV FLEX-GFP. There was expression of GFP in astrocytes; the white arrows show expression of GFP in neurons within the CA1, CA3 and dentate gyrus. **D.** As in **B**, but for *Slc1a3-Cre/ERT* transgenic mice showing expression of GFP in neurons with white arrows. **E.** As in **B**, but for *Gjb6-Cre/ERT2* BAC transgenic mice showing expression of GFP in astrocytes as well as neurons. **F.** As in **B**, but for *Slc6a11-Cre/ERT2* BAC transgenic mice. All sections were stained for GFP (green) and S100 $\beta$  (red).

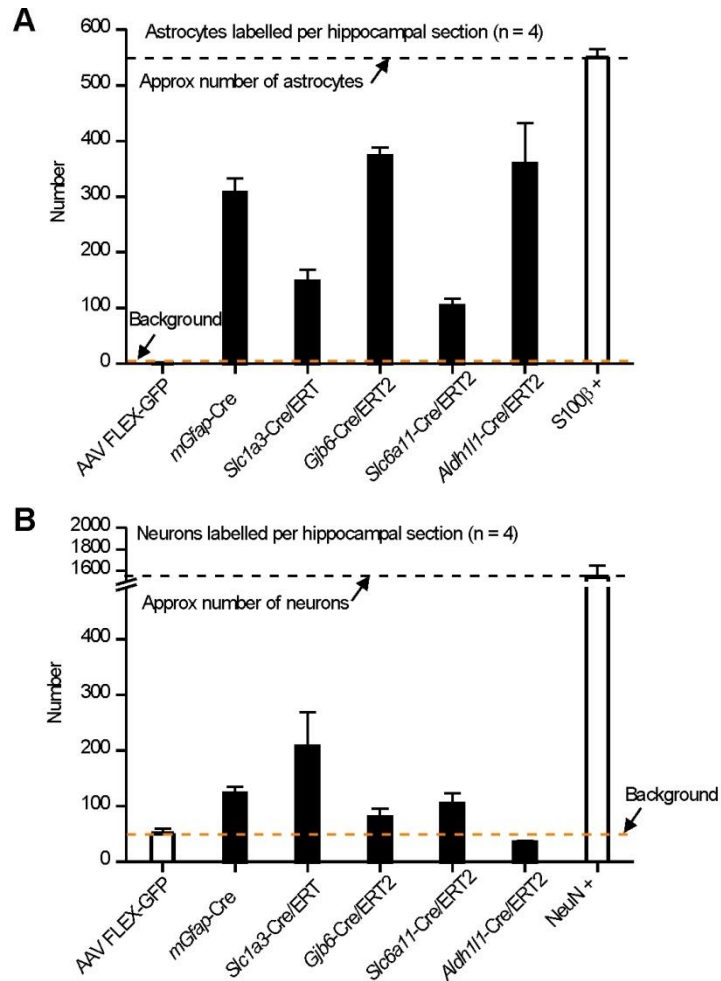


**Figure 3.4: Comparing transgenic lines following AAV FLEX-GFP injection. A.** Bar graphs showing the number of astrocytes in hippocampal montages from each transgenic line following AAV FLEX-GFP virus injection. White bars show the total number of S100 $\beta$  positive astrocytes observed in controls without tamoxifen injection. **B.** Bar graphs showing the number of neurons in hippocampal montages from each transgenic line following AAV FLEX-GFP injection. White bars show the total number of NeuN positive neurons in hippocampal montages.

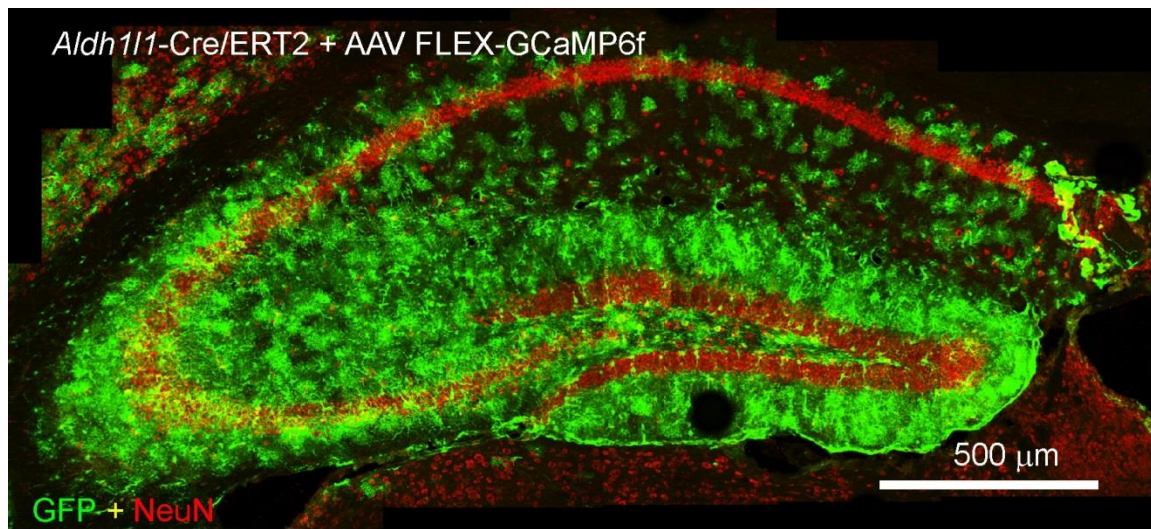


**Figure 3.5: *Aldh1l1*-Cre/ERT2 BAC transgenic mice using AAV FLEX-GCaMP6f.**

Representative hippocampal montage of *Aldh1l1*-Cre/ERT2 transgenic mice stained for GFP (green) and NeuN (red) after injection with AAV FLEX GcaMP6f (immunostained with GFP antibodies) and tamoxifen (75 mg/kg i.p for 5 consecutive days) shows expression of GFP in astrocytes, but not in neurons.

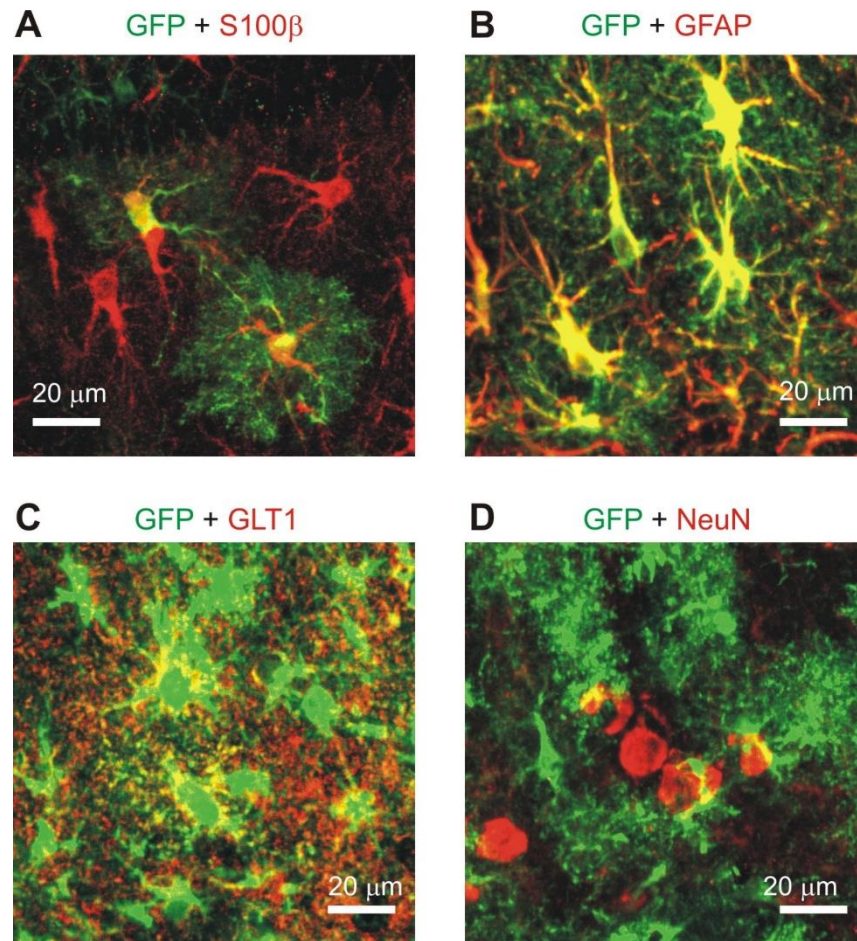


**Figure 3.6: High magnification images of CA1 s.r. astrocytes in *Aldh1l1-Cre/ERT2* mice.** Representative images in the *Aldh1l1-Cre/ERT2* transgenic mouse injected with AAV FLEX-GFP virus, followed by 75 mg/kg i.p. tamoxifen for 5 days, showing co-staining for S100β (A), GFAP (B), GLT1 (C), but not NeuN (D).

co-localization between GFP and S100 $\beta$  (**Figure 3.7**).

### **Section 3.4: *Ex vivo* and *in vivo* validation of the *Aldh111*-Cre/ERT2 BAC line**

#### **Validating *Aldh111*-Cre/ERT2 mice by cross with Ai95 mice**

We crossed Ai95 mice with *Slc1a3*-Cre/ERT and *Aldh111*-Cre/ERT2 mice. We induced gene expression with tamoxifen (75 mg/kg once per day for five days at ~P56) in the offspring that were heterozygous for both alleles and studied GcaMP6f expression two to three weeks later with IHC (i.e. at ~P80, **Figures 3.8-3.11**). We did not examine reporter expression in neonatal mice or in adult mice greater than 3 weeks after tamoxifen.

Cyto-GcaMP6f expression was sparse with *Slc1a3*-Cre/ERT mice, but was ubiquitous and high with *Aldh111*-Cre/ERT2 mice (**Figure 3.8**; n = 4 mice each). Indeed, the entire brain was green when cyto-GcaMP6f was driven with the *Aldh111*-Cre/ERT2 mouse line (**Figure 3.8B**). Occasional astrocytes that did not express GcaMP6f appeared as dark patches in an otherwise uniformly green neuropil, clearly seen in higher magnification images (white arrows; **Figure 3.9**). These dark patches contained S100 $\beta$  positive cells (**Figure 3.9**). It was clear that cyto-GcaMP6f were expressed in the vast majority of S100 $\beta$  positive cells in the hippocampus, visual cortex and striatum, with occasional patches of S100 $\beta$  positive cells that lacked the GECIs (**Figure 3.9**). Furthermore, examination of example brain areas in sagittal sections showed that *Aldh111*-Cre/ERT2 resulted in astrocyte GcaMP6f expression throughout the brain (**Supplemental movie 1**).

Overall, *Aldh111*-Cre/ERT2 mice resulted in GECI expression in >90% of astrocytes in the hippocampal CA1, CA3 and DG regions, in V1 of the visual cortex and in the striatum (**Figure 3.10**; n = 4 mice for each case). In contrast *Slc1a3*-Cre/ERT resulted in expression of cyto-GcaMP6f in ~20-40% of astrocytes in the same areas (**Figure 3.10**; n = 4 mice each).

As expected (Slezak et al., 2007), *Slc1a3*-Cre/ERT resulted in GECI expression in granule cells of the dentate gyrus (yellow arrow, **Figure 3.8A**; n = 4 mice). No similar neuronal expression was observed with *Aldh111*-Cre/ERT2 mice (**Figure 3.8B**; n = 4 mice). We also performed a specific set of experiments to evaluate GcaMP6f expression in neurogenic zones of the brain by examining colocalization with NeuN, which is one of several markers that label newly born neurons (Garcia et al., 2004). Thus, we found no significant colocalization between NeuN and GcaMP6f driven by *Aldh111*-Cre/ERT2 in the subgranular zone, dentate gyrus, subventricular zone, rostral migratory stream or the granule cell layer of the olfactory bulb (**Figure 3.11**; n = 4 mice each). This is in contrast to the *Aldh111*-Cre line, which has neuronal expression in these neurogenic zones and also in the upper layers of the cortex (Foo and Dougherty, 2013). Although a few neurons in the dentate gyrus (0.7%) and olfactory bulb granule cell layer (0.15%) seemingly colocalized with NeuN, the average data were not statistically significant from 0% co-labelling (**Figure 3.11**; n = 4 mice in each case). Thus, the possibility of significant neuronal expression of reporters with the *Aldh111*-Cre/ERT2 mice under the conditions we have examined is extremely low. The data illustrate the pan-astrocyte and specific nature of Cre-dependent gene expression driven by *Aldh111*-Cre/ERT2 in adult mice at ~P56 when evaluated ~3 weeks after the final tamoxifen injection with a standard five-day induction protocol.

### **No detectable leaky reporter expression with *Aldh111*-Cre/ERT2 mice**

We examined the possibility of leaky GcaMP6f reporter expression in the absence of tamoxifen in *Aldh111*-Cre/ERT2 mice. The injection of corn oil instead of tamoxifen resulted in no detectable GcaMP6f expression, whereas in parallel controls injection of tamoxifen clearly did (**Figure 3.12**; n = 4 mice each). As reported in earlier sections, in these additional controls, we

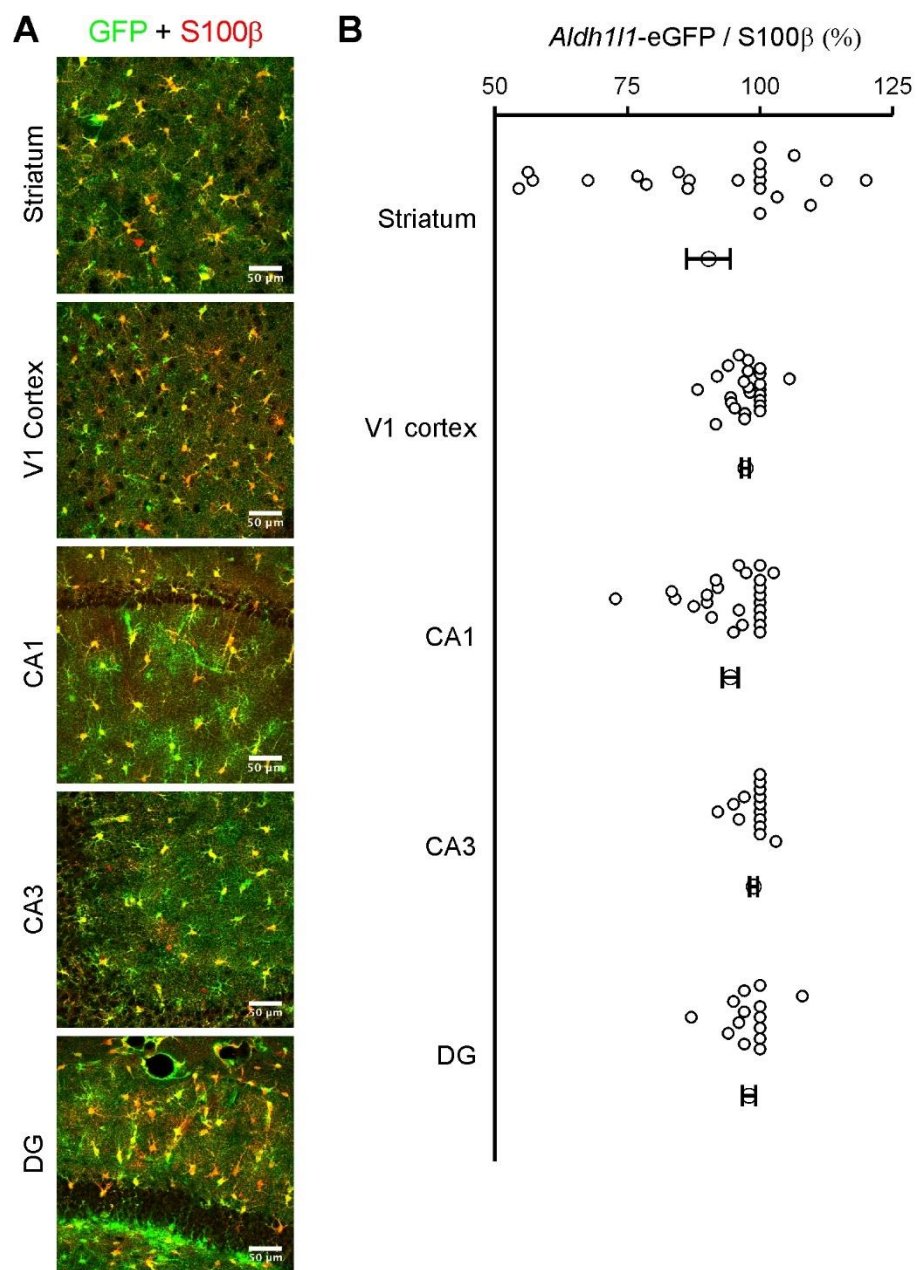


**Figure 3.7: *Aldh111*-eGFP astrocytes colocalize with S100 $\beta$ .** **A.** Representative images in the *Aldh111*-eGFP transgenic mice stained for GFP (green) and S100 $\beta$  (red). **B.** Quantification of IHC from 4 mice. Error bars indicate s.e.m.

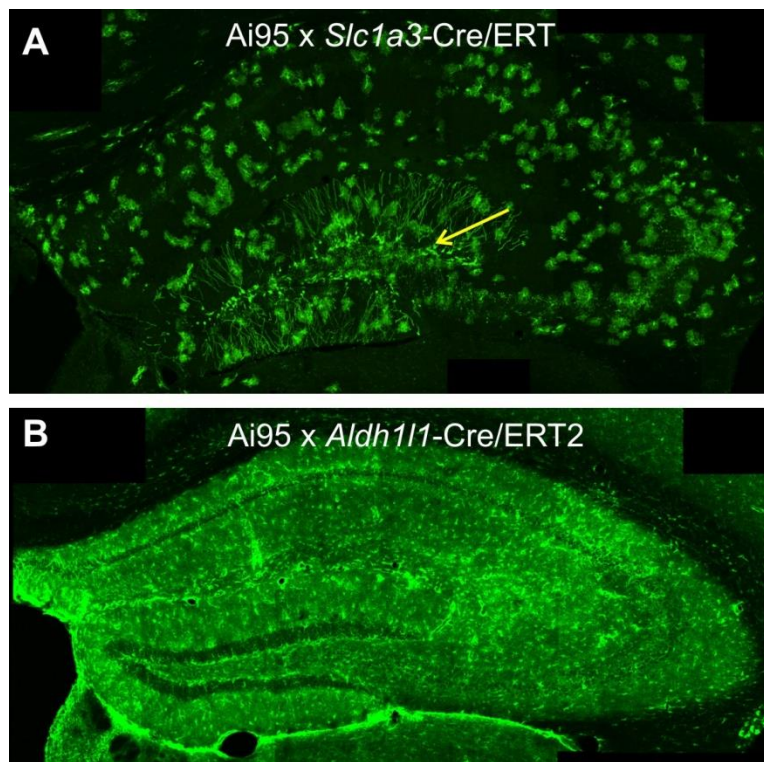


**Figure 3.8: Characterization of Lck-GcaMP6<sup>fl</sup>ox x Aldh111-Cre/ERT2 double transgenic mice.** **A.** Representative montage of Ai95 x *Slc1a3*-Cre/ERT double transgenic mice injected with tamoxifen and stained for cyto-GcaMP6f. The yellow arrow points to an example neuron with cyto-GcaMP6f expression. **B.** Representative hippocampal montage of Ai95 x *Aldh111*-Cre/ERT2 double transgenic mice injected with tamoxifen and stained with a GFP antibody shows GcaMP6f expression in nearly all astrocytes of the hippocampus.

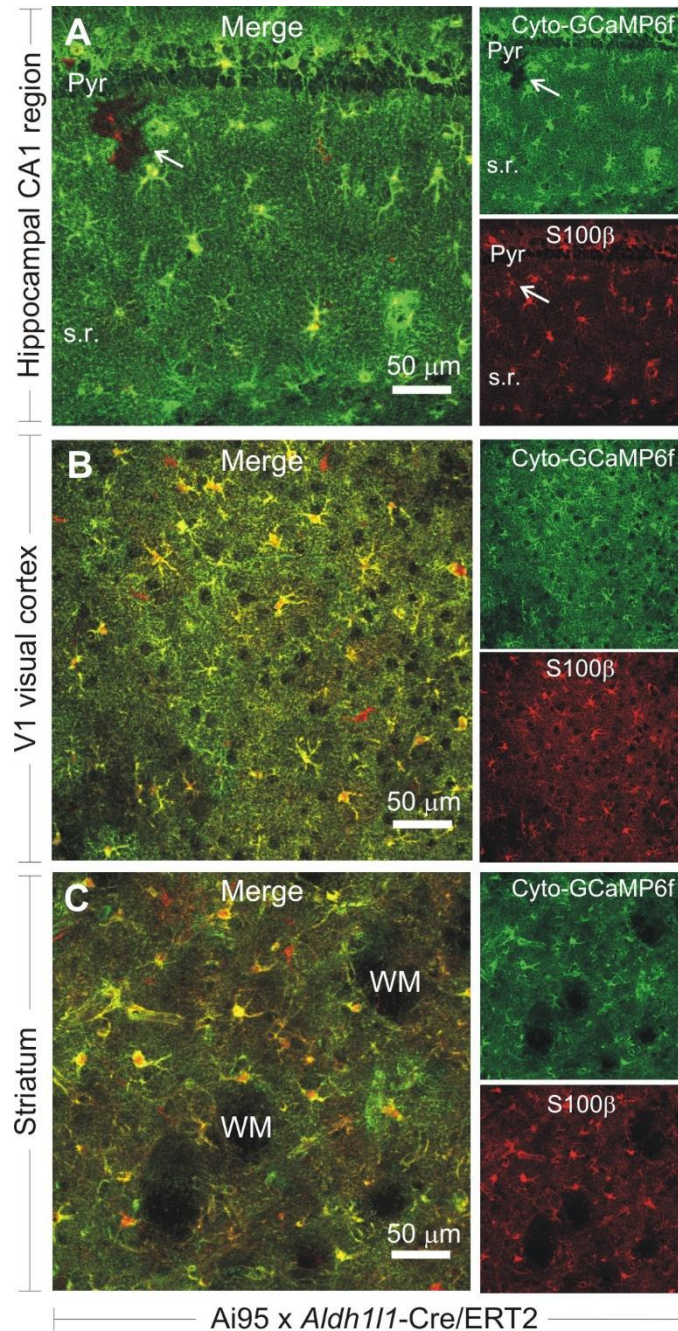


**Figure 3.9: Characterization of *Lck-GcaMP6<sup>fllox</sup>* x *Aldh111-Cre/ERT2* double transgenic mice.** **A.** Representative image of the hippocampal CA1 region from *Ai95 x Aldh111-Cre/ERT2* double transgenic mice injected with tamoxifen and stained for cyto-GcaMP6f (green) and S100β (red); the pyramidal cell layer (Pyr) and s.r. are indicated. The white arrow shows an astrocyte with S100β lacking cyto-GcaMP6f expression. **B-C.** As in **A**, but for V1 of the visual cortex and striatum, respectively. WM: White matter.

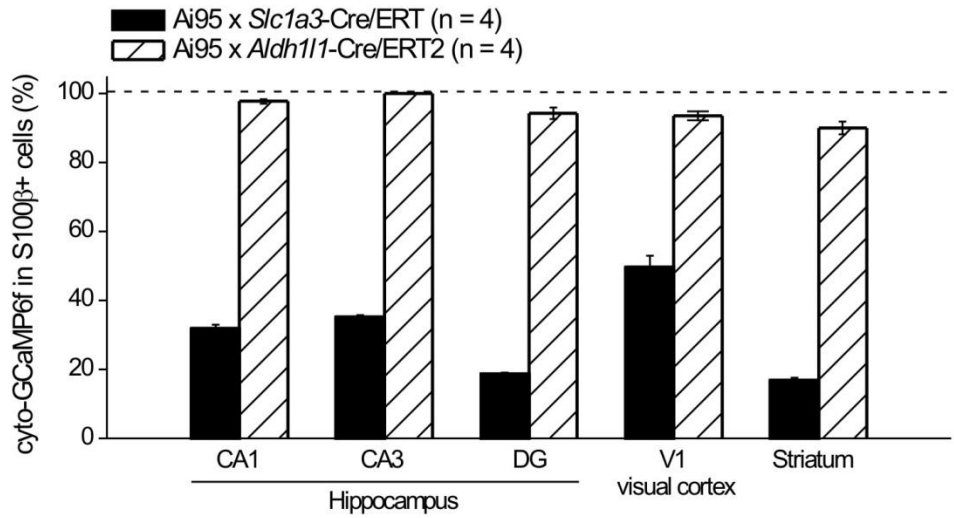


**Figure 3.10: Comparison of *Slc1a3-Cre/ERT* and *Aldh111-Cre/ERT2* transgenic mice.** Bar graph showing the percentage of S100 $\beta$ + astrocytes that express Lck-GcaMP6f in the Ai95 x *Slc1a3-Cre/ERT* and Ai95 x *Aldh111-Cre/ERT2* double transgenic mice in the hippocampal CA1, CA3, and DG areas, in the V1 visual cortex and d.l. striatum.

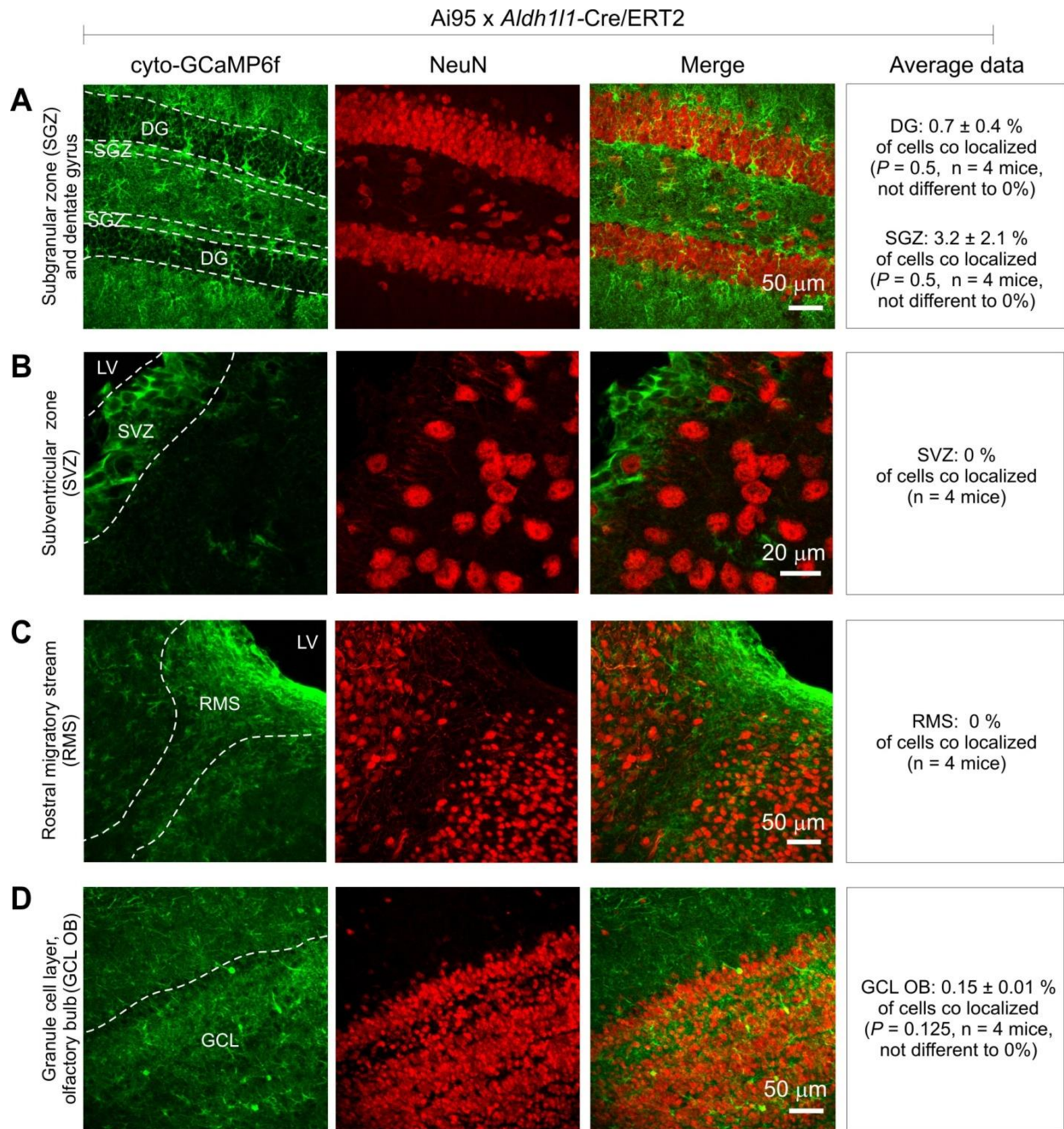


**Figure 3.11: No expression of cyto-GCaMP6f in NeuN positive cells when driven by *Aldh111*-Cre/ERT2 in Ai95 mice at ~P80.** The representative images show no colocalization between cyto-GCaMP6f and NeuN in the subgranular zone (A), the subventricular zone (B), the rostral migratory stream (C) or the granule cell later of the olfactory bulb (D).

did not find any evidence for GcaMP6f colocalization with NeuN when tamoxifen was administered (**Figure 3.12**). In the absence of tamoxifen, there was no detectable GcaMP6f expression (**Figure 3.12**; n = 4 mice). As far as we can ascertain, there was no leakiness in the *Aldh111-Cre/ERT2* mouse line. As expected, the level of GcaMP6f expression in the hippocampus, V1 visual cortex or striatum was dependent on the tamoxifen dose (25–225 mg/kg, **Figure 3.13, 3.14**; n = 3 mice). In our standard protocol (Madisen et al., 2010) that we used throughout this study, we administered tamoxifen at 75 mg/kg once per day for five days and assessed gene expression 14-21 days later at ~P80. However, since tamoxifen may accumulate in body compartments over multiple days this protocol cannot be used to reliably assess the tamoxifen dose dependence of gene expression. In order to assess this aspect, we administered tamoxifen only once at 25, 75 and 225 mg/kg (at P56) and assessed gene expression 10 days later in Figure 3.12, as previously described (Chow et al., 2008; Nakamura et al., 2006).

### **Cortical astrocyte Ca<sup>2+</sup> signals *ex vivo* and *in vivo* measured with GECIs driven by *Aldh111-Cre/ERT2***

We next determined whether *Aldh111-Cre/ERT2* mice would drive GECI expression sufficient for astrocyte calcium imaging. Astrocytes respond to endogenously released noradrenaline with calcium elevations mediated by  $\alpha 1$  adrenoceptors (Ding et al., 2013). We first studied astrocyte calcium signals in acute brain slices of V1 visual cortex following tamoxifen induction in adult *Aldh111-Cre/ERT2* x Ai95 double transgenic mice. We probed this process by applying 10  $\mu$ M phenylephrine, an  $\alpha 1$  adrenoceptor agonist, in the continued presence of TTX (0.5  $\mu$ M) to minimize secondary effects of neuronal activation. PE-evoked robust calcium elevations (**Figure 3.15**; n = 12 cells, 5 mice). Spontaneous signals were also

readily detected by *Aldh111*-Cre/ERT2-mediated GECI expression as can be seen in example traces in **Figure 3.15B**.

Astrocytes in the visual cortex respond with robust calcium elevations during arousal/startle due to the release of noradrenaline from noradrenergic projections via a mechanism likely involving  $\alpha$ 1 adrenoceptors on astrocytes (Shigetomi et al., 2016). We next tested if astrocyte GECI expression driven by *Aldh111*-Cre/ERT2 mice could detect calcium signals *in vivo* from non-anesthetized awake behaving mice. We measured spontaneous calcium signals and those triggered by startle, which was elicited by a gentle puff of air to the face (**Figure 2.1**). The representative images and traces shown in **Figure 3.16A** and the average trace in **Figure 3.16B** demonstrate that *Aldh111*-Cre/ERT2 drove GECI expression in cortical astrocytes sufficiently to detect spontaneous and startle-evoked astrocyte calcium signals in awake behaving mice. Overall, *Aldh111*-Cre/ERT2 mediated expression of cyto-GcaMP6f visualized aspects of astrocyte calcium signaling consistent with published work (Ding et al., 2013; Srinivasan et al., 2015).

### **Section 3.5: Establishing the adult cortical astrocyte transcriptome**

In order to determine the cortical astrocyte transcriptome from adult mice we crossed *Aldh111*-Cre/ERT2 mice with RiboTag mice that express the ribosomal protein Rpl22HA in a Cre-dependent manner (Sanz et al., 2009). We found Rpl22HA was strongly expressed in S100 $\beta$  positive cortical astrocytes, but not in NeuN positive neurons (**Figure 3.17**; n = 4 mice). We used standard methods (**Figure 3.18**) to immunoprecipitate (IP) Rpl22HA containing ribosomes and their associated actively translated mRNAs (Sanz et al., 2009), and performed RNA sequencing to determine the transcriptome of cortical astrocytes at P80 (4 biological replicates;

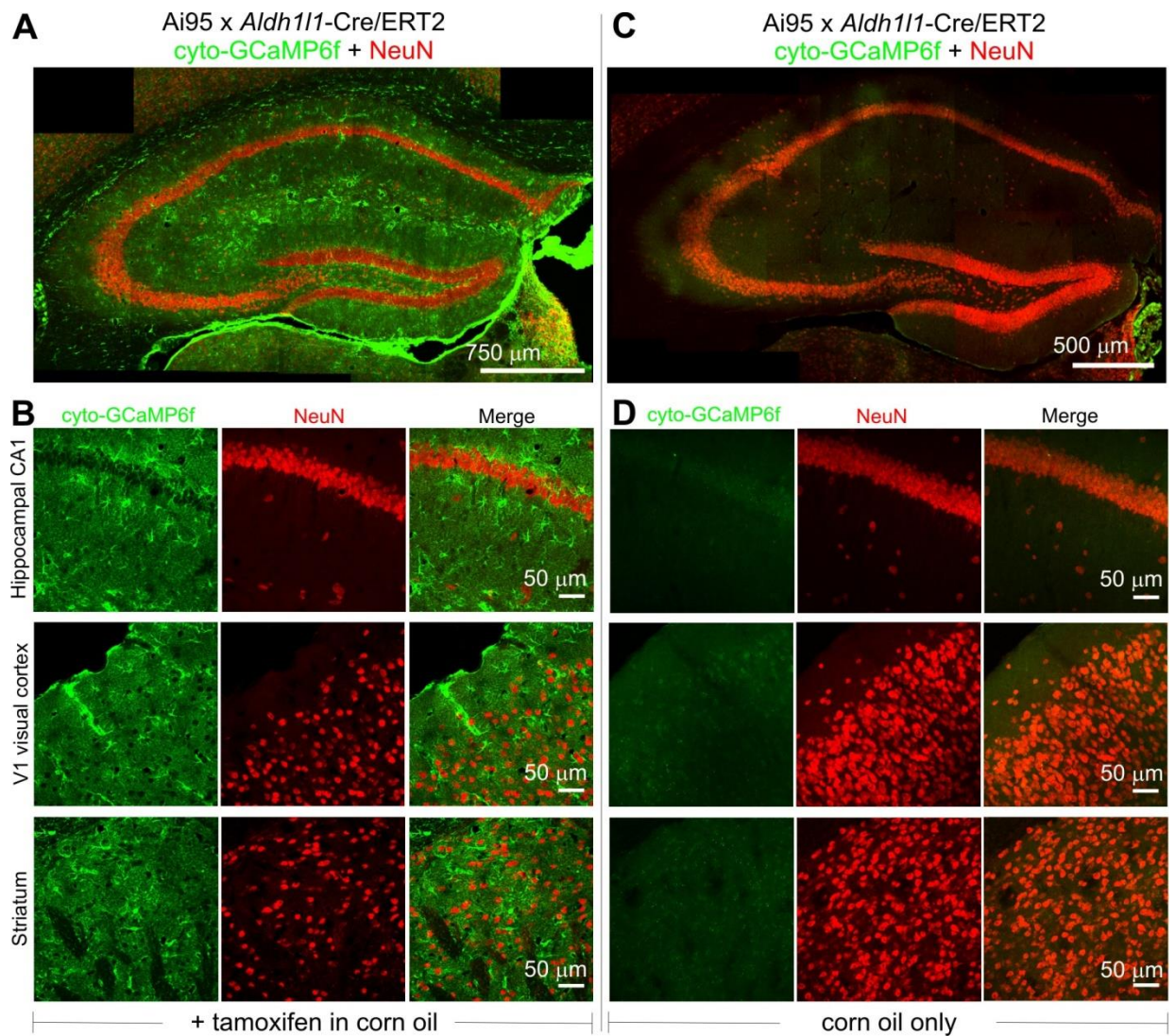


**Figure 3.12: No expression of cyto-GCaMP6f in the absence of tamoxifen when driven by *Aldh111-Cre/ERT2* in Ai95 mice at ~P80. A-B.** Tamoxifen driven cyto-GCaMP6f expression in the hippocampus (A). Higher magnification areas of the hippocampal CA1 region, V1 visual cortex and dorso lateral striatum (B) are also shown. **C-D.** As in A-B, but when no tamoxifen was administered (corn oil was administered instead). There was no detectable cyto-GCaMP6f expression anywhere. The green haze is auto fluorescence. The images are shown with the exact same laser power, acquisition settings and gray scale pixel values. Each image is representative of 4 mice.

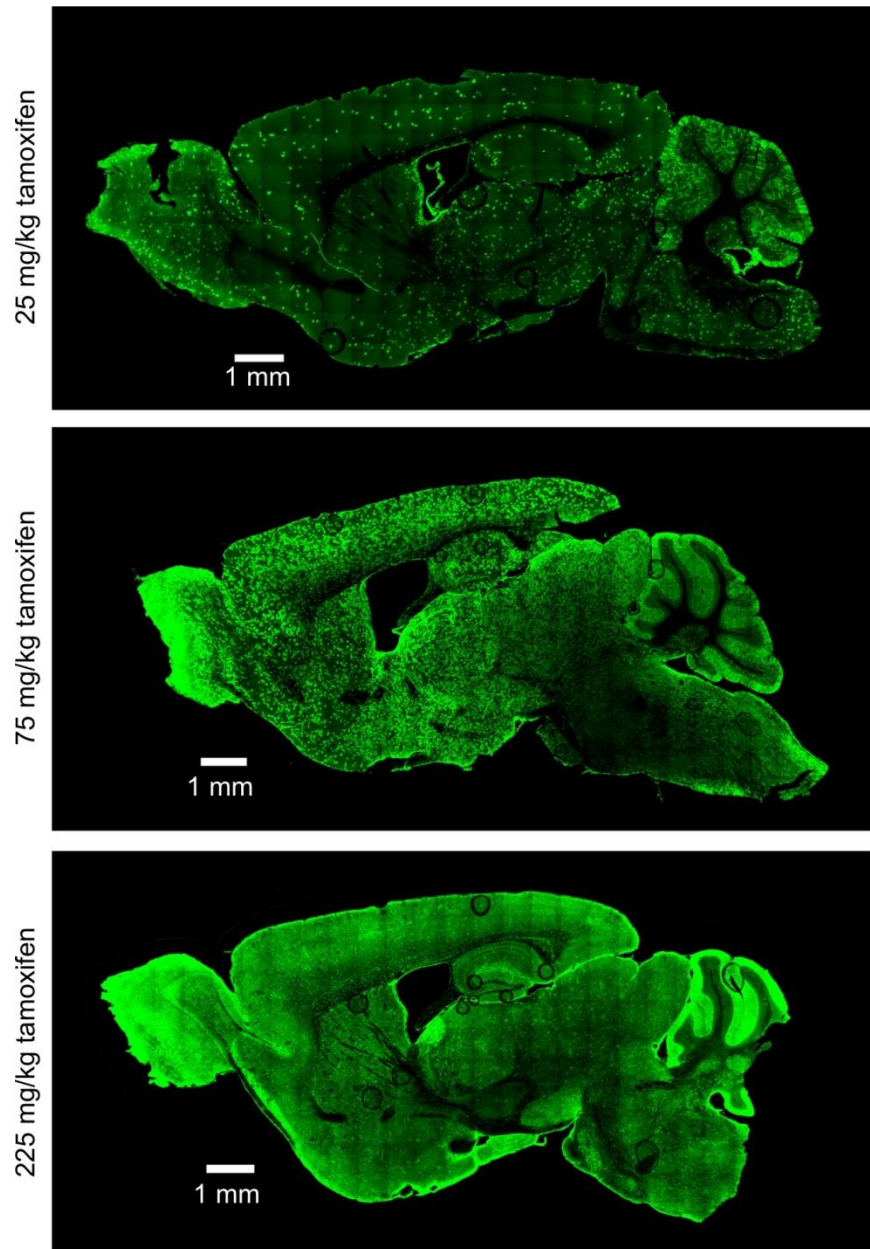


**Figure 3.13: Cyto-GCaMP6f expression when driven by *Aldh1l1*-Cre/ERT2 in ~P66 Ai95 mice varied depending on tamoxifen dose administered *in vivo*.** Representative images showing cyto-GCaMP6f expression as a function of tamoxifen dose in sagittal brain sections. Tamoxifen may accumulate in body compartments over multiple days. Therefore, to reliably assess the tamoxifen dose dependence of gene expression, we administered tamoxifen only once at 25, 75 and 225 mg/kg (at P56) and assessed gene expression 10 days later, as previously described (Chow et al., 2008; Nakamura et al., 2006).

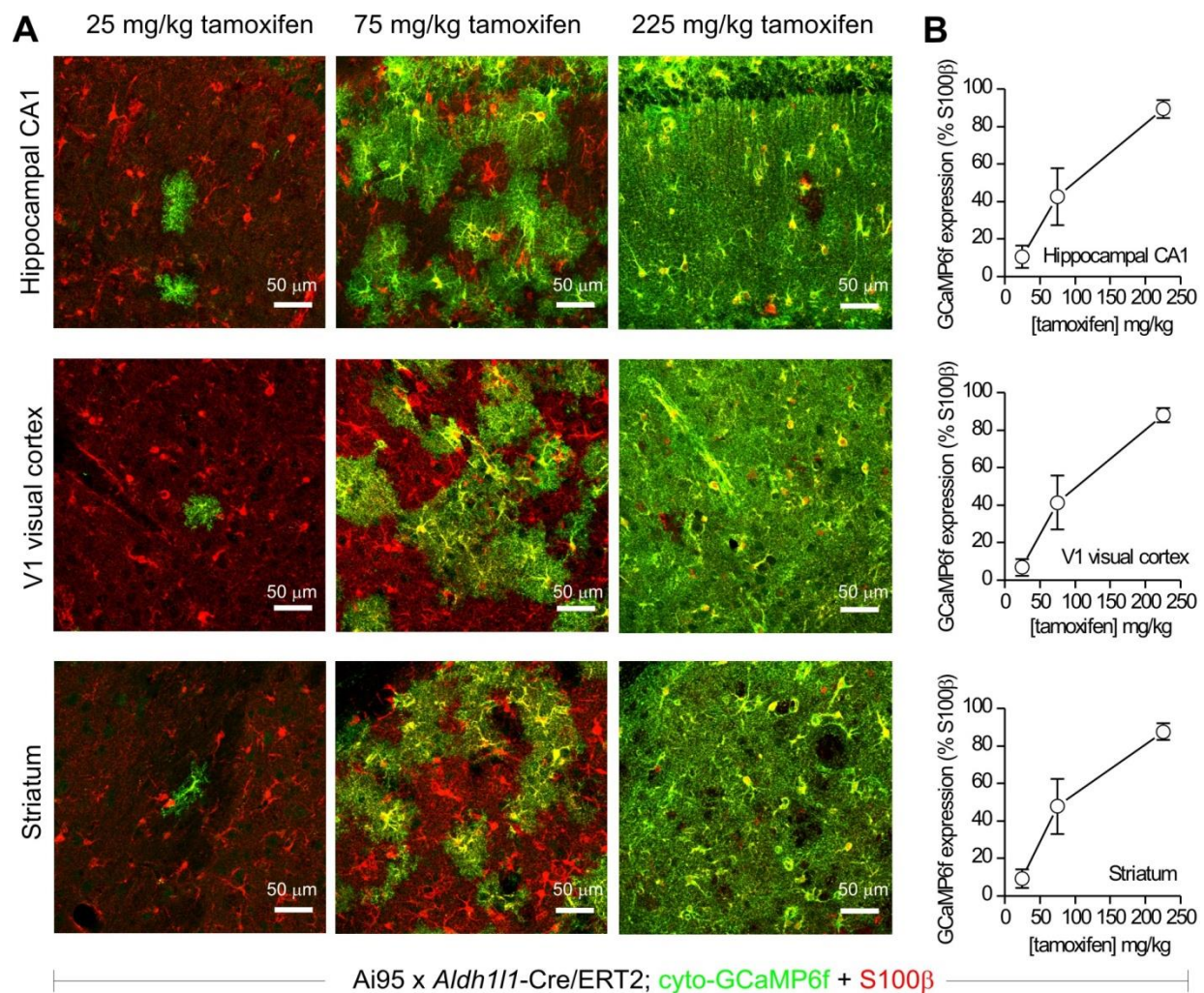


**Figure 3.14: Cyto-GCaMP6f expression when driven by *Aldh11-Cre/ERT2* in Ai95 mice at ~P66 was dependent on the tamoxifen dose administered *in vivo*.** **A.** Representative images at higher magnification than Figure 3.12 showing cyto-GCaMP6f expression as a function of tamoxifen dose in hippocampal CA1, V1 visual cortex and striatal brain sections. **B.** Average data showing the % of S100 $\beta$  positive cells that expressed cyto-GCaMP6f in the three brain areas as a function of tamoxifen dose. In all three brain areas, cyto-GCaMP6f expression was dependent on the tamoxifen dose, but there were no detectable differences between these areas. N = 12 sections per region from 3 mice at each dose. Tamoxifen was administered only once at 25, 75 and 225 mg/kg (at P56) and expression assessed 10 days later as previously described (Chow et al., 2008; Nakamura et al., 2006).

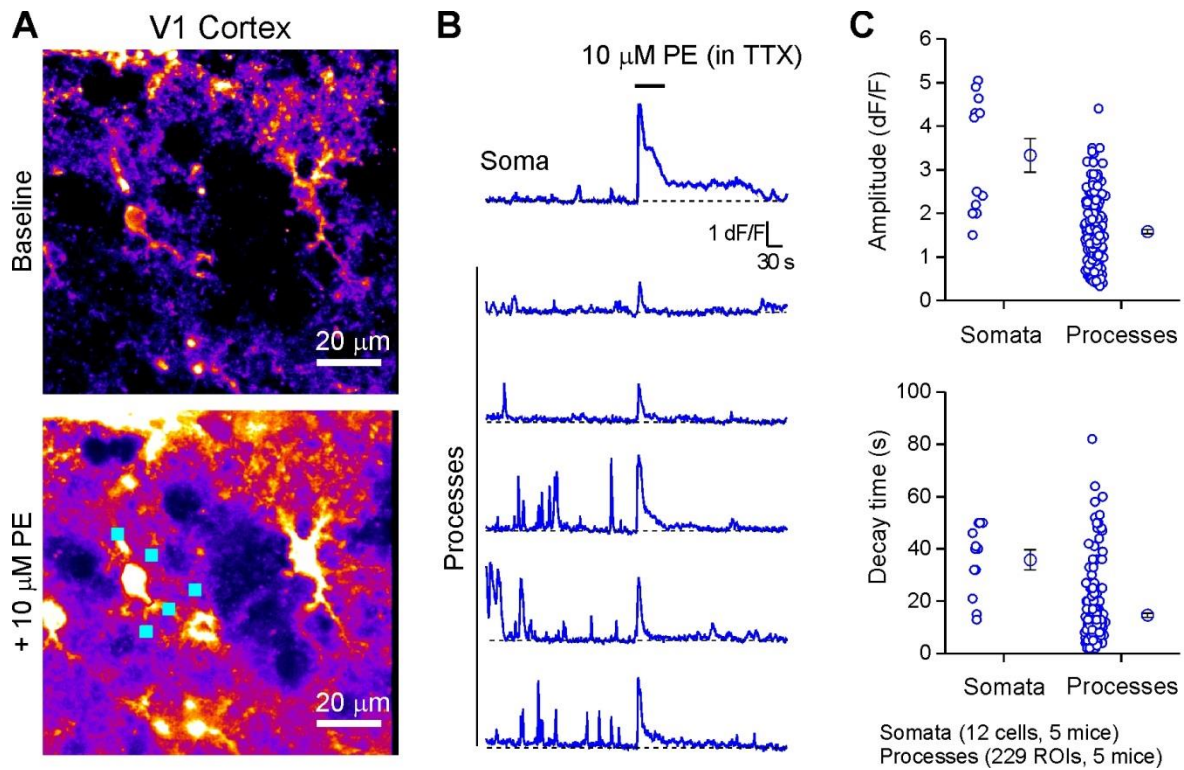


**Figure 3.15: Visual cortex astrocytes from Ai95 x *Aldh111-Cre/ERT2* double transgenic mice display spontaneous and PE-evoked calcium signals.** **A.** Representative images of baseline calcium signals in V1 visual cortex astrocytes, before and during 10  $\mu\text{M}$  phenylephrine (PE). **B.** Representative traces of  $\text{Ca}^{2+}$  signals in the soma and processes of the astrocyte from the mouse shown in **A** (Blue squares are the processes regions of interest (ROIs) used). Both spontaneous and PE-evoked calcium signals are detected. **C.** Scatter plots of PE-evoked calcium signal amplitude and decay times from the somata and processes of visual cortex astrocytes of the Ai95 x *Aldh111-Cre/ERT2* double transgenic mice. Sometimes the bars representing the s.e.m. are smaller than the symbol used for the mean.

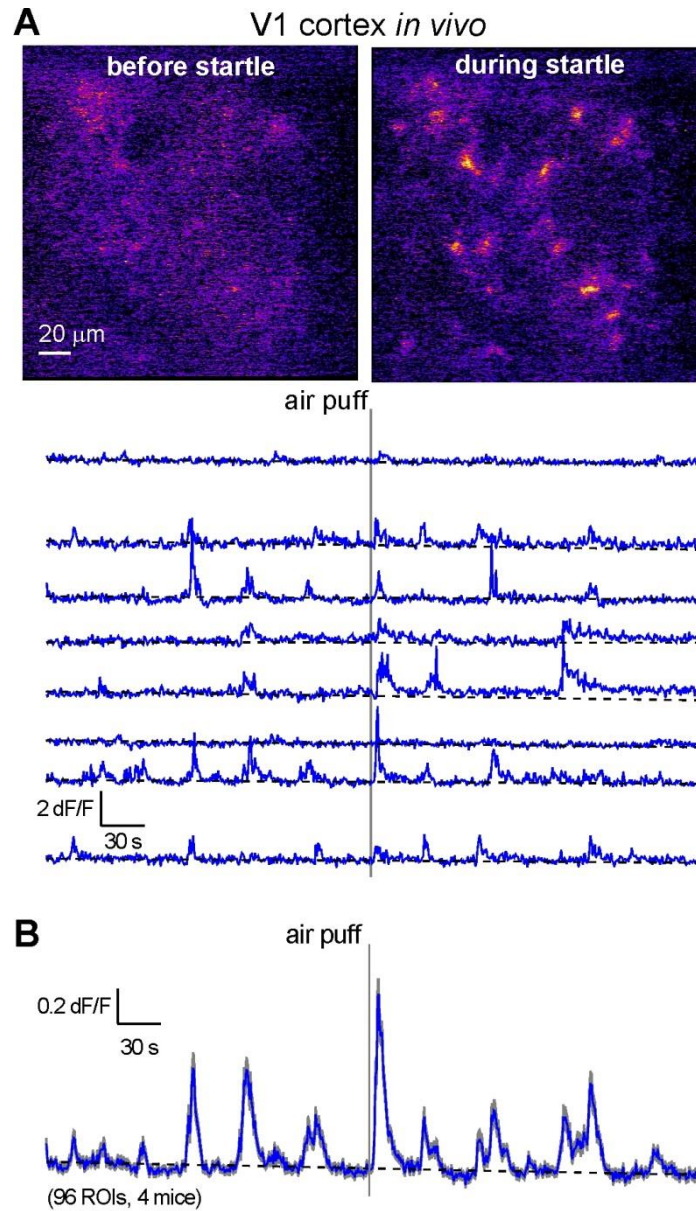


**Figure 3.16: *In vivo* astrocyte calcium signals measured with cyto-GCaMP6f driven by *Aldh111-Cre/ERT2* mice.** **A.** *Top:* Representative pseudo-colored images showing the fluorescence increase of cyto-GCaMP6f in astrocytes of mouse visual cortex before and during startle. *Bottom:* representative  $\Delta F/F$  traces from 8 randomly selected ROIs ( $10 \mu\text{m}^2$  each). The gray vertical line indicates the air puff. The trend for the baseline is shown with a black dashed line. **B.** The average  $\Delta F/F$  trace of 96 ROIs from four cyto-GCaMP6f x *Aldh111-Cre/ERT2* mice (s.e.m. shown in grey for every 5<sup>th</sup> time point).

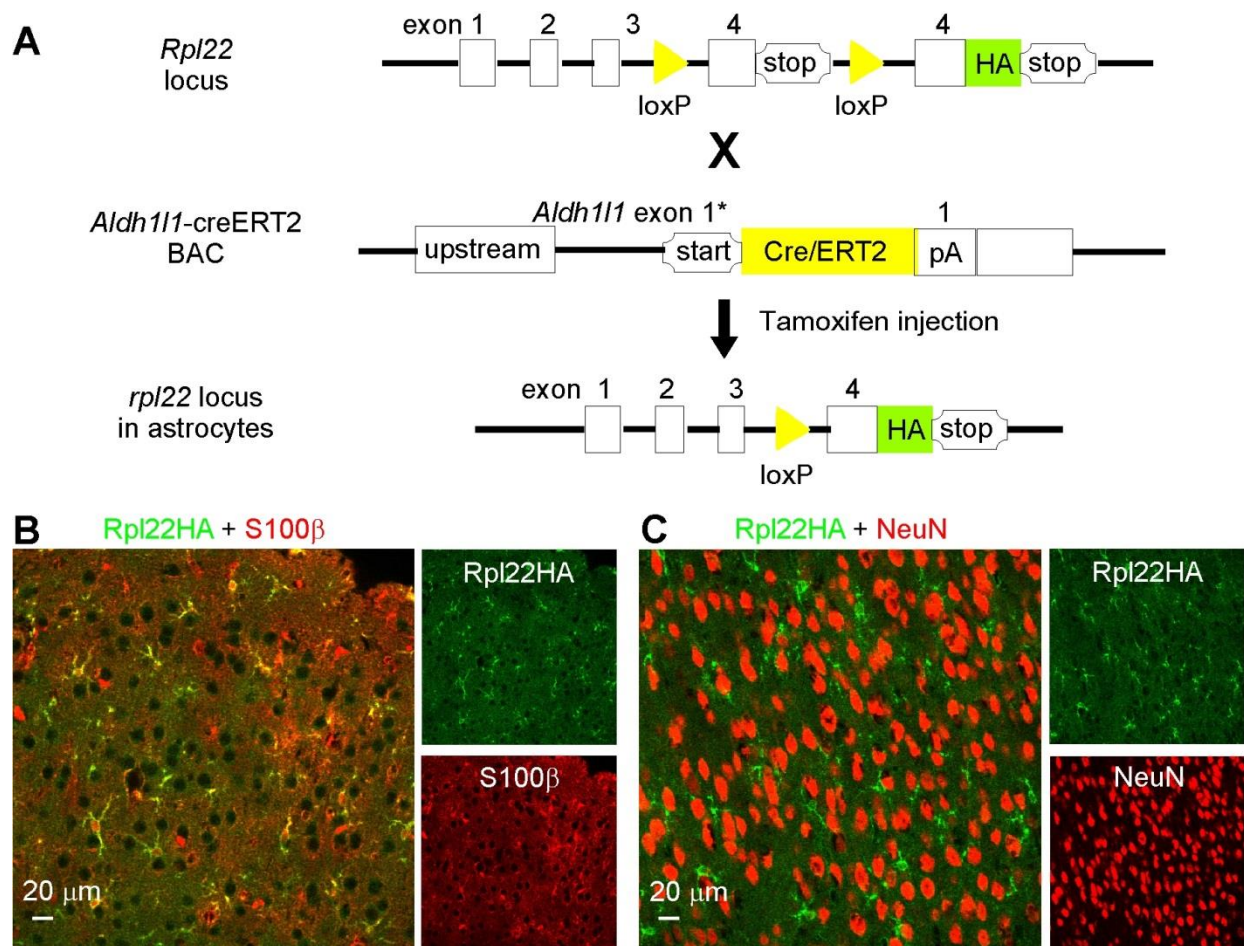


**Figure 3.17: *Aldh111*-Cre/ERT2 x RiboTag mice and the determination of the cortical astrocyte transcriptome at P80.** **A.** Schematic showing the breeding strategy used to create the *Aldh111*-Cre/ERT2 x RiboTag double transgenic mice. **B.** Representative images of IHC data showing strong colocalization between S100 $\beta$  and Rpl22HA in the V1 visual cortex. **C.** Representative images of IHC data showing no colocalization between NeuN and Rpl22HA.

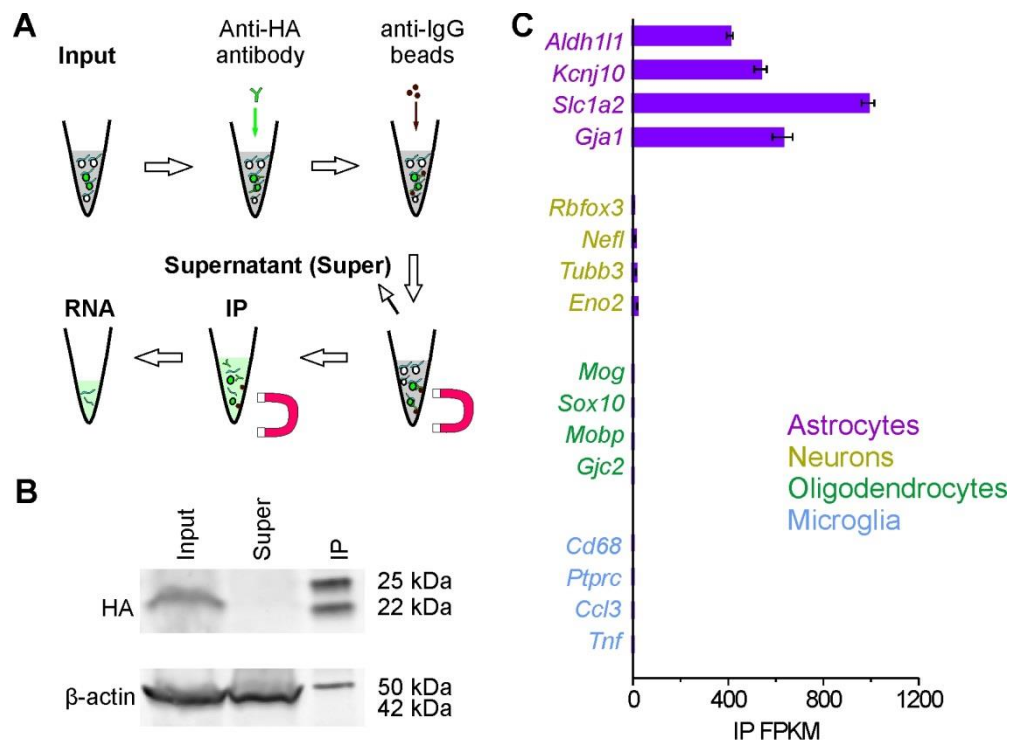


**Figure 3.18: Immuprecipitation of cortex from P80 *Aldh111-Cre/ERT2* x RiboTag mice to purify astrocyte mRNA.** **A.** Schematic of the workflow. **B.** The representative Western blot shows that Rpl22HA was preserved in the IP sample, whereas  $\beta$ -actin was depleted in relation to input. In contrast, there was no Rpl22HA in the supernatant. In the IP lane, the 25 and 50 kD bands are the light and heavy chains of the anti-HA antibody that was used in the IP. **C.** The RNA-Seq FPKM values of well-established markers of astrocytes, neurons, oligodendrocytes, and microglia in the IP samples are plotted as mean  $\pm$  s.e.m. from four biological replicates ( $n = 4$  mice).

**Table 3.2).** Raw and normalized RNA-Seq data have also been deposited in the Gene Expression Omnibus repository (<http://www.ncbi.nlm.nih.gov/geo>) with accession number GSE84540 and can also be found on our searchable website database at Adult Astrocyte RNA-Seq Explorer (<http://astrocyternaseq.org>).

We found the P80 IP samples replete with several known astrocyte markers (Zhang et al., 2014), but depleted of markers for neurons, oligodendrocytes and microglia (**Figure 3.18C**). We further validated that the IP samples represent the P80 astrocyte transcriptome by comparing it to the published database of P7 cortical cells (Zhang et al., 2014). **Figure 3.19** plots the Row z-score values from our P80 data set for the top 50 genes that were astrocyte enriched in P7 cortical astrocytes (Zhang et al., 2014). Furthermore, the top 50 P7 neuronal genes were depleted in our P80 data set (**Figure 3.20**).

Most of the top 50 P7 astrocyte genes were enriched in the P80 data set, but there were exceptions indicating abundant astrocyte-enriched genes which were differentially expressed between IP and input at P80 (**Figure 3.19**). As these genes may reflect changes in astrocytes from pups to young adults, we compared P7 and P80 across the whole dataset. To do this, we determined the 4727 transcripts enriched in astrocytes in either dataset and used the Rank-Rank Hypergeometric Overlap method (Plaisier et al., 2010; Stein et al., 2014) to compare their relative rank according to FPKM percentile (**Figure 3.21**). Most transcripts were significantly clustered along the diagonal, which indicates similarity in rank between P7 and P80 (**Figure 3.21**). However, many transcripts did not cluster near the diagonal, indicating different expression between P7 and P80; these can be seen more clearly in the scatter graph in **Figure 3.21**. **Figure 3.22** plots heat maps for the top 34 differentially expressed genes between P7 and P80 (i.e. delta percentile > 0.1) and **Table 3.3** reports the results of Gene Ontology (GO) analyses for these 34, listed in **Table 3.4**.

Examination of **Figure 3.22** also reveals several genes that are markedly altered

between P7 and P80: the genes encoding membrane proteins (*Slc1a3*) GLAST, (*Slc1a2*) Glt1, (*Slc6a11*) GAT3, (*Slc6a1*) GAT1 and (*Gja1*) Cx43, and the genes for a calcium binding protein and a chondroitin sulfate proteoglycan (*Sparcl1* and *Bcan*). The percentile FPKM of these and several other genes frequently invoked in astrocyte biology are summarized in **Table 3.5**. *S100b* was highly expressed, but increased substantially at P80 (**Table 3.5**). Moreover, as expected (Sun et al., 2013), metabolic glutamate receptor (mGluR) 2 receptor (*Grm2*) was increased in the P80 data set relative to P7, and mGluR5 (*Grm5*) was decreased at P80 relative to P7 (**Table 3.5**). As expected, *Grm2* was not astrocyte enriched at P7 or P80 (N/E in **Table 3.5**). Of the known astrocyte secreted factors, HEVIN (*Sparcl1*) was higher at P80 and thrombospondins 1-3 were lower at P80 relative to P7. Vesicular neurotransmitter transporters for glutamate, Ach, nucleotides, GABA and monoamines were all very low in astrocytes at both P7 and P80, although vesicular glutamate transporter (vGlut) 1 (*Slc17a7*) was higher at P80 than at P7 (**Table 3.6**). None of these transporters were astrocyte enriched (**Table 3.6**). The role of astrocyte vesicular gliotransmission remains debated and our P80 dataset, along with *Aldh111-Cre/ERT2* mice, will be useful to plan specific experiments in adult mice. Broadly, however, our data are in accord with those at P7 (Zhang et al., 2014) and show low mRNA for known vesicular neurotransmitter transporters (**Table 3.6**). This brief analysis illustrates that astrocyte P80 RNA-Seq data provide validation of the *Aldh111-Cre/ERT2* mouse and a resource to explore the functions of specific genes enriched in adult astrocytes (**Figure 3.20-21**) as well as those that are not enriched, but change in relative expression between P7 and P80 astrocytes.

### **Section 3.6: Summary and discussion**

We have developed a much needed transgenic mouse line that will advance our ability our ability to genetically target astrocytes to explore astrocyte biology within neural circuits in

<b>ID</b>	<b>Sex</b>	<b>Age</b>	<b>ng RNA</b>	<b>RIN</b>
579 input	M	P81	561	9.4
579 IP	M	P81	1570	9.8
580 input	M	P81	966	9.4
580 IP	M	P81	2448	9.2
581 input	M	P81	116	9.9
581 IP	M	P81	2150	9.9
595 input	F	P78	82	9.9
595 IP	F	P78	4464	9.5

**Table 3.2:** The quantity and quality of the cortical RNA samples used to create multiplexed paired-end sequencing library. Quality is reported as RIN. N = 4 mice at ~P80.

Gene ontology biological processes	# genes	q-value
behavior (GO:0007610)	9	5.70 E-07
organic anion transport (GO:0015711)	8	3.20 E-07
amino acid import (GO:0043090)	3	3.73 E-06
response to extracellular stimulus (GO:0009991)	7	3.45 E-06
cellular response to external stimulus (GO:0071496)	6	2.39 E-06
anion transport (GO:0006820)	8	2.93 E-06
response to drug (GO:0042493)	7	7.62 E-06
organic acid transport (GO:0015849)	6	7.34 E-06
carboxylic acid transport (GO:0046942)	6	6.99 E-06
cellular response to extracellular stimulus (GO:0031668)	5	5.43 E-06
amino acid transport (GO:0006865)	5	7.65 E-06
single-organism behavior (GO:0044708)	7	8.80 E-06
response to toxic substance (GO:0009636)	5	1.24 E-05
acidic amino acid transport (GO:0015800)	3	1.44 E-05
response to wounding (GO:0009611)	5	2.66 E-05
response to mechanical stimulus (GO:0009612)	5	3.4 E-05
regulation of neurotransmitter levels (GO:0001505)	4	4.22 E-05
learning or memory (GO:0007611)	5	5.87 E-05
regeneration (GO:0031099)	4	5.59 E-05
response to calcium ion (GO:0051592)	4	6.27 E-05
neurotransmitter transport (GO:0006836)	4	6.03 E-05
aging (GO:0007568)	5	6.74 E-05
cellular response to calcium ion (GO:0071277)	3	8.43 E-05
response to axon injury (GO:0048678)	3	9.06 E-05

transport
  response to stimulus
  behavior

**Table 3.3: Gene ontology analysis of astrocyte genes with differential expression (P7 vs P80).** The top 25 biological process terms from gene ontology analysis for the 34 genes whose expression differed between cortical astrocyte enriched genes at P80 and P7 are listed (Figure 3.21). The number of genes in each GO group and the q-value are reported.

Gene name	Zhang <i>et al.</i> , 2014		This study		$\Delta$ percentile
	P7 astrocyte FPKM	P7 percentile	P80 IP FPKM $\pm$ s.e.m.	P80 percentile	
Down at P80					
<i>Fos</i>	3527	1.0000	9.59 $\pm$ 3.55	0.0005	-0.9995
<i>Fabp7</i>	1604	0.4548	348 $\pm$ 70	0.0170	-0.4378
<i>Cst3</i>	3309	0.9383	10747 $\pm$ 972	0.5237	-0.4146
<i>Jun</i>	1164	0.3301	33.4 $\pm$ 10.3	0.0016	-0.3285
<i>Ptprz1</i>	1021	0.2895	59.7 $\pm$ 5.2	0.0029	-0.2866
<i>Sparcl1</i>	1768	0.5014	4453 $\pm$ 178	0.2170	-0.2844
<i>Slc1a3</i>	1144	0.3244	1009 $\pm$ 16	0.0492	-0.2753
<i>Nr4a1</i>	871	0.2469	15.5 $\pm$ 3.8	0.0008	-0.2461
<i>Cyr61</i>	842	0.2388	30.2 $\pm$ 6.1	0.0015	-0.2373
<i>Ptn</i>	914	0.2591	855 $\pm$ 31	0.0417	-0.2174
<i>Bcan</i>	818	0.2319	566 $\pm$ 15	0.0276	-0.2043
<i>Hspa5</i>	680	0.1929	145 $\pm$ 11	0.0071	-0.1858
<i>Tspan7</i>	1145	0.3246	2905 $\pm$ 90	0.1416	-0.1830
<i>Mfge8</i>	730	0.2071	606 $\pm$ 22	0.0295	-0.1775
<i>Fosb</i>	609	0.1728	0.55 $\pm$ 0.14	2.66 e-5	-0.1728
<i>Psap</i>	656	0.1860	292 $\pm$ 6	0.0142	-0.1718
<i>Scd2</i>	893	0.2531	1778 $\pm$ 88	0.0866	-0.1665
<i>Ubc</i>	579	0.1640	80.1 $\pm$ 3.1	0.0039	-0.1601
<i>Slc1a2</i>	732	0.2075	987 $\pm$ 27	0.0481	-0.1594
<i>Slc6a11</i>	564	0.1599	337 $\pm$ 6	0.0164	-0.1435
<i>Malat1</i>	515	0.1461	86.1 $\pm$ 22.6	0.0042	-0.1419
<i>Atp1b2</i>	624	0.1770	1066 $\pm$ 18	0.0519	-0.1251
<i>Slc38a3</i>	451	0.1279	85.0 $\pm$ 4.2	0.0041	-0.1238
<i>Ppap2b</i>	516	0.1464	562 $\pm$ 39	0.0274	-0.1191
<i>Slco1c1</i>	408	0.1158	63.0 $\pm$ 4.2	0.0031	-0.1127
<i>Actg1</i>	450	0.1275	320 $\pm$ 44	0.0156	-0.1119
<i>Gja1</i>	501	0.1420	628 $\pm$ 42	0.0306	-0.1114
<i>Bhlhe40</i>	392	0.1112	45.5 $\pm$ 3.3	0.0022	-0.1090
<i>Slc6a1</i>	425	0.1204	321 $\pm$ 12	0.0157	-0.1047
Up at P80					
<i>Aldoc</i>	512	0.1452	7378 $\pm$ 166	0.3596	0.2144
<i>Glul</i>	740	0.2097	7611 $\pm$ 508	0.3709	0.1612
<i>Ckb</i>	336	0.0953	5206 $\pm$ 333	0.2537	0.1584
<i>Ptgds</i>	1.7	0.0005	3086 $\pm$ 1205	0.0150	0.1499
<i>Apoe</i>	3006	0.8524	20520 $\pm$ 590	1.0000	0.1476

**Table 3.4: 34 cortical astrocyte genes that were differentially expressed between P80 and P7.** The percentile FPKM in each dataset was determined relative to the highest expressed transcript in P80 Ips (*Apoe*) or in P7 astrocytes (*Fos*). The genes listed in the table are ordered according to magnitude of difference in percentile. Genes are color coded green for increased expression at P80 and red for decreased expression at P80.

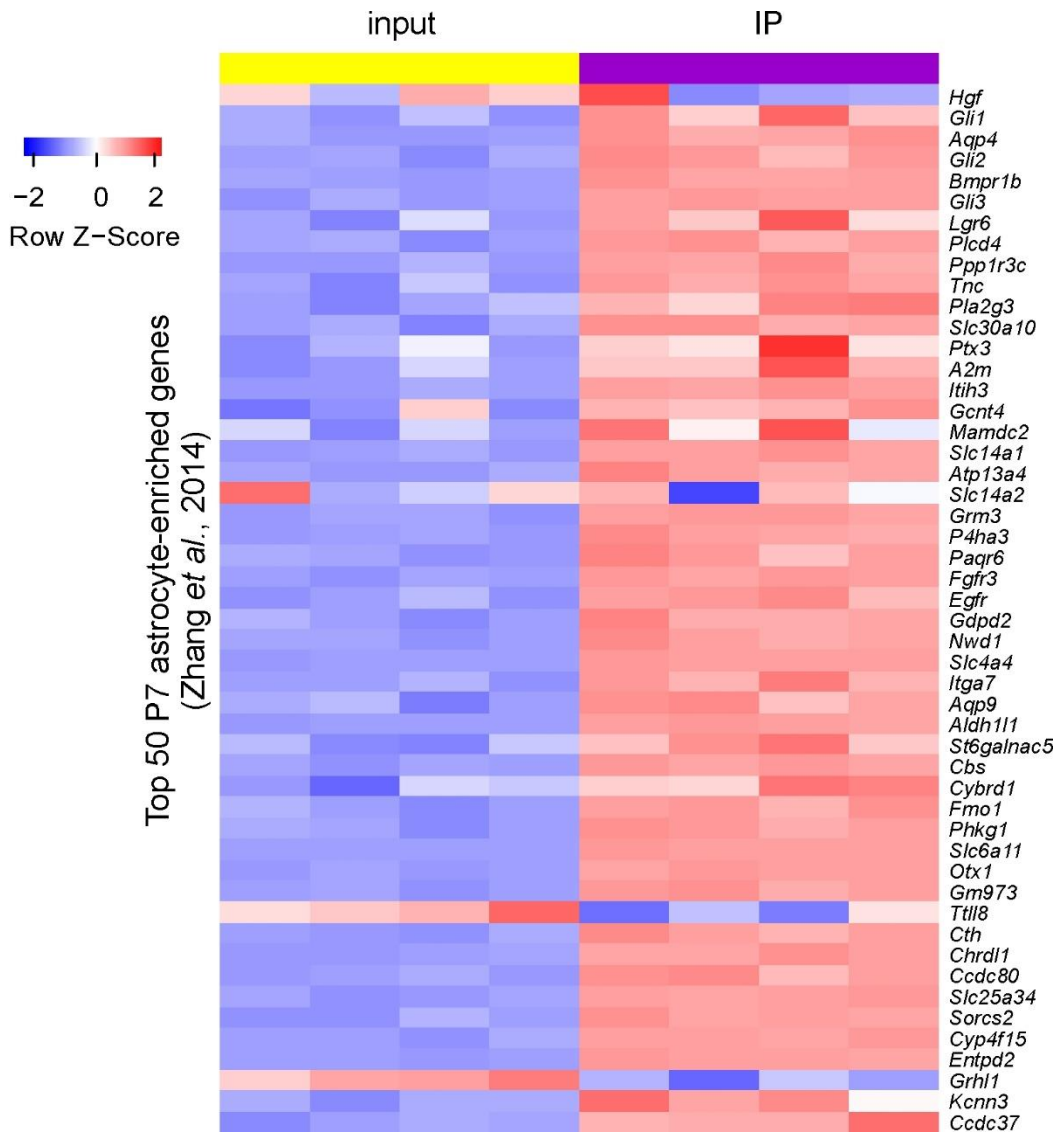


**Figure 3.19: P80 cortical astrocyte transcriptome are enriched for P7 astrocyte genes.** A heatmap showing relative expression (Row z-score) of the top 50 astrocyte genes from the P7 cortical RNA-Seq database in our P80 dataset. Row z-scores are shown as red for relative enrichment and as blue for relative depletion. The data used for P7 were from Zhang *et al.*, (2014).

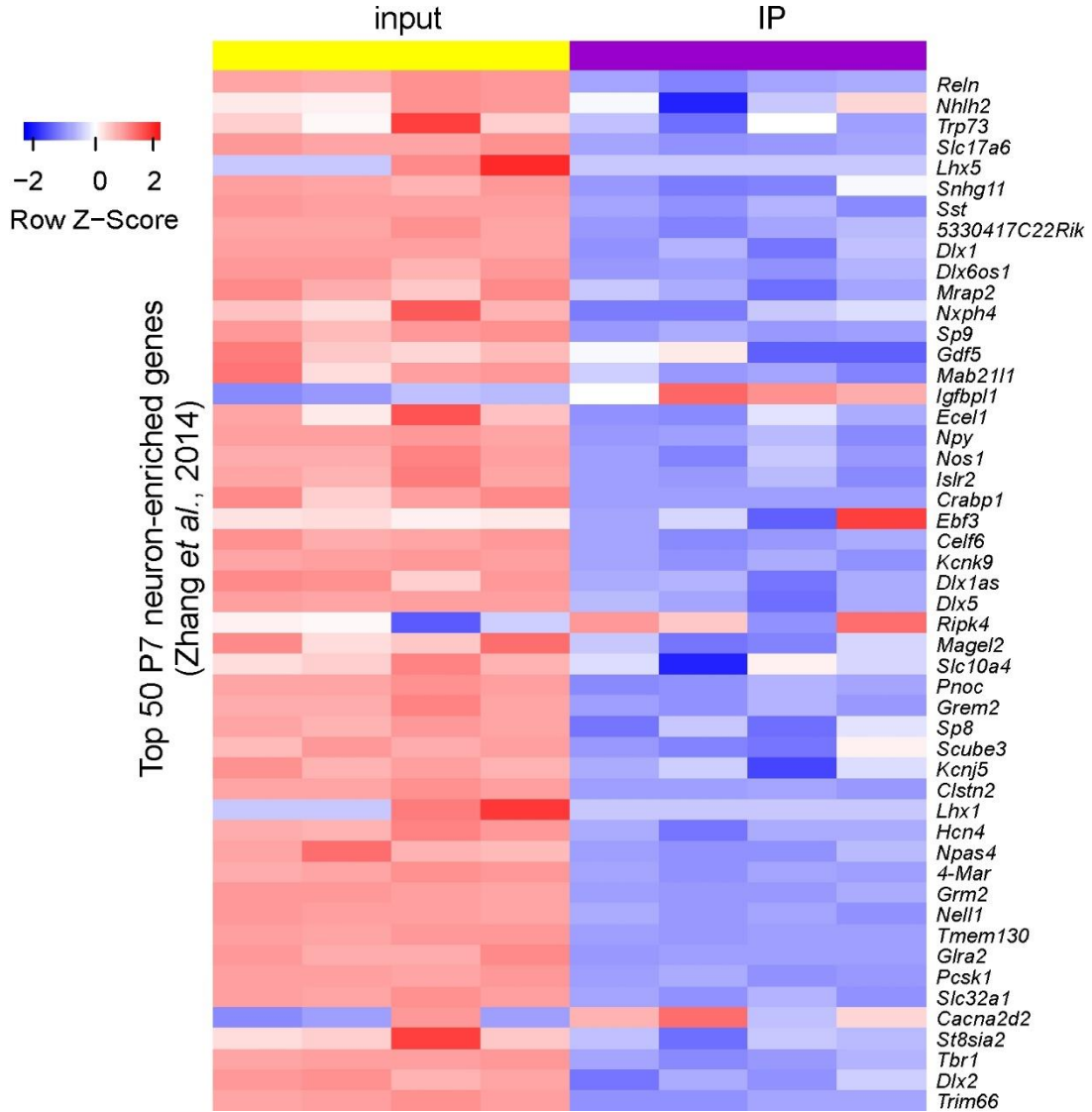


**Figure 3.20: P80 cortical astrocyte transcriptome are depleted of P7 neuronal genes.** A heatmap showing relative expression (Row z-score) of the top 50 neuronal genes from the P7 cortical RNA-Seq database in our P80 dataset. Row z-scores are shown as red for relative enrichment and as blue for relative depletion. The data used for P7 were from Zhang *et al.*, (2014).

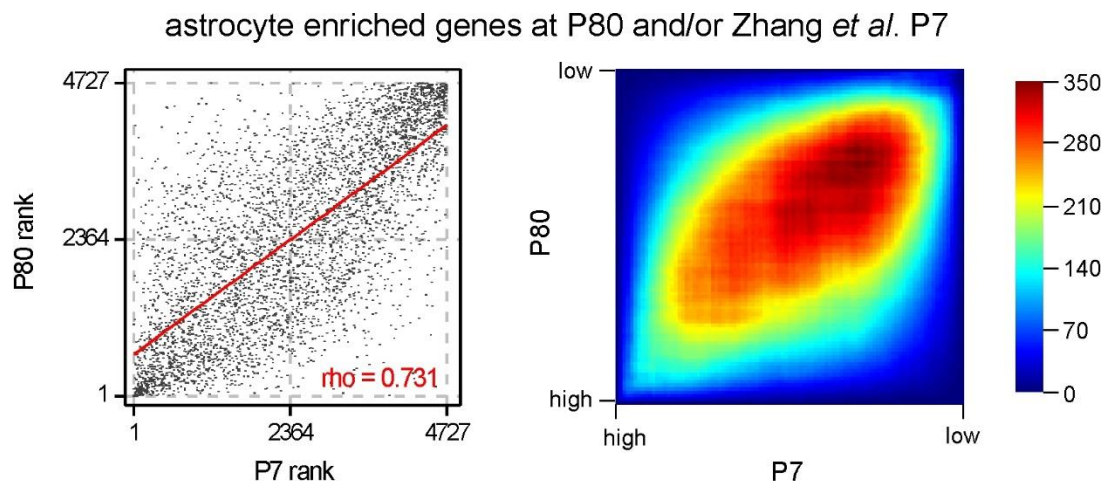


**Figure 3.21: *Aldh111-Cre/ERT2* x *RiboTag* mice and the determination of the cortical astrocyte transcriptome at P80.** Graphs comparing expression of 4727 transcripts enriched in either P80 IP (2-fold enriched over input FDR < 0.05) or P7 astrocytes (2-fold enriched over average of all other cell types) ranked based on FPKM percentile. Genes that were not sequenced in both datasets were excluded from this list. *Left:* Scatter plot representing the rank of each gene in the P80 (x-axis) vs. the P7 (y-axis) dataset. Clustering along the diagonal indicates similar rank in both datasets. *Right:* Rank-rank hypergeometric overlap heatmap. Each pixel represents the significance of overlap between the two datasets ( $-\log_{10}(\text{pvalue})$ , hypergeometric test, bin size = 50). Red cells represent highly significant overlap. Color scale (right) represents a range between  $-\log_{10}(\text{pvalue}) = 0$  ( $p = 1$ ) and 350 ( $p = 10^{-350}$ )

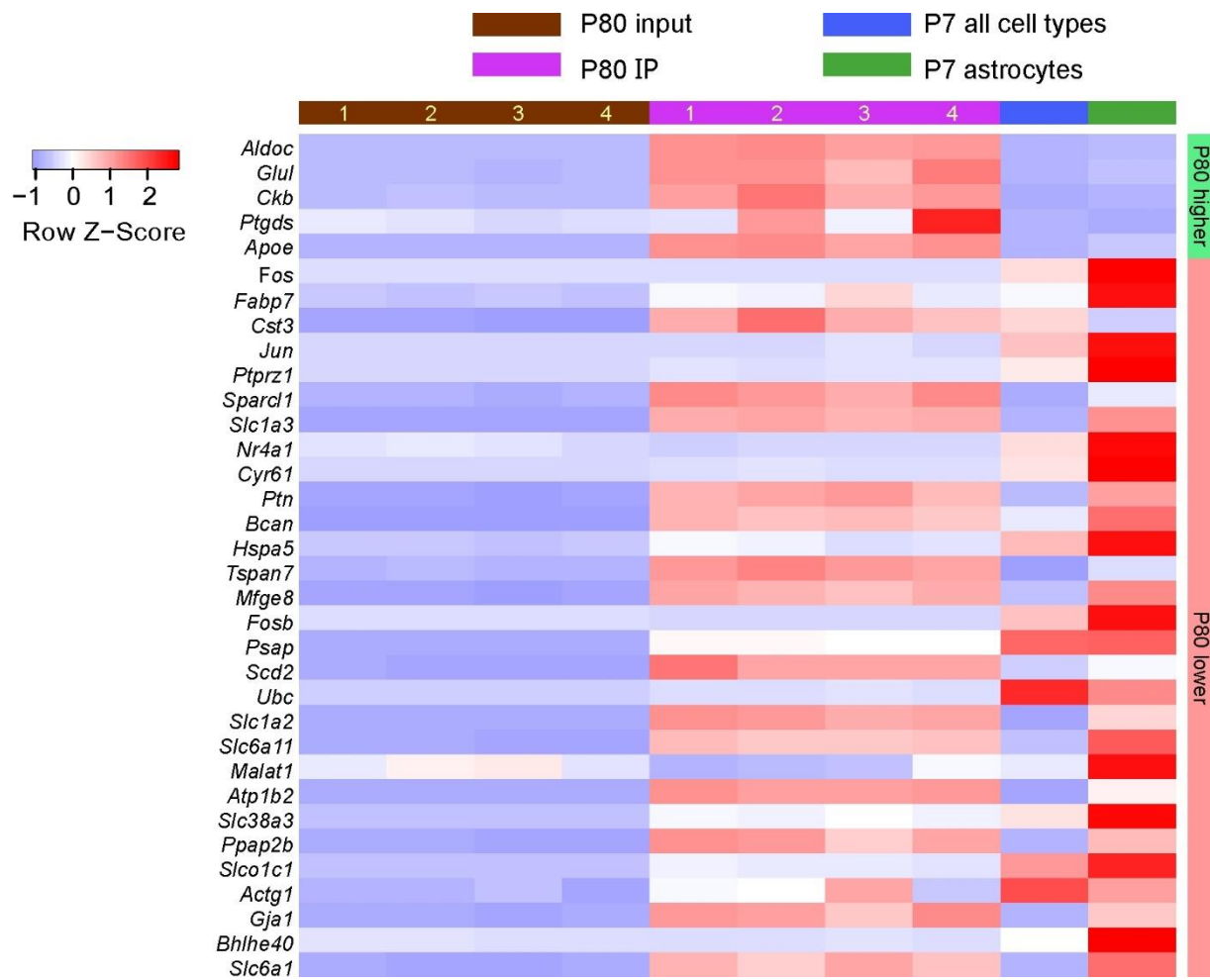


**Figure 3.22: Comparison of cortical astrocyte transcriptome at P80 vs P7.** A heatmap showing relative expression (row z-score) of the 32 genes whose percentile FPKM differ by at least 0.1 between highly expressed P80 and P7 cortical astrocytes determined by Rank-Rank Hypergeometric Overlap algorithm. These genes and their FPKM values are reported in **Table 3.3**. All genes for the analysis in this figure are provided as part of **Supplementary Excel file 1 Table 1**. The data used for P7 were from Zhang *et al.*, (2014).

Gene name	Common name	Zhang <i>et al.</i> , 2014		This study		$\Delta$ percentile P7 to P80
		P7 FPKM	P7 percentile	P80 FPKM $\pm$ s.e.m.	P80 percentile	
<i>Glul</i>	Glutamine synthetase	740	0.21	7611 $\pm$ 508	0.37	+0.16
<i>Sparcl1</i>	HEVIN	1768	0.50	4453 $\pm$ 178	0.22	-0.28
<i>Slc1a3</i>	GLAST-1	1144	0.32	1009 $\pm$ 16	0.049	-0.27
<i>Slc1a2</i>	Glt1	732	0.21	987 $\pm$ 27	0.048	-0.16
<i>S100b</i>	S100 $\beta$	31.2	0.088	933 $\pm$ 46	0.045	-0.043
<i>Gja1</i>	Cx43	501	0.14	628 $\pm$ 42	0.031	-0.11
<i>Gfap</i>	GFAP	127	0.036	548 $\pm$ 178	0.027	-0.009
<i>Kcnj10</i>	Kir4.1	185	0.53	535 $\pm$ 27	0.026	-0.50
<i>Aldh111</i>	Aldh111	145	0.041	406 $\pm$ 13	0.020	-0.019
<i>Sparc</i>	SPARC/Osteonectin	111	0.032	228 $\pm$ 41	0.011	-0.021
<i>Grm3</i>	mGluR3	158	0.045	114 $\pm$ 5	0.0056	-0.039
<i>Mertk</i>	MERTK	33.8	0.0096	85.4 $\pm$ 6.6	0.0042	-0.004
<i>Megf10</i>	MEGF10	25.2	0.0071	17.8 $\pm$ 1.0	0.00087	-0.007
<i>Thbs4</i>	Thrombospondin 4	2.08	0.00059	6.27 $\pm$ 1.12	0.00031	-0.00028
<i>Thbs3</i>	Thrombospondin 3	4.78	N/E	2.72 $\pm$ 0.19	N/E	N/E
<i>Grm2</i>	mGluR2	0.21	N/E	0.91 $\pm$ 0.07	N/E	N/E
<i>Grm5</i>	mGluR5	36.2	0.010	0.76 $\pm$ 0.11	0.000037	-0.010
<i>Thbs2</i>	Thrombospondin 2	1.11	N/E	0.65 $\pm$ 0.07	N/E	N/E
<i>Thbs1</i>	Thrombospondin 1	23.7	0.0067	0.16 $\pm$ 0.05	0.0000076	-0.0067

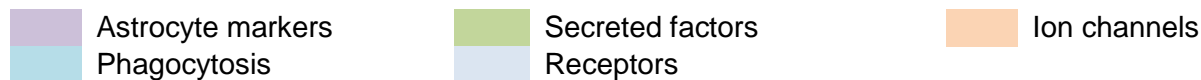


**Table 3.5: Representative astrocyte genes compared between P7 and P80.** The  $\log_2$ (percentile FPKM) at both ages is shown for genes enriched in astrocyte at either P80 (2-fold over input) or at P7 (2-fold over average of all cell types; FPKM > 0.1). As a frame of reference,  $\text{Log}_2(x) = y$ , then  $x = 2^y$ , where  $x$  is the percentile and  $y$  is the  $\text{Log}_2$  percentile. Also, the gene with the highest FPKM at P80 was *ApoE* with a value of 20520, and the gene with the highest FPKM at P7 was *Fos* with a value of 3527. Genes that were not enriched in astrocytes are denoted as “N/E”.

Gene name	Common name	Zhang <i>et al.</i> , 2014		This study		$\Delta$ percentile P7 to P80
		P7 FPKM	P7 percentile	P80 FPKM $\pm$ s.e.m.	P80 percentile	
<i>Slc17a7</i>	vGlut1	0.51	N/E	26.1 $\pm$ 2.3	N/E	N/E
<i>Slc32a1</i>	vGat1	0.19	N/E	1.09 $\pm$ 0.16	N/E	N/E
<i>Slc18a2</i>	vMat2	0.71	N/E	0.75 $\pm$ 0.18	N/E	N/E
<i>Slc17a6</i>	vGlut2	0.13	N/E	0.16 $\pm$ 0.02	N/E	N/E
<i>Slc17a9</i>	vNut1	0.12	N/E	0.06 $\pm$ 0.04	N/E	N/E
<i>Slc17a8</i>	vGlut3	0.12	N/E	0.05 $\pm$ 0.01	N/E	N/E
<i>Slc18a1</i>	vMat1	$\leq$ 0.1	N/E	0.02 $\pm$ 0.01	N/E	N/E
<i>Slc18a3</i>	vAChT	$\leq$ 0.1	N/E	0.002 $\pm$ 0.002	N/E	N/E

**Table 3.6: Expression of genes related to vesicular transport compared between P7 and P80.** The  $\log_2$ (percentile FPKM) at both ages is shown for genes enriched in astrocyte at either P80 (2-fold over input) or at P7 (2-fold over average of all cell types; FPKM > 0.1). As a frame of reference,  $\text{Log}_2(x) = y$ , then  $x = 2^y$ , where  $x$  is the percentile and  $y$  is the  $\text{Log}_2$  percentile. Also, the gene with the highest FPKM at P80 was *ApoE* with a value of 20520, and the gene with the highest FPKM at P7 was *Fos* with a value of 3527. Genes that were not enriched in astrocytes are denoted as “N/E”.

brain slices and *in vivo*. Most importantly, it will allow us to explore differences and similarities between astrocytes located in different brain areas.

First, extending pioneering transcriptome studies (Cahoy et al., 2008), we provide well characterized *Aldh111-Cre/ERT2* mice that allow for specific, regulated and pan-astrocytic gene expression under the conditions we report (induction at ~P56 and assessment at ~P80). These mice will be invaluable to study astrocyte biology at different developmental stages, during disease processes and in the context of injury and trauma. However, we believe the use of these mice will be particularly important to tease apart, through loss- and gain-of-function studies, the roles that astrocytes play at synapses, in neural circuits and their contributions to mouse behavior (Allen, 2014). This has been a challenging problem to attack, especially with regards to gliotransmission (Sloan and Barres, 2014). In addition, several brain diseases are now considered to be non-cell autonomous and to include important astrocyte contributions (Barres, 2008). *Aldh111-Cre/ERT2* mice will allow researchers to directly express and delete the disease causing genes specifically in astrocytes in a temporally controlled manner and thus tease apart disease mechanisms that may yield new therapeutic targets. This has been a critical issue that existing astrocyte specific genetic strategies have not conclusively addressed. With appropriate controls for age, disease settings and brain area in each case, we expect *Aldh111-Cre/ERT2* mice to fill this void.

As exploration of astrocytes in mouse behavior and disease models advances, there will be necessity to perform astrocyte specific, temporally controlled and pan-astrocytic genetic manipulations, as well as study aspects of their signaling in physiologically relevant compartments such as processes. The *Aldh111-Cre/ERT2* transgenic mouse line reported here fulfills all of these requirements. However, we emphasize that we did not examine tamoxifen inducible reporter expression in very young mice or in adult mice greater than 3 weeks after tamoxifen administration; we evaluated mice at ~P80. Hence, our results need to be interpreted

with this in mind and future users of the *Aldh111*-Cre/ERT2 mice will need to perform their own controls: it is important not to extrapolate to all brain areas, all ages, all experimental settings and all reporter mice from any one study, including ours. Hence, our studies do not obviate the need for controls, especially in disease related research where gene expression patterns and cell fates may change significantly. We have specifically focused on adult mice and the expression of GECIs at levels appropriate for imaging in brain slices and *in vivo*. These analyses reveal *Aldh111*-Cre/ERT2 mice to be valuable tools to study astrocyte biology.

Second, we provide an RNA-Seq dataset for astrocyte-enriched genes at P80, which can be used in conjunction with a previously reported dataset for P7 to focus on individual genes and molecular pathways at these two ages. The combination of these two datasets will permit precise exploration of astrocyte signaling *in vivo* and allow for exploration of mechanisms based on knowledge of adult gene expression patterns in the cortex. Initial analyses already suggest several new mechanisms to explore (see **Figure 3.21**; **Table 3.2-3**). The adult mouse cortical dataset is also valuable to compare with human mature astrocyte transcriptome datasets that have recently become available (Zhang et al., 2016). The *Aldh111*-Cre/ERT2 x RiboTag mice are the tools of choice to document astrocyte similarities and differences between distinct areas of the brain. Thus, our RNA-Seq data provide a basis to explore astrocyte diversity between specific adult neural circuits and brain areas (Khakh and Sofroniew, 2015; Zhang and Barres, 2010).

Astrocytes exist throughout the nervous system and are proposed to affect neural circuits and behavior. However, studying astrocytes has proven difficult because of the lack of tools permitting astrocyte selective genetic manipulations. Here, we report the generation of *Aldh111*-Cre/ERT2 transgenic mice to selectively target astrocytes *in vivo*. We characterized *Aldh111*-Cre/ERT2 mice using imaging, immunohistochemistry, AAV-FLEX-GFP microinjections and crosses to RiboTag and Ai95 Cre-dependent cyto-GCaMP6f mice. Two-to-three weeks after

tamoxifen induction, *Aldh1l1*-Cre/ERT2 selectively targeted essentially all adult (P80) brain astrocytes with no detectable neuronal contamination, resulting in expression of cyto-GCaMP6f and permitting subcellular astrocyte calcium imaging during startle responses *in vivo*. Crosses with RiboTag mice allowed sequencing of actively translated mRNAs and determination of the adult cortical astrocyte transcriptome. Thus, we provide well characterized, easy-to-use resources with which to selectively study astrocytes *ex vivo* and *in vivo* in multiple experimental scenarios.

## CHAPTER 4: EXPLORATION OF MOLECULAR ASTROCYTE DIVERSITY BETWEEN ADULT NEURAL CIRCUITS

### Section 4.1: Introduction

Gene expression profiling is a well-established method to molecularly differentiate cell populations (Sung et al., 2012). Microarrays and RNA-Seq can reveal new cell markers, such as *Aldh111* (Cahoy et al., 2008), and are powerful tools in our pursuit to understand the molecular machinery of astrocytes and their potential diversity. Rather than examining a small number of gene targets, these omic approaches allow agnostic exploration of cell populations. However, RNA and protein levels do not necessarily correlate due to stalled mRNA and post-translational modification. Therefore, RNA and protein expression should be assessed in parallel (Kitchen et al., 2014). We described in **Chapter 3.5** the *Aldh111*-Cre/ERT2 x RiboTag mice and the adult cortical transcriptome, which form the basis to explore astrocyte diversity between adult neural circuits at the level of RNA. To explore molecular diversity at the level of protein expression, we used mass spectrometry based discovery proteomics on sorted eGFP positive astrocytes from freshly dissociated striatal and hippocampal cells of *Aldh111*-eGFP reporter mice (see **Chapter 2.17**). Using these two omic approaches in parallel, we sought to establish and compare striatal and hippocampal astrocyte transcriptomes and proteomes to directly test whether astrocytes in different adult neural circuits were molecularly distinct or largely similar.

### Section 4.2: Generating striatal and hippocampal astrocyte transcriptomes

Using the *Aldh111*-Cre/ERT2 x RiboTag mice described in **Chapter 3.5**, we generated RNA-Seq data of adult (P63) astrocytes from striata and hippocampi (Sanz et al., 2009). In both the striatum and the hippocampus, Rpl22HA co-localized with S100 $\beta$ , but not with NeuN (**Figures 4.1-4.2**). Rpl22HA expressed throughout astrocyte soma and major processes, as can

be appreciated from higher magnification images in **Figure 4.1B**. Immunoprecipitations of Rpl22HA and associated actively translated mRNAs from striata and hippocampi of single animals served as individual replicates (**Figure 4.3, Table 4.1**; 4 mice). RNA from the input, i.e. whole tissue lysate, were used as controls. The IP samples were replete with astrocyte markers (Cahoy et al., 2008), but depleted of markers for neurons, oligodendrocytes and microglia (**Figure 4.4A**). This is consistent with IP of adult cortex (**Figure 3.17C**). Furthermore, the top 100 adult cortical astrocyte genes (Srinivasan et al., 2016) were enriched in striatal and hippocampal IP samples (**Figure 4.4B**), providing further evidence that the IP samples represented striatal and hippocampal astrocytes.

### **Section 4.3: Comparing striatal and hippocampal astrocyte transcriptomes**

To directly test whether striatal and hippocampal astrocytes were molecularly distinct cell populations, we used principal component analysis (PCA) to cluster our samples based on the 2000 most variable genes across all samples. The two most differentiating features separated our 16 samples by brain region (striatal versus hippocampal) and sample group (input versus IP) (**Figure 4.5**). Importantly, clustering based on the first 2 principal components revealed that striatal and hippocampal astrocytes represent distinct cell populations (**Figure 4.5**).

To understand whether the gene expression differences were functionally relevant, we ran a Gene Set Enrichment Analysis (GSEA) on all genes sequenced in striatal and/or hippocampal IP samples with a threshold q-value < 0.15. The list of all IP genes were ranked according to  $\log_2$ ratio of differential expression between striatal IP and hippocampal IP (LimmaVoom; no FDR threshold). GSEA revealed 21 gene sets enriched in striatal astrocytes and 4 gene sets enriched in hippocampal astrocytes (**Figure 4.6, Tables 4.2 & 4.3**), illustrating that these two populations have functionally relevant molecular differences. Several of the 21

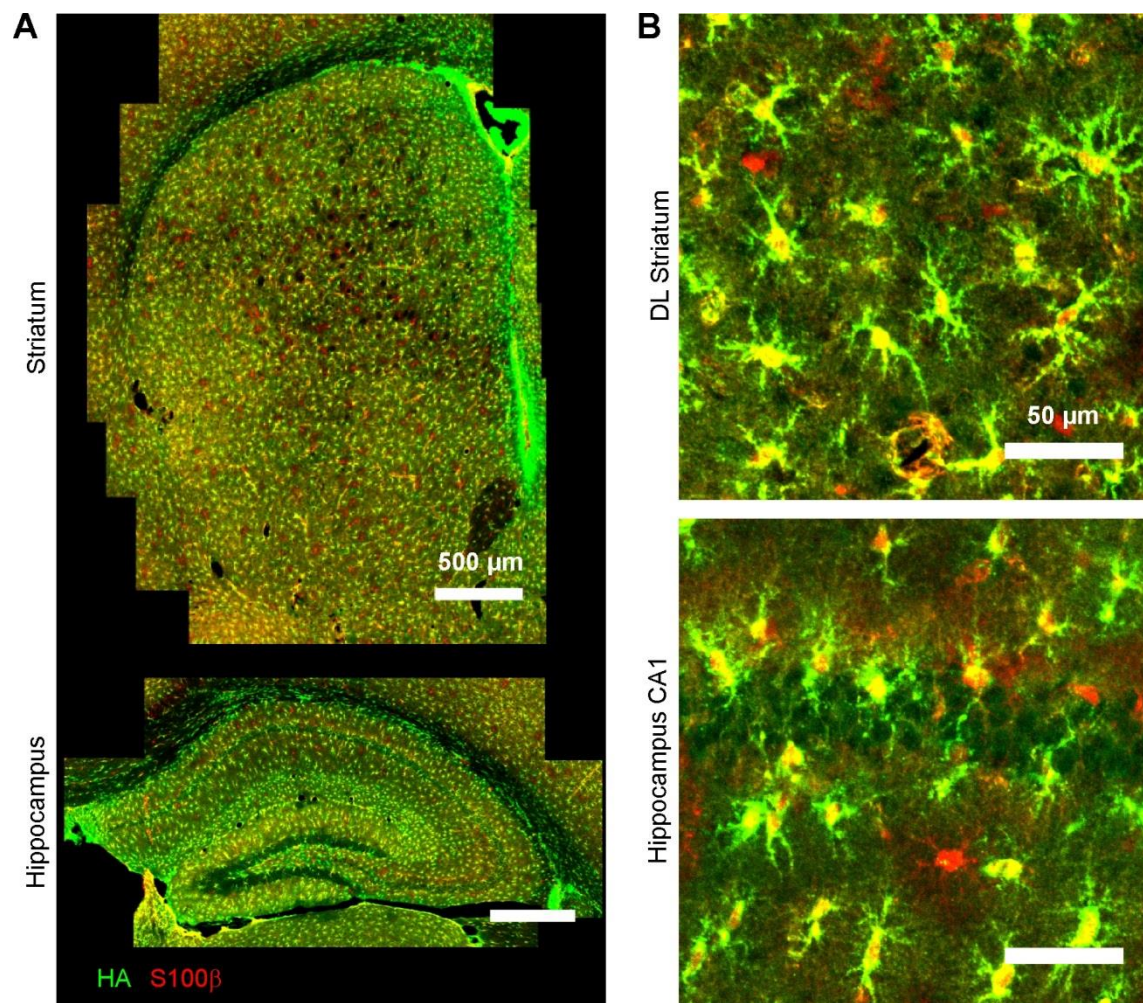


**Figure 4.1: *Aldh111*-Cre/ERT2 drives expression of Rpl22HA exclusively in astrocytes to enable purification of striatal and hippocampal astrocyte mRNA.** **A.** Representative montage of the striatum from *Aldh111*-Cre/ERT2 x RiboTag mice 2 weeks after the last tamoxifen injection. Rpl22HA (green) strongly colocalized with astrocytes (S100β, red). **B.** Zoomed-in image shows Rpl22HA expression in the soma and many branches of astrocytes.

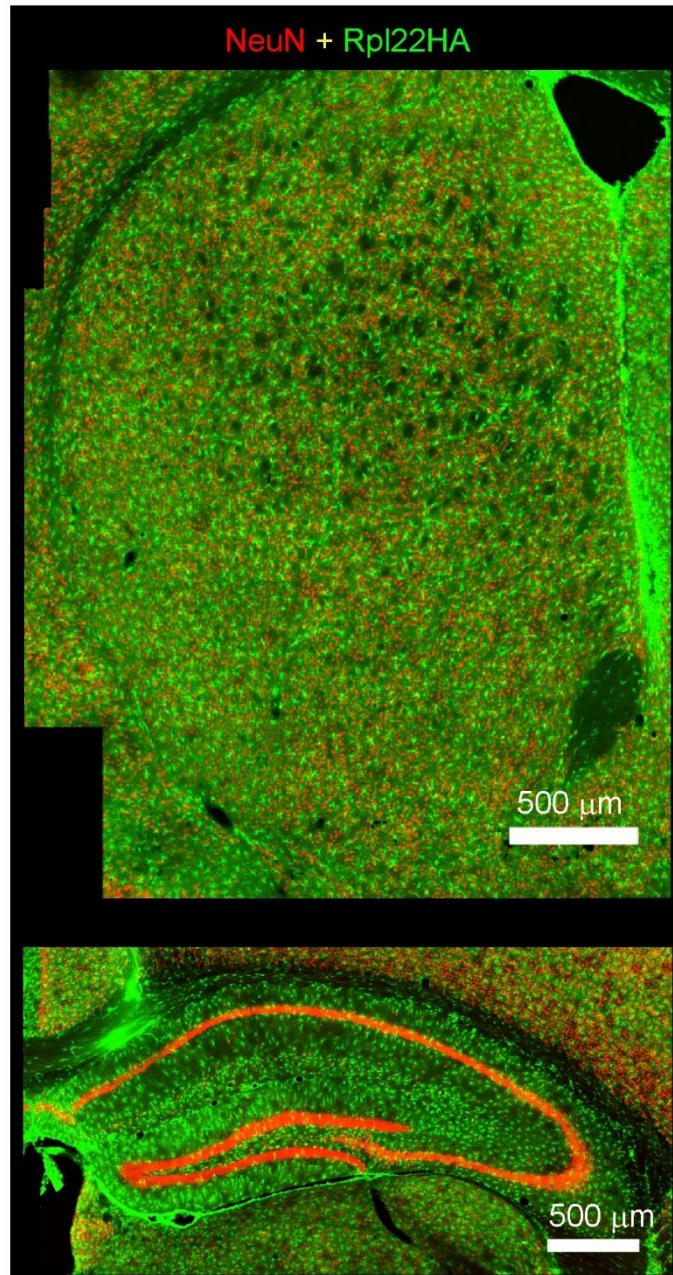


**Figure 4.2: Representative montages of the striatum and hippocampus from *Aldh11-Cre/ERT2* x *RiboTag* mice (2 weeks after the last tamoxifen injection). Rpl22HA (green) shows with no colocalization with neuronal marker NeuN (red).**

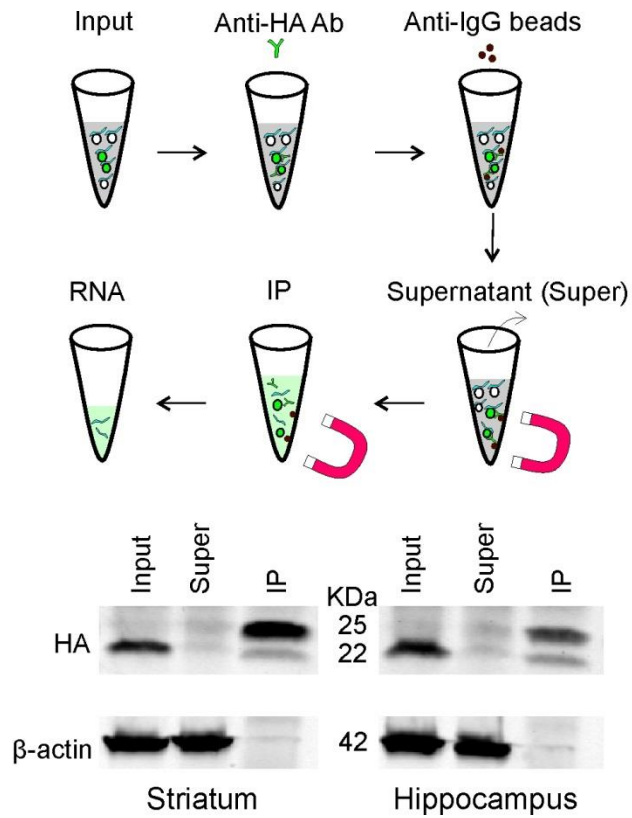


**Figure 4.3: Schematic of immunoprecipitation to isolate astrocyte RNA.** A representative Western blot below shows that Rpl22HA was preserved in the IP samples, whereas  $\beta$ -actin was depleted in relation to input. In contrast, there was little Rpl22HA in the supernatant. In the IP lanes, the 25 band is the light chain of the anti-HA antibody that was used in the IP.

ID	Sex	ng RNA	RIN
970 Str input	F	460	8.8
970 Str IP	F	260	8.5
970 Hip input	F	412	8.7
970 Hip IP	F	336	8.2
971 Str input	F	361	8.6
971 Str IP	F	200	9.3
971 Hip input	F	258	8.7
971 Hip IP	F	478	9.0
974 Str input	M	222	8.8
974 Str IP	M	158	8.6
974 Hip input	M	187	8.9
974 Hip IP	M	214	8.7
977 Str input	M	241	8.2
977 Str IP	M	173	8.6
977 Hip input	M	277	8.1
977 Hip IP	M	276	8.3

**Table 4.1:** The quantity and quality of the striatal and hippocampal RNA samples used to create multiplexed paired-end sequencing library. Quality is reported as the RNA Integrity Number (RIN). n = 4 mice at P63.

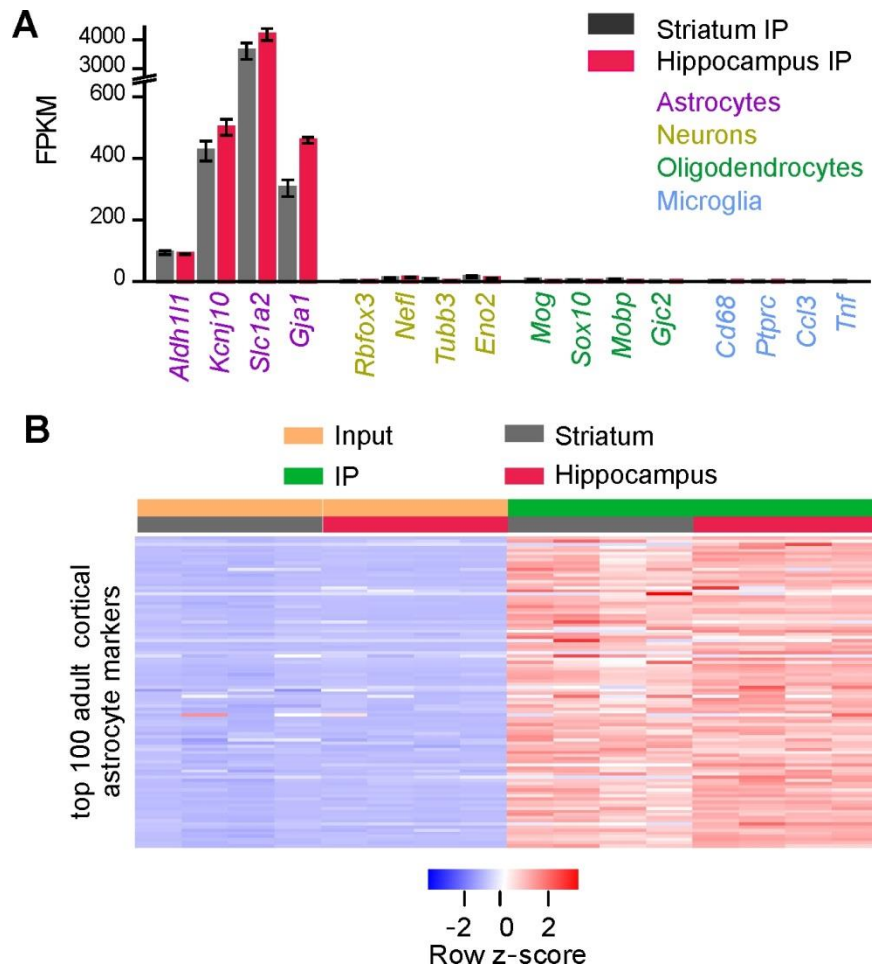


**Figure 4.4: Validation of adult striatal and hippocampal astrocyte transcriptomes. A.** Gene expression levels (measured in FPKM) of markers for astrocytes, neurons, oligodendrocytes, and microglia in IP samples (n = 4 animals). **B.** Heatmap representing 16 RNA-Seq samples from 4 mice showing relative enrichment (red) or depletion (blue) of the top 100 adult cortical astrocyte markers. Row z-scores were calculated using FPKM.

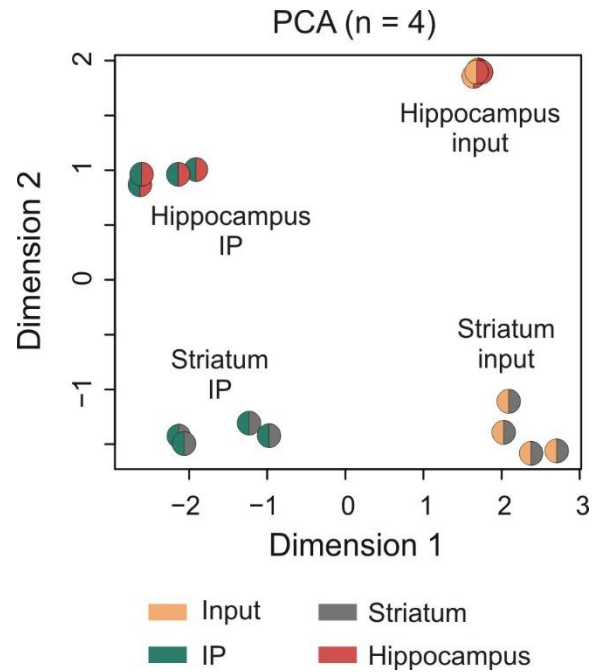


**Figure 4.5: Principal component analysis of adult striatal and hippocampal astrocyte transcriptomes.** Striatal and hippocampal astrocytes were molecularly distinct cell populations as determined by principal component analysis of the 2000 most variable genes across 16 samples.

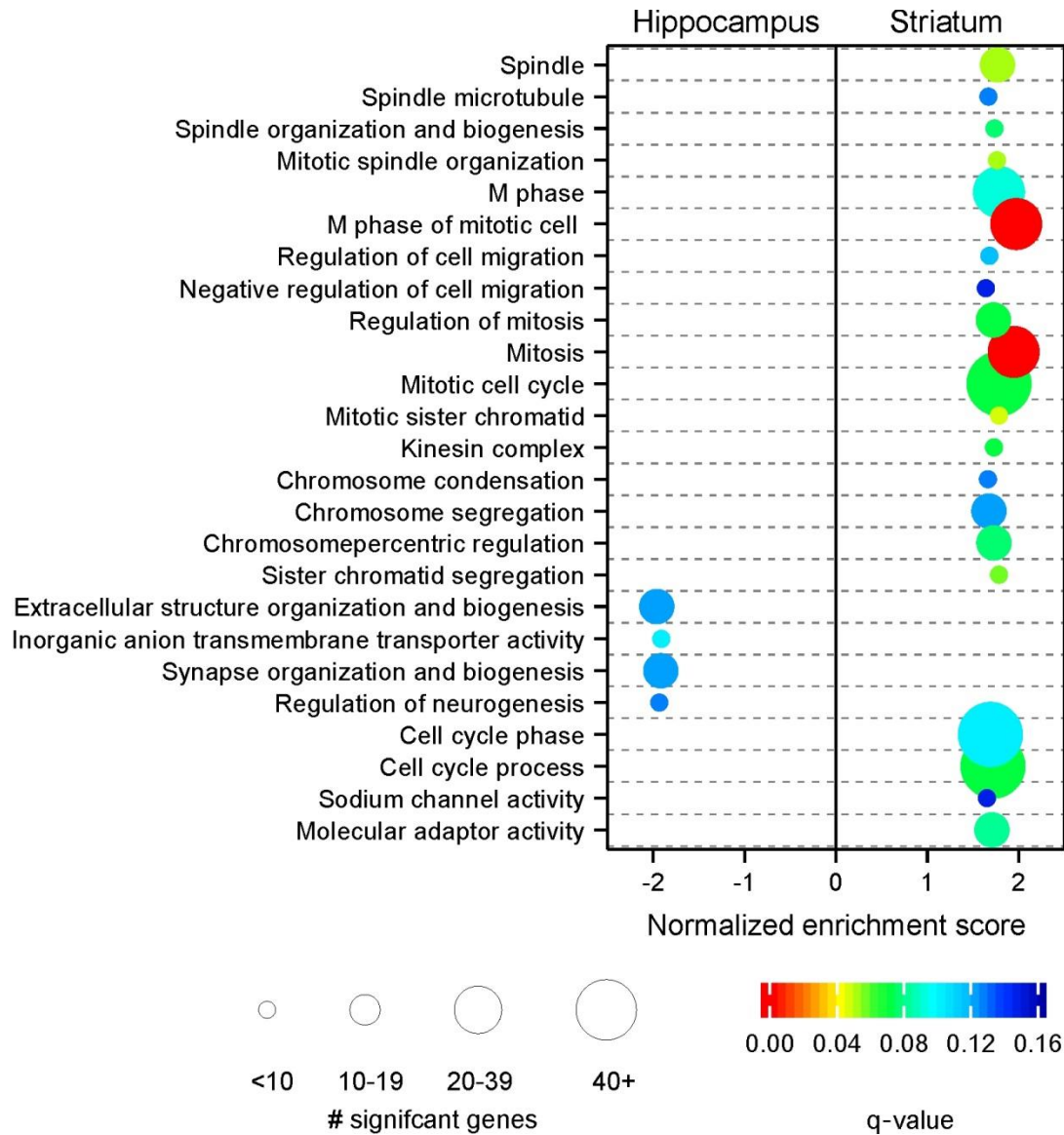


**Figure 4.6: Gene Set Enrichment Analysis (GSEA) of adult striatal and hippocampal astrocyte transcriptomes.** GSEA with all genes sequenced in striatal and hippocampal IP sample (threshold q-value < 0.15) identified 21 gene sets enriched in striatal astrocytes and 4 gene sets enriched in hippocampal astrocytes. The size of the circle corresponds to the number of significant genes whereas the color indicates the significance of the regional enrichment based on normalized enrichment score.

Gene set name	Gene set size	Normalized Enrichment Score	q-value
M PHASE OF MITOTIC CELL CYCLE	82	1.968	0.0013
MITOSIS	79	1.943	0.0015
MITOTIC SISTER CHROMATID SEGREGATION	15	1.781	0.0474
MITOTIC SPINDLE ORGANIZATION AND BIOGENESIS	10	1.761	0.0531
SPINDLE	37	1.765	0.0546
SISTER CHROMATID SEGREGATION	16	1.781	0.0566
MITOTIC CELL CYCLE	147	1.781	0.0705
REGULATION OF MITOSIS	40	1.722	0.0714
KINESIN COMPLEX	13	1.726	0.0727
CELL CYCLE PROCESS	186	1.717	0.0730
CHROMOSOME PERICENTRIC REGION	30	1.728	0.0761
SPINDLE ORGANIZATION AND BIOGENESIS	11	1.732	0.0781
MOLECULAR ADAPTOR ACTIVITY	46	1.707	0.0814
M PHASE	110	1.782	0.0920
CELL CYCLE PHASE	163	1.690	0.1029
REGULATION OF CELL MIGRATION	26	1.679	0.1166
CHROMOSOME SEGREGATION	31	1.673	0.1203
SPINDLE MICROTUBULE	15	1.666	0.1270
CHROMOSOME CONDENSATION	10	1.661	0.1288
NEGATIVE REGULATION OF CELL MIGRATION	13	1.638	0.1464
SODIUM CHANNEL ACTIVITY	14	1.649	0.1483

**Table 4.2: 21 striatal enriched gene sets.** The exact numbers for gene set size, q-value, and normalized enrichment score.

<b>Gene set name</b>	<b>Gene set size</b>	<b>Normalized Enrichment Score</b>	<b>q-value</b>
INORGANIC ANION TRANSMEMBRANE TRANSPORTER ACTIVITY	16	-1.909	0.1046
EXTRACELLULAR STRUCTURE ORGANIZATION AND BIOGENESIS	32	-1.959	0.1221
SYNAPSE ORGANIZATION AND BIOGENESIS	23	-1.913	0.1247
REGULATION OF NEUROGENESIS	14	-1.932	0.1256

**Table 4.3: 4 hippocampal enriched gene sets.** The exact numbers for gene set size, q-value, and normalized enrichment score.

striatal gene sets were related to the cell cycle, cell migration, or chromosome structure (**Figure 4.6; Table 4.2**). Three of the four gene sets enriched in hippocampal astrocytes are related to synapse structure and neuronal activity (**Figure 4.6; Table 4.3**). We also found an abundance of evidence (**Table 4.4**) at the RNA level for key molecules involved in synapse formation and removal in adult astrocytes (Chung et al., 2015b). There were some genes expressed at significantly higher levels in hippocampal astrocytes, namely *Sparcl1*, *Gpc4*, and *Thbs4* (**Table 4.4**); this evidence at the individual gene level is consistent with the GSEA result.

Differential expression analysis with LimmaVoom (FDR < 0.05; adjusted for block effect of each animal) revealed 2,818 differentially expressed transcripts: 1,180 striatal and 1,638 hippocampal (**Figure 4.7; Supplemental Excel file 1 Table 2**). This represents more than 15% of the genes detected in both IP samples.

The set of genes highly expressed in IP, but not differentially expressed between striatum and hippocampus is also extremely interesting (**Figure 4.8**), as this suggests that they are involved in core astrocyte functions in the striatum and hippocampus. Indeed, genes known to have functional importance in astrocytes such as *Slc1a2*, *Sparc*, *Kcnj10* and *Slc6a11* were found in the striatal and hippocampal lists of 40 most highly expressed astrocyte genes (**Figure 4.8**). **Figure 4.9** reports in order the top 40 most differentially expressed genes in striatal and hippocampal astrocytes and defines the molecular basis by which striatal and hippocampal astrocytes differ. Within these top 40, the most highly expressed striatal astrocyte gene is *Crym*, and the most highly expressed hippocampal astrocyte gene is *Gfap*. We study these further in a later section, but the RNA-Seq data demonstrate that striatal and hippocampal astrocytes are molecularly distinct cell populations and provide a valuable resource for future hypothesis-driven experiments.

<b>Gene</b>	<b>Proposed function</b>	<b>Striatal IP FPKM</b>	<b>Hippocampa IP FPKM</b>	<b>LimmaVoom FDR</b>
<i>Thbs1</i>	Induce formation of normal synapses	0.119 ± 0.025	0.238 ± 0.088	0.172
<i>Thbs2</i>	Induce formation of normal synapses	0.534 ± 0.172	0.747 ± 0.087	0.109
<i>Thbs3</i>	Induce formation of normal synapses	2.31 ± 0.73	1.17 ± 0.24	0.260
<i>Thbs4</i>	Induce formation of normal synapses	48.23 ± 6.13	85.20 ± 10.60	0.002
<i>Sparc</i>	Excitatory synaptogenesis	531.5 ± 120.2	613.9 ± 56.1	0.274
<i>Sparcl1</i>	Excitatory synaptogenesis	2899.0 ± 187.3	3563.3 ± 121.4	0.031
<i>Gpc4</i>	Excitatory synaptogenesis	12.75 ± 1.1	20.69 ± 0.56	0.001
<i>Gpc6</i>	Excitatory synaptogenesis	23.36 ± 1.74	22.49 ± 1.32	0.725
<i>Megf10</i>	Synapse elimination	37.64 ± 4.54	39.67 ± 0.52	0.376
<i>Mertk</i>	Synapse elimination	123.1 ± 8.4	132.6 ± 3.1	0.218
<i>ApoE</i>	Synapse elimination	2958.8 ± 176.1	3377.7 ± 91.7	0.444

**Table 4.4: Genes related to synapse formation and removal.** Genes differentially expressed (LimmaVoom FDR < 0.05) between striatal and hippocampal astrocytes are shaded in blue. See **Table 1.1** for description of evidence of function.

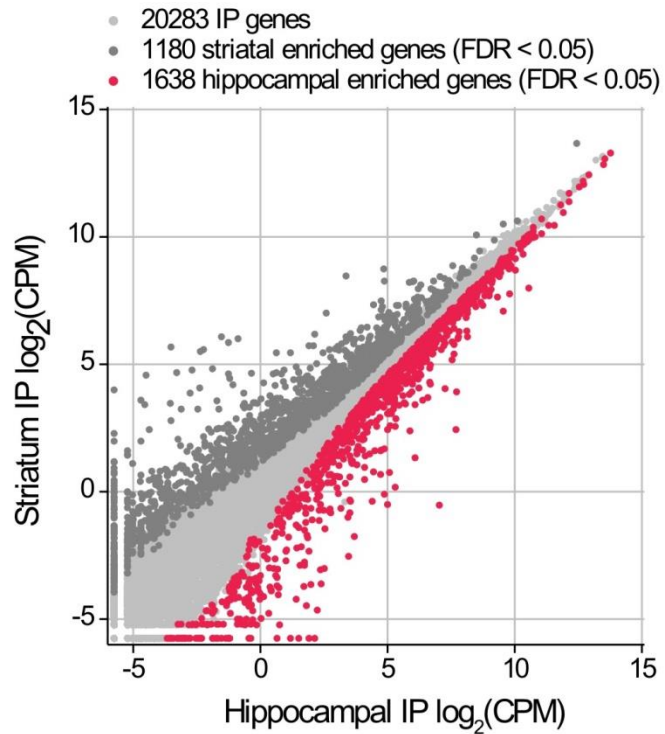


**Figure 4.7: Adult striatal and hippocampal astrocyte transcriptomes differ by ~15%.** Differential expression analysis comparing striatal and hippocampal IP samples identified 1180 striatal and 1638 hippocampal enriched astrocyte genes (threshold FDR < 0.05, **Supplemental Excel file 1 Table 2**).

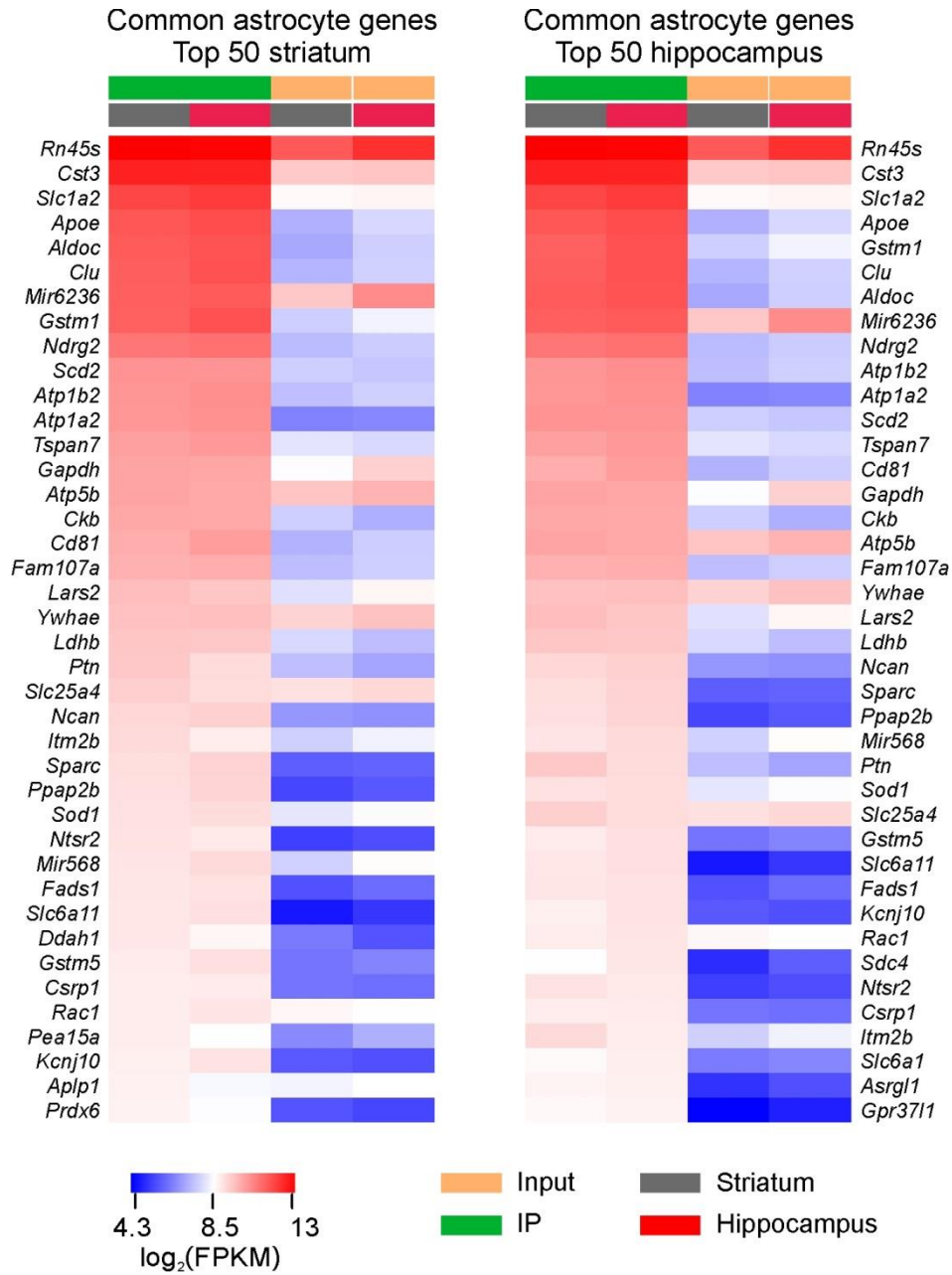


**Figure 4.8:** FPKM heatmaps of the top 40 astrocyte genes that were not differentially expressed between regions as ranked by IP FPKM value.  $\log_2(\text{FPKM})$  ranged from 4.3 (blue, relatively low expression) to 13 (red, relatively high expression).

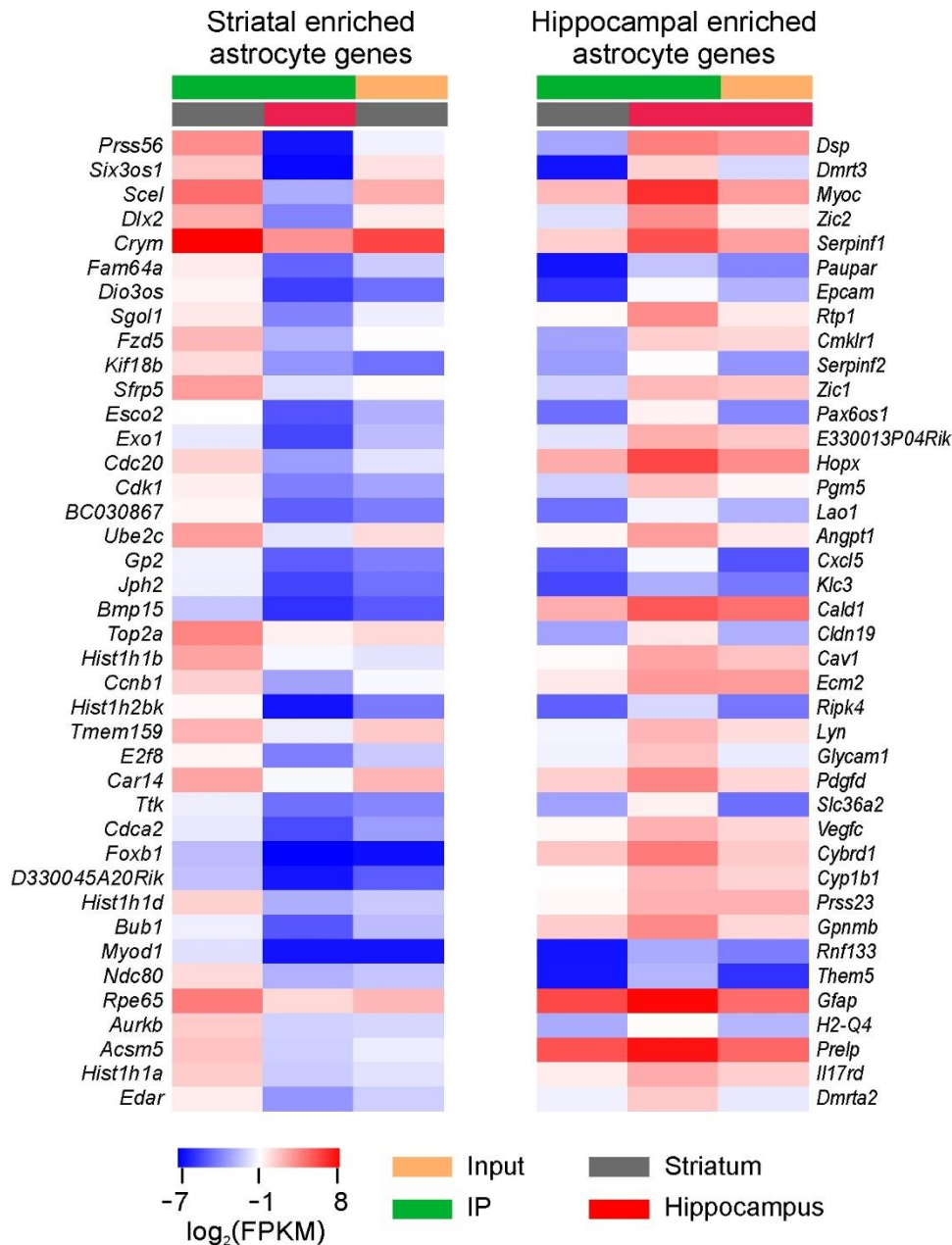


**Figure 4.9:** FPKM heatmaps of the 40 most differentially expressed astrocyte genes between striatal and hippocampal astrocytes as ranked by differential expression LimmaVoom log ratio. The most highly expressed striatal astrocyte gene is *Crym*, and the most highly expressed hippocampal astrocyte gene is *Gfap*.  $\log_2(\text{FPKM})$  ranged from -7 (blue, relatively low expression) to 8 (red, relatively high expression).

#### **Section 4.4: Generating striatal and hippocampal astrocyte proteomes**

We next documented the proteomes of striatal and hippocampal astrocytes from sorted cells from P30 *Aldh1l1*-eGFP mice (Cahoy et al., 2008). We first confirmed with western blotting that the cell lysate of the eGFP positive fraction contained GFP and GFAP proteins whereas the eGFP negative fraction did not (**Figure 4.10**). We then further validated the expression profiles of isolated cells using microarrays. For both striatum and hippocampus, the eGFP positive fraction isolated by FACS showed high expression of astrocyte markers (**Figure 4.11A**), and could be considered *bona fide* astrocytes. Similar to that observed with RNA-Seq, expression profiles of astrocytes from striatum and hippocampus were distinct (**Figure 4.11B**). We next quantitatively compared proteomes by independently labelling samples from striata and hippocampi with low (28 Da) or intermediate (32 Da) molecular weight dimethyl labels prior to pooling for LC-MS/MS (Boersema et al., 2009). Mass spectrometry data were processed using Sequest and Thermo Proteome Discoverer 1.4 (e.g. **Figure 4.12**). This permitted determination of the ratio of low and intermediate dimethyl labels (i.e. relative abundance in striatal and hippocampal astrocytes) and identification of proteins.

#### **Section 4.5: Comparing striatal and hippocampal astrocyte proteomes**

From four biological replicates, we identified 3509 protein groups corresponding to 3322 genes (**Supplemental Excel file 2 Table 1**). Of these, 2879 genes were also found in our astrocyte RNA-Seq data, thus further validating our starting material for MS. To explore robust commonalities and differences between striatal and hippocampal astrocyte proteomes, we performed high-stringency analyses (**Chapter 2.20**), which resulted in a list of 692 proteins (**Figure 4.13; Supplemental Excel file 2 Table 2**). We next considered the 143 proteins that were detected in all four experiments (**Figure 4.13**). We evaluated the correlation between RNA ( $\log_2$  FPKM) and protein ( $\log_2$  abundance) levels in both striatum and hippocampus

(**Figure 4.14**). There was a clear correlation between the two variables, implying that RNA-Seq reflects abundance of most proteins. However, there were notable exceptions and around 10% of the proteins showed high abundance, but very low FPKM values (<10) for striatal and hippocampal data sets (**Figure 4.14**). This is comparable to the 15% differentially expressed genes found in the RNA-Seq data.

Statistical analyses revealed that out of 143 proteins, the abundance of 113 proteins was not significantly different between striatum and hippocampus, i.e. the common and likely most abundant proteins (**Figure 4.15; Supplemental Excel file 2 Table 3**). However, 18 proteins in the striatum and 12 proteins in the hippocampus emerged as significantly region enriched (**Figure 4.15; Supplemental Excel file 2 Tables 4 & 5**). Furthermore, comparison of the ratios for the common, striatal enriched and hippocampal enriched proteins showed that these groups were significantly different (**Figure 4.15**). As far as we know, these data represent the first unbiased identification of proteins that define subpopulations of astrocytes in the brain. The most differentially expressed striatal and hippocampal astrocyte proteins were  $\mu$ -crystallin (gene: *Crym*) and GFAP (gene: *Gfap*), respectively (**Figure 4.15**), which also had the highest expression among the most differentially expressed genes in striatal versus hippocampal astrocytes (**Figure 4.9**).

We further assessed the 143 proteins discovered by high-stringency analyses (for simplicity proteins are referred to by their gene name in this section). We ranked the common proteins by abundance; the top 20 are shown in **Figure 4.16**. Of these, 19 are also astrocyte enriched by RNA-Seq and include well-established astrocyte molecules, e.g. *Slc1a3* (GLAST) and *Slc1a2* (GLT1). A quarter (e.g. *Actb*, *Dpysl2*, *Tubb4b* and *Cfl1*) are implicated in cytoskeleton remodeling, and some, although highly abundant and common, are still of poorly defined function (e.g. *Phgdh*). These top common proteins represent a valuable resource to explore core astrocyte functions.

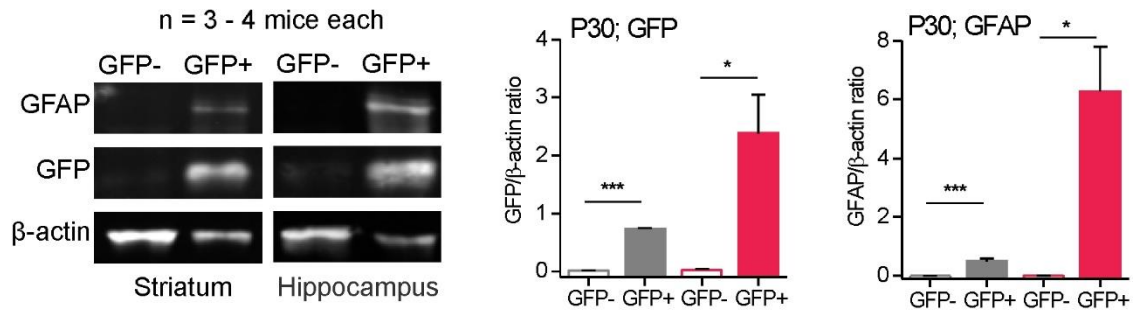


**Figure 4.10: Purification of striatal and hippocampal astrocytes.** Western blot for GFAP and GFP from both GFP negative and GFP positive FACS purified fractions. Signal quantification is shown normalized to  $\beta$ -actin signal. Both, GFP and the astrocyte marker GFAP, were enriched in GFP positive fractions and were not detectable in the negative fractions.

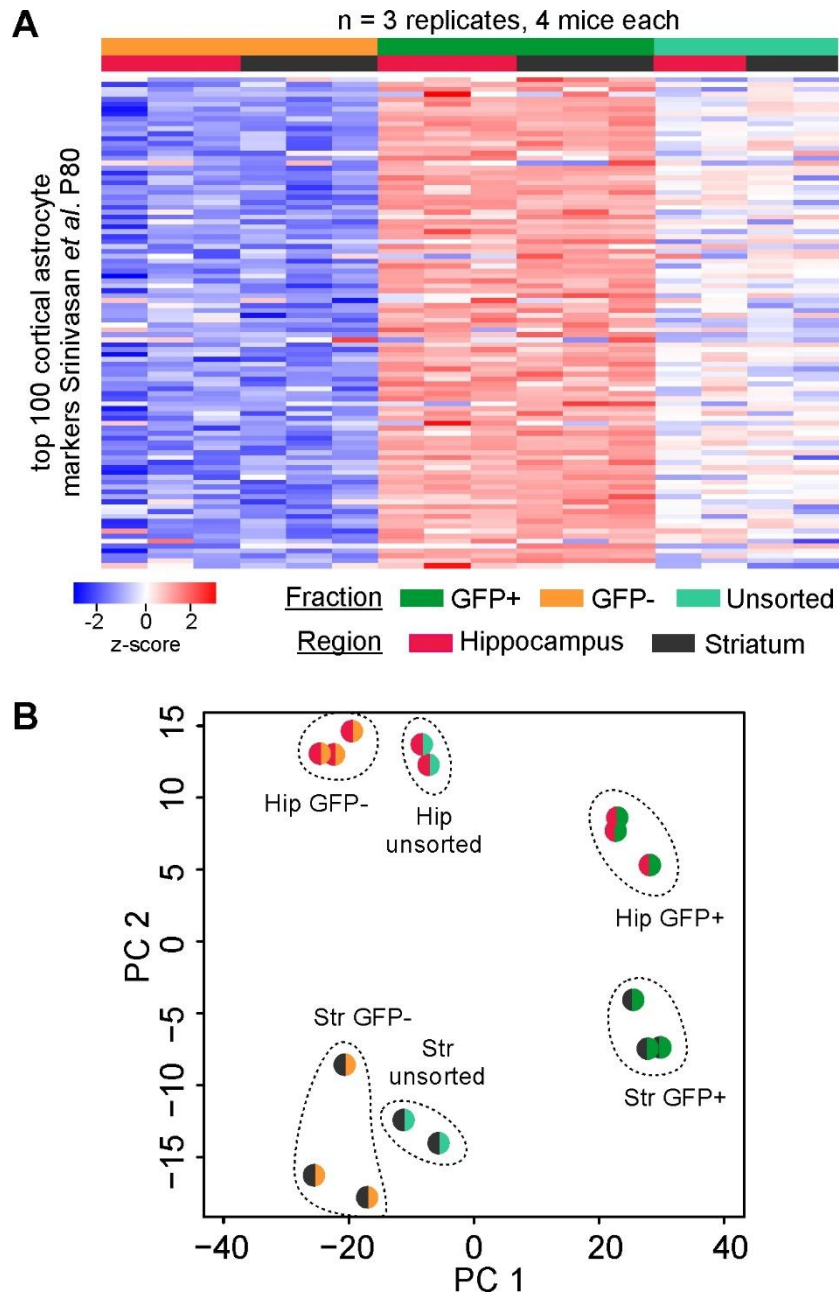


**Figure 4.11: Microarray validation of FACS astrocyte purification.** **A.** Relative expression of the top 100 cortical astrocyte markers in hippocampal and striatal GFP negative and GFP positive fractions as well as unsorted cells. GFP positive samples showed high expression levels of adult astrocyte enriched genes, as opposed to the GFP negative samples. **B.** Principal component analysis of gene expression microarray data using the 1000 transcripts with the most variable expression across all samples. Astrocytes cluster separate from non-GFP-positive cells. Hippocampal and striatal astrocytes form two different clusters.

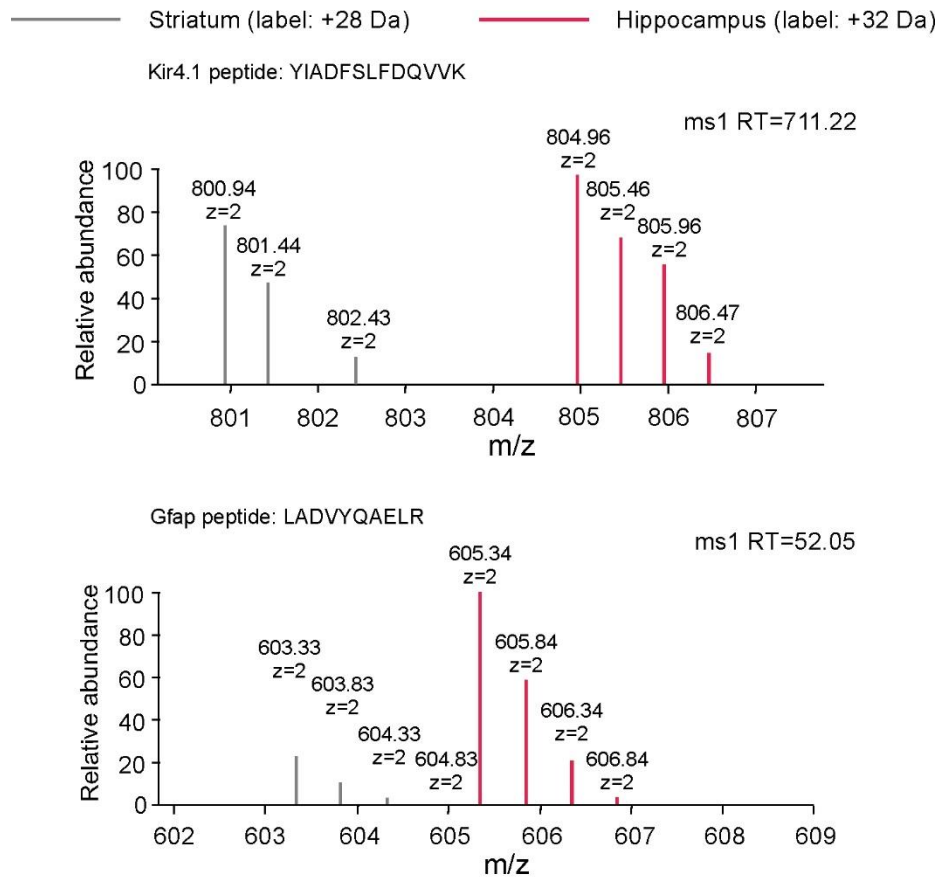


**Figure 4.12: Example spectra for proteomics peptide detection and labeling.** Representative LC-MS/MS spectra for Kir4.1 “QTTVSNSQQAYQEAFEISK” peptide and GFAP “LADVYQAELR” peptide. The labeling of hippocampal peptides with a heavier label was seen in the spectra by a shift in the m/z value. GFAP spectra showed higher relative amount of that peptide in the hippocampus than in the striatum.

### Maximum-stringency protein identification

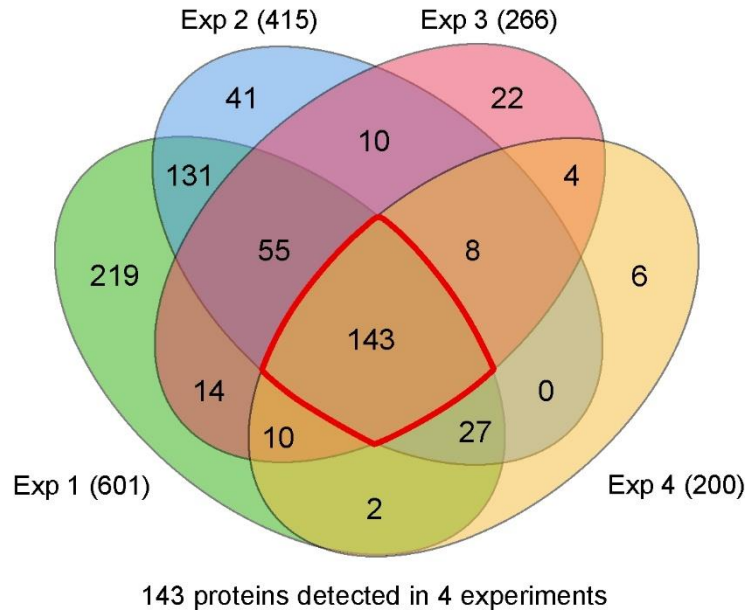


**Figure 4.13: High-stringency identified 692 unique proteins across 4 replicates.** Venn diagram of the number of protein groups identified in the 4 replicates using high-stringency filters. 143 proteins were observed in all four replicates (center outlined in red).

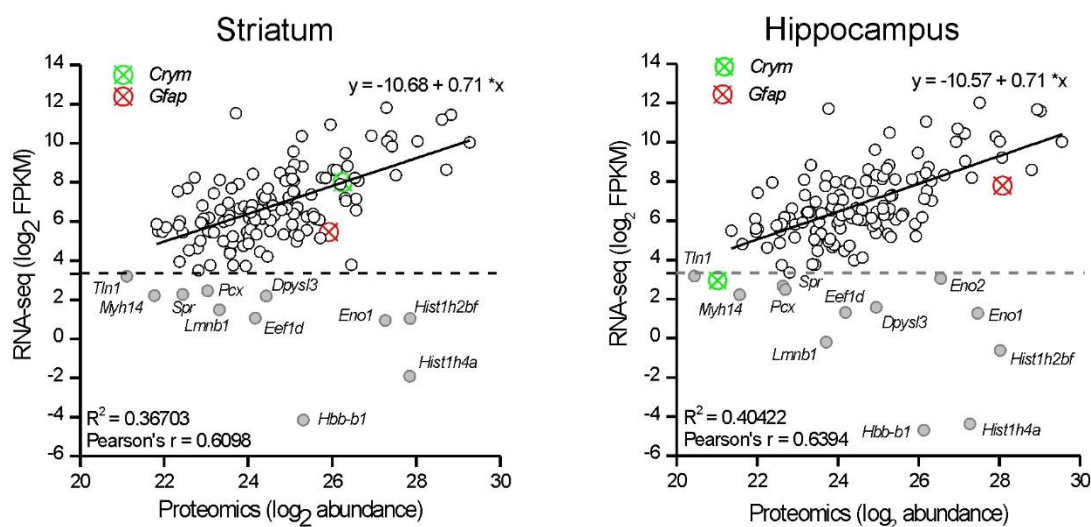


**Figure 4.14: Striatal and hippocampal astrocyte protein expression largely correlate with gene expression but with clear exceptions.** Scatter plot comparing RNA and protein abundance for the 143 proteins detected in the proteomics high-stringency dataset. Most of the proteins show close correlation with RNA levels. However, a subset of proteins (grey filled circles) had high protein levels but low RNA expression (FPKM < 10, dashed line).

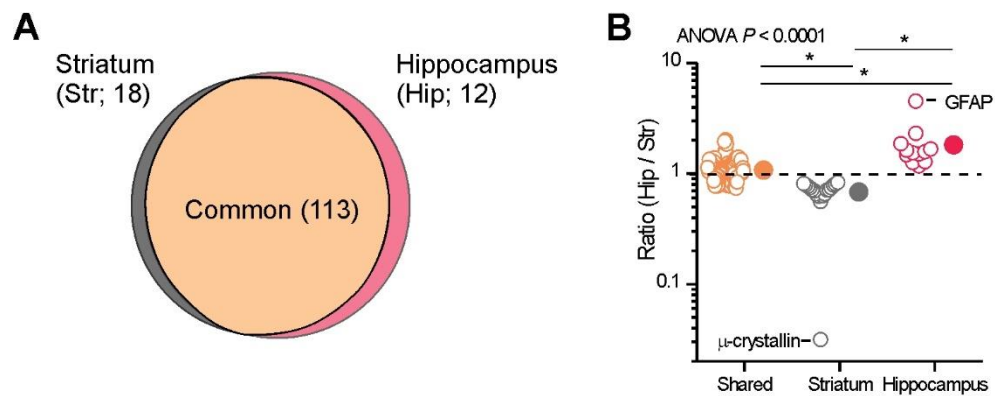


**Figure 4.15: Comparison of striatal and hippocampal astrocyte proteomes.** **A.** Venn diagram of the common, striatal enriched and hippocampal enriched proteins in the high-stringency proteomics dataset. Paired  $t$ -test analysis was used to determine the differentially expressed proteins between hippocampus and striatum. **B.** Hip/Str ratio distribution of the 143 proteins contained in **A**. Ratio of common proteins is significantly different from the proteins enriched in striatum or hippocampus (Kruskal-Wallis ANOVA with \*  $P < 0.05$  post hoc Dunn's multiple comparison test). *Crym* and *Gfap* emerge as the most different among these proteins.

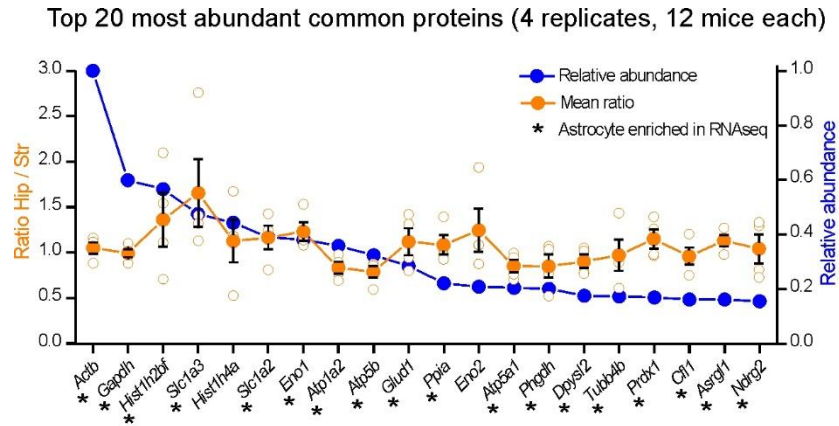


**Figure 4.16: Top 20 most abundant common astrocyte proteins.** \* indicates genes that were also astrocyte enriched in the RNA-Seq data. In these panels, proteins are listed by their gene name for simplicity. In some cases, the error bars representing s.e.m are smaller than the symbol used to show the mean.

Among the 18 striatal-enriched proteins, the most highly enriched was *Crym* ( $\mu$ -crystallin; **Figure 4.17**). *Crym* binds to thyroid hormone. Another exemplar striatal astrocyte enriched protein was *Aldh5a1*, which participates in GABA degradation – this appears relevant given that the striatum consists mainly of GABAergic MSNs. In hippocampal astrocytes, 12 proteins were significantly enriched (**Figure 4.17**), including *Gfap*, an intermediate filament, and *Car2*, a carbonic anhydrase.

Of note, many of the top 100 P7 astrocyte markers (**Figure 4.18**) were strongly represented in the astrocyte proteomic data, but most of the 100 P7 neuronal markers were not (**Figure 4.18**). Thus our analyses of gene and protein expression in the FACS isolated astrocytes speaks to the purity of the cells, as shown in previous work (Foo, 2013), but we emphasize that FACS is by definition a disruptive procedure and future users of this method ought to perform their own controls. Furthermore, the finding that PCA analyses of gene expression using microarrays and RNA-Seq were similar (**Figures 4.5, 4.11B**) also speaks to the relative purity of our samples as RNA-Seq did not require FACS. Of course, we cannot completely rule out neuronal “contamination” in the FACS isolated material. This is a known limitation of the method and is also expected since astrocytes phagocytose neurons (Chung et al., 2015b). From these perspectives, our FACS samples are best described as strongly astrocyte enriched, rather than a totally astrocyte pure population.

#### **Section 4.6: Validating the top striatal and hippocampal astrocyte enriched genes**

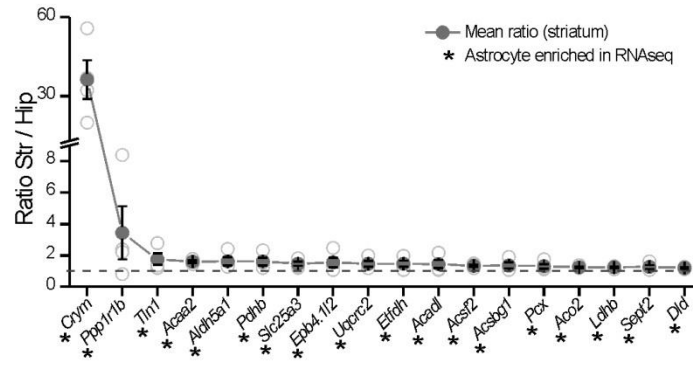
Proteomics and RNA-Seq revealed  $\mu$ -crystallin (*Crym*) and GFAP (*Gfap*) as highly abundant and differentially expressed between striatal and hippocampal astrocytes (**Figure 4.17, 4.19A**). To validate this further, we performed qPCR for *Crym* and *Gfap* with astrocyte RNA obtained from P63 *Aldh111*-Cre/ERT2 x Rpl22HA mice (**Figure 4.19B**) and P30 *Aldh111*-eGFP astrocytes isolated by FACS (**Figure 4.19C**). In both cases, we found that RNA levels of *Crym*

were significantly higher in striatal astrocytes, and undetectable in hippocampal astrocytes. Similarly, *Gfap* RNA was enriched in hippocampal astrocytes in relation to striatal astrocytes. The data were validated at the protein level by Western blot of FACS-isolated astrocytes (**Figure 4.19D**). There was no detectable expression of  $\mu$ -crystallin in hippocampal astrocytes whereas GFAP expression was 12 time higher as compared to striatal astrocytes.

We further confirmed these findings using IHC in *Aldh1l1*-eGFP reporter mice (**Figure 4.20**). Only  $7 \pm 2\%$  of astrocytes in the d.l. striatum showed GFAP staining (1314 cells examined from  $n = 4$  mice; **Figure 4.20A**), whereas GFAP was expressed in 100% of CA1 s.r. astrocytes (620 cells examined from  $n = 4$  mice; **Figure 4.20B**). Furthermore, no immunostaining was observed for  $\mu$ -crystallin in hippocampal astrocytes ( $n = 3$  mice), although it was found in pyramidal neurons within the same optical sections (**Figure 4.20D**). In the d.l. striatum,  $\mu$ -crystallin immunostaining was obvious within  $50 \pm 6\%$  of astrocytes (**Figure 4.20C**;  $n = 3$  mice).

We also observed that  $\mu$ -crystallin positive astrocytes displayed a gradient in the striatum: their density increased along the dorsal-to-ventral axis, peaking in numbers and intensity in the ventro-medial region in the nucleus accumbens (**Figure 4.21**). This gradient was not shared with eGFP (from the *Aldh1l1*-eGFP mice), S100 $\beta$ , Kir4.1 or GLT1 (**Figure 4.22**). This provides strong evidence that the density of astrocytes is consistent throughout the striatum, but that  $\mu$ -crystallin specifically displays a gradient. Furthermore, we evaluated  $\mu$ -crystallin expression in *Aldh1l1*-eGFP positive astrocytes broadly in the brain and found it only within striatal astrocytes (**Figure 4.23**).

**A** Striatum enriched proteins (4 replicates, 12 mice each)



**B** Hippocampus enriched proteins (4 replicates, 12 mice each)

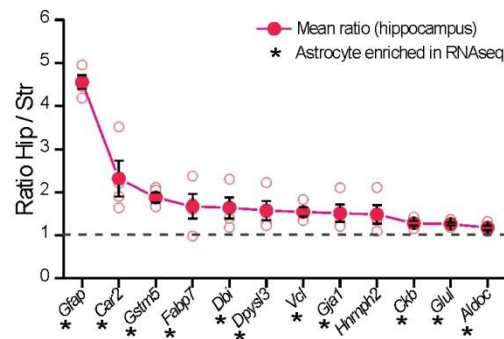


**Figure 4.17: Differentially expressed proteins in striatal and hippocampal astrocytes. A.** Striatum enriched proteins. **B.** Hippocampus enriched proteins. \* indicates genes that were also astrocyte enriched in the RNA-Seq data. In these panels, proteins are listed by their gene name for simplicity. In some cases, the error bars representing s.e.m are smaller than the symbol used to show the mean.

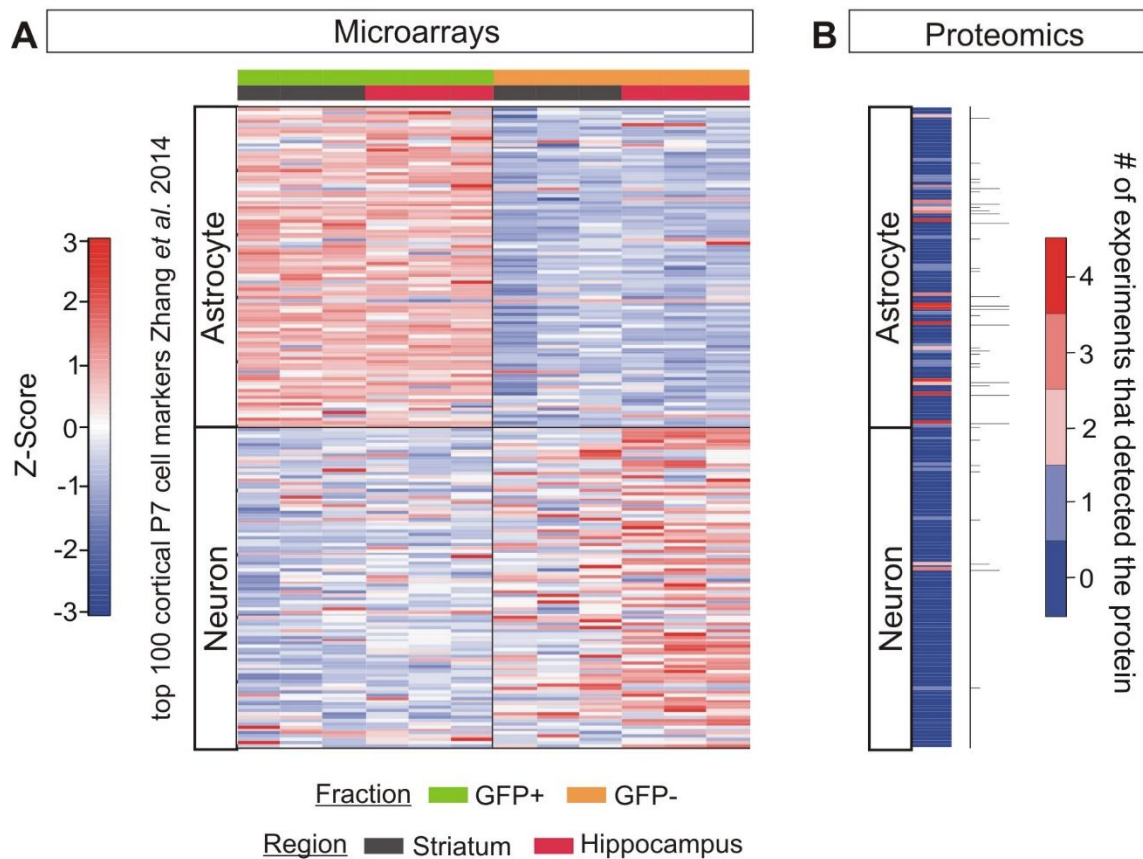


**Figure 4.18: Further validation of sorted eGFP positive cells as strongly astrocyte enriched.** **A.** Relative expression of the top 100 P7 cortical astrocyte markers in hippocampal and striatal GFP negative and GFP positive fractions as well as unsorted cells. GFP positive samples showed high expression levels of adult astrocyte enriched genes, as opposed to the GFP negative samples. In contrast, the top 100 P7 neuron markers were depleted in the GFP positive fractions and enriched in the GFP negative fractions. **B.** Presence of the top 100 P7 astrocyte and neuron enriched proteins in the proteomics dataset. On the left, a heat map that represents the number of replicates in which the proteins were detected. On the right, raster plot showing the proteins that were detected at least in one experiment. Our proteomic data sets were enriched in known astrocyte markers, but relatively depleted of known neuronal markers.

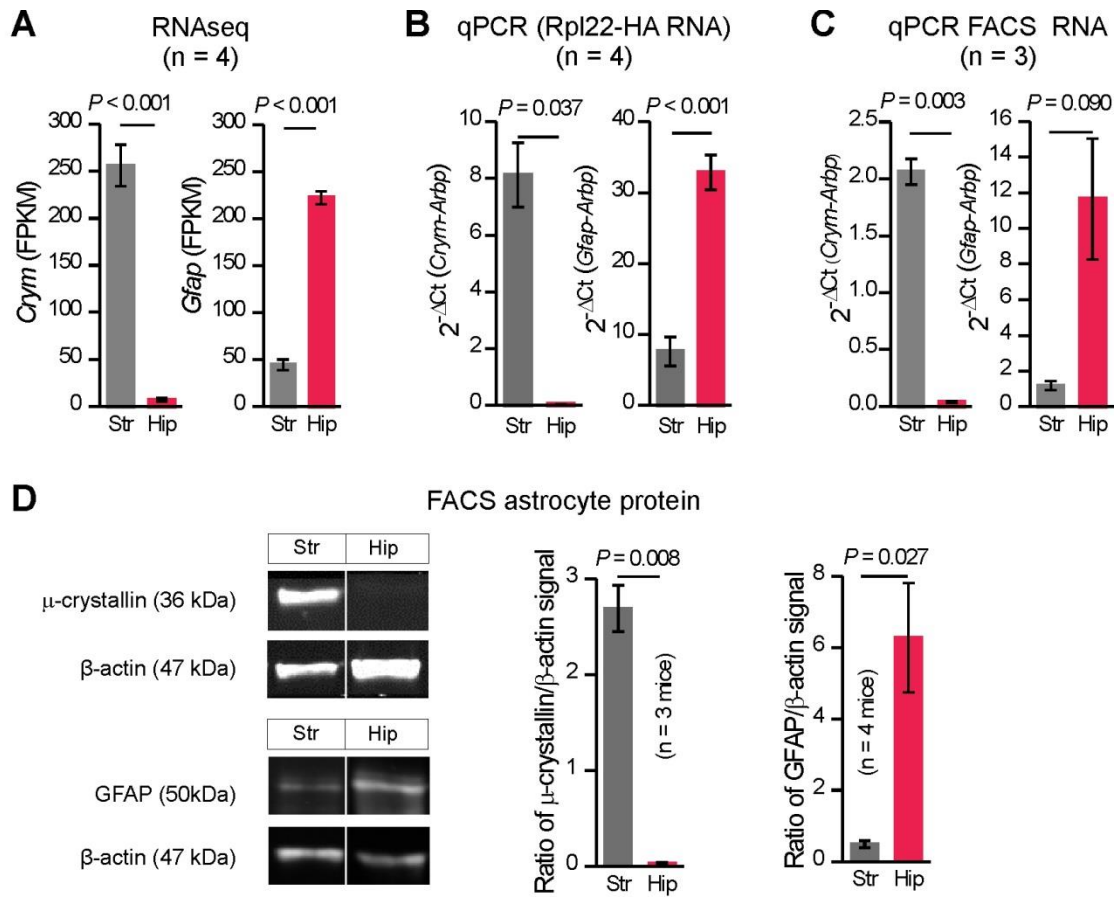


**Figure 4.19: Validating GFAP and  $\mu$ -crystallin expression in striatal and hippocampal astrocytes.** **A.** RNA-Seq FPKM values for *Crym* and *Gfap* in striatum and hippocampus. **B.** qPCR of RNA extracted from P63 *Aldh11-Cre/ERT2* x *RiboTag* mice for *Crym* and *Gfap* in striatum and hippocampus. **C.** qPCR of mRNA extracted from FAC P30 sorted astrocytes for *Crym* and *Gfap* in striatum and hippocampus. **D.** Western blot for  $\mu$ -crystallin and GFAP from striatal and hippocampal FACS astrocytes, and quantification normalized to  $\beta$ -actin signal.

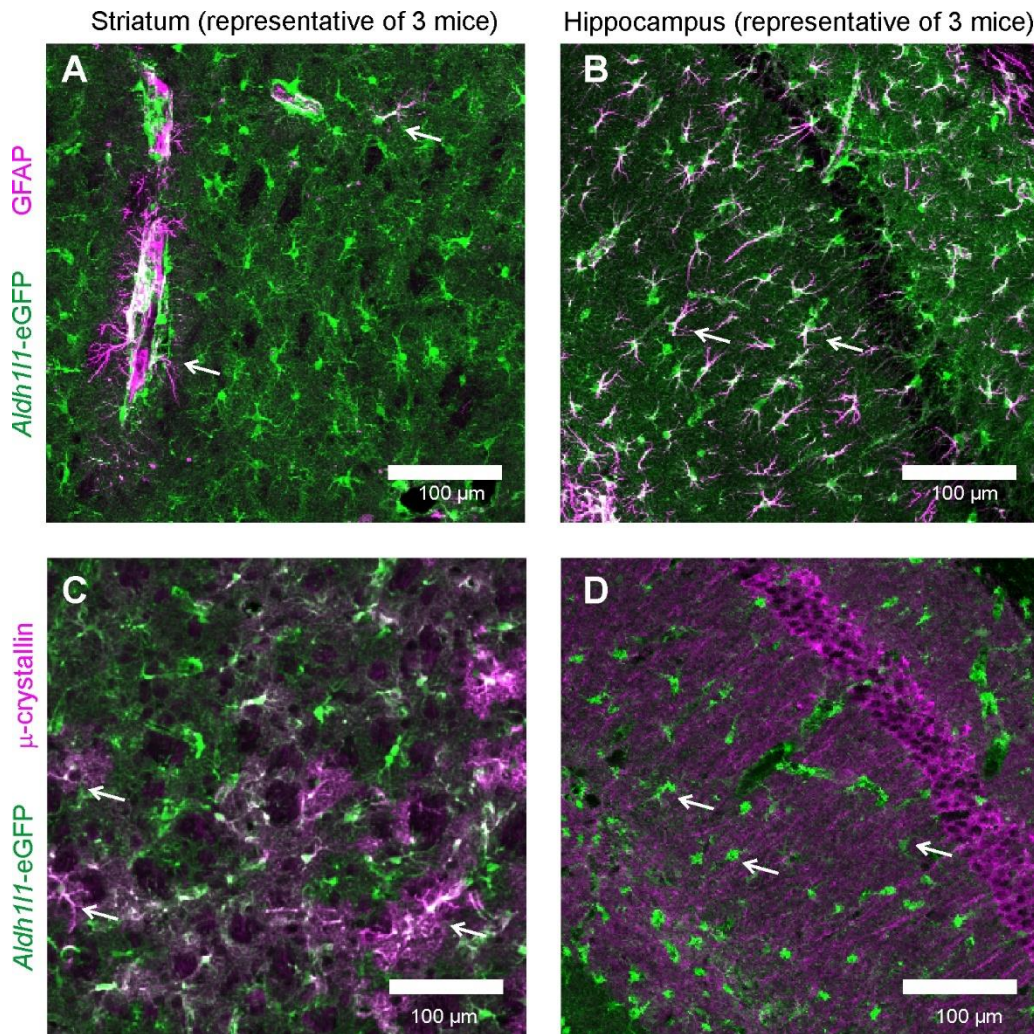


**Figure 4.20: Validating GFAP and  $\mu$ -crystallin expression in striatal and hippocampal astrocytes.** **A & B.** IHC of GFAP and  $\mu$ -crystallin in striatum and hippocampus of *Aldh111*-eGFP mice. GFAP is expressed in most of the astrocytes in hippocampus [arrows in **B**], however in the striatum most of the astrocytes are GFAP negative [arrows in **A**]. **C.** In the Striatum, a high proportion of astrocytes stain for  $\mu$ -crystallin [arrows]. **D.**  $\mu$ -crystallin was expressed in the pyramidal cell layer of CA1, but not in astrocytes of the hippocampus [arrows].

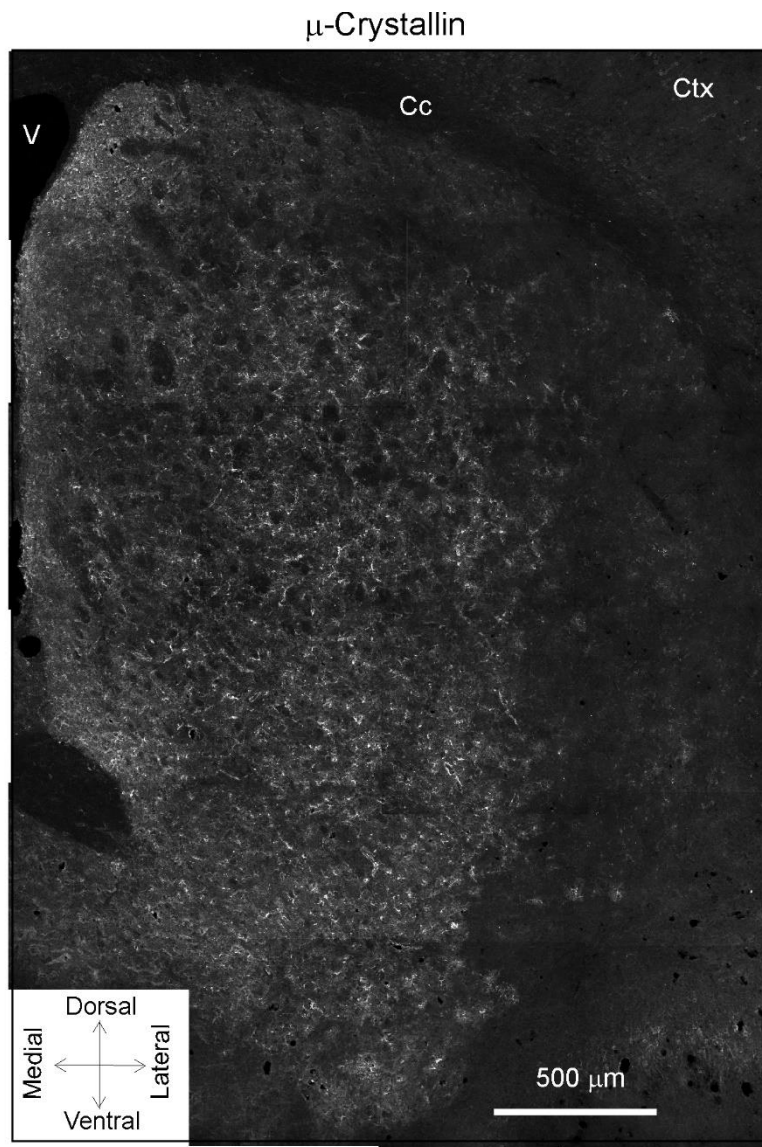


**Figure 4.21:  $\mu$ -crystallin expression displays a gradient in striatal astrocytes.**  $\mu$ -crystallin immunostaining in striatum showing its spatial gradient of expression (V = ventricle, Cc = corpus callosum, Ctx = cortex).

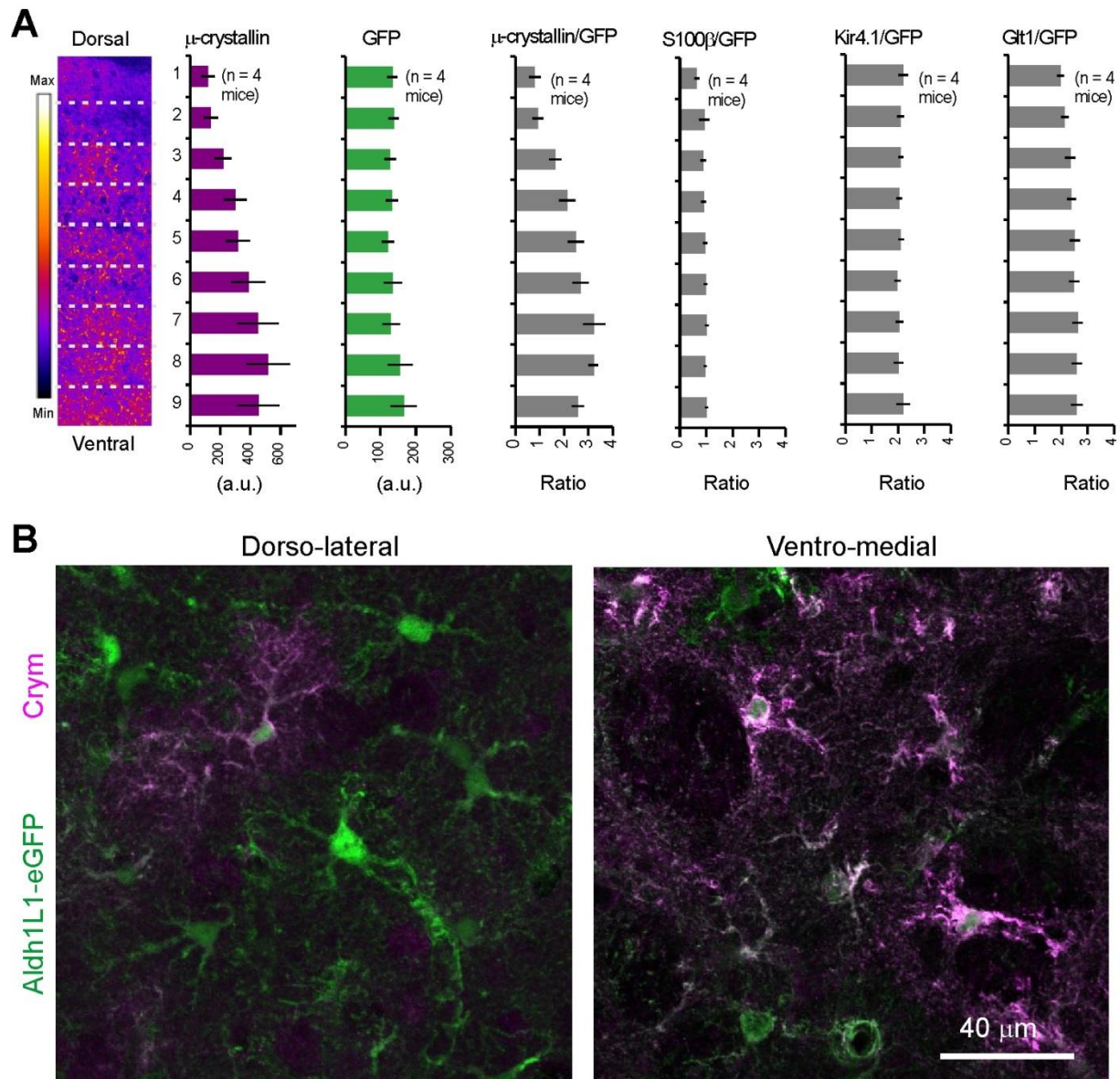


**Figure 4.22:  $\mu$ -crystallin expression in striatal and hippocampal astrocytes. A.** Quantification of  $\mu$ -crystallin, S100 $\beta$ , Kir4.1 and GLT1 signal intensity in *Aldh1l1*-eGFP mice along the dorso-ventral axis of the striatum. The signal was normalized to GFP signal. **B.**  $\mu$ -crystallin immunostaining in dorso-lateral and ventro-medial striatum of *Aldh1l1*-eGFP mice.

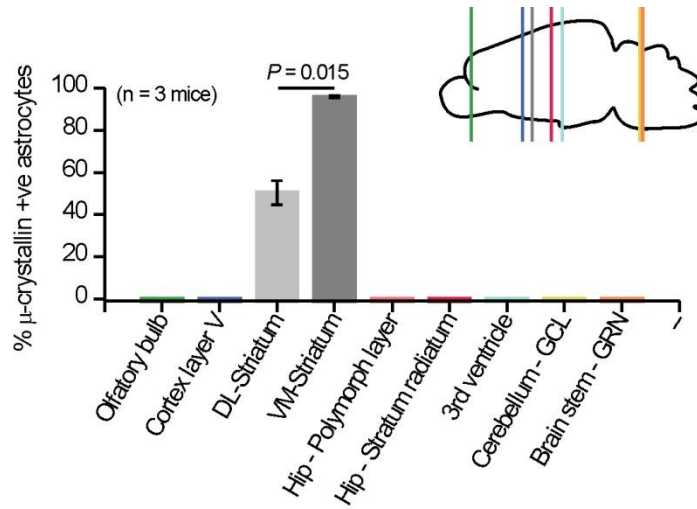


**Figure 4.23:  $\mu$ -Crystallin expression in striatal and hippocampal astrocytes.** Quantification of  $\mu$ -crystallin positive astrocytes in 9 brain regions.  $\mu$ -crystallin expressing astrocytes were only observed in the striatum. Up to 100% of the astrocytes in the ventro-medial striatum were  $\mu$ -crystallin positive.

## Section 4.7: Summary and discussion

The data set is available at the Gene Expression Omnibus with accession number GSE94010. The proteomic data have been deposited at the Proteome Exchange Consortium via PRIDE with accession number PXD005852 (<https://www.ebi.ac.uk/pride>). The RNA-Seq and proteomic data of adult striatal and hippocampal astrocytes have been made available as a searchable website at <http://astrocyternaseq.org/>.

The adult RNA-Seq and proteomic data provide much needed resources to explore astrocyte functions in hypothesis driven experiments employing genetic and functional approaches. For example, the list of the 20 most abundant astrocyte proteins shared between striatal and hippocampal astrocytes reveals several whose functions are unclear, but are nonetheless astrocyte enriched (Zhang et al., 2014). It is likely these underlie core and important astrocyte physiological processes.

The top striatal and hippocampal astrocyte enriched genes and proteins identified by RNA-Seq and LC-MS/MS were validated by qPCR, immunostaining and Western blot analyses. The finding that GFAP was low in striatal astrocytes across all our measurements explains why past studies may have concluded that the striatum has few astrocytes (Cui et al., 2016), emphasizing the limitations of GFAP and speaking to the greater utility of the *Aldh1l1* locus (Cahoy et al., 2008; Srinivasan et al., 2016). Our result is also consistent with past *ex vivo* hybridization experiments (<http://mouse.brain-map.org/gene/show/14356>; (Lein et al., 2007). Admittedly, GFAP is known to have several different isoforms in humans and at least 2 isoforms in rodents with possible structural difference between central and peripheral GFAP (Middeldorp and Hol, 2011). However, sequences belonging to both mouse GFAP isoforms were found in our RNA-Seq data.

To our knowledge, the discovery that  $\mu$ -crystallin is specific for striatal astrocytes provides the first molecular marker that defines a region-specific astrocyte population. Moreover,

striatal astrocytes are known to be altered in Huntington's disease (HD) (Benraiss et al., 2016; Liddelw et al., 2017; Tong et al., 2014), and  $\mu$ -crystallin levels decrease in humans and mouse models of HD (Francelle et al., 2015). Interestingly, six of the top 40 striatal enriched astrocyte genes are histones, which is consistent with the GSEA results that chromosome structure-related gene sets were striatal enriched. The striatal enrichment of cell cycle and mitosis-related genes in astrocytes may indicate that striatal astrocytes are more poised to respond to stimuli with proliferation, for example as may occur in the context of striatal diseases such as HD.

Adult striatal and hippocampal astrocytes are clearly molecularly distinct cell populations at RNA and protein levels. 10-15% of identified genes and proteins were differentially expressed between striatal and hippocampal astrocytes including molecules with known functional importance in astrocytes, e.g. Connexins, GPCRs,  $K^+$  and  $Ca^{2+}$  channels and signaling pathways. The analyses at single molecule level complements the GSEA result that astrocytes in these two neural circuits exhibit functionally relevant molecular differences. While exciting, these results must be interpreted in the context of other astrocyte properties, as was done in the interneuron field (Kepecs and Fishell, 2014). In the following chapters, we demonstrate the power of these large omic datasets to link astrocyte morphology, function, and molecules in the study of astrocyte diversity.

## CHAPTER 5: ASTROCYTE MORPHOLOGICAL DIVERSITY BETWEEN ADULT NEURAL CIRCUITS

### Section 5.1: Introduction

Protoplasmic astrocytes have remarkably complex morphology with thousands of processes that create characteristically “bushy” appearances (Shigetomi et al., 2013; Tong et al., 2013). Modulation of neurons and blood vessels is proposed to occur via interactions with these astrocyte processes. In 1895, Ramón y Cajal and colleagues put forth and then abandoned the hypothesis that processes of neuroglial cells are dynamic and intervene physically between neuronal connections to decrease signal transduction (Ramón y Cajal and DeFelipe, 1988). We now know that the role of glia in modulating synaptic function and strength is not a physical barrier. Rather, microglia processes, which are indeed dynamic as Cajal had suspected, prune synapses by using the complement cascade via C3 (reviewed in Schafer and Stevens, 2015). Astrocytes also modulate synaptogenesis and synapse strength; this is thought to occur through secreted and membrane-bound factors during development (**Table 1.1**), controlling the levels of extracellular neurotransmitters and ions, and possibly some form of phagocytosis. These functions rely on extensively ramified astrocyte processes and thus, regional functional differences may be reflected in astrocyte morphology.

Traditionally, astrocyte morphology has been studied based on GFAP staining. GFAP is an intermediate filament protein long considered to be the astrocyte marker of choice. GFAP is responsible in part for the astrocyte cytoskeleton; vimentin, another intermediate filament protein, and actin microfilaments also provide structural support (Chiu et al., 1981; Yang and Wang, 2015). GFAP staining has been the basis for assessing astrocyte morphological diversity in physiology (Bailey and Shipley, 1993; Kulkarni et al., 2015; Ramón y Cajal and DeFelipe, 1988) and in pathology (Middeldorp and Hol, 2011; Sofroniew and Vinters, 2010). By labeling only the major processes, GFAP staining permits quantification of branching pattern using Sholl

analysis, a technique developed to analyze neuronal arborization patterns (Sholl, 1953). GFAP is not expressed in the finest astrocyte processes and thus cannot visualize the full extent of astrocyte morphology (Bushong et al., 2002; Middeldorp and Hol, 2011; Shigetomi et al., 2013; Sosunov et al., 2014; Tong et al., 2013). Dye filling of astrocytes and electron microscopy work have shown that the ramification of astrocyte processes begins close to the soma and progressively branch into the finest astrocyte processes both near the soma and in distal parts of the territory (Bushong et al., 2002; Kosaka and Hama, 1986; Shigetomi et al., 2013). Therefore, GFAP staining clearly underestimates the volume and complexity of astrocytes.

Astrocytes represent ~40% of brain cells, but their regional density varies (Khakh and Sofroniew, 2015). It has been suggested that the striatum contains low numbers of astrocytes based on GFAP staining (Cui et al., 2016; Emsley and Macklis, 2006). However, astrocyte expression of GFAP is not uniform and some astrocytes don't express GFAP at all (Sofroniew and Vinters, 2010; Sosunov et al., 2014). Indeed we have already shown that GFAP expression is low in the striatum (**Chapter 4**). Therefore, GFAP cannot be used assess astrocyte density or morphology.

## **Section 5.2: Astrocyte density assessed with cleared brain tissue**

We began our morphological analysis by comparing the density of astrocytes in the hippocampus and striatum using *ScaleS* brain clearing (Hama et al., 2015) of *Aldh1l1*-eGFP reporter mice. From the cleared brain tissue, astrocytes appear to tile the grey matter, as consistent with past morphological analysis done at the single cell level for CA1 s.r. (Bushong et al., 2002). We found that astrocyte densities were similar for d.l. striatum and hippocampus CA1 s.r. at  $8 \pm 2$  and  $11 \pm 1$  astrocytes per  $100 \mu\text{m}^3$ , respectively (**Figure 5.1, Supplemental movie 2 and 3**,  $P > 0.05$ ,  $n = 3$  mice). The density of astrocytes in the whole striatum and whole hippocampus were not different, although astrocyte density from hippocampus trended higher

(**Figure 5.1C**). This was due to higher astrocyte densities in hippocampal subfields that were not the focus of this project, e.g. the dentate gyrus (**Figure 5.1B, Supplemental movie 3**). Astrocyte distribution in the striatum, which lacks the structural architecture seen in the hippocampus, was more uniform (**Figure 5.1A, Supplemental movie 2**). This is supported by the similarity in astrocyte density between the d.l. striatum and the whole striatum (**Figure 5.1C**). In contrast, whole hippocampus astrocyte density trended higher than that seen in the CA1 s.r. (**Figure 5.1C**).

It has been previously shown that striatum and hippocampus have different astrocyte densities based on GFAP staining (Emsley and Macklis, 2006). However, astrocyte densities as calculated from GFAP and S100 $\beta$  immunohistochemistry (at most 1 cell per 100  $\mu\text{m}$  cube of striatum; 3 to 12 or more cells per 100  $\mu\text{m}$  cube of hippocampus) (Emsley and Macklis, 2006) were lower than that found using cleared *Aldh111*-eGFP brains (**Figure 5.1**). Some of the differences could arise from Emsley and Macklis counting from 30  $\mu\text{m}$  sections (Emsley and Macklis, 2006), and thus damage to section surfaces will decrease the number of positively stained cells counted. However, counting ScaleS cleared brains found higher astrocyte density in whole hippocampus than striatum (**Figure 5.1C**), which is consistent with finding from GFAP and S100 $\beta$  IHC.

By using *Aldh111*-eGFP reporter mice and NeuN staining (**Figure 5.2**) we also measured the ratio of neurons-to-astrocytes in volumes of the d.l. striatum and CA1 s.r. There were six neurons to every astrocyte in the d.l. striatum whereas there were seven astrocytes to every neuron in CA1 s.r. (**Figure 5.2B**). This is expected as the CA1 s.r. region is where CA3 Schaffer collaterals synapse onto the apical dendrites of CA1 pyramidal cells and is known to only have sparse interneurons. Thus, despite existing in microcircuits with different levels neuronal investment, astrocytes in d.l. striatum and CA1 s.r. have similar densities.

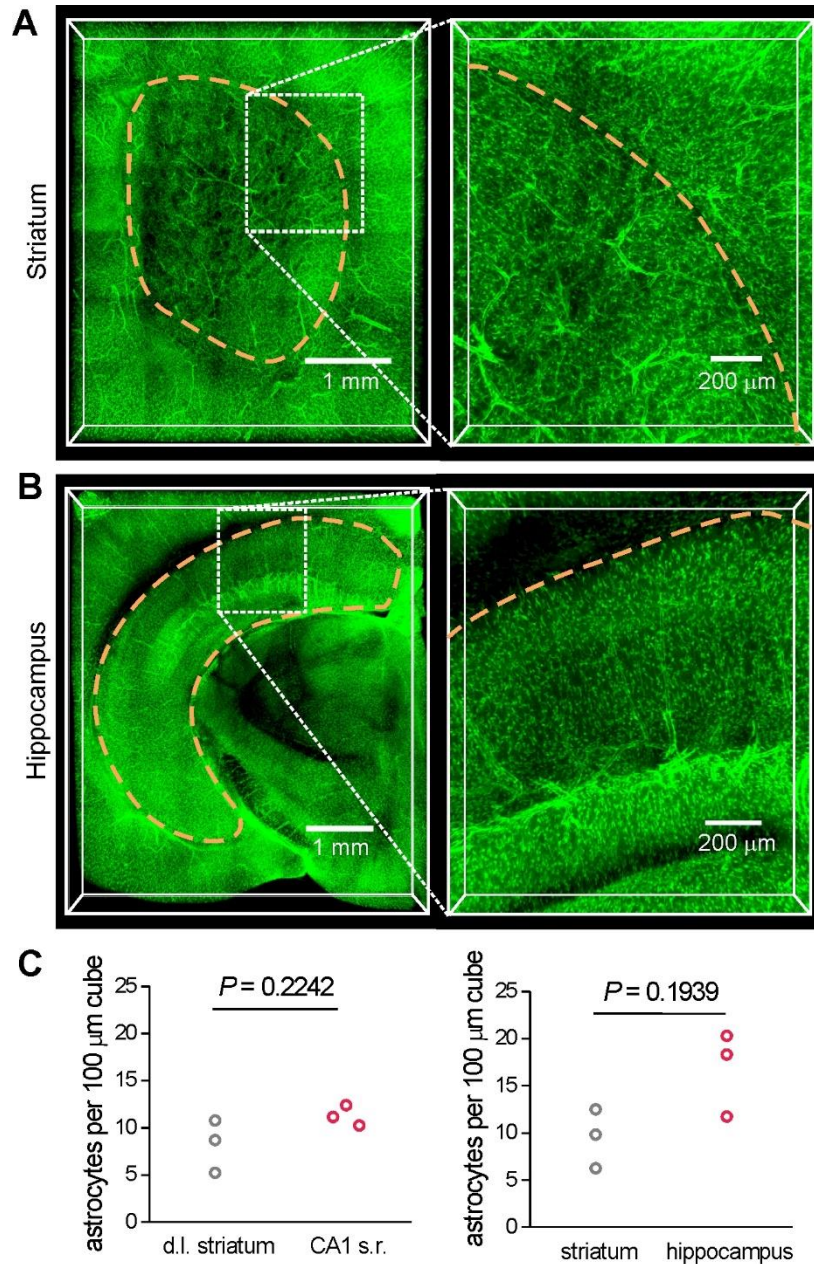


**Figure 5.1: Evaluating astrocyte density in d.l. striatum and hippocampal CA1 s.r. A & B.**

Coronal sections of *Alzh111*-eGFP brains were cleared using ScaleS and imaged using confocal microscopy to measure astrocyte density. The striatum (**A**) is enclosed by orange dashed line with the inset showing a close-up of the d.l. striatum. The hippocampus (**B**) is enclosed by orange dashed line with the inset showing a close-up of the CA1 s.r.. **C**. Plots for astrocyte density from d.l. striatum, CA1 s.r., whole striatum, and whole hippocampus.

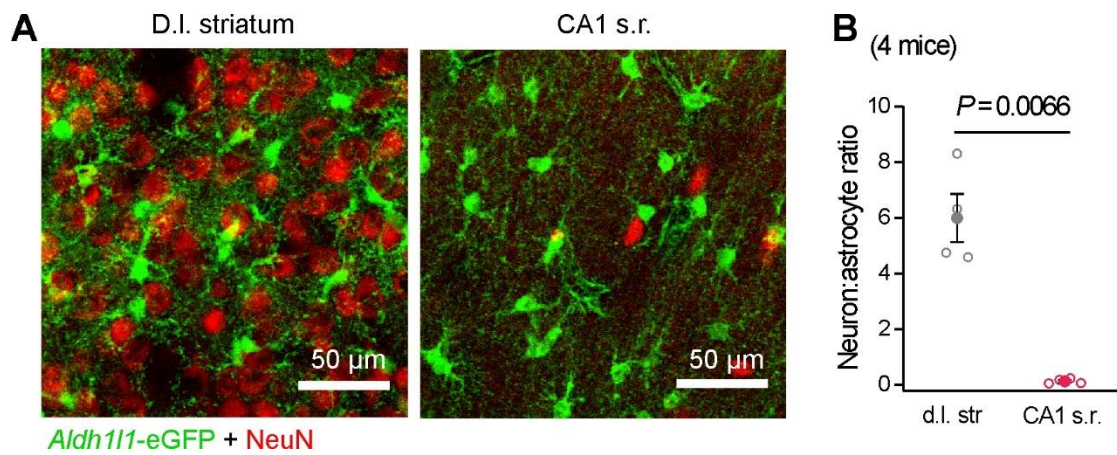


**Figure 5.2: Astrocyte neuron ratio in d.l. striatum and CA1 s.r.** **A.** Representative maximum z-projection of *Aldh111*-eGFP striatum and hippocampus sections immunostained for GFP (green) and NeuN (red). **B.** The ratio of green astrocytes and red neurons quantified from confocal images as shown in **A** from 4 mice.

### Chapter 5.3: Astrocyte morphology assessed with light microscopy

We next used intracellular iontophoresis of Lucifer Yellow (LY) in lightly-fixed brain tissue (Bushong et al., 2002) to directly assess astrocyte cell morphology. LY-filling of astrocytes revealed their characteristic highly complex bushy shapes (**Supplemental movie 4**). Using 3D-reconstructions, we determined the volumes enclosed by single astrocytes in the d.l. striatum and CA1 s.r. (**Figure 5.3**). NeuN co-staining of LY-filled astrocytes showed that ~20 neuronal cell bodies completely or partially intersected with a single d.l. striatal astrocyte territory, whereas at most one neuronal cell body intersected with CA1 s.r. astrocytes (**Figure 5.3C, Div**), confirming at the single-cell level that neuronal investment per astrocyte is much higher in the striatum. We also found that striatal and hippocampal astrocytes displayed equivalent somatic volumes and the same cell volumes (**Figure 5.3Di-ii**). However, the territory volume of d.l. striatal astrocytes was significantly larger than that of CA1 s.r. astrocytes (**Figure 5.3Diii**). The spread of striatal astrocyte territory volumes suggests potentially a bimodal distribution (**Figure 5.3Diii**). Therefore, we separated the striatal astrocytes into two groups by territory volume. As expected, striatal astrocytes with larger territories tended to have larger cell volumes and this subset of d.l. striatal astrocytes had 1.5 times the volume of CA1 s.r. astrocytes (**Figure 5.4**).

Using the 3D reconstructions, we also quantified the number and size of astrocyte primary branches, i.e. those that arose from the soma (**Figure 5.5**). Striatal and hippocampal astrocytes have similar number of primary branches (median d.l. striatum 6, CA1 s.r. 7; **Figure 5.5B**). These dye-filled astrocytes also allows for comparison of branch diameter. Striatal branches were significantly thicker than hippocampal ones whether comparing average per cell or pooled diameters (**Figure 5.5C**). Through looking at the dye-filled astrocytes, we noticed that some astrocyte primary branches were particularly thick ( $>3\ \mu\text{m}$ ; **Figure 5.5C**). A greater proportion of striatal astrocytes appear to have these thick primary branches, as compared to hippocampal ones, although this was not statistically significant (**Figure 5.5D**).

To quantify the shape of astrocytes, we analyzed the shape of 2D astrocyte territories z-projected along the anterior-posterior axis (filled astrocytes were from coronal sections). Previous work have noted that fibrous astrocytes have more elongated shapes as compared to protoplasmic astrocytes by GFAP immunoreactivity (Lundgaard et al., 2014). We found that these differences were also found within protoplasmic astrocytes. Specially, hippocampal astrocytes had less circular territories than striatal astrocytes (**Figure 5.6**). As noted previously, pyramidal cell dendrites course through CA1 s.r. region and thus in some ways resemble the microenvironment of fibrous astrocytes where many axonal fibers exist. The relatively elongated hippocampal astrocyte shape could therefore reflects the local anatomy of the neuronal network.

Dye-filling of individual astrocytes found that striatal astrocytes have thicker primary branches with larger and more circular territories than hippocampal ones, and impinge upon significantly greater numbers of neuronal somata. Thus, there are clear regional differences in astrocyte morphology when examined at the light microscopy level.

#### **Section 5.4: Astrocyte-synapse proximity assessed with SBF-SEM**

The proximity of the finest astrocyte processes to synapses cannot be measured with dye-filled astrocytes as the finest leaflets are on the order of nanometers and thus below the resolution of light microscopy. We used serial block-face scanning electron microscopy (SBF-SEM) to examine the proximity and interaction between astrocyte processes, presynaptic terminals and postsynaptic spines in the d.l. striatum and hippocampus CA1 s.r. (**Figure 5.7; Supplemental movie 5**).

To evaluate whether astrocyte interactions with synapses differed between the two regions, we measured the vector between astrocyte processes and the center of the post-synaptic density (PSD). We found that striatal astrocyte processes were further away from PSD

centers (**Figure 5.8A**). Larger spines, such as mushroom spines, have larger volumes and bigger PSDs (Arellano et al., 2007). Thus, this regional difference may simply be a reflection of regional difference in spine morphology. Therefore, we classified the type of spine for all traced synapses (**Figure 5.8B**). The majority of spines on medium spiny neurons were thin spines (**Figure 5.8B**), consistent with published work in rats (Bello-Medina et al., 2016). In the hippocampus, the majority of excitatory spines were mushroom (**Figure 5.8B**). Importantly for this analysis, if the difference in astrocyte-synapse proximity were due to spine size, we would have observed the opposite finding. Instead, striatal astrocyte processes were further away from PSD centers regardless of spine type (**Figure 5.8C**). As expected within each region, astrocyte processes were located more distally to mushroom spine PSDs when compared to thin and other spine types (**Figure 5.8C**).

In addition, fewer synaptic interfaces in the striatum displayed astrocytic contacts (**Figure 5.9A**) although the difference is subtle. In those synapses with contact, the coverage of synaptic interface perimeter, as defined by where the axon bouton meets the head of the synapse, was not different between the two regions (**Figure 5.9B**). Examination of astrocyte morphology at the ultrastructural level reveals that the majority of excitatory synapses are physically contacted by fine astrocyte processes, and hippocampal astrocytes display significantly greater and tighter physical interactions with excitatory synapses than those in the striatum.

## **Section 5.5: Summary and discussion**

The clear morphological difference between d.l. striatal and CA1 s.r. astrocytes is that hippocampal astrocyte processes and excitatory synapses share a closer physical relationship. This is consistent with the finding from RNA-Seq that two of the four gene sets enriched in

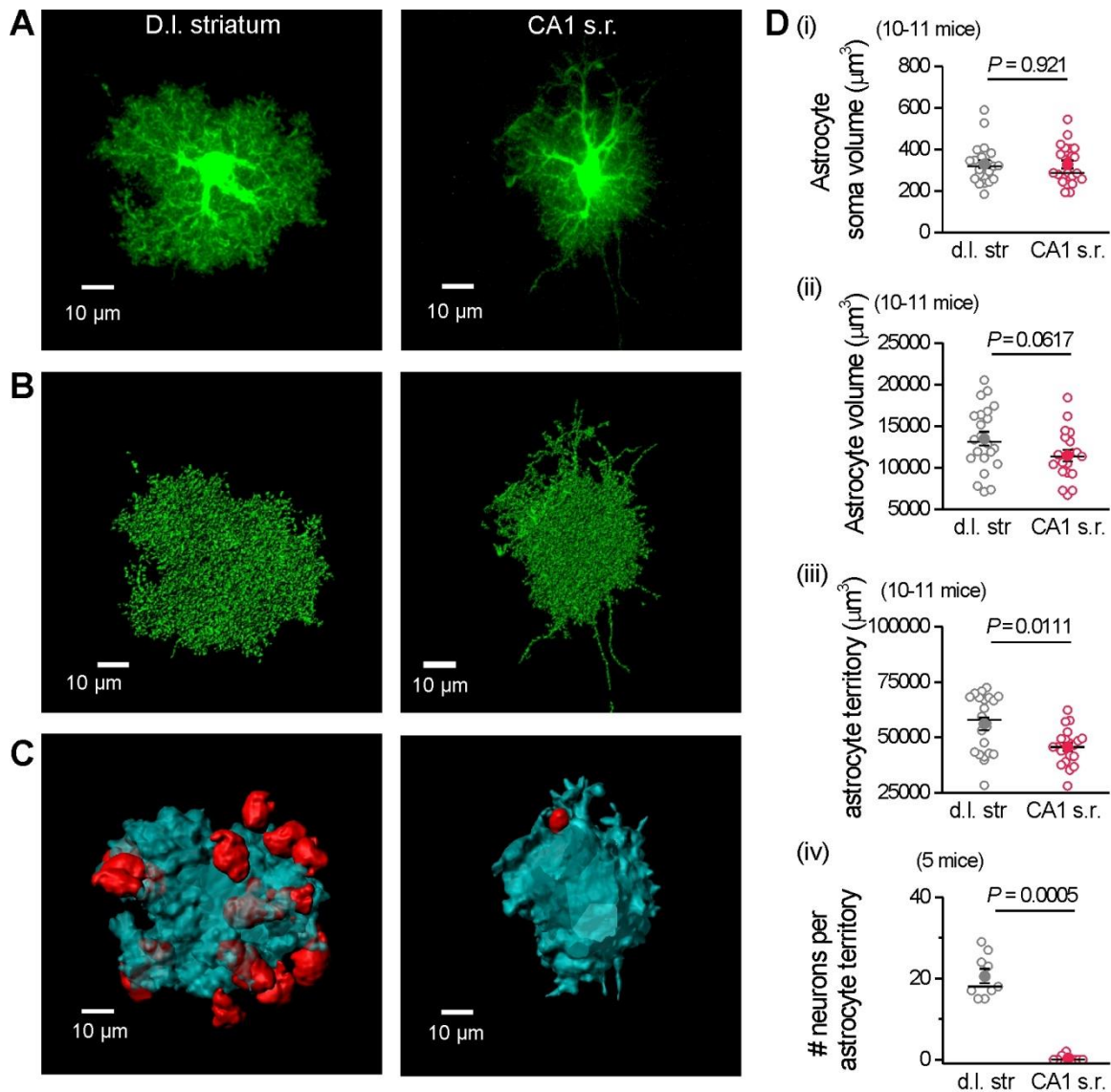


**Figure 5.3: Comparison of striatal and hippocampal astrocyte morphology.** **A.** Example confocal volumes of Lucifer yellow filled astrocytes in wild-type Swiss-Webster mice. **B.** 3D reconstructions of confocal volumes from **A.** **C.** 3D reconstructions of volumes enclosed by astrocyte territories in blue and nearby NeuN co-stained neuronal somata in red. **D. i-iii.** Astrocyte somata volume (i), astrocyte cell volume (ii), and astrocyte territory volume (iii) were compared for striatal versus hippocampal astrocytes ( $n = 19-22$  from 10-11 mice). **iv.** Number of neurons in a single astrocyte territory as determined by reconstructions in **C** was compared ( $n = 8-9$  from 5 mice). Striatal data are shown in grey whereas hippocampal data are in red. Open circles are raw data with closed circle indicating mean  $\pm$  s.e.m and a horizontal line for the median. In some cases, the error bars representing s.e.m are smaller than the symbol used to show the mean.

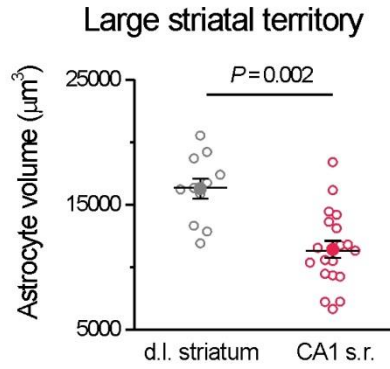


**Figure 5.4: Striatal astrocytes with large territory volume have large striatal volumes.** For striatal astrocytes whose territories were greater than the median, astrocyte cell volumes were compared for against hippocampal astrocytes ( $n = 11-19$  from 8 mice). Open circles are raw data with closed circle indicating mean  $\pm$  s.e.m and a horizontal line for the median. In some cases, the error bars representing s.e.m are smaller than the symbol used to show the mean.

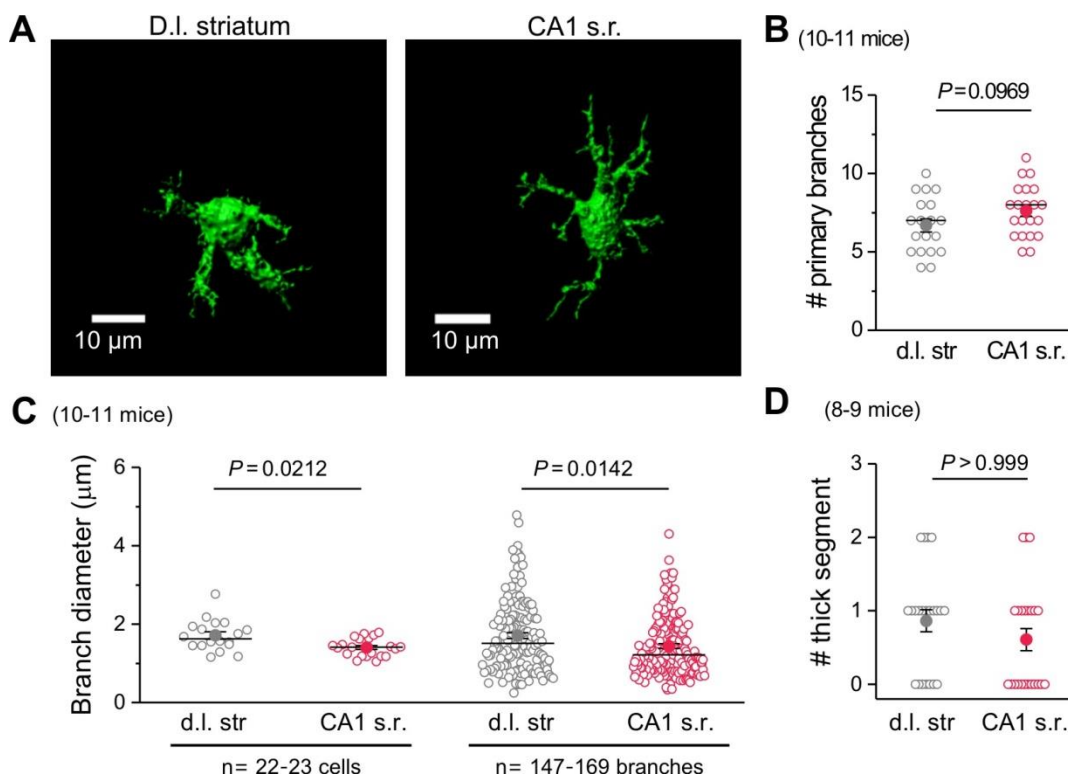


**Figure 5.5: Comparison of striatal and hippocampal astrocyte primary branches.** **A.** 3D reconstructions of somata and primary branches of confocal volumes from **Figure 5.3A**. **B.** The number of primary branches were compared for striatal versus hippocampal astrocytes ( $n = 19-22$  cells from 10-11 mice). **C.** Striatal astrocyte primary branches were thicker than hippocampal ones whether compared as average per cell (*left*) or pooled across all cells (*right*). **D.** The number of thick somatic processes (diameter  $> 3 \mu\text{m}$ ) was compared. Striatal data are shown in grey whereas hippocampal data are in red. Open circles are raw data with closed circle indicating mean  $\pm$  s.e.m and a horizontal line for the median. In some cases, the error bars representing s.e.m are smaller than the symbol used to show the mean.

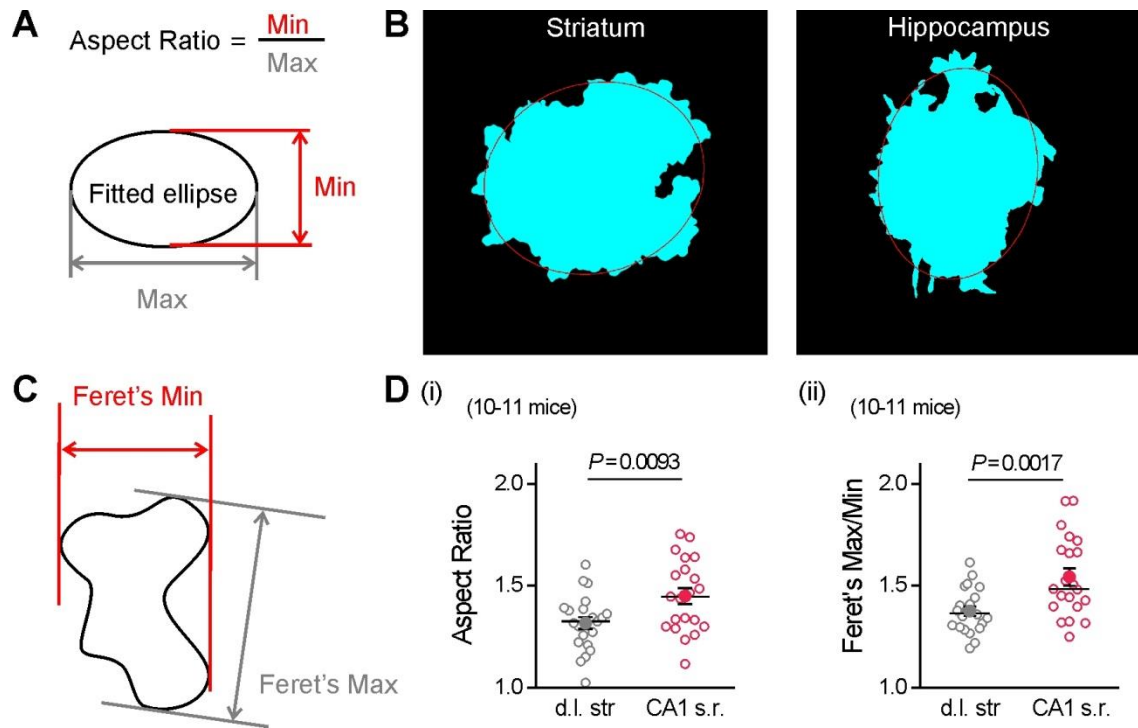


**Figure 5.6: Striatal astrocytes are less elongated compared to hippocampal astrocytes.** The aspect ratio was measured from 2D z-projected astrocyte territories (**A**, **B**, **Di**). Feret's Max/Min were also measured (**C**, **Dii**). Striatal data are shown in grey whereas hippocampal data are in red. Open circles are raw data with closed circle indicating mean  $\pm$  s.e.m and a horizontal line for the median. In some cases, the error bars representing s.e.m are smaller than the symbol used to show the mean.

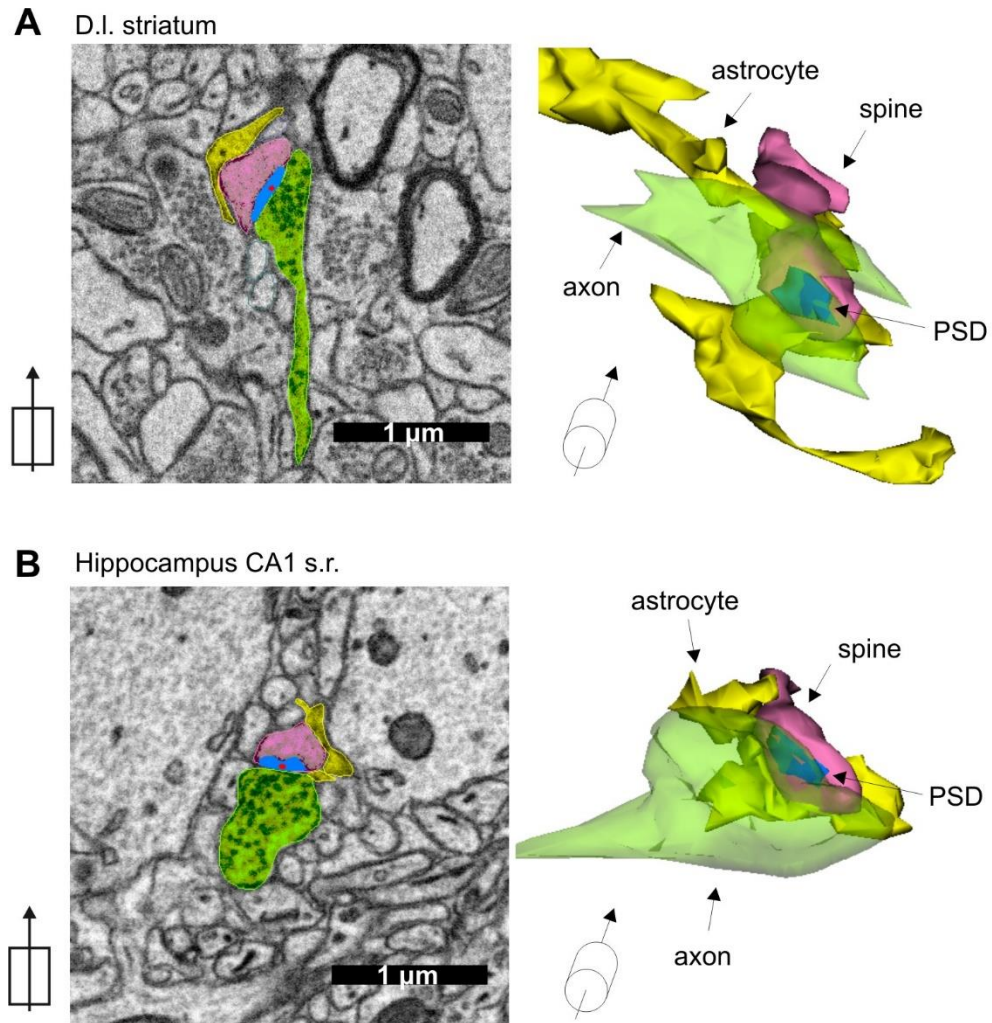


**Figure 5.7: Comparison of striatal and hippocampal astrocyte proximity to synapses. A.** Example of SBF-SEM image (*left*) from the striatum with corresponding 3D rendering (*right*). The synaptic structures and closest astrocyte processes are colored as follows: *yellow* astrocytes, *blue* post-synaptic densities (PSDs), *green* axons, and *pink* spines. The center of the PSD is denoted with a *red* dot. **B.** As in **A**, but for hippocampus.

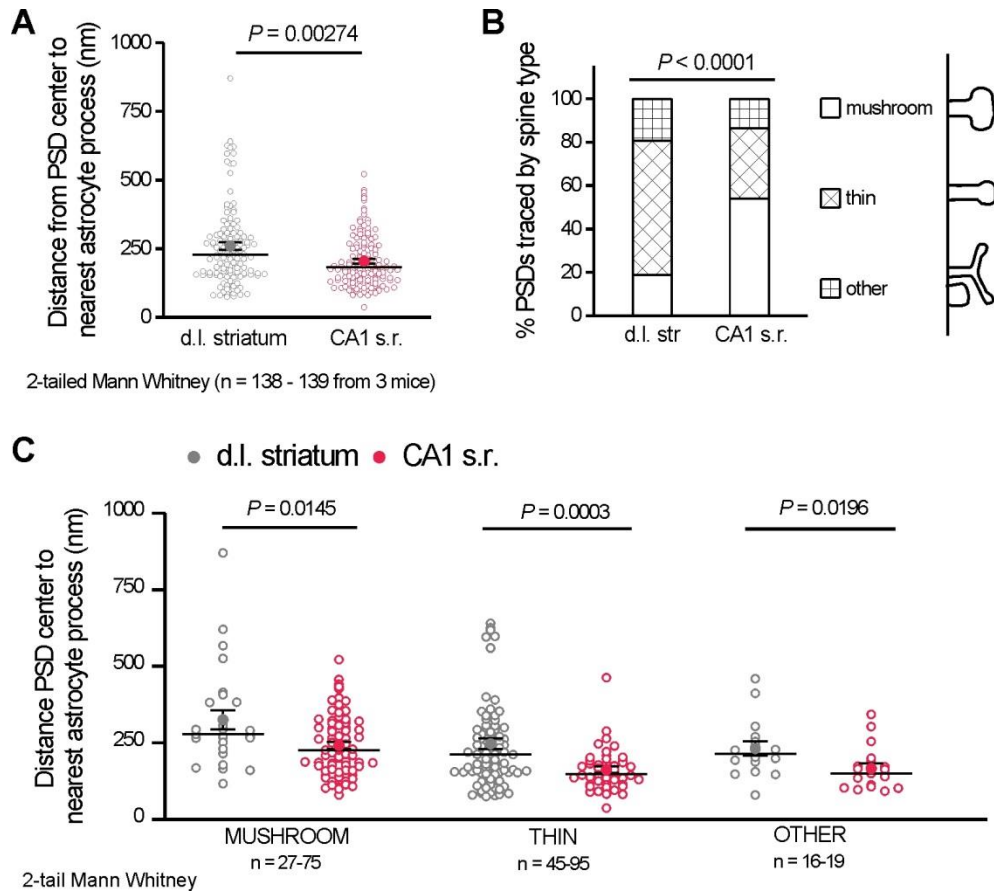
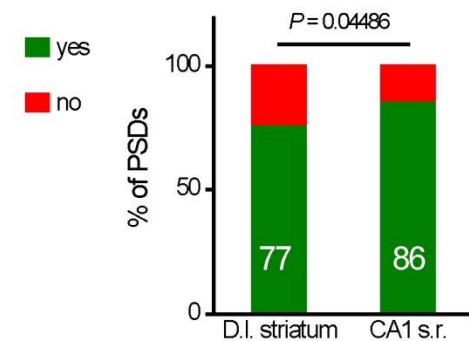


**Figure 5.8: Comparison of striatal and hippocampal astrocyte proximity to synapses. A.**

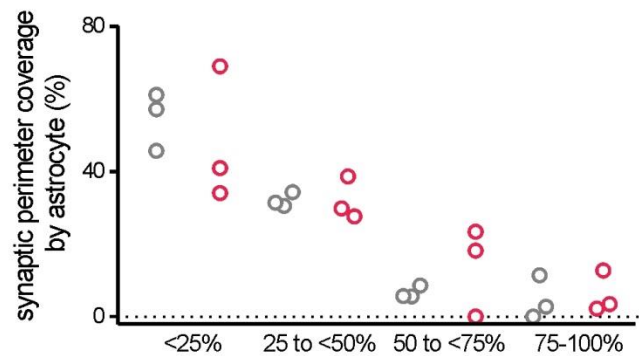
The vector lengths of the shortest straight line from the center of the PSD to the nearest astrocyte process are shown. **B.** The types of excitatory spines were significantly different between striatum and hippocampus (Fisher's test n = 138-139 PSDs from 3 mice). Mushroom, thin, and other (stubby and branched) spines were defined based on conventional electron microscopy criteria as in (Harris et al., 1992) and detailed in the **Chapter 2.16**. **C.** The distances between centers of the PSD and nearest astrocyte process are shown according to the spine type of the PSD. *mushroom* n = 27-75, *thin* n = 45-95, *other* n = 16-19 synapses. Striatal data are shown in grey whereas hippocampal data are in red. Open circles are raw data with closed circle indicating mean  $\pm$  s.e.m and a horizontal line for the median. In some cases, the error bars representing s.e.m are smaller than the symbol used to show the mean.

**A** physical interaction between synaptic interface and astrocyte process



Fisher's test  
n = 138-139 PSDs (3 mice)

**B**



2-way ANOVA  $P = 0.8893$   
n = 29-47 synapses per mouse (3 mice)

**Figure 5.9: Comparison of striatal and hippocampal astrocyte contact with and coverage of synapses.** **A.** A greater proportion of synapses in CA1 s.r. were physically contacted by astrocyte processes as compared to d.l. striatum (Fisher's test n = 138-139 PSDs from 3 mice). **B.** Of the synapses with astrocytic contact, the coverage of the synaptic interface perimeter was classified into quarters.

hippocampal astrocytes were related to synapses (synapse organization and biogenesis, extracellular structure organization and biogenesis) (**Figure 4.8**). The closer physical relationship between hippocampal astrocyte process and excitatory synapses was not due to hippocampal astrocytes having a larger volume as, if anything, striatal astrocytes trended towards larger volumes.

At the level of single cell morphology, striatal astrocytes had larger and more circular territories and thicker primary branches but did not have significantly different cell volumes or number of primary branches (**Figures 5.3, 5.5**). Although similar, the number of primary branches are higher than those previously reported in literature (~4 per astrocyte in either region) using GFAP staining (Garcia et al., 2004). The GFAP staining may have underestimated the number of primary branches as thinner branches are known to not have GFAP (Garcia et al., 2004). With Lucifer-yellow filled astrocytes, finer primary branches (see spread of branch diameter recorded in **Figure 5.4**) were visualized. The morphological complexity captured by dye-filling prevented the use of Sholl analysis to describe branching pattern. We observed numerous branching points moving distally from the astrocyte soma to give rise to branchlets and fine astrocyte leaflets, which makes up more than 95% of the astrocyte volume (**Figure 5.3**; (Shigetomi et al., 2013). Additionally, we observed in both d.l. striatum and CA1 s.r. that astrocyte processes past a branching point sometimes run adjacent to each other. These fine processes potentially are reflexively gap-junction coupled to each other (Genoud et al., 2015). To be able to quantitatively analyze astrocyte branching beyond the first branching point, new algorithms and software must be developed with consideration for these unique morphological features of astrocytes.

Striatal astrocytes do encompass a larger territory volume which contact many more neuronal cell bodies even though the overall astrocyte densities did not differ between the d.l. striatum and CA1 s.r. regions. However, it is possible that the slight trend towards lower striatal

astrocyte density would achieve statistical significance with increased sampled size. This would not be unexpected as astrocytes are thought to tile the central nervous system with little overlap in territory, although this has been only definitively shown for CA1 s.r. (Bushong et al., 2002). We noted no indication that the d.l. striatum would be an exception in our morphological analyses, although admittedly we did not specifically examine astrocyte tiling. The density of excitatory synapses in the rat striatum and hippocampus is  $\sim 0.9$  and  $\sim 2.0$  per  $\mu\text{m}^3$  (Harris et al., 1992; Ingham et al., 1998) implying that single hippocampal CA1 s.r. astrocyte encompasses more excitatory synapses than d.l. striatal astrocyte, based on our territory volumes.

Here, we have shown that astrocytes in the two neural circuits examined differ in partner for neuronal interaction. The d.l. striatum has significantly more neuronal somata to each astrocyte as compared to CA1 s.r. The excitatory synapses of MSNs were mostly thin whereas those of CA1 pyramidal neurons were mostly mushroom. As thin spines are generally considered more plastic than mushroom spines (Bello-Medina et al., 2016; Bourne and Harris, 2007), these findings imply that the striatal circuit may be more dynamic. The finding that spines of CA1 pyramidal neurons are mostly mushroom is in contrast to published work in adult rats where majority of spines were thin (Harris et al., 1992). This could be due to species difference and my exclusion of non-apical dendrites. Nevertheless, it is evident that astrocytes from these two distinct neural circuits exhibit clear morphological differences, which is the focus here.

In this chapter we have presented evidence that striatal and hippocampal astrocytes have morphological differences at cellular and ultrastructural levels. The key finding is that hippocampal astrocyte processes and excitatory synapses share a closer physical relationship. Functional importance cannot be determined from these purely anatomical studies. Therefore, we explored the functional correlate of astrocyte-synapse proximity and many other astrocyte functions in the remaining chapters.

## CHAPTER 6: EXPLORING DIVERSITY OF ASTROCYTE INTRINSIC PROPERTIES

### Section 6.1: Introduction

In this chapter, we begin to explore whether the inter-regional molecular and morphological differences that we have already described are reflected in function. One well-known function of astrocytes is their ability to act as a  $K^+$  sink due to high membrane permeability to  $K^+$  (Kuffler, 1967). Inwardly rectifying  $K^+$  channels, and in particular Kir4.1, are predominantly responsible for  $K^+$  permeability (Tang et al., 2009). Our lab found that in Huntington's disease mice, astrocytes from the striatum displayed larger Kir4.1 currents and marked Kir4.1-deficits whereas those from the hippocampus did not (Tong et al., 2014), thus providing evidence for circuit specific difference in pathology. We sought to determine whether striatal and hippocampal astrocytes exhibit differences in passive membrane properties in the healthy brain.

Astrocytes can modulate neuronal signaling in large volumes of the brain through networks of coupled cells (Giaume et al., 2010; Kang et al., 1998). These networks occur through intercellular gap junctions, which are made up of Connexin 30 and 43 for the most part in astrocytes (Juszczak and Swiergiel, 2009; Nagy et al., 1999; Nagy and Rash, 2000; Nakase and Naus, 2004; Pannasch et al., 2014). Astrocyte networks are known to be involved in the regulation of extracellular glutamate and  $K^+$  levels, thereby affecting neuronal excitability (Nakase and Naus, 2004; Theis et al., 2003). Indeed, astrocyte gap junction networks can pass both beneficial and harmful metabolites after stroke (Li et al., 2014). Hippocampal astrocytes lacking Connexin 43 display a 50% decrease in astrocyte network size with increased spreading depression (Theis et al., 2003). Loss of astrocyte intercellular coupling in the barrel cortex also causes deficits in whisking-based learning (Han et al., 2014). A recent study showed a 50% decrease in astrocyte networks in Connexin 30 knockout mice and reduced synaptic transmission (Pannasch et al., 2014). Hippocampal astrocyte do not exhibit gap-junction

coupling in Connexins 43 and 30 double knockout mice (Pannasch et al., 2011). Electrophysiological evidence suggests functional diversity between the striatum (Adermark and Lovinger, 2008) and hippocampus (Tang et al., 2009; Xu et al., 2009) in the size of gap-junction coupled astrocyte network. However, data directly comparing astrocytes in the striatum and hippocampus do not exist. Meta analyses of data from past studies are beset by the fact that the available studies used different recording conditions, species, and ages (Adermark and Lovinger, 2008; Pannasch et al., 2014; Shigetomi et al., 2008; Theis et al., 2003; Xu et al., 2009). Therefore, we will directly compare striatal and hippocampal astrocyte networks due to gap junction coupling in adult mice and provide the first direct comparison of astrocyte network topography between neural circuits.

## **Section 6.2: Astrocyte membrane properties in d.l. striatum and hippocampus CA1 s.r.**

We used whole-cell patch-clamp electrophysiology to directly compare hippocampal CA1 s.r. and d.l. striatal astrocytes (**Figure 6.1A,B**). We recorded macroscopic current-voltage relations, slope conductances and resting membrane potentials ( $V_m$ ) under control conditions and in the presence of 300  $\mu\text{M}$   $\text{Ba}^{2+}$  to block Kir4.1 channels (**Figures 6.1, 6.2**) that contribute to astrocyte membrane properties (Nwaobi et al., 2016). As expected, astrocytes in both brain regions displayed negative membrane potentials and, unlike neurons, did not fire action potentials upon current injection (**Figure 6.1A,B**; (Barres, 2008; Kuffler and Potter, 1964). The basic membrane properties of astrocytes in the striatum and hippocampus were similar (**Table 6.1**) and  $\text{Ba}^{2+}$  was effective at reducing the membrane conductance and in depolarizing  $V_m$  (**Figures 6.1; 6.2B,C**). However, the  $\text{Ba}^{2+}$ -sensitive currents were larger in the hippocampus than in the striatum at  $V_m$  values with greatest driving force (**Figure 6.2A**). In both brain regions, the  $\text{Ba}^{2+}$ -sensitive currents reversed at -86.5 mV, which is close to the  $\text{K}^+$  equilibrium potential (**Figure 6.2A**).

### Section 6.3: Astrocyte network size in striatum and hippocampus

To visualize networks of intracellularly coupled astrocytes (Giaume et al., 2010). We dialyzed single astrocytes via the patch pipette with biocytin, a gap junction permeable molecule, and *post hoc* assessed the extent of gap-junctional coupling in the hippocampus and striatum using IHC (**Figure 6.3**). Under identical conditions, we found that biocytin spread to ~120 cells in the hippocampus and striatum from a single patched astrocyte in CA1 s.r. and d.l. striatum, respectively (**Figure 6.3B**). In both brain areas, slice pre-incubation with the gap junction blocker carbenoxolone (CBX; 100  $\mu$ M) significantly reduced coupling (**Figure 6.3**). However, in the presence of CBX the extent of remaining gap-junctional coupling was higher in the hippocampus ( $33 \pm 6$  cells) than the striatum ( $11 \pm 6$  cells; **Figure 6.3B**;  $P = 0.0403$ ). This amounts to a 91% reduction in biocytin+ cells in the striatum but only a 71% reduction in the hippocampus. Correspondingly, CBX decreased astrocyte membrane conductance by 50% in d.l. striatum, but only 26% in CA1 s.r. (**Figure 6.4**).

The dye-coupling experiments were done in *Aldh111*-eGFP transgenic mice, which confirmed that the majority of coupled cells are *Aldh111*+ astrocytes (biocytin+ and GFP+) (**Figure 6.5**). A small number of coupled cells (average 11 in striatum and 10 in hippocampus) were not GFP+ (**Figure 6.5B**). Based on soma size and cell shape, these cells were not interneurons. Gap-junction coupling between astrocytes and oligodendrocytes has been documented in several brain regions, including the hippocampus (Griemsmann et al., 2015; Wasseff and Scherer, 2011), so these cells could be oligodendrocytes. Alternatively, these coupled cells could represent *Aldh111*-negative astrocytes.

### Section 6.4: Summary and discussion

Here we have shown significant differences in membrane properties and intercellular communication between astrocytes located in the d.l. striatum and hippocampus CA1 s.r.

Hippocampal astrocytes had larger Ba<sup>2+</sup>-sensitive K<sup>+</sup> currents and had CBX-resistant gap-junctional coupling. This suggests that hippocampal astrocytes have greater K<sup>+</sup> buffering ability as individual cells and as a network. This is consistent with the fact the striatum comprises predominantly GABAergic neurons with hyperpolarized membrane potentials and presumably has a lower requirement for K<sup>+</sup> buffering and dissipation.

The RNA and protein analyses provide potential molecular explanations for these findings. At both RNA and protein level, we found higher expression of *Gja1* (encoding Connexin 43) in hippocampal astrocytes (**Supplemental Excel file 1 Table 2; Figure 4.17**). The higher levels of Connexin 43 in the hippocampus might be related to the greater degree of CBX-resistant gap-junction coupling in that region (**Figure 6.3**). The gene and protein expression of *Kcnj10* (encoding Kir4.1) was not significantly different between the two regions, although expression trended higher in the hippocampus by ~10-15% (**Figure 6.6**). Hence, Kir4.1 expression differences do not satisfactorily explain why hippocampal astrocytes displayed larger Ba<sup>2+</sup>-sensitive currents, although it is feasible that the relationship between RNA, protein and measurement of function is complex.

However, evaluation of all K<sup>+</sup> channel genes identified several candidate K<sup>+</sup> channel genes. We found significant expression (FPKM > 10) for ten K<sup>+</sup> channel genes in either hippocampus or striatum (**Figure 6.6**). Of these, six were differentially expressed (**Figure 6.6**), including another inwardly rectifying K<sup>+</sup> channel Kir5.1 (*Kcnj16*). Hence, hippocampal and striatal astrocytes display remarkable richness in the potential K<sup>+</sup> channels they express, which is consistent with the modest depolarization observed by blocking Kir4.1 (**Figure 6.1**). We suggest that a currently uncharacterized K<sup>+</sup> channel likely contributes markedly to the high resting K<sup>+</sup> conductance of astrocytes and our RNA-Seq data provide potential candidates to explore in these regards in future studies.

In summary, we found significant physiological differences between d.l. striatum and CA1 s.r. astrocytes and, in conjunction with RNA and protein analyses from **Chapter 4**, provide new hypotheses to explore the nature of the large resting  $K^+$  conductance that is a hallmark of astrocytes and gap-junction coupling. These differences add further credence to the hypothesis that astrocyte from striatum and hippocampus are distinct.

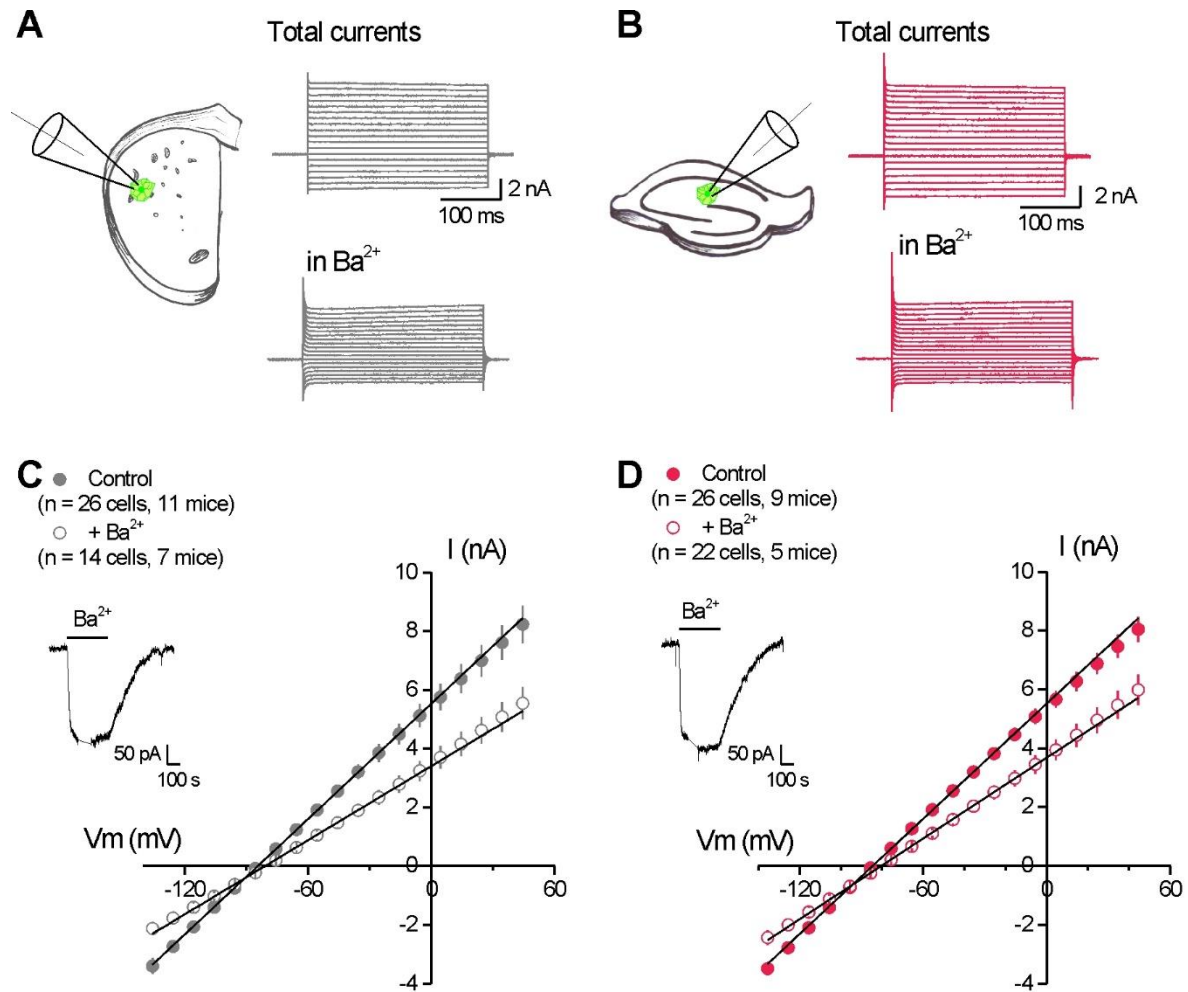


**Figure 6.1: Evaluating astrocyte physiological properties in striatal and hippocampal circuits.** Whole-cell voltage-clamp was performed on d.l. striatal (**A**) and CA1 s.r. (**B**) astrocytes, before and in the presence of 300  $\mu\text{M}$   $\text{Ba}^{2+}$ . Example waveforms are shown for total and  $\text{Ba}^{2+}$ -insensitive currents. **C.** Average current-voltage relations are plotted for striatal astrocytes. *Inset:* Application of  $\text{Ba}^{2+}$  causes a reversible decrease in membrane current at -70 mV; the space is when the recording was paused for voltage jumps. **D.** Same as **C** but for CA1 s.r. astrocytes.

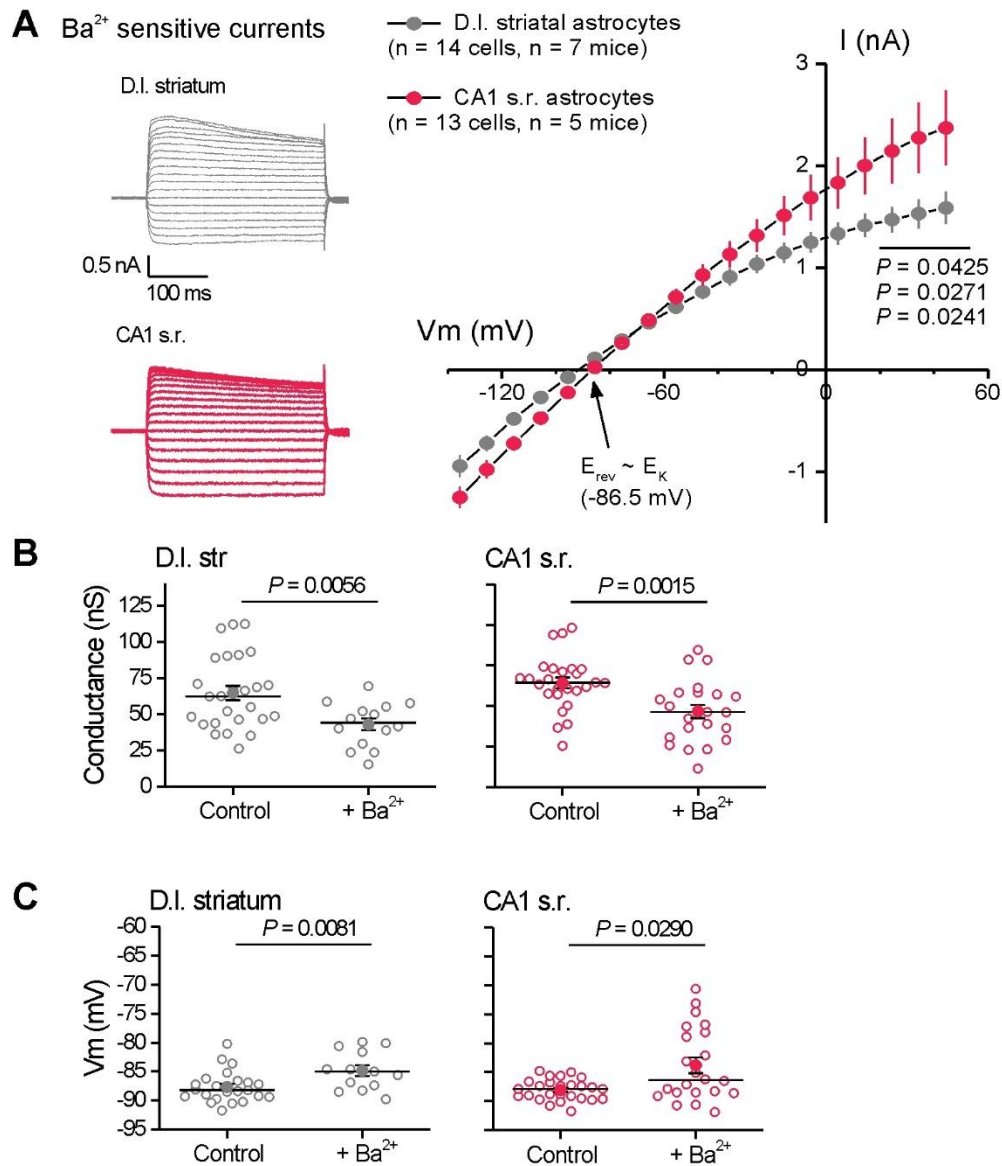


**Figure 6.2: Hippocampal astrocytes have larger  $Ba^{2+}$ -sensitive currents.** **A.** Subtraction of  $Ba^{2+}$ -insensitive currents from total currents reveals  $Ba^{2+}$ -sensitive currents in astrocytes. *Left:* Example waveforms of  $Ba^{2+}$ -sensitive currents. *Right:* The plot of average  $Ba^{2+}$ -sensitive current-voltage relations shows that striatal astrocytes have significantly less  $Ba^{2+}$ -sensitive current at depolarizing voltages. **B & C** Membrane conductance (**B**) and resting membrane potential (**C**) of striatal and hippocampal astrocytes are shown for control conditions and in the presence of 300  $\mu M$   $Ba^{2+}$ .

	<b>Striatal astrocytes</b>	<b>Hippocampal astrocytes</b>	<b>P value</b>	<b># cells (hip, str)</b>	<b># mice (hip, str)</b>
<b>Basic membrane properties</b>					
V <sub>m</sub> (mV)	-88.2 ± 0.6	-88.5 ± 0.3	0.5619	14, 10	5, 6
R <sub>total</sub> (MΩ)	21.3 ± 2.6	18.4 ± 1.3	0.2832	14, 10	5, 6
R <sub>s</sub> (MΩ)	14.7 ± 0.9	13.5 ± 0.9	0.3657	14, 10	5, 6
R <sub>m</sub> = R <sub>total</sub> - R <sub>s</sub> (MΩ)	6.7 ± 1.9	5.1 ± 0.8	0.4119	14, 10	5, 6
Apparent capacitance (pF)	42.6 ± 5.5	35.9 ± 2.8	0.2468	14, 10	5, 6
<b>Macroscopic IVs</b>					
Slope conductance (nS)	64.1 ± 3.3	64.7 ± 4.9	0.9246	14, 10	5, 6
Peak (+60 mV, pA)	6935 ± 547	7339 ± 579	0.6310	14, 10	5, 6
<b>E<sub>rev</sub> (mV)</b>	-84.1 ± 1.1	-85.3 ± 0.4	0.3747	14, 10	5, 6

**Table 6.1: Basic electrophysiological properties of astrocytes.** The measurements were made with identical intra- and extracellular solutions and within 10 min of attaining whole-cell mode. R<sub>s</sub>, R<sub>total</sub>, R<sub>m</sub> and apparent capacitance were calculated from small voltage-jumps (5-10mV) from a holding voltage of -70 mV. The electrode resistance was ~5 MΩ in all cases. The data are reported with the knowledge that the fidelity of voltage-clamp is compromised when R<sub>m</sub> value is not far greater than R<sub>s</sub>, as in the case of astrocytes. By virtue of resting active conductances both striatal and hippocampal astrocytes have low R<sub>m</sub> values and the electrophysiology needs to be interpreted with this in mind. It seems highly unlikely that the elaborate astrocyte processes are voltage-clamped adequately. With these caveats, there were no significant differences between striatal and hippocampal astrocytes. The data were normally distributed and were compared by unpaired Student's *t* tests. Abbreviations: R<sub>m</sub>, resting membrane potential; R<sub>total</sub>, total resistance; R<sub>s</sub>, series resistance; R<sub>m</sub>, membrane resistance; E<sub>rev</sub>, reversal potential.

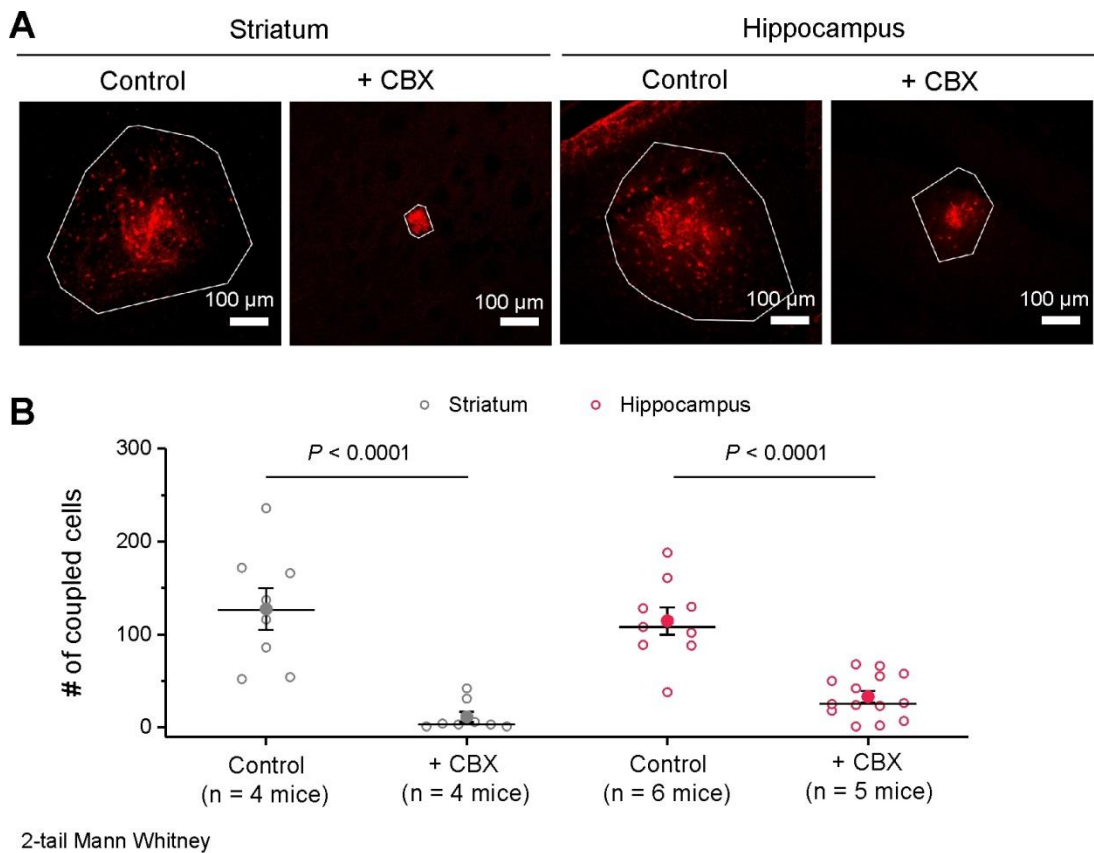


**Figure 6.3: Evaluating astrocyte gap-junction coupled networks. A.** Representative images of patch-loaded biocytin (30 min; red) filled astrocyte syncytium in the striatum and hippocampus with and without 100  $\mu$ M carbenoxolone (CBX) to block gap junctions. The white polygon delineates the extent of dye spread. **B.** The number of coupled cells in control conditions and in the presence of 100  $\mu$ M CBX. Dye coupling in the hippocampus was more resistant to CBX block. Open circles are raw data with closed circle indicating mean  $\pm$  s.e.m and a horizontal line for the median. In some cases, the error bars representing s.e.m are smaller than the symbol used to show the mean.

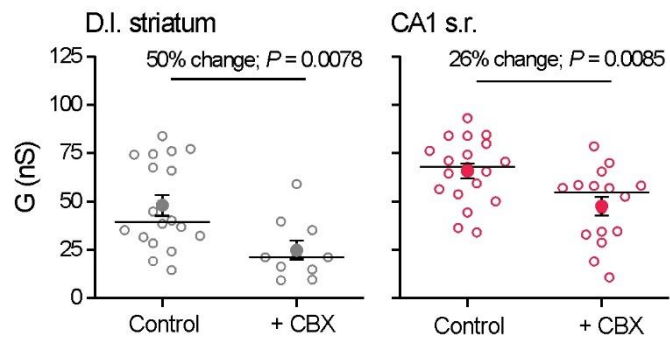


**Figure 6.4: Hippocampal CA1 s.r. astrocyte membrane conductance is less sensitive to CBX.** Striatal data are shown in grey whereas hippocampal data are in red. Open circles are raw data with closed circle indicating mean  $\pm$  s.e.m and a horizontal line for the median.

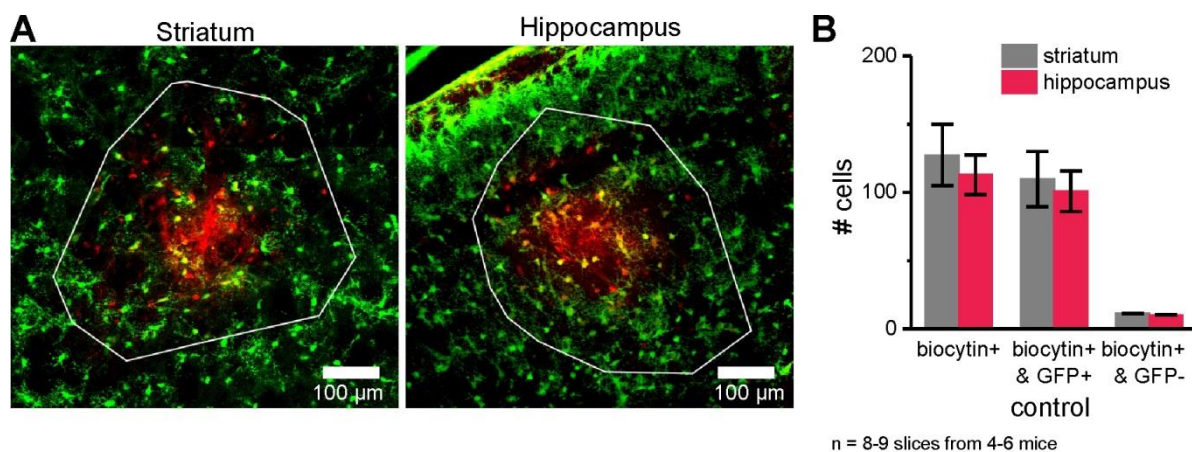


**Figure 6.5: Evaluating astrocyte physiological similarities and differences in striatal and hippocampal circuits.** **A.** Representative images of patch-loaded biocytin (30 min; red) filled astrocyte syncytium in the striatum and hippocampus in *Aldh1l1*-eGFP mice (green). The white polygon delineates the extent of dye spread. These examples correspond to the images in **Figure 6.3A**. **B.** The average number of coupled cells (biocytin+) in control conditions are separated by GFP expression.

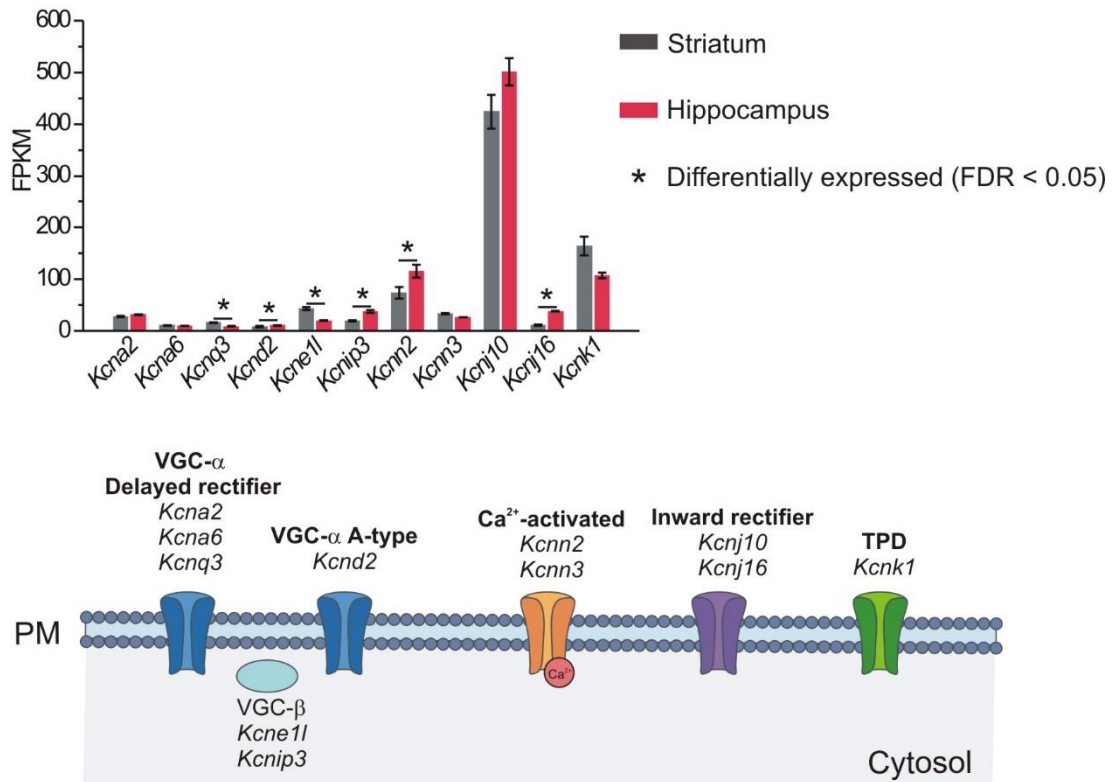


**Figure 6.6: RNA-Seq analyses of K<sup>+</sup> channels in striatal and hippocampal astrocytes.** K<sup>+</sup> channel RNAs that were expressed in astrocytes from striatum or hippocampus with an FPKM > 10. The graph shows FPKM values in striatum and hippocampus and the schematic shows the channel families to which the genes in the graph belong.

## CHAPTER 7: EXPLORING FUNCTIONAL DIVERSITY OF ASTROCYTE CALCIUM SIGNALING

### Section 7.1: Introduction

Although astrocytes do not fire action potentials, they do exhibit spontaneous and evoked intracellular  $\text{Ca}^{2+}$  signals, which are an important aspect of astrocyte biology (Nedergaard et al., 2010; Shigetomi et al., 2016). Astrocytes display spontaneous  $\text{Ca}^{2+}$  signals that are independent of neuronal activity (Nett et al., 2002; Tamura et al., 2014) but also exhibit  $\text{Ca}^{2+}$  elevations in response to strong stimulation of the local neuronal circuit (Haustein et al., 2014; Porter and McCarthy, 1996).

Intracellular  $\text{Ca}^{2+}$  signaling may be utilized by astrocytes to communicate with blood vessels (Otsu et al., 2014; Tong et al., 2013) and integrate local signal during behavior (Halassa and Haydon, 2010; Shigetomi et al., 2016). Cortical astrocytes *in vivo* show  $\text{Ca}^{2+}$  responses with whisker stimulation (Wang et al., 2006), startle (Ding et al., 2013; Srinivasan et al., 2015), and locomotion (Paukert et al., 2014); the latter two appear to be mediated at least in part through norepinephrine acting on  $\alpha 1$  adrenoceptors, a GPCR of the Gq class. In addition to *in vivo* evidence from the cortex, activation of Gq-coupled GPCRs have also been shown to induce intracellular  $\text{Ca}^{2+}$  increase in astroglial cultures (Enkvist et al., 1989) and acute brain slices from cortex, hippocampus, and striatum (Porter and McCarthy, 1995; Srinivasan et al., 2015; Tamura et al., 2014). Activation of Gi/o and Gs GPCRs can also cause intracellular  $\text{Ca}^{2+}$  increase, as seen in hippocampal CA3 stratum lucidum astrocytes in adult mice (Haustein et al., 2014) and VTA and CA1 s.r. astrocytes in young rats (Gould et al., 2014; Kang et al., 1998).

Astrocyte  $\text{Ca}^{2+}$  signals include significant transmembrane contributions and vary in their dependence on  $\text{Ca}^{2+}$  entry and release from intracellular stores (Jackson and Robinson, 2015; Khakh and Sofroniew, 2015; Melom and Littleton, 2013; Shigetomi et al., 2016; Srinivasan et al.,

2015). Although earlier work with IP3R2 knockout mice concluded that spontaneous and GPCR-dependent astrocyte  $\text{Ca}^{2+}$  signals depended entirely on ER  $\text{Ca}^{2+}$  stores (Petraovicz et al., 2014), we and others have shown that these  $\text{Ca}^{2+}$  signals persist even in these knockout animals and could come from a variety of intracellular  $\text{Ca}^{2+}$  sources including non-IP3R2-mediated ER release and from  $\text{Ca}^{2+}$  influx (**Figure 7.1**; (Agarwal et al., 2017; Di Castro et al., 2011; Otsu et al., 2014; Srinivasan et al., 2015).

Astrocytes in different brain regions also display differences in  $\text{Ca}^{2+}$  signaling. Astrocytes in CA1 s.r. exhibit  $\text{Ca}^{2+}$  elevations with minimal stimulation of Schaffer collateral fibers (Panatier et al., 2011) whereas CA3 stratum lucidum do not (Haustein et al., 2014). Activation of mGluR1/5, a Gq-coupled receptor, increases calcium in olfactory glomerular astrocytes (Otsu et al., 2014), but not hippocampal CA3 astrocytes (Haustein et al., 2014). Clearly, astrocytes display rich intracellular  $\text{Ca}^{2+}$  signaling and exploring how these signals differ between neural circuits is critical to understanding their role in neural circuits and behavior.

Astrocyte  $\text{Ca}^{2+}$  signals were first observed in cultured astrocytes using organic  $\text{Ca}^{2+}$  indicator dyes (Cornell-Bell et al., 1990a; Tsien, 1988). The use of organic  $\text{Ca}^{2+}$  indicator dyes in conjunction with preferentially astrocyte-labeling dye sulforhodamin 101 in culture and in acute brain slices has contributed significantly to our current understanding of astrocyte  $\text{Ca}^{2+}$  signals in the context of neuronal activity (Khakh and McCarthy, 2015). The majority of these experiments used bulk loading of membrane-permeable indicators, which does not work well for adult tissue and is restricted largely to the soma, thus missing signaling in finer processes (Khakh and McCarthy, 2015). Intracellular loading of high concentrations of membrane-impermeable indicators can improve visualization of many, but not all of these finer processes. However high concentration of  $\text{Ca}^{2+}$  indicators could alter  $\text{Ca}^{2+}$  signaling and cell function due to potential  $\text{Ca}^{2+}$  buffering by the indicator and dialysis of cellular components (Khakh and McCarthy, 2015). These drawbacks do not invalidate organic  $\text{Ca}^{2+}$  indicator dyes as a useful

tool to study astrocyte  $\text{Ca}^{2+}$  signals. The discovery of intracellular  $\text{Ca}^{2+}$  signals and intercellular  $\text{Ca}^{2+}$  waves and exploration of underlying mechanisms of these phenomenon have all benefited from *in vitro*, *ex vivo*, and *in vivo* use of organic  $\text{Ca}^{2+}$  indicator dyes (Cornell-Bell et al., 1990a; Cornell-Bell et al., 1990b; Hirase et al., 2004; Porter and McCarthy, 1996; Wang et al., 2006).

Genetically encoded calcium indicators (GECIs) have become the standard tool to monitor astrocyte  $\text{Ca}^{2+}$  signals in *ex vivo* and *in vivo* experiments. Perhaps the most popular GECI is the GCaMP series, based on circularly permuted GFP. First introduced in 2001, GCaMP has gone through many permutations to its current generation as GCaMP6 (Akerboom et al., 2012; Chen et al., 2013; Nakai et al., 2001; Tian et al., 2009) and comes in cytosolic and membrane-tethered flavors (Shigetomi et al., 2013; Shigetomi et al., 2010; Srinivasan et al., 2015; Srinivasan et al., 2016). GCaMP6 binds and unbinds  $\text{Ca}^{2+}$  as quickly as organic  $\text{Ca}^{2+}$  indicator dyes (Chen et al., 2013). Our lab and others have expressed GECIs in astrocytes *in vivo* using AAVs and transgenic mice (as in **Chapter 3**) to study astrocyte  $\text{Ca}^{2+}$  signals *in vivo* and *ex vivo* in acute brain slices. Importantly, GECIs and other reporters can be selectively delivered to astrocytes using AAVs without detectable astrogliosis (**Figure 7.2**; (Haustein et al., 2014; Jiang et al., 2016; Rungta et al., 2016; Shigetomi et al., 2013). Using AAV delivery of cytosolic GCaMP6f (**Figure 2.2B**), we compared several aspects of  $\text{Ca}^{2+}$  signaling between striatal and hippocampal astrocytes, to determine if astrocytes differed in these regards.

## **Chapter 7.2: Astrocyte spontaneous $\text{Ca}^{2+}$ signaling in d.l. striatum and CA1 s.r.**

Spontaneous  $\text{Ca}^{2+}$  signal frequency *per se* was higher in the hippocampus than striatum under control conditions ( $P = 0.0469$ ; **Figure 7.3, 7.4; Table 7.1**), in TTX ( $P = 0.0165$ ), and in  $\text{Ca}^{2+}$ -free ( $P = 0.0228$ ; **Figure 7.3, 7.4**). To determine the contribution of neuronal activity to spontaneous astrocyte  $\text{Ca}^{2+}$  signals, we applied 250 nM tetrodotoxin (TTX) to block action

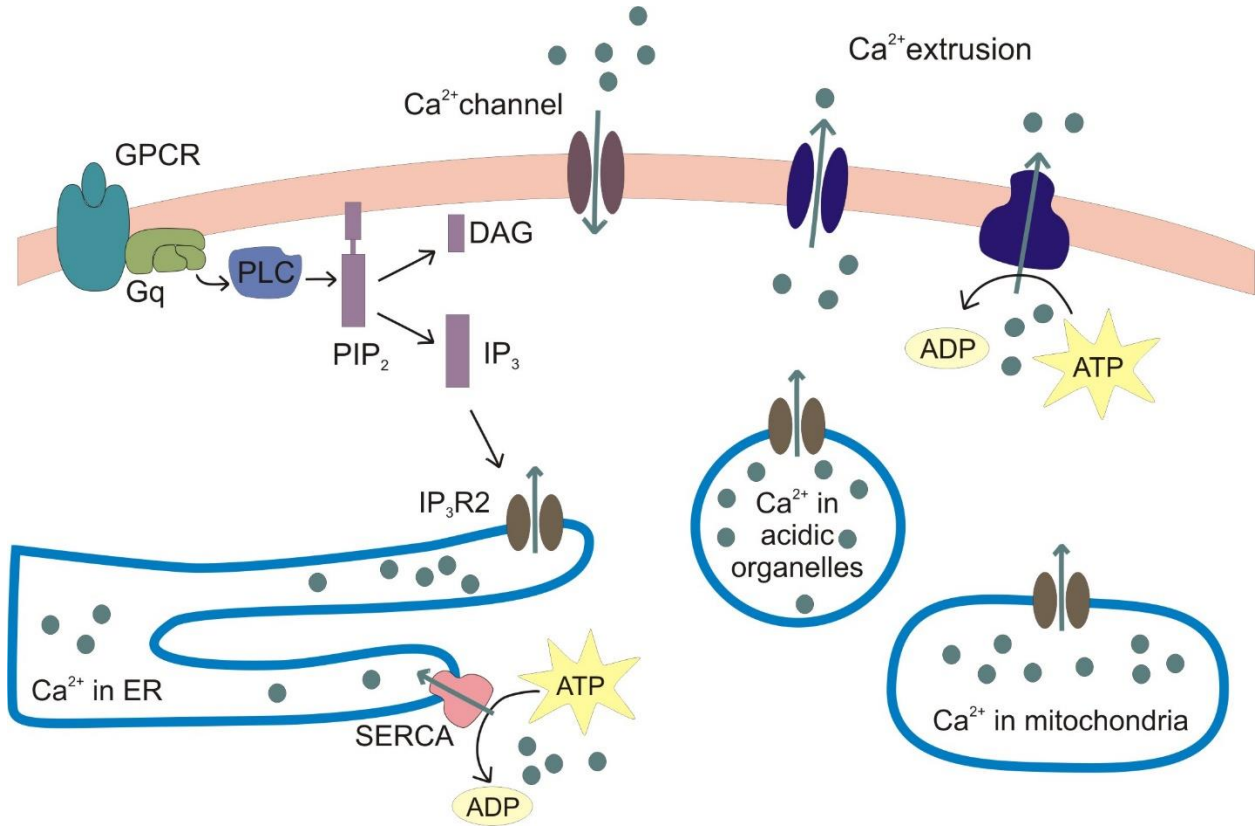


**Figure 7.1: The canonical Gq-coupled GPCR mediated intracellular calcium increase.**

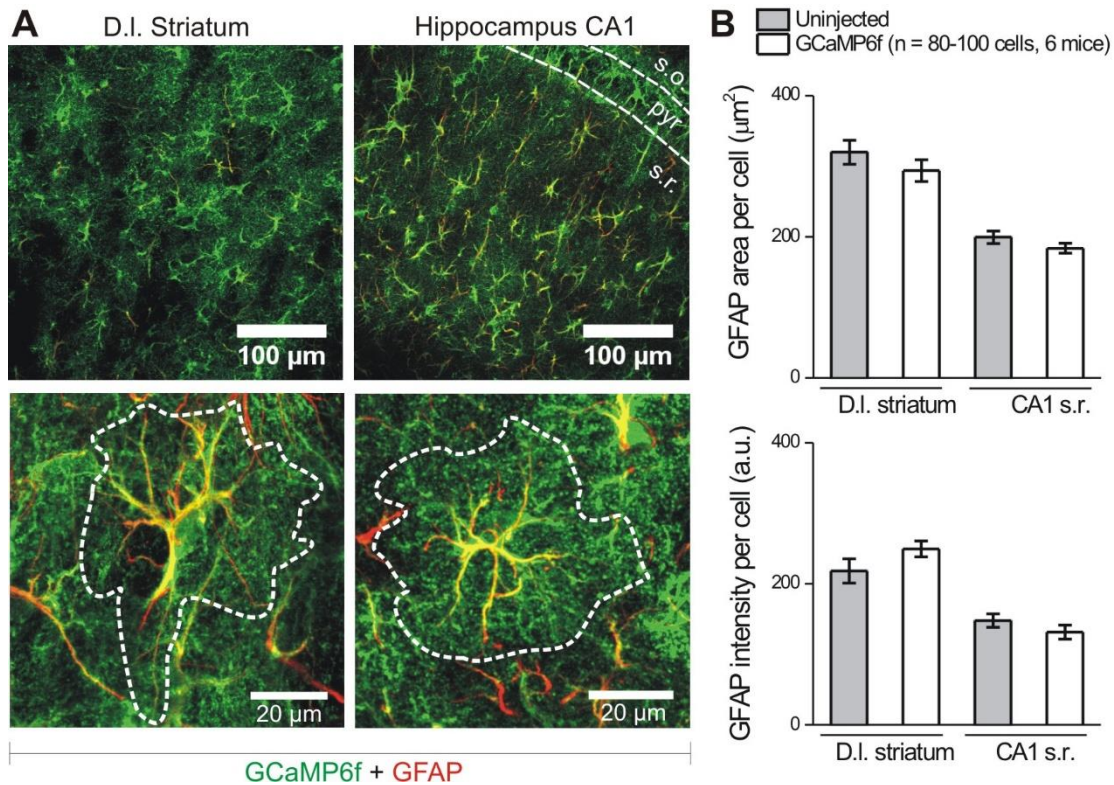


**Figure 7.2: Intracranial injection of AAV2/5 GfaABC<sub>1</sub>D-GCaMP6f into striatum and hippocampus robustly expresses GCaMP6f in astrocytes with no overt reactivity. A.** A schematic of the AAV2/5 showing GCaMP6f driven by the GfaABC<sub>1</sub>D promoter. **B.** Representative images showing GCaMP6f and GFAP in sections from Swiss-Webster mice two to three weeks after virus injection. *Top:* Many astrocytes in both the striatum and hippocampus expressed GCaMP6f (s.o. stratum oriens, pyr pyramidal cells layer, s.r. stratum radiatum). *Bottom:* Zoomed in images show astrocytes expressed GCaMP6f throughout their entire territory, as delineated approximately by the dashed line. GFAP expression was more confined to the soma and primary branches. **C.** Neither astrocyte GFAP area (*top*) nor GFAP intensity (*bottom*) increased detectable with AAV2/5 mediated GCaMP6f expression (n = 80-100 cells from 6 animals). Bars are mean  $\pm$  s.e.m.

potentials (APs). As is evident from the traces and the pooled data, TTX did not decrease the frequency of astrocyte  $\text{Ca}^{2+}$  signals in somata, branches, or microdomains in either brain region (**Figures 7.3, 7.4**), nor did it decrease their amplitude or duration (**Table 7.1**). Hence, in adult mice, astrocyte spontaneous  $\text{Ca}^{2+}$  signals are not caused by ongoing AP-dependent neuron-astrocyte interactions.

To determine whether  $\text{Ca}^{2+}$  signals in the striatum and hippocampus vary in their dependence on  $\text{Ca}^{2+}$  entry, we applied  $\text{Ca}^{2+}$  free extracellular buffers. The example traces and pooled data show dramatic reductions in the frequency of spontaneous  $\text{Ca}^{2+}$  signals in all compartments for both striatal and hippocampal astrocytes (**Figures 7.3, 7.4**). The effect of  $\text{Ca}^{2+}$  free buffers was equivalent between the striatum and hippocampus, indicating similar dependence on  $\text{Ca}^{2+}$  entry for frequency of spontaneous signals (**Figure 7.4**).

We examined the somatic events more closely and classified them as global events that encompassed the entire soma and some major branches or as non-global events that included only a sub region (**Figure 7.5**). In control conditions, a significantly greater proportion of somatic events in hippocampal astrocytes were global events (**Figure 7.5**;  $P = 0.0052$ ). Although the frequency of somatic events decreased significantly with removal of extracellular  $\text{Ca}^{2+}$  (**Figures 7.3, 7.4**), global events were relatively spared in  $\text{Ca}^{2+}$ -free, indicating an intracellular origin (**Figure 7.5**). Of note, the inter-regional difference remained significant in  $\text{Ca}^{2+}$ -free buffers (**Figure 7.5**,  $P = 0.032$ ). Hence, both hippocampal and striatal astrocytes display spontaneous  $\text{Ca}^{2+}$  signals, but with some substantial differences.

### **Section 7.3: Astrocyte $\text{Ca}^{2+}$ homeostasis in d.l. striatum and CA1 s.r.**

We assessed  $\text{Ca}^{2+}$  homeostasis more carefully in striatal and hippocampal astrocytes by using standard ER store-depletion protocols (**Figure 7.6**). Astrocytes from the striatum relied

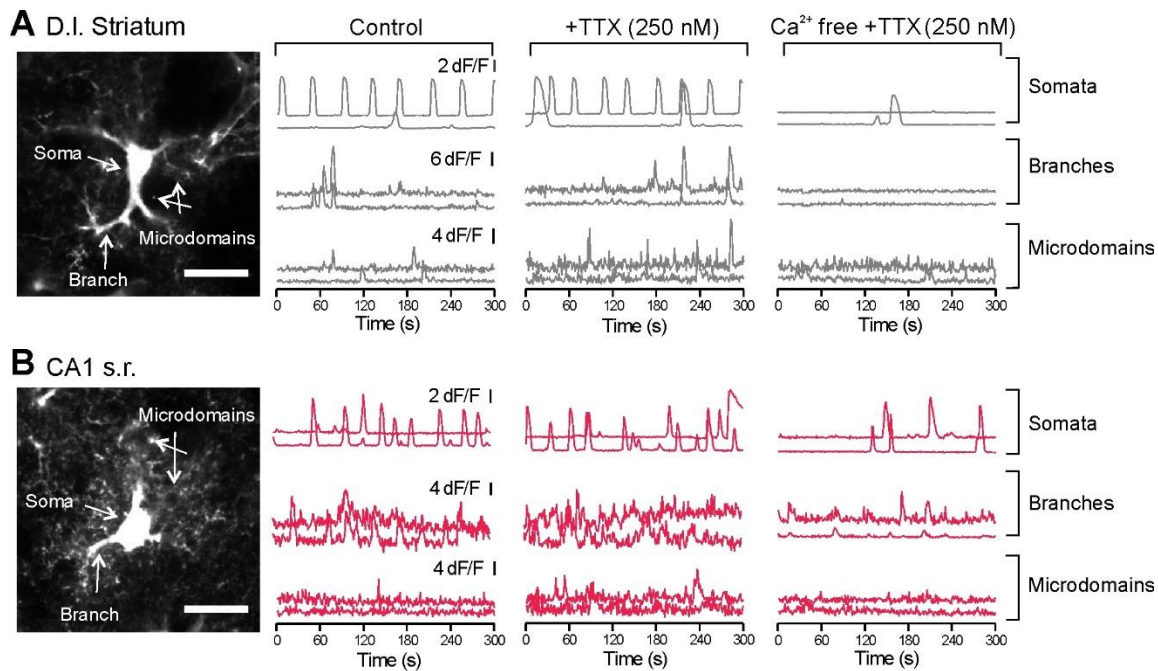


**Figure 7.3: Spontaneous Ca<sup>2+</sup> signals in striatal and hippocampal astrocytes.** *Left:* Time series projection of GCaMP6f expressing striatal (**A**) and hippocampal (**B**) astrocytes with arrows indicating three compartments with Ca<sup>2+</sup> signals: somata, branches, and microdomains. *Right:* Representative traces of GCaMP6f dF/F are shown for control conditions, in the presence of 0.25  $\mu$ M tetrodotoxin (TTX), and in nominally Ca<sup>2+</sup> free extracellular recording buffer (Ca<sup>2+</sup> free) with TTX. Ca<sup>2+</sup> free buffer reduced frequency of astrocyte Ca<sup>2+</sup> signals in all three compartments in both brain regions (average data reported in the text and in **Table 7.1**).

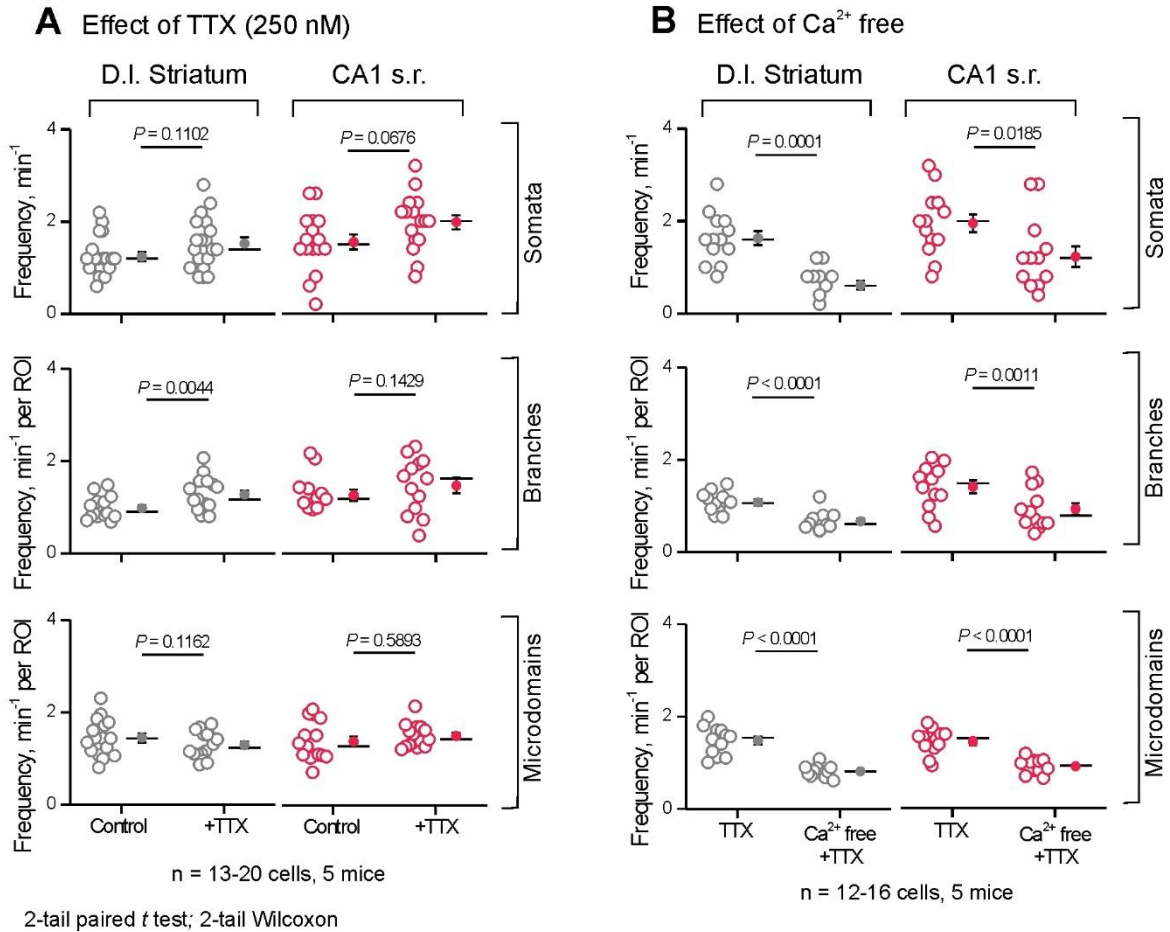


**Fig 7.4: Properties of  $\text{Ca}^{2+}$  signals in striatal and hippocampal astrocytes. A.** The frequencies of  $\text{Ca}^{2+}$  signals in somata, branches, and microdomains in control conditions and with  $0.25 \mu\text{M}$  TTX were compared. Open circles represent raw data with closed circle indicating mean  $\pm$  s.e.m. **B.** The frequencies of  $\text{Ca}^{2+}$  signals in somata, branches, and microdomains in TTX and in  $\text{Ca}^{2+}$ -free conditions were compared. Open circles represent raw data with closed circle indicating mean  $\pm$  s.e.m

	Frequency (min <sup>-1</sup> )		Amplitude (dF/F)		Half-width (s)	
	Control	+ TTX	Control	+ TTX	Control	+ TTX
Striatum						
Somata	1.24 ± 0.10 <sup>1</sup>	1.53 ± 0.12 <sup>2</sup>	0.94 ± 0.26 <sup>1</sup>	1.17 ± 0.29 <sup>2</sup>	4.32 ± 0.56 <sup>2</sup>	4.30 ± 0.43 <sup>1</sup>
Branches	0.98 ± 0.06 <sup>2</sup>	1.27 ± 0.09 <sup>2</sup>	1.19 ± 0.10 <sup>2</sup>	1.18 ± 0.16 <sup>2</sup>	2.56 ± 0.13 <sup>2</sup>	3.20 ± 0.16 <sup>2</sup>
Microdomains	1.45 ± 0.10 <sup>2</sup>	1.29 ± 0.07 <sup>2</sup>	1.18 ± 0.08 <sup>1</sup>	1.18 ± 0.13 <sup>2</sup>	1.66 ± 0.09 <sup>2</sup>	1.68 ± 0.15 <sup>1</sup>
Hippocampus						
Somata	1.72 ± 0.23 <sup>2</sup>	2.10 ± 0.16 <sup>2</sup>	1.53 ± 0.33 <sup>1</sup>	1.43 ± 0.26 <sup>2</sup>	3.31 ± 0.40 <sup>1</sup>	3.49 ± 0.47 <sup>1</sup>
Branches	1.26 ± 0.12 <sup>2</sup>	1.47 ± 0.17 <sup>2</sup>	1.76 ± 0.17 <sup>2</sup>	1.57 ± 0.18 <sup>1</sup>	2.35 ± 0.10 <sup>2</sup>	3.03 ± 0.15 <sup>2</sup>
Microdomains	1.41 ± 0.12 <sup>2</sup>	1.48 ± 0.07 <sup>2</sup>	2.10 ± 0.19 <sup>2</sup>	1.48 ± 0.10 <sup>2</sup>	1.67 ± 0.08 <sup>2</sup>	1.45 ± 0.11 <sup>2</sup>

**Table 7.1: Spontaneous astrocyte Ca<sup>2+</sup> signals are not dependent on action potentials.**

Blocking APs with 250 nM TTX did not prevent spontaneous astrocyte Ca<sup>2+</sup> signals. We also compared control frequency, amplitude, and half-width between striatal and hippocampal astrocyte calcium signals in control conditions. Ca<sup>2+</sup> signals were more frequent in hippocampal astrocyte somata and branches and had higher amplitude in all three compartments in hippocampal astrocytes compared to their striatal counterparts. Data from each cell were pooled and averaged (n = 13-19 cells from 5-7 mice). Key to table: All numbers reported are mean ± s.e.m. <sup>1</sup>non-Gaussian distribution. <sup>2</sup>normal distribution. Unpaired 2-tailed Mann-Whitney or unpaired 2-tail *t* test with Welch correction was used to compare between brain regions. Wilcoxon matched-pair test or paired 2-tail *t* test was used to analyze effect of TTX.

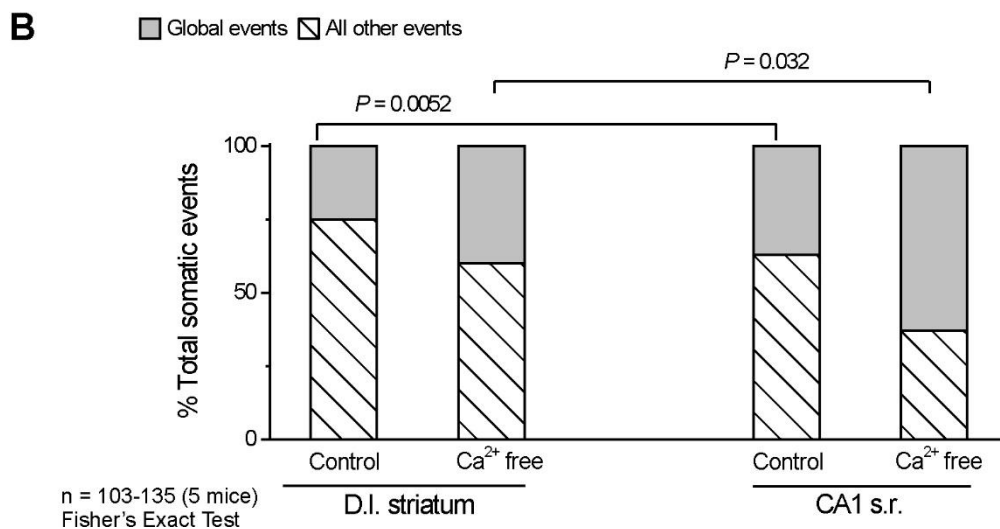
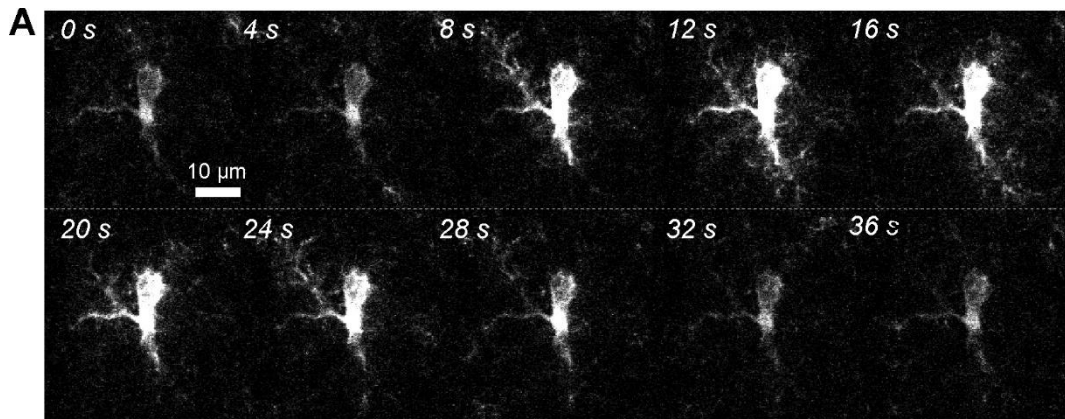


**Figure 7.5: Characterization of somatic events.** **A.** Kymographs shows a global wave over time (sec). **B.** The proportion of global and non-global somatic events in control and Ca<sup>2+</sup>-free (with 0.25 μM TTX) conditions were compared between striatum and hippocampus astrocytes (n = 13-17 cells from 5 animals; Fisher's test).

more heavily on extracellular entry for basal  $\text{Ca}^{2+}$  levels than astrocytes from the hippocampus as determined by measuring the drop in baseline after transitioning to  $\text{Ca}^{2+}$ -free extracellular buffer (**Figures 7.6, 7.7**). Other aspects such as the size of  $\text{Ca}^{2+}$  stores, the rate of  $\text{Ca}^{2+}$  extrusion, and store-depletion mediated  $\text{Ca}^{2+}$  influx were similar ( $P > 0.05$  in each case).

#### **Section 7.4: Astrocyte evoked $\text{Ca}^{2+}$ signaling in d.l. striatum and CA1 s.r.**

We assessed AP-dependent evoked astrocyte  $\text{Ca}^{2+}$  signals in striatal and hippocampal astrocytes following electrical field stimulation (EFS) of cortical and Schaffer-collateral inputs, respectively (**Figure 7.8**). In accord with recent studies (Haustein et al., 2014; Jiang et al., 2016; Tang et al., 2015) we found that striatal and hippocampal astrocytes responded equally weakly to EFS of glutamatergic input during brief trains of EFS (4 APs at 10 Hz; **Figure 7.8**). Hippocampal astrocytes responded more reliably to longer trains (40 APs at 10 Hz), but striatal astrocytes did not (**Figure 7.8**). Astrocytes in both areas responded strongly to bath application of the  $\alpha_1$  adrenoceptor agonist phenylephrine (10  $\mu\text{M}$ ; **Figure 7.8B**) and therefore capable of responding to stimuli with robust intracellular calcium increase.

#### **Section 7.5: Astrocyte GPCR mediated $\text{Ca}^{2+}$ signaling in d.l. striatum and CA1 s.r.**

Astrocytes are replete with Gq-, Gi/o- and Gs-coupled GPCRs that may mediate  $\text{Ca}^{2+}$  signals when activated. We thus explored if striatal and hippocampal astrocytes differed in the ability of GPCR pathways to evoke  $\text{Ca}^{2+}$  signals (we performed the experiments in the presence of 250 nM TTX to reduce effects on neurons). We began by using Designer Receptors Exclusively Activated by Designer Drugs (DREADDs) expressed in astrocytes (**Figure 7.9**) to selectively stimulate GPCR Gq, Gs and Gi pathways with hM3D, rM3D and hM4D DREADDs, respectively (Roth, 2016). Each of these receptors was activated by clozapine-N-oxide

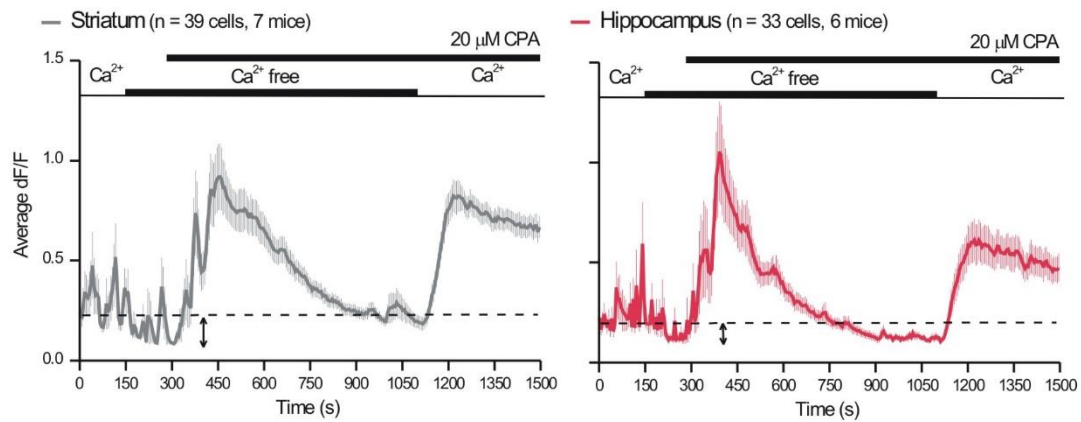
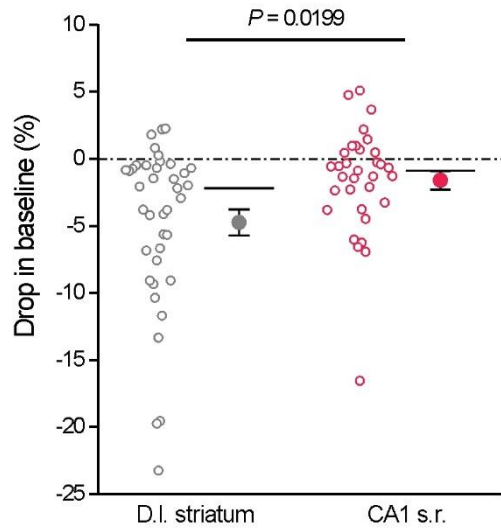


**Figure 7.6: Average GCaMP6f dF/F trace with s.e.m. of striatal and hippocampal astrocytes.** Dashed line indicates the baseline whereas the arrow indicates the drop in baseline with Ca<sup>2+</sup>-free buffer (see **Fig 7.7** for quantification per cell). 0.25 μM TTX was present throughout this experiment (n = 33-39 cells from 6-7 animals). CPA = cyclopiazonic acid.



2-tail Mann Whitney (n = 33-39; 6-7 mice)

**Figure 7.7: The drop in baseline  $\text{Ca}^{2+}$  levels from normal  $\text{Ca}^{2+}$  to  $\text{Ca}^{2+}$ -free conditions for both regions.** Open circles represent raw data with closed circle indicating mean  $\pm$  s.e.m and a line for the median.  $0.25 \mu\text{M}$  TTX was present throughout this experiment (n = 33-39 cells from 6-7 animals). CPA = cyclopiazonic acid.

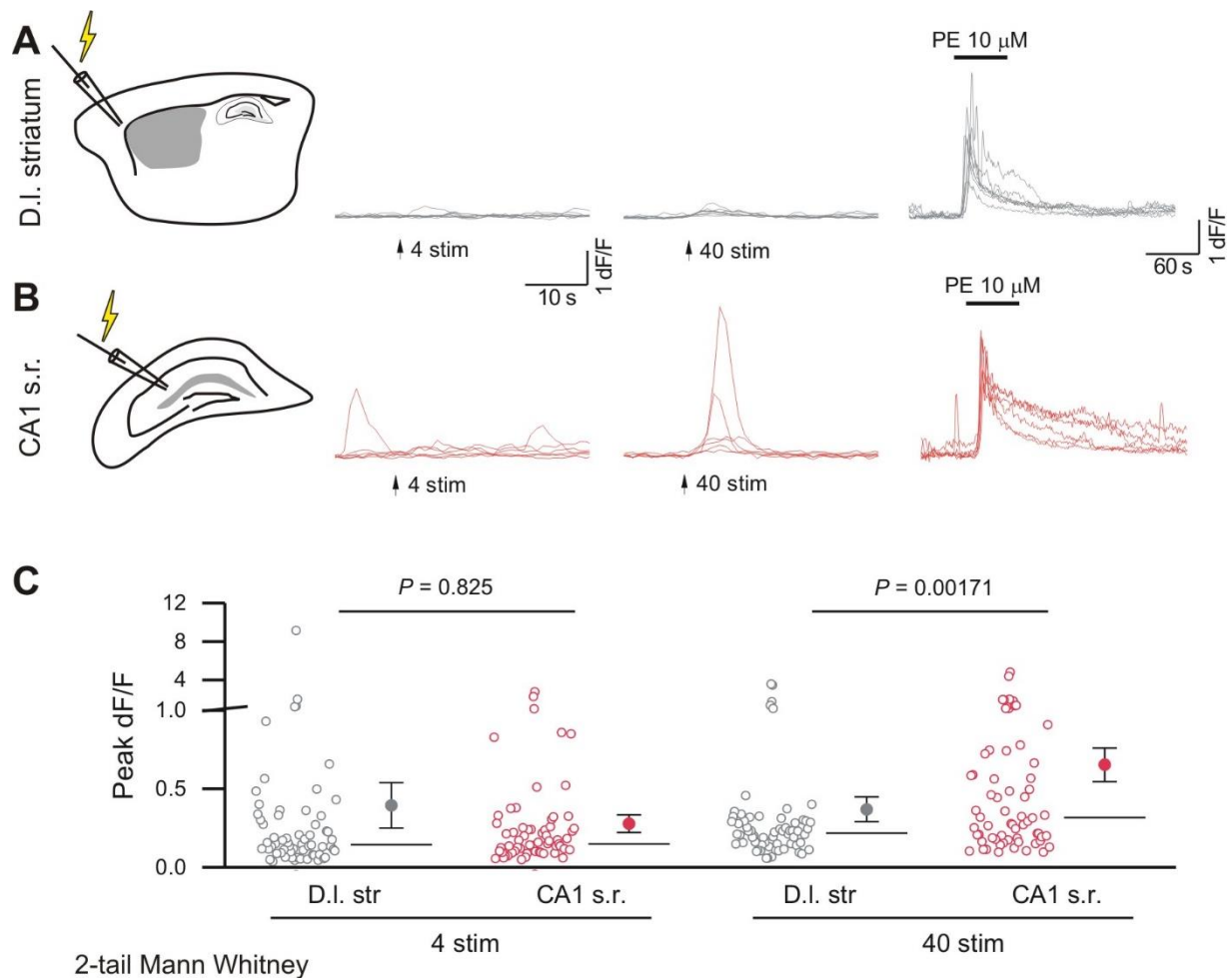


**Figure 7.8: Action potential-dependent evoked astrocyte  $\text{Ca}^{2+}$  signals.** **A-B.** EFS of cortical input to the striatum (**A**) and EFS of Schaffer-collaterals in the hippocampus (**B**) evoked similar, but modest  $\text{Ca}^{2+}$  signals. In the same cells, phenylephrine (PE) evoked large astrocyte  $\text{Ca}^{2+}$  elevations. **C.** Peak dF/F within 10 seconds after stimulation for all cells. Open circles represent raw data with closed circle indicating mean  $\pm$  s.e.m and a line for the median.

(CNO; 1  $\mu$ M). In astrocytes expressing hM3D, CNO evoked robust increases in intracellular  $\text{Ca}^{2+}$  in hippocampal and striatal astrocyte somata and processes (**Figures 7.9, 7.10**). Activation of rM3D and hM4D with CNO also increased  $\text{Ca}^{2+}$  in striatal astrocytes, but the effects of activating  $G_s$  or  $G_i$  DREADDs were much smaller in hippocampal astrocytes (**Figures 7.9, 7.10**). The similarities between activating hM3D for striatal and hippocampal astrocytes, and the marked differences between activating rM3D and hM4D for eliciting  $\text{Ca}^{2+}$  signals in astrocytes from these two regions were evident from the kymographs (**Figure 7.9**). In order to quantify these data, we plotted the integrated GCaMP6f fluorescence (area under the curve; AUC) before and during CNO application (see **Chapter 2.10** for detailed methods; **Figures 7.10**). The quantification shows that activating  $G_i$ -coupled hM4D did not significantly increase  $\text{Ca}^{2+}$  in hippocampal astrocyte somata or processes (**Figure 7.10**). To account for differences in baseline spontaneous  $\text{Ca}^{2+}$  signals (**Table 7.1**), we compared CNO-evoked fold-change in GCaMP6f fluorescence to compare between striatal and hippocampal astrocytes (**Figure 7.11**). This confirmed statistically that activating rM3D and hM4D elicits greater  $\text{Ca}^{2+}$  signals in striatal astrocytes.

Since  $G_i$ -coupled hM4D  $\text{Ca}^{2+}$  responses exhibited the greatest difference between striatal and hippocampal astrocytes, we examined the downstream effects of this functional difference on gene expression. To do this, we activated striatal and hippocampal astrocytes expressing hM4D *in vivo* with CNO (1 mg/kg) and examined levels of c-Fos, an immediate early gene, after one hour (**Figure 7.12**). Activation of hM4D caused an increase in the number of c-Fos expressing astrocytes in both striatum and hippocampus (**Figure 7.12**). However, in astrocytes with c-Fos, activation of hM4D caused a greater increase in c-Fos levels in striatal astrocytes when compared to hippocampal astrocytes (6-fold for striatum *versus* 2-fold for hippocampus; **Figure 7.12**). Thus, the differences between hippocampal and striatal astrocytes

in terms of Gi-coupled GPCR signaling may be reflected as differences in gene expression regulation.

Next, we tested whether  $\text{Ca}^{2+}$  signals evoked by activation of endogenous GPCRs were different between striatal and hippocampal astrocytes by measuring agonist-evoked fold-change in GCaMP6f fluorescence. Consistent with past work,  $\alpha_1$  adrenoceptor agonist phenylephrine (10  $\mu\text{M}$ ) evoked similarly robust increases in striatal and hippocampal astrocyte  $\text{Ca}^{2+}$  in somata and branches (**Figures 7.13-7.16**). ATP (100  $\mu\text{M}$ ) also evoked robust increases in astrocyte  $\text{Ca}^{2+}$  in both brain regions (**Figures 7.14-7.16**). However, response to 100  $\mu\text{M}$  DHPG, the agonist for mGluR1/5 receptors, was very weak in both regions, consistent with the finding that this receptor is downregulated in adult astrocytes (Haustein et al., 2014; Srinivasan et al., 2016; Sun et al., 2013). We also tested Gi/o-coupled mGluR2/3 agonist LY354740, and measured robust  $\text{Ca}^{2+}$  response in striatal somata and processes, but no significant response for hippocampal s.r. astrocytes (**Figures 7.13-7.16**), which extends the hM4D DREADD data (**Figures 7.9-7.11**). However, activation of Gi/o-coupled GABA<sub>B</sub> GPCRs (50  $\mu\text{M}$  R-baclofen) evoked similar, weak responses in striatal and hippocampal astrocyte somatic  $\text{Ca}^{2+}$  signals (**Figures 7.14, 7.16**). The striatum receives strong dopaminergic input from the ventral tegmental area and the substantia nigra pars compacta; however, we observed at most weak responses to activation of Gs-coupled D<sub>1/5</sub> receptors and Gi/o-coupled D<sub>2</sub> and D<sub>3</sub> receptors (by 10  $\mu\text{M}$  A77636, 10  $\mu\text{M}$  sumanirole, and 50  $\mu\text{M}$  PD128907) in striatal astrocytes (**Figures 7.14, 7.15**). Hippocampal astrocytes showed a similarly weak response (**Figures 7.14-7.16**).

## **Section 7.6: Summary and discussion**

There are many similarities and differences in astrocyte  $\text{Ca}^{2+}$  signaling between d.l. striatum and hippocampus CA1 s.r. These experiments reveal that striatal astrocyte cytosolic  $\text{Ca}^{2+}$  levels rely more heavily on extracellular calcium entry. Given the finding that global waves

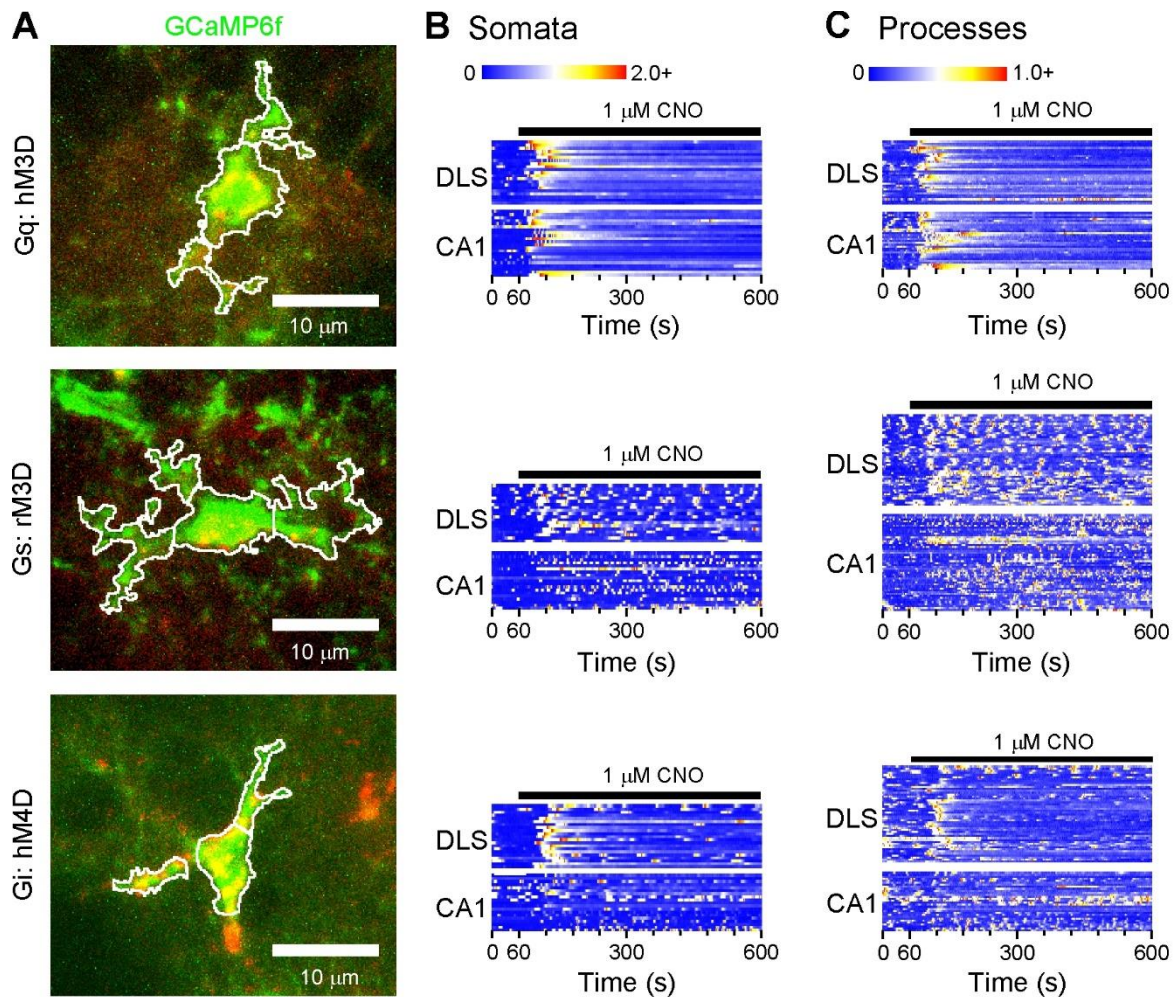


**Figure 7.9: Striatal and hippocampal astrocytes differ in GPCR mediated  $\text{Ca}^{2+}$  responses.**

**A.** Example images of astrocytes co-expressing GCaMP6f (green) and each of the three mCherry-tagged DREADDs (red) from appropriately AAV2/5 injected mice. Somata and process ROIs are outlined in white. **B.** Kymographs of astrocyte somatic  $\text{Ca}^{2+}$  signals (GCaMP6f dF/F) upon activation of different DREADDs with 1  $\mu\text{M}$  clozapine-N-oxide (CNO) at 1 min. Each row represents a single cell ( $n = 15-21$  cells from 3-5 mice). **C.** Kymographs of astrocyte processes  $\text{Ca}^{2+}$  signals (GCaMP6f dF/F) upon activation of different DREADDs with 1  $\mu\text{M}$  CNO at 1 min. Each row represents a single branch ( $n = 29-49$  processes from 3-5 mice).

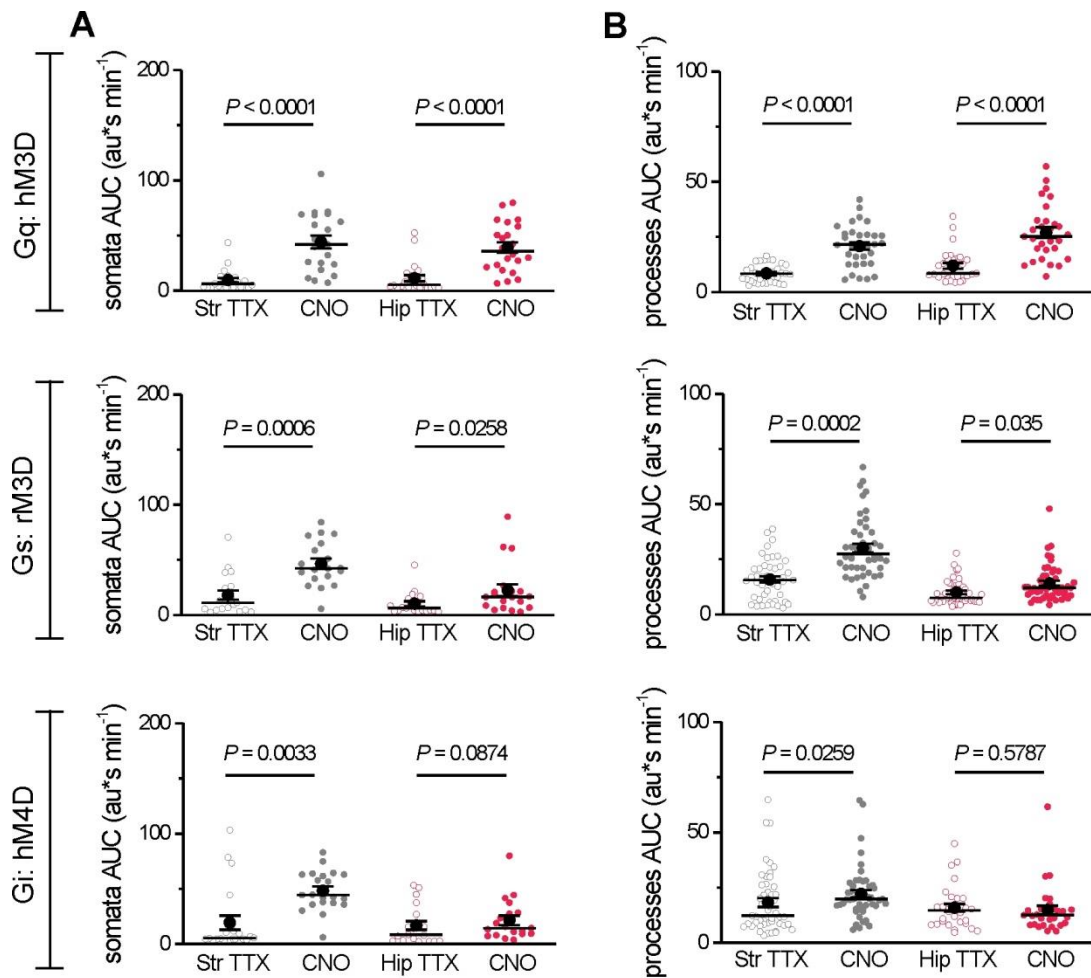


**Figure 7.10: Astrocyte Ca<sup>2+</sup> responses to activation of different G-protein coupled GPCRs.**

The CNO-evoked fold-change in area under the curve (AUC) for astrocyte somata (**A**) and processes (**B**) are compared before and during CNO application. Raw data are shown with open circles with closed circles indicating the average value  $\pm$  s.e.m. Where appropriate, the median is shown with a line.

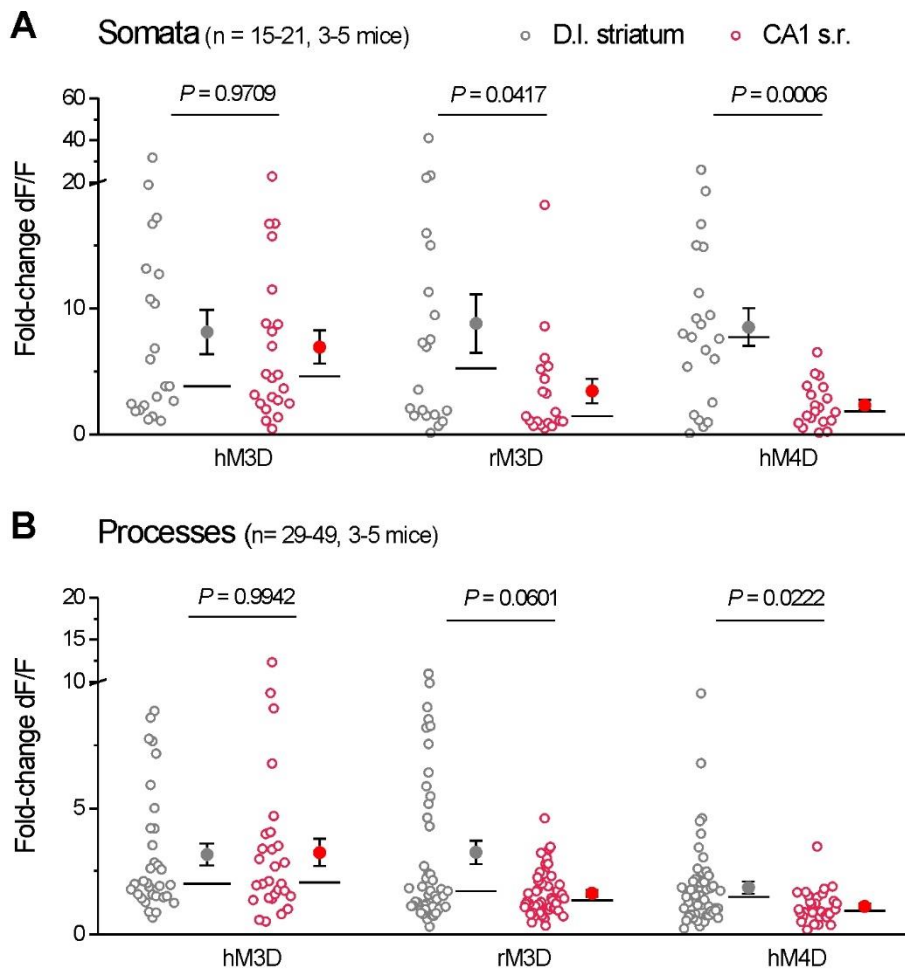


**Figure 7.11: Striatal and hippocampal astrocytes differ in GPCR mediated  $\text{Ca}^{2+}$  responses.** The CNO-evoked fold-change in area under the curve for astrocyte somata (**A**) and processes (**B**) are compared between striatal and hippocampal astrocytes. Raw data are shown with open circles with closed circles indicating the average value  $\pm$  s.e.m. Where appropriate, the median is shown with a line.

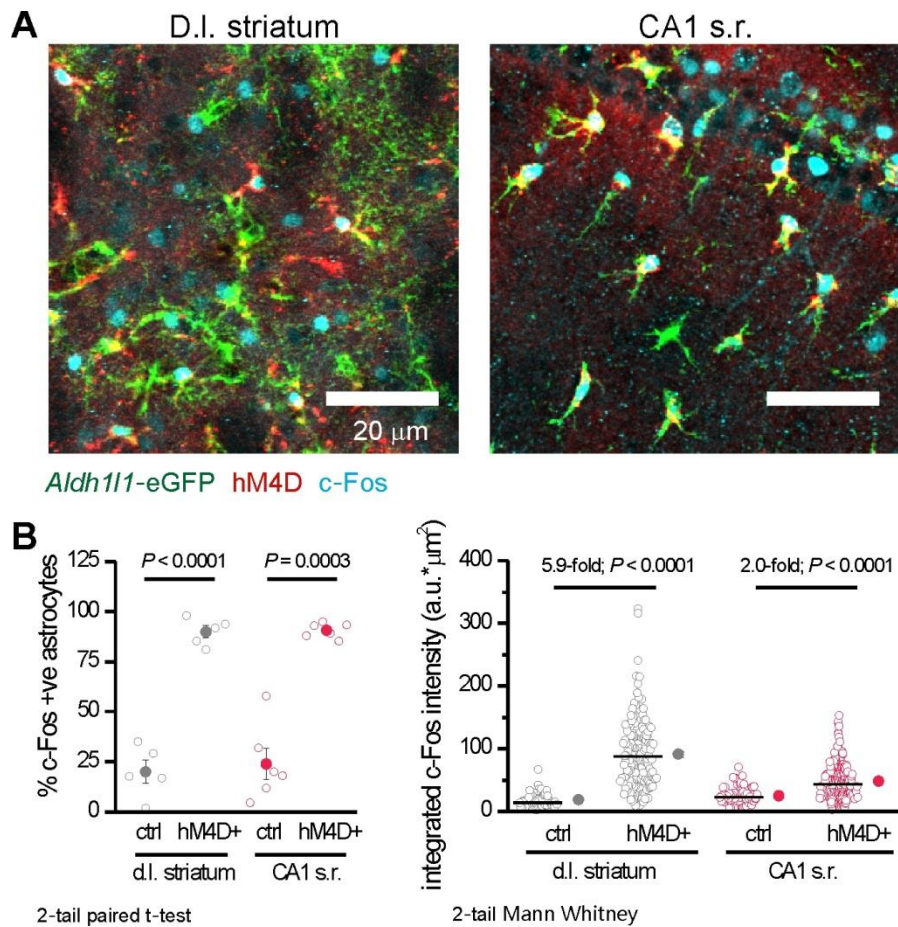


**Figure 7.12: Activation of HM4D in astrocytes causes increase in expression of immediate early gene *c-Fos*.** **A.** Representative images show hM4D (red) expressing astrocytes (green) with increased levels of *c-Fos* (cyan) in both d.l. striatum and CA1 s.r. One hour after CNO i.p. injection. **B. Left:** The % of *c-Fos*+ astrocytes was much higher in ipsilateral hM4D injected compared to contralateral uninjected. **Right:** Of the *c-Fos*+ astrocytes, the integrated *c-Fos* intensity (as measured by area \* mean intensity value / 1000) was much greater in hM4D expressing astrocytes. Raw data are shown with open circles with closed circles indicating the average value  $\pm$  s.e.m. In some cases, the whiskers are smaller than the symbol. Where appropriate, the median is shown with a line. Data was collected from 5-6 sections from 3 mice. Integrated *c-Fos* intensity was measured in 57-227 cells.

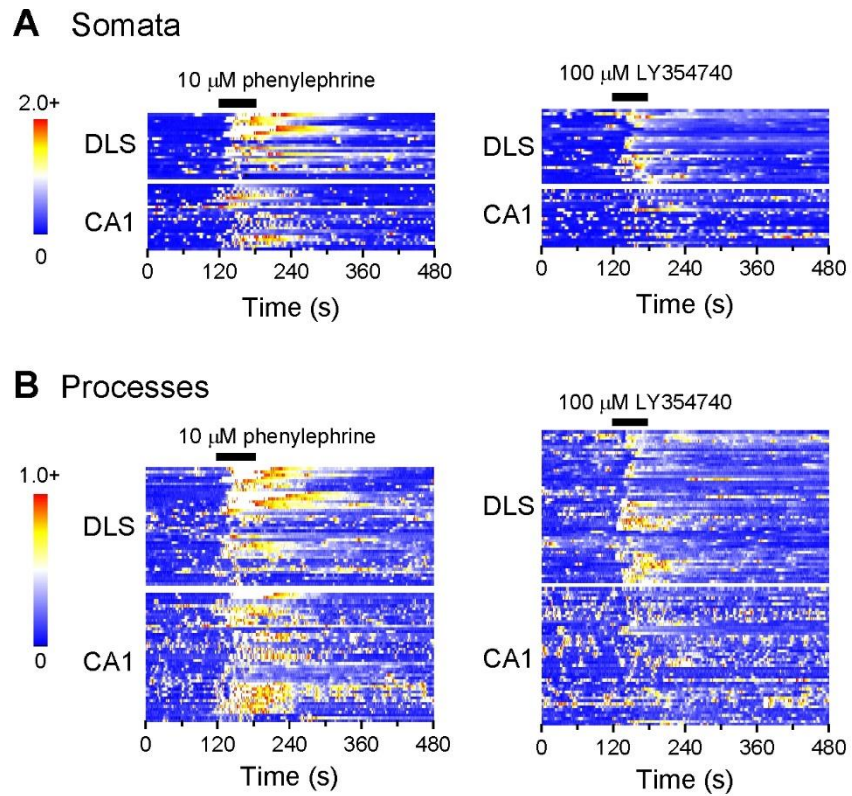


**Figure 7.13: Endogenous GPCR mediated  $\text{Ca}^{2+}$  responses in astrocytes.** **A.** Kymographs of somatic  $\text{Ca}^{2+}$  signals (GCaMP6f  $\text{dF}/\text{F}$ ) upon transient activation (60 s at 2 min) of Gq-coupled  $\alpha 1$ adrenoceptor with phenylephrine ( $10 \mu\text{M}$ ) and Gi/o-coupled mGluR2/3 with LY354740 ( $100 \mu\text{M}$ ). **B.** Kymographs of process  $\text{Ca}^{2+}$  signals (GCaMP6f  $\text{dF}/\text{F}$ ) upon transient activation of Gq-coupled  $\alpha 1$ adrenoceptor with phenylephrine ( $10 \mu\text{M}$ ) and Gi/o-coupled mGluR2/3 with LY354740 ( $100 \mu\text{M}$ ). Each row represents a single branch. Red on the contour plot indicates highly increased fluorescence with at least 1  $\text{dF}/\text{F}$  ( $n = 40\text{-}52$  processes from 5-6 mice).

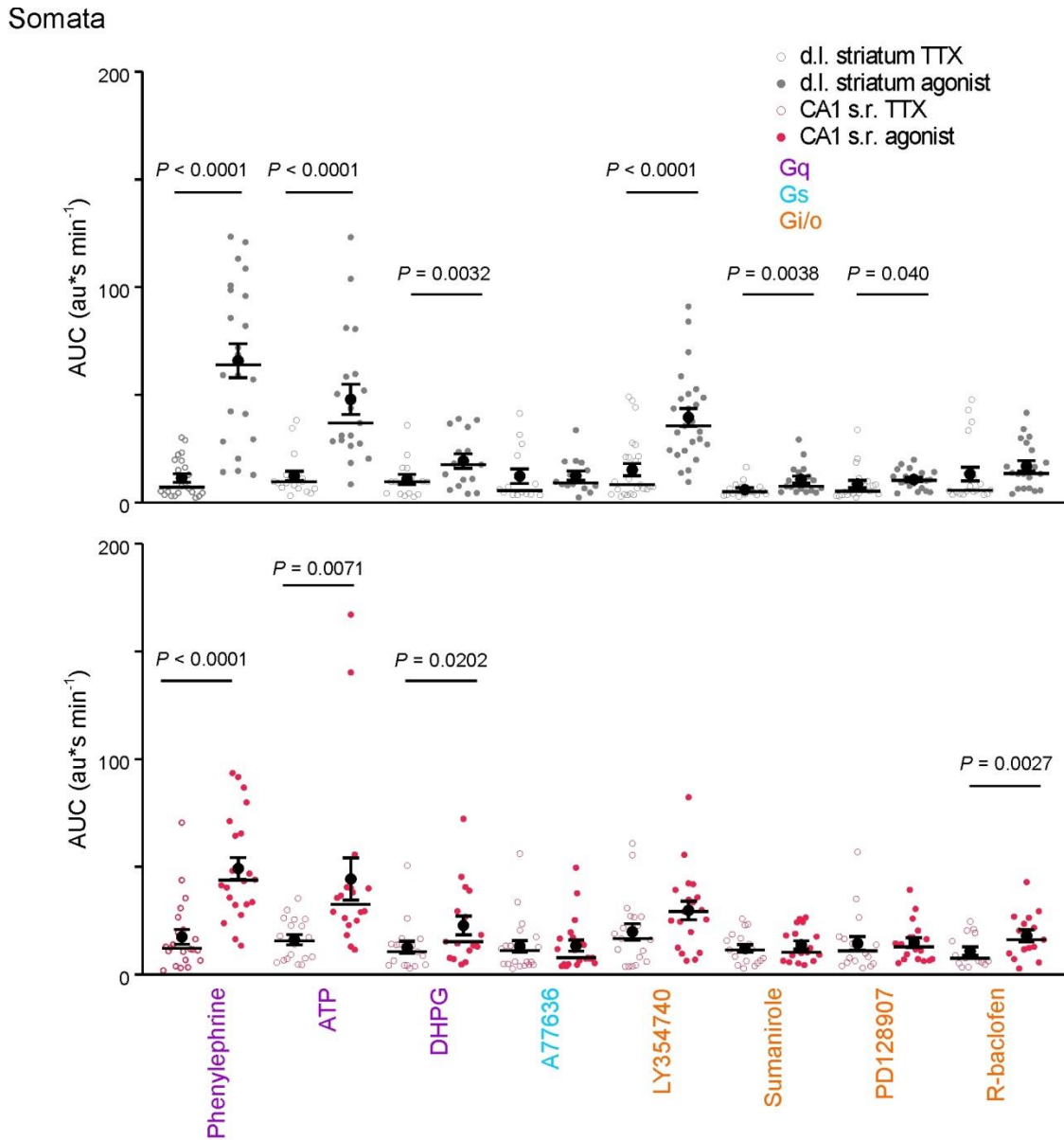


**Figure 7.14: GPCR mediated somatic  $\text{Ca}^{2+}$  responses.** The area under the curve for striatal (top) and hippocampal (bottom) astrocyte somatic  $\text{Ca}^{2+}$  signals are shown for before and during activation of endogenous Gq-, Gs-, and Gi/o-coupled GPCRs:  $\alpha_1$  adrenoceptors with  $10 \mu\text{M}$  phenylephrine, mGluR1/5 with  $100 \mu\text{M}$  DHPG, mGluR2/3 with  $100 \mu\text{M}$  LY354740, dopamine coupled  $D_{1/5}$  receptors with  $10 \mu\text{M}$  A77636, dopamine  $D_2$  receptor with  $10 \mu\text{M}$  sumanitrole, dopamine  $D_3$  receptor with  $50 \mu\text{M}$  PD128907, and GABA<sub>B</sub> receptor with  $50 \mu\text{M}$  R-baclofen ( $n = 15-25$  cells and  $36-52$  processes from  $5-6$  mice).  $0.25 \mu\text{M}$  TTX is present throughout these experiments. Striatal data are in grey and hippocampal data are in red. Filled black circles are mean  $\pm$  s.e.m. Medians are indicated with a horizontal line. 2-tailed paired student  $t$  test or Wilcoxon test was performed.

## Processes

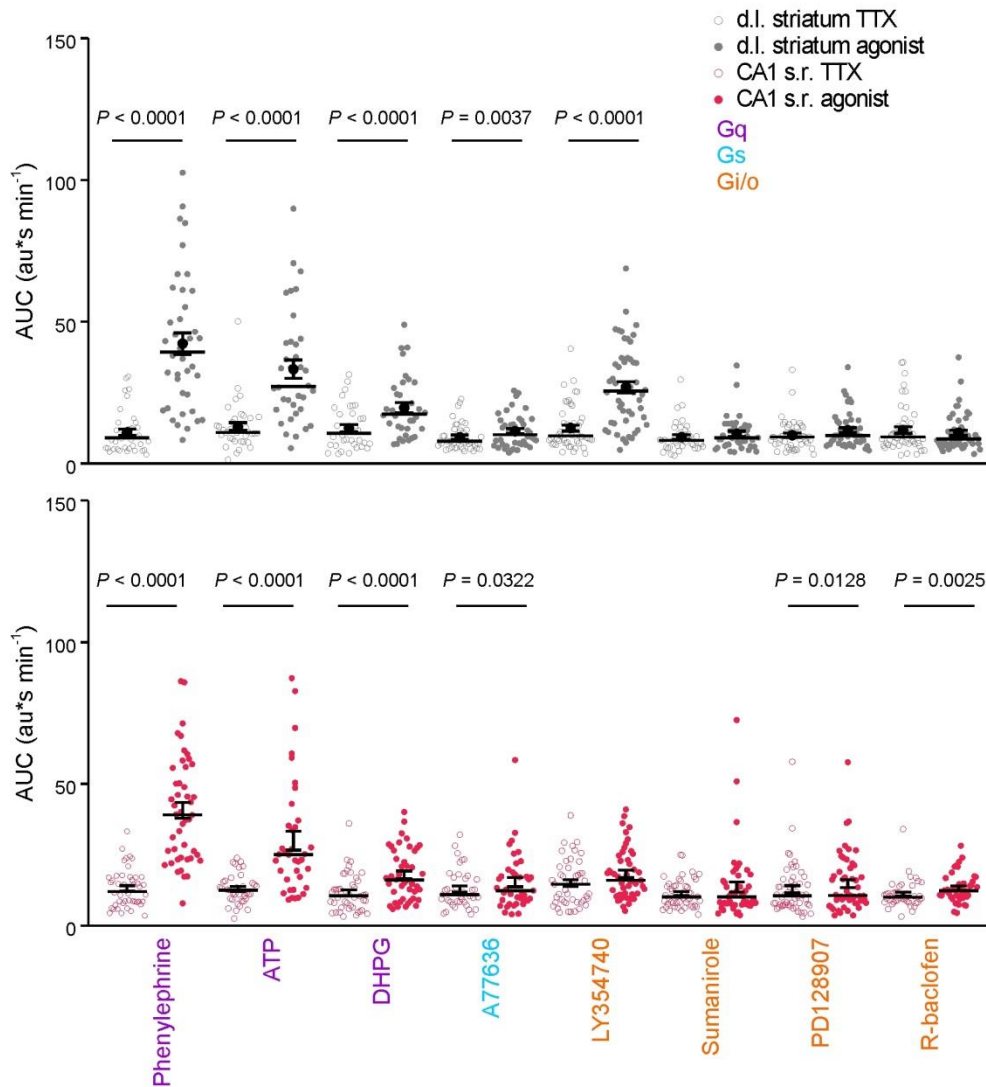


**Figure 7.15: GPCR mediated Ca<sup>2+</sup> responses in major processes.** The area under the curve for striatal (top) and hippocampal (bottom) astrocyte Ca<sup>2+</sup> signals in processes are shown for before and during activation of endogenous Gq-, Gs-, and Gi/o-coupled GPCRs:  $\alpha$ 1 adrenoceptors with 10  $\mu$ M phenylephrine, mGluR1/5 with 100  $\mu$ M DHPG, mGluR2/3 with 100  $\mu$ M LY354740, dopamine coupled D<sub>1/5</sub> receptors with 10  $\mu$ M A77636, dopamine D<sub>2</sub> receptor with 10  $\mu$ M sumanirole, dopamine D<sub>3</sub> receptor with 50  $\mu$ M PD128907, and GABA<sub>B</sub> receptor with 50  $\mu$ M R-baclofen ( $n = 15-25$  cells and 36-52 processes from 5-6 mice). 0.25  $\mu$ M TTX is present throughout these experiments. Striatal data are in grey and hippocampal data are in red. Filled black circles are mean  $\pm$  s.e.m. Medians are indicated with a horizontal line. 2-tailed paired student  $t$  test or Wilcoxon test was performed.

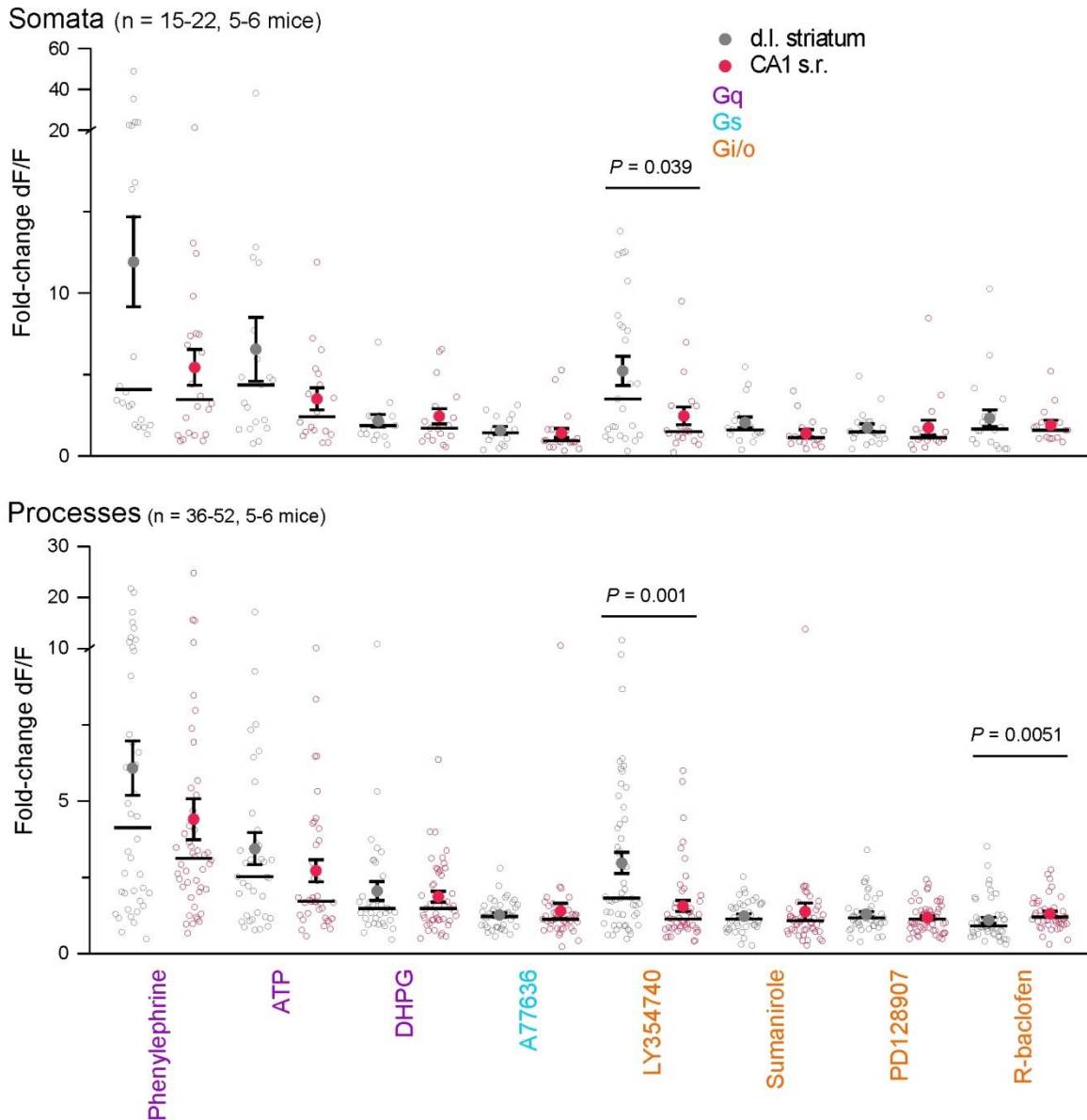


**Figure 7.16: Striatal and hippocampal astrocytes differ in GPCR mediated  $\text{Ca}^{2+}$  responses.**

The average agonist-evoked fold-change in area under the curve for astrocyte somata (top) and processes (bottom) are shown for activation of endogenous Gq-, Gs-, and Gi/o-coupled GPCRs:  $\alpha 1$  adrenoceptors with 10  $\mu\text{M}$  phenylephrine, mGluR1/5 with 100  $\mu\text{M}$  DHPG, mGluR2/3 with 100  $\mu\text{M}$  LY354740, dopamine coupled  $\text{D}_{1/5}$  receptors with 10  $\mu\text{M}$  A77636, dopamine  $\text{D}_2$  receptor with 10  $\mu\text{M}$  sumanitrole, dopamine  $\text{D}_3$  receptor with 50  $\mu\text{M}$  PD128907, and  $\text{GABA}_B$  receptor with 50  $\mu\text{M}$  R-baclofen ( $n = 15-25$  cells and 36-52 processes from 5-6 mice). 0.25  $\mu\text{M}$  TTX is present throughout these experiments. Striatal data are in grey and hippocampal data are in red. Filled circles are mean  $\pm$  s.e.m. Medians are indicated with a horizontal line. 2-tailed unpaired statistical testing was performed.

are less frequent in the striatum, perhaps the generation of those waves relies on extracellular calcium entry.

Of the known transmembrane  $\text{Ca}^{2+}$  flux pathways (**Supplemental Excel file 1 Table 3**) we found significant gene expression (FPKM > 10) for 23 molecules, of which nine were differentially expressed. These genes included  $\text{Ca}^{2+}$  permeable channels and pumps on the plasma membrane and within intracellular organelles and are consistent with idea that there are multiple sources of astrocyte  $\text{Ca}^{2+}$ . Furthermore, of the 249 known  $\text{Ca}^{2+}$  binding EF-hand containing proteins (**Supplemental Excel file 1 Table 4**), 68 were found in hippocampal or striatal astrocytes and 18 were differentially expressed. The P7 cortical astrocyte transcriptome (Zhang et al., 2014) also shows the presence of several channel and pump mRNAs that may underlie astrocyte calcium signals. These data illustrate that adult astrocytes contain a surprising richness in terms of  $\text{Ca}^{2+}$  flux pathways and proteins likely to buffer and respond to  $\text{Ca}^{2+}$ . The similarity and differences in expression of these proteins likely underlie the observed functional differences in  $\text{Ca}^{2+}$  signaling between d.l. striatum and hippocampus CA1 s.r. astrocytes.

Agonists at endogenous GPCRs are likely not as specific as the use of DREADDs, because they may have actions at other receptors and cells within slices – which is avoided with DREADDs (Roth, 2016). Hence, we draw robust conclusions based on results from the use of DREADDs as guided by results from endogenous GPCRs. This was that activation of Gq was equally effective in striatal and hippocampal astrocytes, but that activation of Gi/o was significantly more effective in striatal astrocytes than in hippocampal astrocytes, emphasizing neural-circuit-specific differences in the ability of GPCRs to elicit  $\text{Ca}^{2+}$  signals to modulate gene expression.

Surprisingly, despite significant innervation of the d.l. striatum by dopaminergic inputs, d.l. striatal astrocytes responded weakly to agonists of endogenous dopamine receptors D<sub>1</sub>, D<sub>2</sub>,

D<sub>3</sub>, D<sub>5</sub> (**Figure 7.14, 7.15**). Perhaps the simplest explanation is that dopamine receptors are not expressed in striatal astrocytes. According to our RNA-Seq data, *Drd2* (encoding D<sub>2</sub> receptor) showed moderate expression (FPKM 31.9 ± 9.5), although as discussed in **Chapter 4**, RNA expression alone is insufficient to demonstrate protein expression and function. For example, *Adra1a*, *Adra1b*, and *Adra1d* (encoding α1 adrenoceptor) RNAs were not expressed at high levels (FPKMs < 4) even though α1 adrenoceptor activation in astrocytes consistently resulted in robust increases in intracellular Ca<sup>2+</sup> signals. Therefore, we cannot exclude the possibility that dopamine receptors are not expressed on astrocytes. Another explanation is that dopamine receptors are expressed but not functionally coupled to downstream Gi-mediated Ca<sup>2+</sup> increase. Striatal astrocyte Ca<sup>2+</sup> response to hM4D activation clearly demonstrates that a pathway exists. hM4D is Gi-coupled only (Armbruster et al., 2007), and the extent to which Go protein, the most abundant G protein in the brain, is involved in Gi/o-coupled GPCR signaling is still a matter of debate (Jiang and Bajpayee, 2009; Sternweis and Robishaw, 1984). Therefore, the weak striatal astrocyte response to dopamine receptor activation could be due to functional uncoupling of GPCR signaling to Ca<sup>2+</sup> increase at or downstream of the G protein (**Figure 7.1**).

The functions of astrocyte Ca<sup>2+</sup> signaling are an active area of exploration in the field, and several functions have been described. Astrocyte Ca<sup>2+</sup> increases due to neuronal activity, such as synaptic release of neurotransmitters (Dani et al., 1992; Tang et al., 2009) activating GPCRs (Porter and McCarthy, 1995, 1996), from local connections and distal projections, and thus may participate in integrating these signals to modulate circuit function and behavior. The d.l. striatum receives inputs from cortex and numerous midbrain nuclei, and is involved in repetitive innate behaviors and habitual actions (Balleine et al., 2007; Berendse and Groenewegen, 1990; Everitt and Robbins, 2013; Graybiel, 2008; Palmiter, 2008). Integrating norepinephrine-mediated alertness, direct sensorimotor information, thalamic processing, and dopamine-mediated movement production and motivation would be critical to d.l. striatal

behaviors. In this chapter, we showed that d.l. striatal astrocyte intracellular  $\text{Ca}^{2+}$  signals increase with activation of glutamatergic, adrenergic, and dopaminergic receptors, and therefore could play a role in habit formation and innate behaviors. One potential mechanism for astrocyte  $\text{Ca}^{2+}$  signals to modulate neuronal circuits is to change the structure and protein function of perisynaptic astrocyte processes to affect local extracellular levels of neurotransmitters and  $\text{K}^+$ , thus modulating synaptic function (Khakh and Sofroniew, 2015). Other possibilities include changes in astrocyte endfeet to increase local bloodflow (Bazargani and Attwell, 2015; Li et al., 2014; Otsu et al., 2014) and in glycogenesis to increase local energy availability. We have described in this chapter astrocyte-targeted DREADDs that can increase astrocyte  $\text{Ca}^{2+}$  signals in the striatum and hippocampus. The creation of a similarly genetically targetable method to decrease astrocyte  $\text{Ca}^{2+}$  signals would provide the complimentary tool to directly study the effect of astrocyte  $\text{Ca}^{2+}$  signals in a specific brain region on nearby neurons, circuit function, and related behavior.

In summary, there are clear differences between d.l. striatum and hippocampus CA1 s.r. in astrocyte basal  $\text{Ca}^{2+}$ , spontaneous  $\text{Ca}^{2+}$  signaling, neuronal activity dependent  $\text{Ca}^{2+}$  signaling, and GPCR-mediated  $\text{Ca}^{2+}$  signaling.

## CHAPTER 8: ASTROCYTE Ca<sup>2+</sup>-DEPENDENT GLUTAMATE EXOCYTOSIS

### Section 8.1: Introduction

Recent studies suggest that hippocampal and striatal astrocytes from young rodents display Ca<sup>2+</sup>-dependent glutamate exocytosis (Araque et al., 2014; Araque et al., 2000; D'Ascenzo et al., 2007; Martín et al., 2015; Navarrete and Araque, 2008; Perea and Araque, 2007), but the existence of this phenomenon remains controversial and debated (Bazargani and Attwell, 2015). The concept of astrocyte Ca<sup>2+</sup>-dependent glutamate exocytosis originated from evidence showing that increases in astrocyte Ca<sup>2+</sup> caused Ca<sup>2+</sup> increases in nearby neurons in co-culture (Parpura et al., 1994) and in cortical and hippocampal brain slices from rat pups (Angulo et al., 2004; Bezzi et al., 1998; Pasti et al., 1997). The authors showed that Ca<sup>2+</sup> elevations in astrocytes preceded neuronal Ca<sup>2+</sup> increase. Furthermore, Ca<sup>2+</sup> increase in neurons was blocked by mGluR antagonists (Bezzi et al., 1998; Parpura et al., 1994; Pasti et al., 1997). Depolarization of a single MSN led to non-action potential mediated increase in extracellular glutamate in striatal slices from young mice (Martín et al., 2015). Moreover, in other works, patch-dialysis of Ca<sup>2+</sup> chelator BAPTA into astrocytes could prevent increased synaptic activity (Jourdain et al., 2007) and synaptic failure rate (Pاناتier et al., 2011). From these findings, it was concluded that astrocytes exhibit Ca<sup>2+</sup>-dependent glutamate release onto neurons.

However, there are a number of concerns with the methods deployed. Some authors used mGluR agonists, in particular for mGluR1/5 (Angulo et al., 2004; Pasti et al., 1997), prostaglandins (Bezzi et al., 1998), bradykinin (Parpura et al., 1994), or endocannabinoid (Martín et al., 2015) to increase astrocyte Ca<sup>2+</sup>. Their conclusions ignore the likelihood that some or all of these receptors are also expressed on other cells including neurons. Others use nonphysiological electrical stimulation of astrocytes to induce Ca<sup>2+</sup>-dependent glutamate release (Jourdain et al., 2007). As previously discussed in relation to intracellular loading of organic Ca<sup>2+</sup>

indicator dyes, patching cells can dilute intracellular components and result in functional changes; thus patch-dialyzing BAPTA into astrocytes may also be nonphysiological (Nedergaard et al., 2010). Another worry is that BAPTA from the patch-pipette could enter into nearby neuronal structures during the patching process due to compromised plasma membrane integrity or leak via hemichannels. The finding that patch-dialysis of astrocytes with active light-chain of tetanus neurotoxin prevents increase in neuronal mEPSC frequency (Jourdain et al., 2007) shares some of these concerns. Therefore, the methods used to manipulate astrocyte  $\text{Ca}^{2+}$  may be nonphysiological and not specific to astrocytes. In addition, they have largely been deployed for astrocytes in young rodents.

Overall, there is evidence for and against  $\text{Ca}^{2+}$ -dependent glutamate exocytosis from astrocytes, but this topic remains highly controversial. We decided to take another look at this for adult astrocytes based on our RNA-Seq data of known molecules that mediate  $\text{Ca}^{2+}$ -dependent glutamate exocytosis.

Astrocyte  $\text{Ca}^{2+}$ -dependent glutamate exocytosis requires vesicular transporters (vGLUTs) and the components of the SNARE complex including a calcium sensor. RNA-Seq of P7 cortical astrocytes did not detect *Vglut1*, *Vglut2*, or *Vglut3*, although RNA of some components of the SNARE complex were expressed (Zhang et al., 2014). However, single cell PCR from hippocampal astrocytes of young adult rats found RNA expression of VGLUT1 and VGLUT2 (Bezzi et al., 2004). These authors also showed that VGLUT1 and VGLUT2 were expressed in hippocampal astrocytes from fixed brains and cultured cells using immunogold labeling electron microscopy (Bezzi et al., 2004). In adult astrocytes, others have found no colocalization between VGLUT1, 2, and 3 with astrocyte markers GLT1, S100 $\beta$ , and aquaporin 4 (Li et al., 2013). Transgenic mice that expressed dominant negative SNARE (dn-SNARE) in astrocytes had decreased extracellular adenosine, another transmitter, resulting in altered synaptic activity, although evidence for glutamate exocytosis was not found (Pascual et al., 2005). dn-SNARE

was targeted to astrocyte using the *Gfap* promoter, which we now know can also target some neurons (Fujita et al., 2014), although a more recent paper shows evidence to the contrary (Sultan et al., 2015). Therefore, the molecularly mechanisms for Ca<sup>2+</sup>-dependent glutamate exocytosis may exist in astrocytes.

Given the controversies surrounding astrocyte Ca<sup>2+</sup>-dependent glutamate exocytosis, we sought to shed light on this issue for adult astrocytes. Based on RNA-Seq and proteomic data, as well as parallel experiments that showed differences in signaling and morphology between striatal and hippocampal astrocytes (**Chapters 4, 5, 7**), we explored if Ca<sup>2+</sup>-dependent glutamate exocytosis also differed.

## **Section 8.2: Lack of molecular or morphological evidence for glutamate exocytosis**

**Figure 8.1** plots striatal and hippocampal astrocyte FPKM values for genes involved in Ca<sup>2+</sup>-dependent exocytosis (4 synaptobrevins, 4 SNAPs, 4 syntaxins, 5 synaptotagmins, 4 complexins, 4 syntaxin binding proteins and 3 vGluts). To assess these data, we plotted FPKM values for known astrocyte markers, neuron markers and housekeeping genes (**Figure 8.1**, n = 4). The asterisks in **Figure 8.1** highlight FPKM values that were significantly greater than 10, which is the threshold defined by well-established neuronal markers ( $P < 0.05$  by one-sample t test). Notably, striatal and hippocampal astrocytes express *Vamp2*, *Vamp3*, *Vamp4*, *Snap25*, *Snap29*, *Snap47*, *Stx4a*, *Syt11*, *Cplx2*, *Stxbp3a* and *Stxbp4* mRNAs above this threshold (**Figure 8.1**). However, neither striatal nor hippocampal astrocytes expressed significant levels of transcripts for vGluts or Ca<sup>2+</sup>-sensitive synaptotagmins. Synaptotagmin 11 (encoded by *Syt11*) was significantly expressed in our data and in past work (Zhang et al., 2014), but it does not bind Ca<sup>2+</sup> due to the absence of essential aspartates and is of unknown function (Pang and Südhof, 2010; von Poser et al., 1997). Of the molecules related to Ca<sup>2+</sup>-dependent exocytosis, only VAMP2 was found in the high-stringency proteomic data, although several were found in

the low-stringency dataset (**Supplementary Excel file 2**). Furthermore, although we readily observed vesicles in 138 striatal and 139 hippocampal synapses (**Figure 5.7**), we observed no astrocyte processes that contained structures akin to neurotransmitter vesicles at the same synapses. Hence, the astrocyte data indicate membrane traffic-related gene expression, but little evidence for minimal requirements for  $\text{Ca}^{2+}$ -dependent glutamate exocytosis, i.e. for a  $\text{Ca}^{2+}$  sensor or a vesicular glutamate transporter.

### **Section 8.3: Astrocyte cell surface glutamate imaging**

We next sought to measure astrocyte  $\text{Ca}^{2+}$ -mediated glutamate release from striatal and hippocampal astrocytes. We activated Gq GPCR to robustly increase striatal and hippocampal astrocyte  $\text{Ca}^{2+}$  (**Chapter 7.5**) and visualized glutamate using the genetically-encoded glutamate sensor iGluSnFR, which has requisite kinetics and sensitivity (Haustein et al., 2014; Jiang et al., 2016; Marvin et al., 2013). We targeted iGluSnFR to astrocyte extracellular surfaces and co-expressed it with hM3D DREADDs (**Figure 8.2A**). We found no evidence for spontaneous iGluSnFR fluorescence increases (flashes) in either brain region: 1 of 10 d.l. striatal astrocytes and 0 in 13 CA1 s.r. astrocytes displayed iGluSnFR flashes (**Figure 8.2B**).

We did not find strong evidence for CNO-evoked iGluSnFR flashes even though CNO activation of hM3D always increased astrocyte  $\text{Ca}^{2+}$  levels (**Figures 7.10, 7.11**). With CNO application, 12 of 28 (42%) d.l. striatal and 1 of 16 (6%) CA1 s.r. astrocytes displayed iGluSnFR flashes (**Figure 8.3**). There was a statistically significant increase in iGluSnFR flashes from striatal but not hippocampal astrocytes with CNO, but this corresponds to only one iGluSnFR flash every 10 min (**Figure 8.3**). Blocking GLT1 with 1  $\mu\text{M}$  TBOA caused comparable increase in number of striatal astrocytes displaying iGluSnFR flashes (7 of 16 cells; 44%) and in frequency of flashes (**Figure 8.3**). In striatal astrocytes with CNO application, observed iGluSnFR flashes occasionally occurred within 2 minutes of start of CNO-evoked  $\text{Ca}^{2+}$  increase

(6 out of 12 cells with flashes), but this was not significant at the population level and was also observed within 2 minutes of start of TBOA application (4 out of 7 cells with flashes). CNO also failed to cause any increase in basal iGluSnFR fluorescence. Striatal astrocyte basal iGluSnFR fluorescence was  $534 \pm 41$  a.u. in control and  $348 \pm 21$  a.u. with +CNO. Hippocampal astrocyte basal iGluSnFR fluorescence was  $392 \pm 41$  a.u. in control and  $274 \pm 17$  a.u. with CNO. However, both striatal and hippocampal astrocytes responded to exogenous glutamate (**Figure 8.4**) and EFS of glutamatergic inputs with 4 APs (**Figure 8.5**) with significant astrocyte iGluSnFR signals (Armbruster et al., 2016; Haustein et al., 2014; Jiang et al., 2016). Moreover, application of TBOA to block GLT1 significantly increased EFS-evoked iGluSnFR signals onto hippocampal ( $P = 0.04324$ ), but not striatal astrocytes (**Figure 8.5**;  $P = 0.27489$ ). With these controls, we feel confident that we would have detected comparable glutamate release from astrocytes had it occurred.

#### **Section 8.4: Neuronal extrasynaptic NMDA receptor mediated slow inward current**

Furthermore, in young mice, astrocyte glutamate release may activate neuronal extrasynaptic NMDA receptors to evoke slow inward currents (SICs) (D'Ascenzo et al., 2007; Fiacco et al., 2007; Shigetomi et al., 2008). We thus also recorded from d.l. striatal MSNs and hippocampal CA1 pyramidal neurons in the vicinity of astrocytes expressing hM3D DREADDs and applied CNO (**Figure 8.6**). We could readily measure SICs in both MSNs and pyramidal neurons, but we failed to measure significant CNO-evoked increases in their frequency or amplitude (**Figure 8.7**). We do note that overall, fewer striatal MSNs exhibited SICs as compared to hippocampal CA1 neurons. This further highlights the difference between the two neural circuits.

## Section 8.5: Summary and discussion

Using the breadth of our approaches, we examined the potential for  $\text{Ca}^{2+}$ -dependent glutamate exocytosis from adult astrocytes in d.l. striatum and hippocampal CA1. We found little evidence for the presence of core molecular machinery within adult astrocytes to support  $\text{Ca}^{2+}$ -dependent glutamate exocytosis. Furthermore, although we could evoke large amplitude astrocyte  $\text{Ca}^{2+}$  elevations and image exogenous and neuronal glutamate release onto astrocytes, we found no convincing evidence for  $\text{Ca}^{2+}$ -dependent glutamate release from astrocytes onto astrocytes or nearby neurons in adult mice. This contrasts with some, but not all, aspects of our past work on young mice using less specific pharmacological approaches (Shigetomi et al., 2008). We previously showed that  $\text{Ca}^{2+}$  elevations in astrocytes were not a binary signal for neurons, which underscores the possibility that the relationship between astrocyte  $\text{Ca}^{2+}$  signals and exocytosis is not straightforward.

While we do not negate observations on the possible importance of astrocyte  $\text{Ca}^{2+}$ -dependent gliotransmission for striatal and hippocampal function (Martín et al., 2015; Navarrete and Araque, 2008; Perea and Araque, 2007), we suggest the need for great caution in drawing interpretations for astrocyte glutamate exocytosis in adult neural circuits, behavior and disease (Araque et al., 2014; Oliveira et al., 2015) until compelling evidence is obtained from mature neural circuits. Our evaluations failed to find such evidence in adult mice. Rather, astrocyte  $\text{Ca}^{2+}$ -dependent increase in extracellular glutamate may be due to decreased glutamate uptake, as has been suggested in a recent review (Bazargani and Attwell, 2015). This supports the view that adult astrocytes differ in physiologically relevant and significant ways from those in younger mice (see **Chapter 3**; Sun et al., 2013). Overall, our data are broadly consistent with past evaluations with healthy purified and cultured astrocytes (Foo et al., 2011) and argue against  $\text{Ca}^{2+}$ -dependent glutamate exocytosis as a core or robust astrocyte attribute under physiological conditions. It is possible that such mechanisms exist in pathology in reactive astrogliosis.

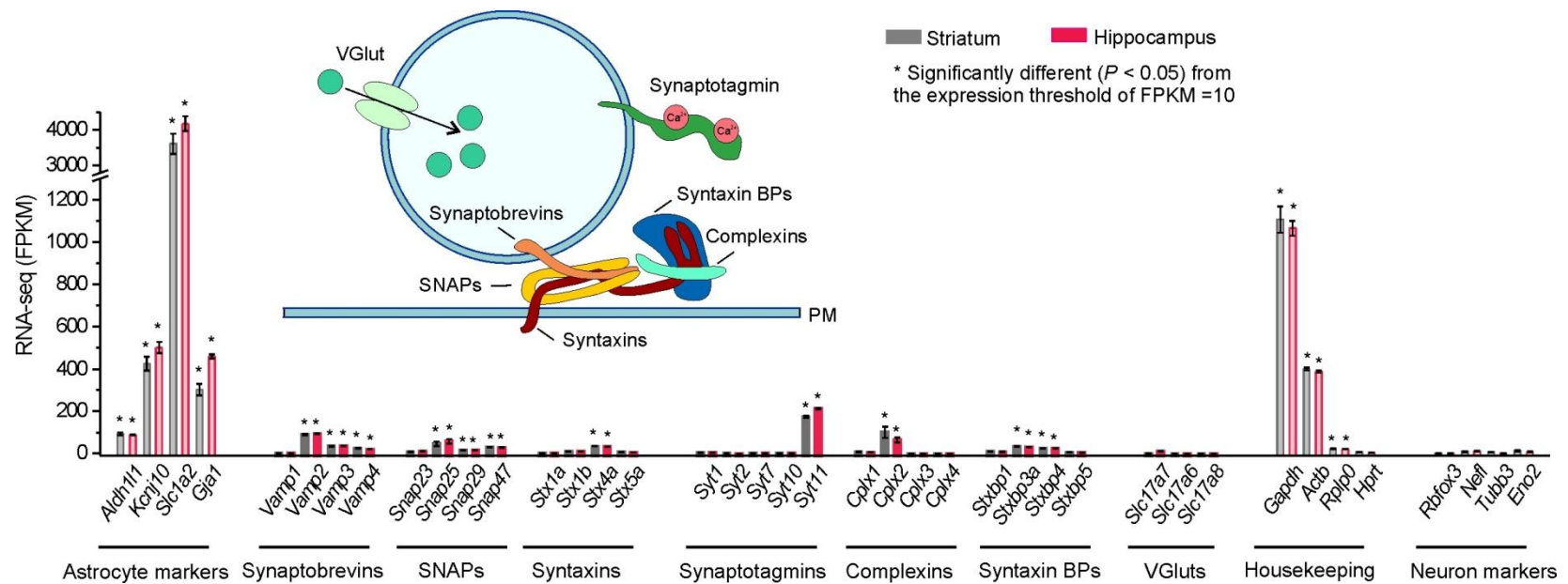


**Figure 8.1: Lack of molecular evidence for  $Ca^{2+}$ -evoked glutamate exocytosis. A.** The expression of known exocytosis genes in striatal and hippocampal RNA-Seq data ( $n = 4$ ) were compared against known markers of astrocytes, neurons, and housekeeping genes. One-sample  $t$  tests were run against the threshold of 10 FPKM based on the expression level of neuronal markers. *Inset:* Schematic showing current understanding of the molecular machinery involved in glutamate exocytosis.

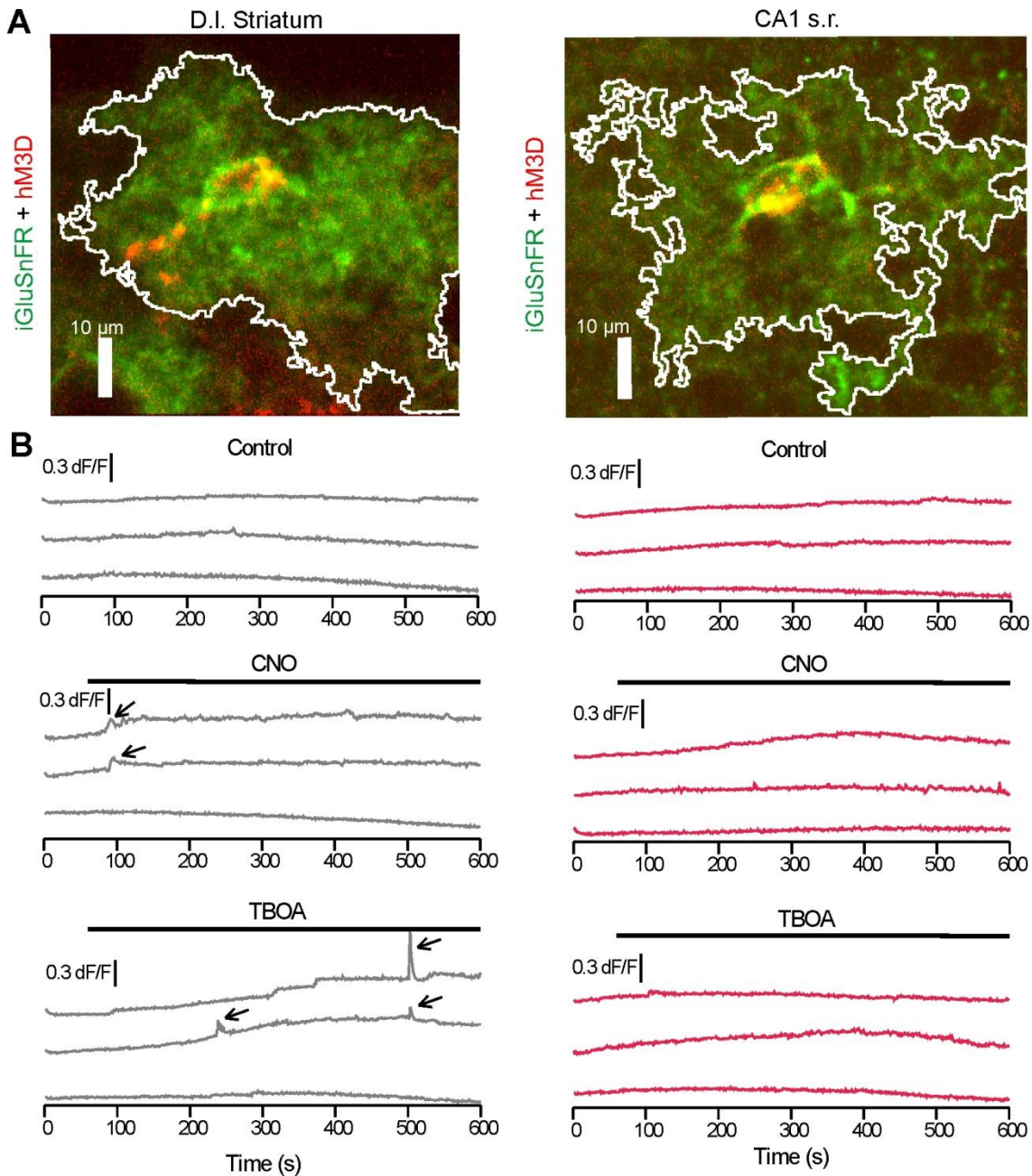


**Figure 8.2: Assessing astrocyte  $\text{Ca}^{2+}$ -evoked increase in extracellular glutamate.** **A.** Example images of iGluSnFR (green) coexpressed with Gq-coupled DREADD hM3D (red) in astrocytes from AAV injected mice. White line indicates area analyzed for iGluSnFR fluorescence. **B.** Example traces from striatal (grey) and hippocampal (red) astrocytes of iGluSnFR dF/F in control conditions, with application of CNO (1  $\mu\text{M}$ ) to increase astrocyte  $\text{Ca}^{2+}$ , or with application of 1  $\mu\text{M}$  TBOA to block glutamate transporters. iGluSnFR flashes are indicated with arrows.

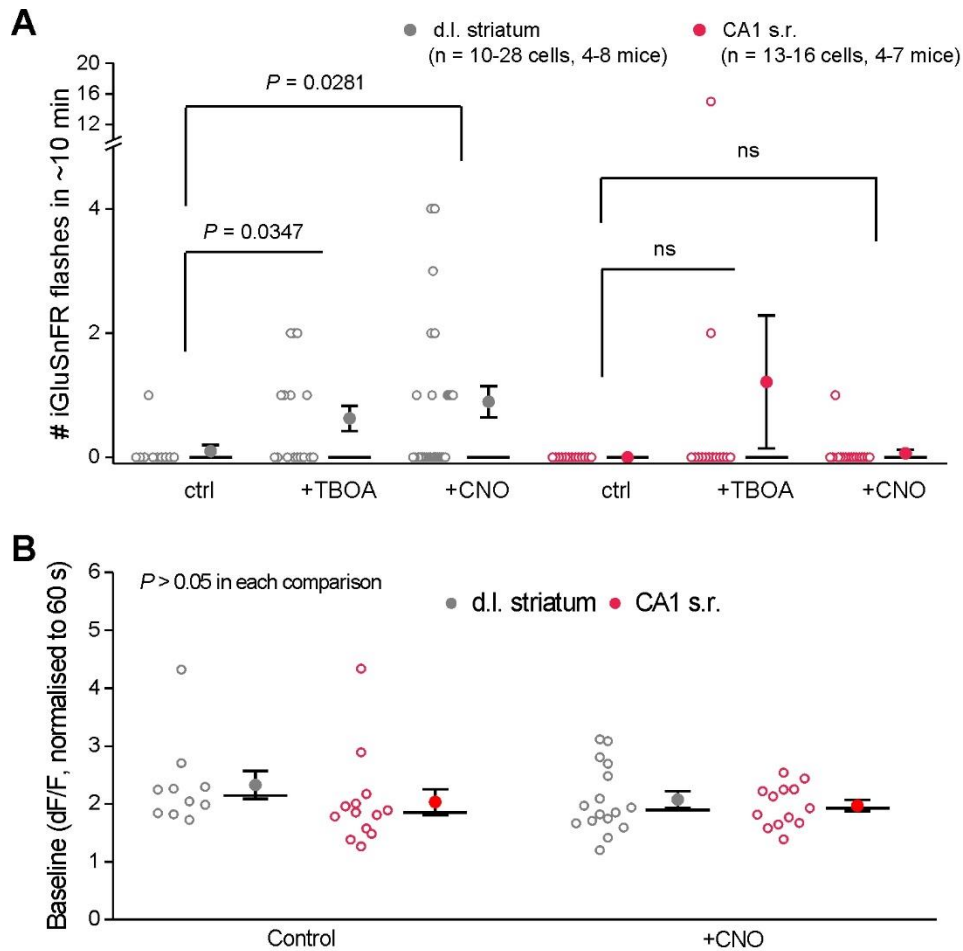


**Figure 8.3: Quantification of astrocyte  $\text{Ca}^{2+}$ -evoked iGluSnFR signals.** The number of iGluSnFR flashes (**A**) and the change in iGluSnFR dF/F (**B**) were compared between control, +CNO, and +TBOA. There was no significant difference in the number of flashes between control, +CNO and +TBOA conditions. Open circles are raw data with closed circle indicating mean  $\pm$  s.e.m and a horizontal line for the median. In some cases, the error bars representing s.e.m are smaller than the symbol used to show the mean.

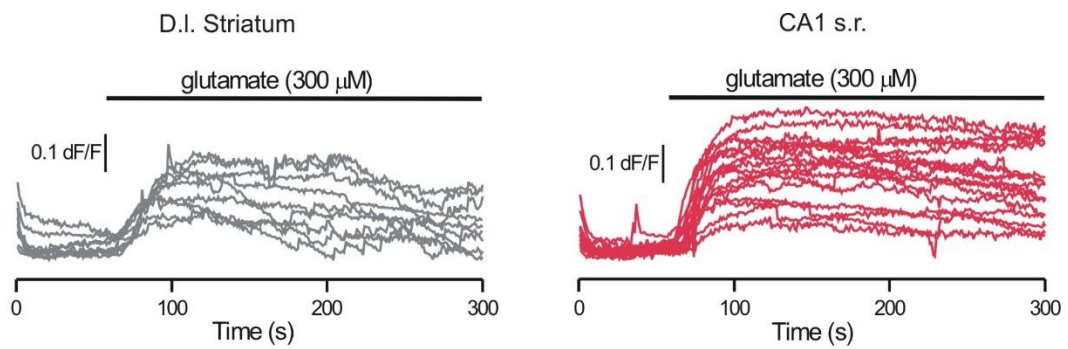


**Figure 8.4: iGluSnFR signals increase in response to exogenous glutamate application.** iGluSnFR traces show increased fluorescence with slow bath application of 300  $\mu\text{M}$  glutamate (in 1  $\mu\text{M}$  TBOA;  $n = 12$  cells per region from 4 mice).

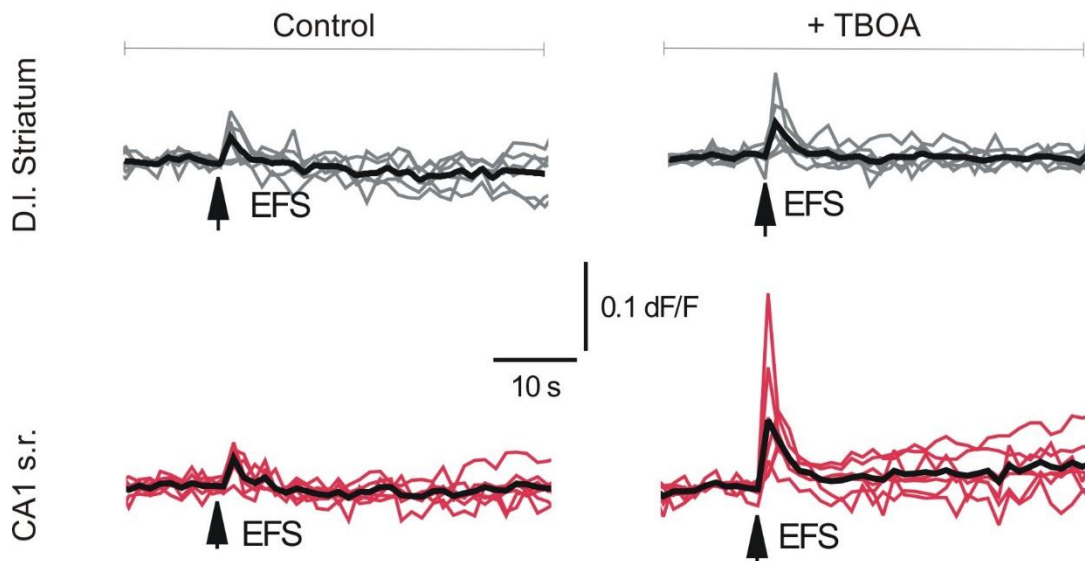


**Figure 8.5: iGluSnFR signals increase in response to synaptic glutamate release.** EFS-evoked (4 APs at 10 Hz) iGluSnFR signals recorded from striatal and hippocampal astrocytes under control conditions and in the presence of TBOA (n = 6 and 7 fields of view from 3 mice each).

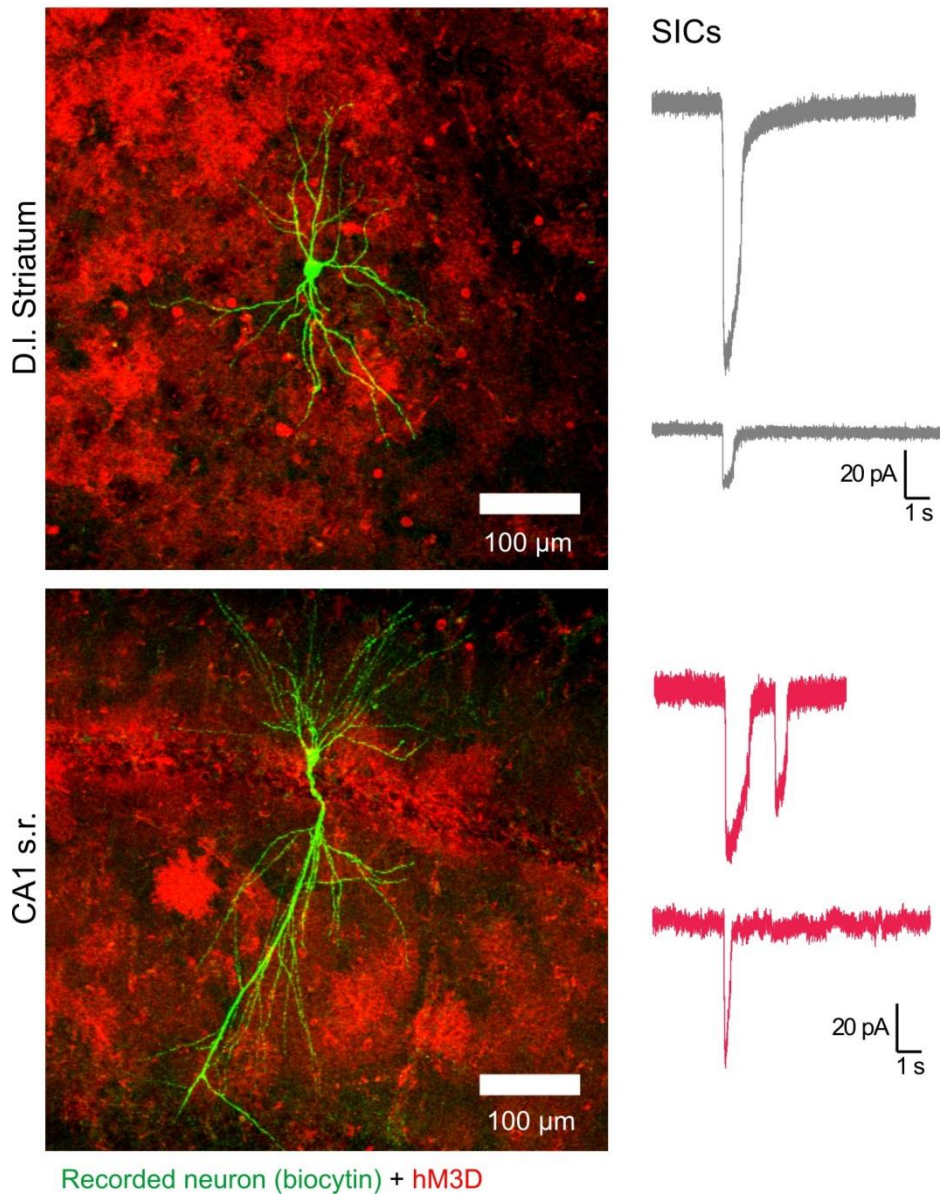


**Figure 8.6: Assessing extrasynaptic glutamate mediated neuronal SICs with striatal and hippocampal astrocyte  $\text{Ca}^{2+}$  increase.** *Left:* A recorded striatal medium spiny neuron (*top*) or CA1 pyramidal neuron (*bottom*) as visualized by biocytin (green) surrounded by hM3D expressing astrocyte (red mCherry signal). *Right:* Example traces from neurons in voltage-clamp shows slow inward currents (SICs) with characteristic slow downward deflections in membrane current at -70 mV.

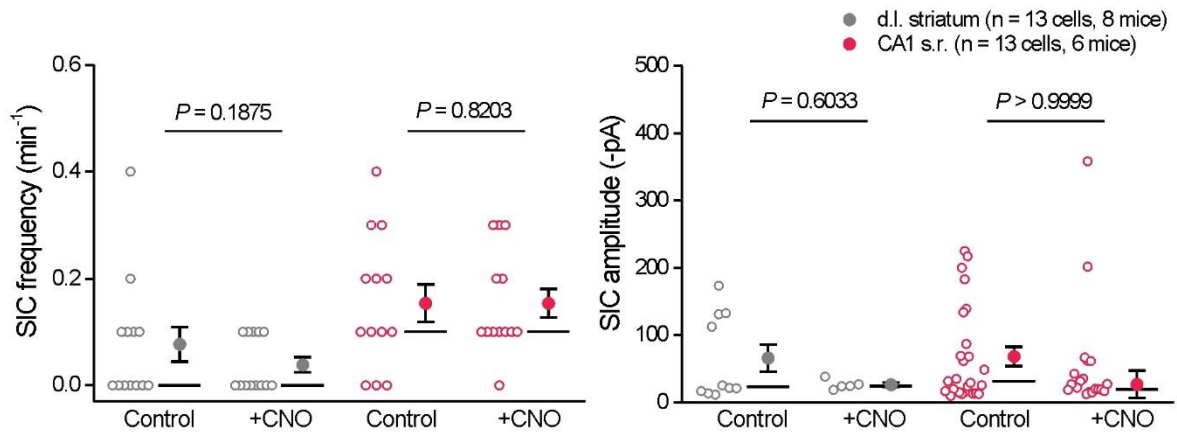


**Figure 8.7: Quantification of neuronal SICs.** The frequency and amplitude of SICs per minute in 10 min of control conditions and 10 min with CNO were not different. 0.25  $\mu$ M TTX was present in all experiments. Open circles are raw data with closed circle indicating mean  $\pm$  s.e.m and a horizontal line for the median. In some cases, the error bars representing s.e.m are smaller than the symbol used to show the mean.

## CHAPTER 9: CONCLUSION

### Section 9.1: Summary of data

Astrocytes have been considered a homogenous cell population since they were first described over a century ago. These cells have thousands of fine processes that mediate multiple supportive, active and homeostatic roles (Chung et al., 2015b; Haim and Rowitch, 2017; Khakh and Sofroniew, 2015). Astrocyte diversity has been widely invoked recently to explain the plethora of physiological processes that astrocytes participate in (Haim and Rowitch, 2017; Khakh and Sofroniew, 2015; Zhang and Barres, 2010). However, as assessment of astrocyte diversity in mature brain neural circuits has been lacking. We used several state-of-the-art methods to assess astrocyte similarity or diversity in two distinct neural circuits mediating distinct functions and largely comprising of distinct neuron types.

Our data show that astrocytes in the hippocampus and striatum share many similarities, but are distinct by several metrics at functional, morphological and molecular levels of evaluation. As far as we know, this work represents the first broad based and integrated evaluation of astrocyte diversity between neural circuits in the adult brain.

At a molecular level, they differed significantly in their transcriptomes and proteomes (**Chapter 4**). Morphologically, striatal and hippocampal astrocytes differed in their territory volume and shape and the proximity of astrocyte processes to excitatory synapses (**Chapter 5**). At a functional level, striatal and hippocampal astrocytes differed significantly in the size of Ba<sup>2+</sup>-sensitive K<sup>+</sup> currents, and gap-junctional coupling as well as spontaneous, electrically-evoked and GPCR-mediated Ca<sup>2+</sup> signals (**Chapters 6 and 7**). They also differed in the effect of blocking glutamate uptake on electrically-evoked glutamate signals (**Chapter 8**).

Our data confirm in adults at the protein and RNA level many known critical astrocyte functions, such as neurotransmitter clearance, K<sup>+</sup> homeostasis, and roles in synapse formation

and pruning. Irrespectively, lower Ba<sup>2+</sup> sensitive currents, CBX-sensitive gap-junctional coupling, and GLAST and glutamine synthetase levels (**Table 9.1**) in striatal astrocytes are consistent with the fact the striatum comprises of predominantly GABAergic neurons with hyperpolarized membrane potentials. Presumably, they have a lower requirement for K<sup>+</sup> handling and glutamate recycling.

To be able to explore circuit-specialized astrocyte properties at multiple biological levels, we created or modified a number of tools to target astrocytes. We have developed a new transgenic mouse line *Aldh1l1-Cre/ERT2* which allows temporally controlled manipulation of the majority of astrocytes in the brain (**Chapter 3**). Using *Aldh1l1-Cre/ERT2* x RiboTag double transgenic mice, we have generated transcriptomes for astrocytes in adult cortex, striatum, and hippocampus (**Chapters 3, 4**). For ease of use, we have made our transcriptomic and proteomic databases available as a searchable website (<http://astrocyternaseq.org>; **Figure 9.1**). RNA-Seq data have also been deposited at the Gene Expression Omnibus repository (<http://www.ncbi.nlm.nih.gov/geo>) with accession numbers GSE84540 and GSE94010; Proteomic data have been deposited at the Proteome Exchange Consortium via PRIDE with accession number PXD005852 for proteomics. Our astrocyte-targeted AAVs are available through the UPenn Vector Core; corresponding plasmids can be found on Addgene.

## **Section 9.2: Hippocampal astrocytes are better responders to neuronal glutamate release**

By using multiple modalities, we found that fine astrocyte processes in CA1 s.r. were better responders to neuronal glutamate release. Blocking glutamate uptake with TBOA during weak EFS-stimulation (4 APs at 10 Hz) resulted in increased astrocyte iGluSnFR signals in CA1 s.r. but not d.l. striatum (**Figure 8.5**). This indicates that CA1 s.r. astrocytes may uptake more synaptically released glutamate. Hippocampal CA1 s.r. but not d.l. striatum astrocytes also

<b>Gene</b>	<b>Protein &amp; Function</b>	<b>Str IP FPKM</b>	<b>Hip IP FPKM</b>	<b>LimmaVoom FDR</b>
<i>Slc1a3</i>	Glutamate transporter EAAT1/GLAST	921.6 ± 69.3	1254.4 ± 31.1	0.007101
<i>Slc1a2</i>	Glutamate transporter EAAT2/GLT1	3613.2 ± 283.9	4175.2 ± 207.0	0.15002
<i>Slc1a1</i>	Glutamate transporter EAAT3, neuronal and epithelial	6.81 ± 2.00	4.28 ± 0.81	0.427426
<i>Slc1a6</i>	Glutamate transporter EAAT4	0.328 ± 0.142	0.570 ± 0.219	0.290732
<i>Glul</i>	Glutamine synthetase	2384.5 ± 245.2	3274.5 ± 254.5	0.030214

**Table 9.1: Genes related to glutamate uptake and recycling.**

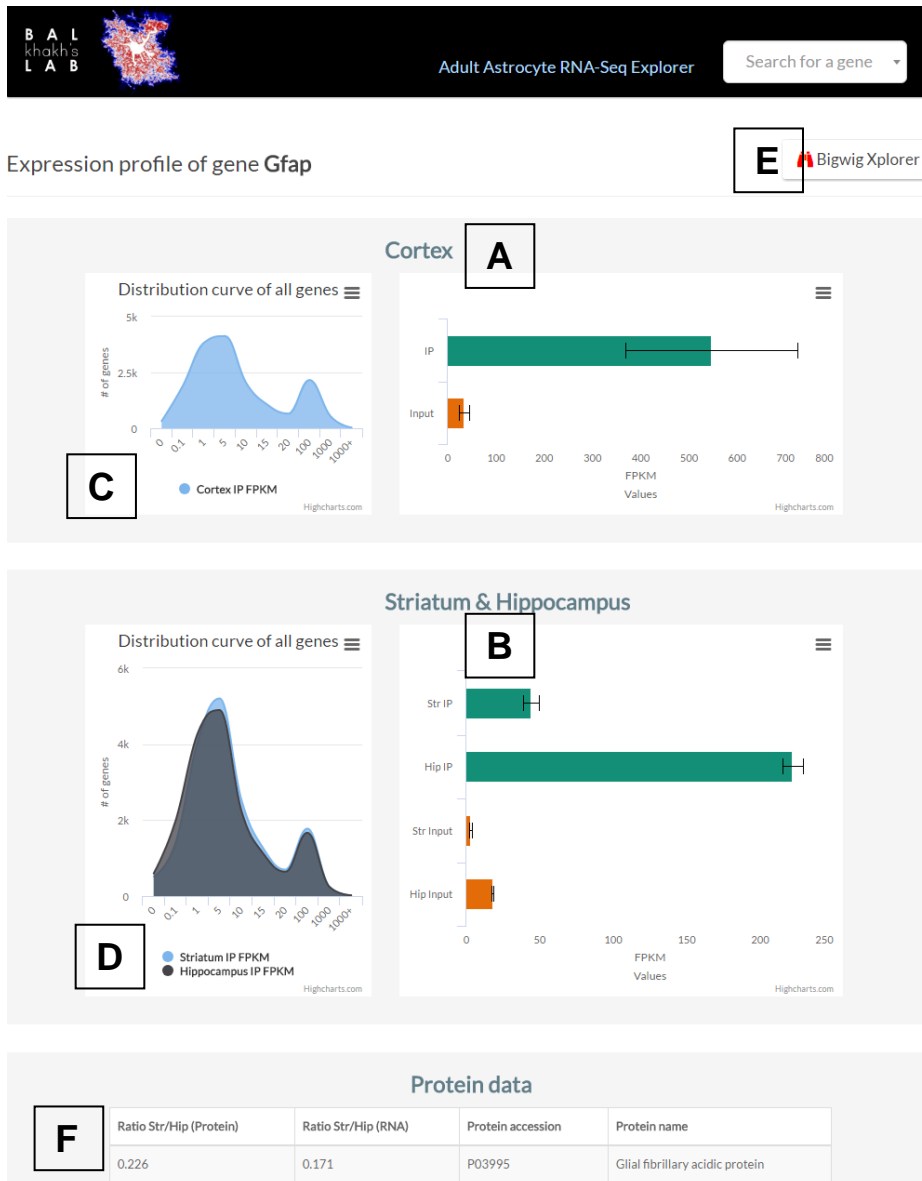


**Figure 9.1: Adult Astrocyte RNA-Seq Explorer.** Search results at <http://astrocyternseq.org> provide gene average FPKM values from cortical IP and input samples (**A**) and from striatal and hippocampal IP and input samples (**B**). Exact numbers will appear by hovering over the bar or error-bar with the cursor. **C & D.** The distribution curves of all sequenced IP gene FPKMs are provided for both datasets to provide context for FPKM values. **E.** The Bigwig Xplorer appends the sequencing tracks for all 24 samples from cortex, hippocampus, and striatum to the bottom of the page. **F.** When the protein corresponding to a gene was identified in the low-stringency proteomic dataset, the protein ratio is shown. The RNA ratio is also provided. Error bars indicate s.e.m.

exhibited increases in intracellular  $\text{Ca}^{2+}$  signals upon EFS-stimulation (40 APs at 10 Hz), suggesting that astrocyte glutamate uptake leads to intracellular calcium increase. Using electron microscopy, we found that CA1 s.r. astrocyte processes have greater physical interaction with excitatory synapses. The RNA-Seq analysis found gene sets related to synapse and extracellular structure organization as hippocampal astrocyte enriched, reminiscent of the functional and morphological observations. Therefore, hippocampal CA1 s.r. have the molecularly machinery and are physically poised to be better responders to neuronal glutamate release. Cultured hippocampal astrocytes extend filopodia after glutamate exposure (Cornell-Bell et al., 1990b) and time-lapse imaging studies suggest that fine astrocyte processes in some brain areas are dynamic structures whose motility increases with synaptic activity (Khakh and Sofroniew, 2015). It is interesting to speculate that the regional difference observed is due to a higher demand for removal of extracellular glutamate in CA1 s.r., and that with increased glutamatergic release in the d.l. striatum, striatal astrocyte processes would become more closely associated with excitatory synapses. However, SBF-SEM captures snapshots in time of the physical relationship between astrocyte fine processes and excitatory synapses, and thus cannot address this hypothesis. A high-resolution tool to monitor the dynamics of astrocyte-synapse interaction needs to be developed in order to explore the interplay between astrocyte morphology and function.

Hippocampal astrocytes more reliably responded with  $\text{Ca}^{2+}$  elevations to synaptic release of glutamate, but bath application of glutamate receptor agonists caused either comparable increase in astrocyte  $\text{Ca}^{2+}$  signals (DHPG for mGluR1/5) or a greater increase in striatal  $\text{Ca}^{2+}$  signals (LY354740 for mGluR2/3) (**Figures 7.16**). The parsimonious explanation for these seemingly contradictory findings is that astrocytes  $\text{Ca}^{2+}$  have functional compartments (Khakh and Sofroniew, 2015; Shigetomi et al., 2016) and activation of perisynaptic versus whole cell glutamate receptors have different downstream effects on  $\text{Ca}^{2+}$  signaling. Given that striatal

astrocytes take up less glutamate near synapses, strong  $\text{Ca}^{2+}$  response to whole cell mGluR2/3 activation may allow striatal astrocytes to respond to unexpectedly high levels of extrasynaptic glutamate.

### **Section 9.3: $\mu$ -Crystallin is specific to striatal astrocytes**

The discovery that  $\mu$ -crystallin is specific for striatal astrocytes provides the first molecular marker that defines a region-specific astrocyte population. Past work suggests  $\mu$ -crystallin may bind thyronines such as triiodothyronine, the active form of thyroid hormone (Suzuki et al., 2007). Type II iodothyronine 5'-deiodinase (encoded by *Dio2*) is a short-lived membrane protein and is rapidly internalized in astrocytes upon exogenous application of thyroid hormone (Farwell et al., 1990). There is also robust expression of *Dio2* in astrocytes in both striatum and hippocampus (FPKM ~150 as compared to *Aldh1l1* ~90). This suggests that thyroid hormone regulation is a key aspect of astrocyte function, and that this function may be more regulated in striatal astrocytes.

$\mu$ -crystallin is interesting from another perspective. It displayed a clearly significant gradient of expression in the striatum and was patchy in the dorso lateral region. This provides strong evidence that even locally arranged astrocytes within a neural circuit (dorsal *versus* ventral striatum) or even more locally (i.e. neighboring astrocytes in the dorso lateral region) may be heterogeneous. However, we suggest that proof for the existence of such highly local heterogeneity should be based on candid assessment of cell markers, gene expression, protein expression, physiology and morphology, thus benefiting from lessons learned from studying interneuron diversity for example (Kepecs and Fishell, 2014). Additional technical advances are necessary to deploy the combination of such methods, as we have done herein, to study with the required rigor single locally intermingled astrocytes. Our data showing that RNA and protein

levels are not necessarily directly correlated in all cases echoes previous work (Kitchen et al., 2014) and provides a strong impetus to assess local diversity with multiple approaches.

#### **Section 9.4: Implications for brain function in disease**

Astrocytes are also involved in disease, as evidenced by analyses of post-mortem human brains and from extensive cell culture and mouse model studies (Chung et al., 2015a; Phatnani and Maniatis, 2015; Tong et al., 2014). Our lab found that astrocytes from the striatum displayed larger Kir4.1 currents and Kir4.1 deficits in Huntington's disease mice, whereas those from the hippocampus did not (Tong et al., 2014). Here we have shown that physiologically hippocampal astrocytes have a greater ability to buffer and dissipate K<sup>+</sup> as individual cells and as a network.

Both beneficial and harmful effects have been attributed to astrocytes in mouse models of stroke. Reactive astrocytes release proinflammatory factors, molecules inhibiting axon growth, and even neurotoxic levels of nitric oxide (Li et al., 2014; Neufeld and Liu, 2003). However, other evidence suggest beneficial effects of glial scar formation in neuronal survival in the ischemic boundary zone, thus actually limiting the area of damage (Li et al., 2014; Liu et al., 2014; Nakase et al., 2004; Nawashiro et al., 2000). The striatum and hippocampus are both affected in stroke (Nikonenko et al., 2009; Qureshi et al., 2001; Rovira et al., 2005). 10-30% of all strokes are intracerebral hemorrhagic; these occur most commonly in the basal ganglia (Qureshi et al., 2001; Zhang et al., 2003). Striatal neurons are also sensitive to ischemic injury (Nikonenko et al., 2009). The hippocampus is particularly vulnerable to ischemic stroke due to the high energy demand of the CA1 pyramidal neurons with a significant amount of delayed neuronal death in the peri-infarct area (Kirino et al., 1984; Nikonenko et al., 2009; Pulsinelli et al., 1982), which astrocytes are thought to help ameliorate (Li et al., 2014; Liu et al., 2014; Nakase et al., 2004; Nawashiro et al., 2000). CA1 pyramidal neuronal dendrites course through the s.r.

(Fan and Fu, 2014), a region replete with astrocytes (Bushong et al., 2002). Interestingly, the s.r. is resistant to delayed neuronal death post-ischemia with relatively less astrocyte reactivity (Nikonenko et al., 2009). Perhaps the greater ability of hippocampal astrocytes for glutamate uptake in a region with relatively fewer neurons contributes to the relative resistance of the s.r. to ischemic injury.

Our data provide proof for the existence of neural-circuit specialized astrocytes in the adult brain, extending work from the spinal cord during development (Molofsky et al., 2014) and extending emerging work on astrocytes during disease-like states (Liddelow et al., 2017; Soreq et al., 2017). More generally, our data raise the concept of exploiting neural-circuit specialized astrocytes to derive benefit in brain disorders that affect specific micro- and macrocircuits such as the d.l. striatum and basal ganglia, respectively.

### **Section 9.5: Overall conclusion**

In summary, integrated optical, anatomical, electrophysiological, transcriptomic, and proteomic approaches were deployed to explore astrocyte similarities and differences in two neural circuits under a common set of experimental conditions. Candid evaluation of the data across ten approaches provided direct evidence for astrocyte diversity and provided resources and a tool-based experimental workflow to explore astrocyte diversity across the brain in health and disease. Our data provide direct evidence for neural-circuit specialized astrocytes in the adult brain and portend their therapeutic exploitation for the modulation and treatment of neural-circuit specific disease states. It should now be possible to determine how specific astrocytes change in particular disease states, and then exploit this information in developing new therapeutic strategies to decrease disease burden. These are exciting possibilities with potentially far reaching impact.

## CHAPTER 10: BIBLIOGRAPHY

Adermark, L., and Lovinger, D.M. (2008). Electrophysiological properties and gap junction coupling of striatal astrocytes. *Neurochemistry International* 52, 1365-1372.

Agarwal, A., Wu, P.H., Hughes, E.G., Fukaya, M., Tischfield, M.A., Langseth, A.J., Wirtz, D., and Bergles, D.E. (2017). Transient Opening of the Mitochondrial Permeability Transition Pore Induces Microdomain Calcium Transients in Astrocyte Processes. *Neuron* 93, 587-605.e587.

Akerboom, J., Chen, T.W., Wardill, T.J., Tian, L., Marvin, J.S., Mutlu, S., Calderon, N.C., Esposti, F., Borghuis, B.G., Sun, X.R., *et al.* (2012). Optimization of a GCaMP calcium indicator for neural activity imaging. *J Neurosci* 32, 13819-13840.

Allen, N.J. (2014). Astrocyte regulation of synaptic behavior. *Annu Rev Cell Dev Biol* 30, 439-463.

Allen, N.J., Bennett, M.L., Foo, L.C., Wang, G.X., Chakraborty, C., Smith, S.J., and Barres, B.A. (2012). Astrocyte glypicans 4 and 6 promote formation of excitatory synapses via GluA1 AMPA receptors. *Nature* 486, 410-414.

Amaral, D., and Lavenex, P. (2006). Hippocampal Neuroanatomy. In *The Hippocampus Book*, P. Andersen, R. Morris, D. Amaral, T. Bliss, and J. O'Keefe, eds. (Oxford University Press).

Anders, S., Pyl, P.T., and Huber, W. (2015). HTSeq—a Python framework to work with high-throughput sequencing data. *Bioinformatics* 31, 166-169.

Anderson, M.A., Burda, J.E., Ren, Y., Ao, Y., O'Shea, T.M., Kawaguchi, R., Coppola, G., Khakh, B.S., Deming, T.J., and Sofroniew, M.V. (2016). Astrocyte scar formation aids central nervous system axon regeneration. *Nature* 532, 195-200.

Andriezen, W.L. (1893). The neuroglia elements in the human brain. *British Medical Journal* 2, 227-230.

Angulo, M.C., Kozlov, A.S., Charpak, S., and Audinat, E. (2004). Glutamate released from glial cells synchronizes neuronal activity in the hippocampus. *J Neurosci* 24, 6920-6927.

Araque, A., Carmignoto, G., Haydon, P.G., Oliet, S.H., Robitaille, R., and Volterra, A. (2014). Gliotransmitters travel in time and space. *Neuron* 81, 728-739.

Araque, A., Li, N., Doyle, R.T., and Haydon, P.G. (2000). SNARE protein-dependent glutamate release from astrocytes. *J Neurosci* 20, 666-673.

Arellano, J.I., Benavides-Piccione, R., DeFelipe, J., and Yuste, R. (2007). Ultrastructure of dendritic spines: correlation between synaptic and spine morphologies. *Frontiers in Neuroscience* 1, 131-143.

Armbruster, B.N., Li, X., Pausch, M.H., Herlitze, S., and Roth, B.L. (2007). Evolving the lock to fit the key to create a family of G protein-coupled receptors potently activated by an inert ligand. *Proc Natl Acad Sci U S A* 104, 5163-5168.

Armbruster, M., Hanson, E., and Dulla, C.G. (2016). Glutamate Clearance Is Locally Modulated by Presynaptic Neuronal Activity in the Cerebral Cortex. *J Neurosci* 36, 10404-10415.

Ascoli, G., Alonso-Nanclares, L., Anderson, S., Barrionuevo, G., Benavides-Piccione, R., Burkhalter, A., Buzsáki, G., Cauli, B., DeFelipe, J., Fairén, A., *et al.* (2008). Petilla terminology: nomenclature of features of GABAergic interneurons of the cerebral cortex. *Nature Reviews Neuroscience* 9, 557-568.

Atasoy, D., Aponte, Y., Su, H.H., and Sternson, S.M. (2008). A FLEX switch targets Channelrhodopsin-2 to multiple cell types for imaging and long-range circuit mapping. *J Neurosci* 28, 7025-7030.

Bailey, M.S., and Shipley, M.T. (1993). Astrocyte subtypes in the rat olfactory bulb: Morphological heterogeneity and differential laminar distribution. *The Journal of Comparative Neurology* 328, 501-526.

- Balleine, B.W., Delgado, M.R., and Hikosaka, O. (2007). The role of the dorsal striatum in reward and decision-making. *J Neurosci* 27, 8161-8165.
- Barbin, G., Katz, D.M., Chamak, B., Glowinski, J., and Prochiantz, A. (1988). Brain astrocytes express region-specific surface glycoproteins in culture. *Glia* 1, 96-103.
- Barres, B.A. (2008). The Mystery and Magic of Glia: A Perspective on Their Roles in Health and Disease. *Neuron* 60, 430-440.
- Bazargani, N., and Attwell, D. (2015). Astrocyte calcium signalling: the third wave. *Nature neuroscience* *accepted*.
- Bello-Medina, P.C., Flores, G., Quirarte, G.L., McGaugh, J.L., and Prado Alcalá, R.A. (2016). Mushroom spine dynamics in medium spiny neurons of dorsal striatum associated with memory of moderate and intense training. *Proceedings of the National Academy of Sciences* 113, E6516-E6525.
- Benraiss, A., Wang, S., Herrlinger, S., Li, X., Chandler-Militello, D., Mauceri, J., Burm, H.B., Toner, M., Osipovitch, M., Jim, X.Q., *et al.* (2016). Human glia can both induce and rescue aspects of disease phenotype in Huntington disease. *Nat Commun Jun 7;7:11758. doi: 10.1038/ncomms11758*.
- Berendse, H.W., and Groenewegen, H.J. (1990). Organization of the thalamostriatal projections in the rat, with special emphasis on the ventral striatum. *The Journal of Comparative Neurology* 299, 187-228.
- Bezzi, P., Carmignoto, G., Pasti, L., Vesce, S., Rossi, D., Rizzini, B.L., Pozzan, T., and Volterra, A. (1998). Prostaglandins stimulate calcium-dependent glutamate release in astrocytes. *Nature* 391, 281-285.

Bezzi, P., Gunderson, V., Galbete, J.L., Seifert, G., Steinhauser, C., Pilati, E., and Volterra, A. (2004). Astrocytes contain a vesicular compartment that is competent for regulated exocytosis of glutamate. *Nature neuroscience* 7, 613-620.

Boersema, P.J., Raijmakers, R., Lemeer, S., Mohammed, S., and Heck, A.J. (2009). Multiplex peptide stable isotope dimethyl labeling for quantitative proteomics. *Nat Protoc* 4, 484-494.

Bourne, J., and Harris, K.M. (2007). Do thin spines learn to be mushroom spines that remember? *Current Opinion in Neurobiology* 17, 381-386.

Brown, L.L., Feldman, S.M., Smith, D.M., Cavanaugh, J.R., Ackermann, R.F., and Graybiel, A.M. (2002). Differential Metabolic Activity in the Striosome and Matrix Compartments of the Rat Striatum during Natural Behaviors. *The Journal of Neuroscience* 22, 305.

Bushong, E.A., Martone, M.E., Jones, Y.Z., and Ellisman, M.H. (2002). Protoplasmic astrocytes in CA1 stratum radiatum occupy separate anatomical domains. *J Neurosci* 22, 183-192.

Cahoy, J.D., Emery, B., Kaushal, A., Foo, L.C., Zamanian, J.L., Christopherson, K.S., Xing, Y., Lubischer, J.L., Krieg, P.A., Krupenko, S.A., *et al.* (2008). A transcriptome database for astrocytes, neurons, and oligodendrocytes: a new resource for understanding brain development and function. *J Neurosci* 28, 264-278.

Cauli, B., Audinat, E., Lambolez, B., Angulo, M.C., Ropert, N., Tsuzuki, K., Hestrin, S., and Rossier, J. (1997). Molecular and physiological diversity of cortical nonpyramidal cells. *J Neurosci* 17, 3894-3906.

Charles, A.C., Merrill, J.E., Dirksen, E.R., and Sanderson, M.J. (1991). Intercellular signaling in glial cells: calcium waves and oscillations in response to mechanical stimulation and glutamate. *Neuron* 6, 983-992.

Chen, T.W., Wardill, T.J., Sun, Y., Pulver, S.R., Renninger, S.L., Baohan, A., Schreiter, E.R., Kerr, R.A., Orger, M.B., Jayaraman, V., *et al.* (2013). Ultrasensitive fluorescent proteins for imaging neuronal activity. *Nature* 499, 295-300.

Chiu, F.-C., Norton, W.T., and Fields, K.L. (1981). The Cytoskeleton of Primary Astrocytes in Culture Contains Actin, Glial Fibrillary Acidic Protein, and the Fibroblast-Type Filament Protein, Vimentin. *Journal of Neurochemistry* 37, 147-155.

Chow, L.M., Zhang, J., and Baker, S.J. (2008). Inducible Cre recombinase activity in mouse mature astrocytes and adult neural precursor cells. *Transgenic Res* 17, 919-928.

Christopherson, K.S., Ullian, E.M., Stokes, C.C., Mallowney, C.E., Hell, J.W., Agah, A., Lawler, J., Mosher, D.F., Bornstein, P., and Barres, B.A. (2005). Thrombospondins are astrocyte-secreted proteins that promote CNS synaptogenesis. *Cell* 120, 421-433.

Chung, W.-S., Clarke, L.E., Wang, G.X., Stafford, B.K., Sher, A., Chakraborty, C., Joung, J., Foo, L.C., Thompson, A., Chen, C., *et al.* (2013). Astrocytes mediate synapse elimination through MEGF10 and MERTK pathways. *Nature* 504, 394-400.

Chung, W.-S., Verghese, P.B., Chakraborty, C., Joung, J., Hyman, B.T., Ulrich, J.D., Holtzman, D.M., and Barres, B.A. (2016). Novel allele-dependent role for APOE in controlling the rate of synapse pruning by astrocytes. *Proceedings of the National Academy of Sciences* 113, 10186-10191.

Chung, W.-S., Welsh, C.A., Barres, B.A., and Stevens, B. (2015a). Do glia drive synaptic and cognitive impairment in disease? *Nature neuroscience* 18, 1539-1545.

Chung, W.S., Allen, N.J., and Eroglu, C. (2015b). Astrocytes Control Synapse Formation, Function, and Elimination. *Cold Spring Harb Perspect Biol* Feb 6;7(9). *pii*: a020370. *doi*: 10.1101/cshperspect.a020370.

Cornell-Bell, A.H., Finkbeiner, S.M., Cooper, M.S., and Smith, S.J. (1990a). Glutamate induces calcium waves in cultured astrocytes: long-range glial signaling. *Science* *247*, 470-473.

Cornell-Bell, A.H., Thomas, P.G., and Smith, S.J. (1990b). The excitatory neurotransmitter glutamate causes filopodia formation in cultured hippocampal astrocytes. *Glia* *3*, 322-334.

Cui, Q., Pitt, J.E., Pamukcu, A., Poulin, J.F., Mabrouk, O.S., Fiske, M.P., Fan, I.B., Augustine, E.C., Young, K.A., Kennedy, R.T., *et al.* (2016). Blunted mGluR Activation Disinhibits Striatopallidal Transmission in Parkinsonian Mice. *Cell Rep* *17*, 2431-2444.

D'Ascenzo, M., Fellin, T., Terunuma, M., Revilla-Sanchez, R., Meaney, D.F., Auberson, Y.P., Moss, S.J., and Haydon, P.G. (2007). mGluR5 stimulates gliotransmission in the nucleus accumbens. *Proc Natl Acad Sci U S A* *104*, 1995-2000.

Dani, J.W., Chernjavsky, A., and Smith, S.J. (1992). Neuronal activity triggers calcium waves in hippocampal astrocyte networks. *Neuron* *8*, 429-440.

Davila, D., Thibault, K., Fiacco, T.A., and Agulhon, C. (2013). Recent molecular approaches to understanding astrocyte function in vivo. *Front Cell Neurosci* *Dec 24;7:272*. doi: [10.3389/fncel.2013.00272](https://doi.org/10.3389/fncel.2013.00272).

Di Castro, M.A., Chuquet, J., Liaudet, N., Bhaukaurally, K., Santello, M., Bouvier, D., Tiret, P., and Volterra, A. (2011). Local Ca<sup>2+</sup> detection and modulation of synaptic release by astrocytes. *Nature neuroscience* *14*, 1276-1284.

Dietschy, J.M., and Turley, S.D. (2004). Thematic review series: Brain Lipids. Cholesterol metabolism in the central nervous system during early development and in the mature animal. *Journal of Lipid Research* *45*, 1375-1397.

Ding, F., O'Donnell, J., Thrane, A.S., Zeppenfeld, D., Kang, H., Xie, L., Wang, F., and Nedergaard, M. (2013). alpha1-Adrenergic receptors mediate coordinated Ca<sup>2+</sup> signaling of cortical astrocytes in awake, behaving mice. *Cell calcium* *54*, 387-394.

Emsley, J.G., and Macklis, J.D. (2006). Astroglial heterogeneity closely reflects the neuronal-defined anatomy of the adult murine CNS. *Neuron glia biology* 2, 175-186.

Enkvist, M.O., Holopainen, I., and Akerman, K.E. (1989). Alpha-receptor and cholinergic receptor-linked changes in cytosolic Ca<sup>2+</sup> and membrane potential in primary rat astrocytes. *Brain research* 500, 46-54.

Eroglu, C. (2009). The role of astrocyte-secreted extracellular matrix proteins in central nervous system development and function. *J Cell Commun Signal* 3, 167-176.

Eroglu, C., Allen, N.J., Susman, M.W., O'Rourke, N.A., Park, C.Y., Ozkan, E., Chakraborty, C., Mulinyawe, S.B., Annis, D.S., Huberman, A.D., *et al.* (2009). Gabapentin receptor alpha2delta-1 is a neuronal thrombospondin receptor responsible for excitatory CNS synaptogenesis. *Cell* 139, 380-392.

Everitt, B.J., and Robbins, T.W. (2013). From the ventral to the dorsal striatum: Devolving views of their roles in drug addiction. *Neuroscience & Biobehavioral Reviews* 37, 1946-1954.

Fan, W., and Fu, T. (2014). Somatostatin modulates LTP in hippocampal CA1 pyramidal neurons: Differential activation conditions in apical and basal dendrites. *Neuroscience Letters* 561, 1-6.

Farwell, A., Lynch, R., Okulicz, W., Comi, A., and Leonard, J. (1990). The actin cytoskeleton mediates the hormonally regulated translocation of type II iodothyronine 5'-deiodinase in astrocytes. *J Biol Chem* 265, 18546-18563.

Fiacco, T.A., Agulhon, C., Taves, S.R., Petravic, J., Casper, K.B., Dong, X., Chen, J., and McCarthy, K.D. (2007). Selective stimulation of astrocyte calcium in situ does not affect neuronal excitatory synaptic activity. *Neuron* 54, 611-626.

Fiala, J.C. (2005). Reconstruct: a free editor for serial section microscopy. *Journal of Microscopy* 218, 52-61.

Foo, L.C. (2013). Purification of astrocytes from transgenic rodents by fluorescence-activated cell sorting. *Cold Spring Harb Protoc* 2013(6), 551-560.

Foo, L.C., Allen, N.J., Bushong, E.A., Ventura, P.B., Chung, W.S., Zhou, L., Cahoy, J.D., Daneman, R., Zong, H., Ellisman, M.H., *et al.* (2011). Development of a method for the purification and culture of rodent astrocytes. *Neuron* 71, 799-811.

Foo, L.C., and Dougherty, J.D. (2013). Aldh1L1 is expressed by postnatal neural stem cells in vivo. *Glia* 61, 1533-1541.

Francelle, L., Galvan, L., Gaillard, M.C., Guillemier, M., Houitte, D., Bonvento, G., Petit, F., Jan, C., Dufour, N., Hantraye, P., *et al.* (2015). Loss of the thyroid hormone-binding protein Crym renders striatal neurons more vulnerable to mutant huntingtin in Huntington's disease. *Hum Mol Genet* 24, 1563-1573.

Fujita, T., Chen, M.J., Li, B., Smith, N.A., Peng, W., Sun, W., Toner, M.J., Kress, B.T., Wang, L., Benraiss, A., *et al.* (2014). Neuronal transgene expression in dominant-negative SNARE mice. *J Neurosci* 34, 16594-16604.

Garcia, A.D., Doan, N.B., Imura, T., Bush, T.G., and Sofroniew, M.V. (2004). GFAP-expressing progenitors are the principal source of constitutive neurogenesis in adult mouse forebrain. *Nature neuroscience* 7, 1233-1241.

Genoud, C., Houades, V., Kraftsik, R., Welker, E., and Giaume, C. (2015). Proximity of excitatory synapses and astroglial gap junctions in layer IV of the mouse barrel cortex. *Neuroscience* 291, 241-249.

Giaume, C., Koulakoff, A., Roux, L., Holcman, D., and Rouach, N. (2010). Astroglial networks: a step further in neuroglial and gliovascular interactions. *Nat Rev Neurosci* 2, 87-99.

Gong, S., Zheng, C., Doughty, M.L., Losos, K., Didkovsky, N., Schambra, U.B., Nowak, N.J., Joyner, A., Leblanc, G., Hatten, M.E., *et al.* (2003). A gene expression atlas of the central nervous system based on bacterial artificial chromosomes. *Nature* 425, 917-925.

Gould, T., Chen, L., Emri, Z., Pirrtimaki, T., Errington, A.C., Crunelli, V., and Parri, H.R. (2014). GABA(B) receptor-mediated activation of astrocytes by gamma-hydroxybutyric acid. *Philosophical transactions of the Royal Society of London Series B, Biological sciences* 369, 20130607.

Goursaud, S., Kozlova, E.N., Maloteaux, J.-M., and Hermans, E. (2009). Cultured astrocytes derived from corpus callosum or cortical grey matter show distinct glutamate handling properties. *Journal of Neurochemistry* 108, 1442-1452.

Graybiel, A.M. (2008). Habits, rituals, and the evaluative brain. *Annu Rev Neurosci* 31, 359-387.

Gregorian, C., Nakashima, J., Le Belle, J., Ohab, J., Kim, R., Liu, A., Smith, K.B., Groszer, M., Garcia, A.D., Sofroniew, M.V., *et al.* (2009). Pten deletion in adult neural stem/progenitor cells enhances constitutive neurogenesis. *J Neurosci* 29, 1874-1886.

Griemsmann, S., Hoft, S.P., Bedner, P., Zhang, J., von Staden, E., Beinhauer, A., Degen, J., Dublin, P., Cope, D.W., Richter, N., *et al.* (2015). Characterization of Panglial Gap Junction Networks in the Thalamus, Neocortex, and Hippocampus Reveals a Unique Population of Glial Cells. *Cerebral cortex (New York, NY : 1991)* 25, 3420-3433.

Haim, L.B., and Rowitch, D.H. (2017). Functional diversity of astrocytes in neural circuit regulation. *Nat Rev Neurosci* 18, 31-41.

Halassa, M.M., and Haydon, P.G. (2010). Integrated brain circuits: astrocytic networks modulate neuronal activity and behavior. *Annu Rev Physiol* 72, 335-355.

Hama, H., Hioki, H., Namiki, K., Hoshida, T., Kurokawa, H., Ishidate, F., Kaneko, T., Akagi, T., Saito, T., Saido, T., *et al.* (2015). ScaleS: an optical clearing palette for biological imaging. *Nature neuroscience* 18, 1518-1529.

Han, Y., Yu, H.X., Sun, M.L., Wang, Y., Xi, W., and Yu, Y.Q. (2014). Astrocyte-restricted disruption of Connexin-43 impairs neuronal plasticity in mouse barrel cortex. *The European journal of neuroscience* 39, 35-45.

Hansson, E. (1984). Enzyme activities of monoamine oxidase, catechol-o-methyltransferase and  $\gamma$ -aminobutyric acid transaminase in primary astroglial cultures and adult rat brain from different brain regions. *Neurochemical Research* 9, 45-57.

Harris, K.M., Jensen, F.E., and Tsao, B. (1992). Three-dimensional structure of dendritic spines and synapses in rat hippocampus (CA1) at postnatal day 15 and adult ages: implications for the maturation of synaptic physiology and long-term potentiation. *J Neurosci* 12, 2685-2705.

Hassel, B., Boldingh, K.A., Narvesen, C., Iversen, E.G., and Skrede, K.K. (2003). Glutamate transport, glutamine synthetase and phosphate-activated glutaminase in rat CNS white matter. A quantitative study. *Journal of Neurochemistry* 87, 230-237.

Haustein, M.D., Kracun, S., Lu, X.H., Shih, T., Jackson-Weaver, O., Tong, X., Xu, J., Yang, X.W., O'Dell, T.J., Marvin, J.S., *et al.* (2014). Conditions and constraints for astrocyte calcium signaling in the hippocampal mossy fiber pathway. *Neuron* 82, 413-429.

Henneberger, C., Papouin, T., Oliet, S.H., and Rusakov, D.A. (2010). Long-term potentiation depends on release of D-serine from astrocytes. *Nature* 463, 232-236.

Herculano-Houzel, S. (2014). The glia/neuron ratio: How it varies uniformly across brain structures and species and what that means for brain physiology and evolution. *Glia* 62, 1377-1391.

Hirase, H., Qian, L., Bartho, P., and Buzsaki, G. (2004). Calcium dynamics of cortical astrocytic networks in vivo. *PLoS biology* 2, E96.

Ingham, C.A., Hood, S.H., Taggart, P., and Arbuthnott, G.W. (1998). Plasticity of synapses in the rat neostriatum after unilateral lesion of the nigrostriatal dopaminergic pathway. *Journal of Neuroscience* 18, 4732-4743.

Jackson, J.G., and Robinson, M.B. (2015). Reciprocal Regulation of Mitochondrial Dynamics and Calcium Signaling in Astrocyte Processes. *J Neurosci* 35, 15199-15213.

Jiang, M., and Bajpayee, N.S. (2009). Molecular mechanisms of Gq signaling. *Neurosignals* 17, 23-41.

Jiang, R., Diaz-Castro, B., Tong, X., Looger, L.L., and Khakh, B.S. (2016). Dysfunctional calcium and glutamate signaling in striatal astrocytes from Huntington's disease model mice. *J Neurosci* 36, 3453-3470.

Jiang, R., Hausteiner, M.D., Sofroniew, M.V., and Khakh, B.S. (2014). Imaging intracellular Ca<sup>2+</sup> signals in striatal astrocytes from adult mice using genetically-encoded calcium indicators. *Journal of Visualized Experiments*, e51972.

Jourdain, P., Bergersen, L.H., Bhaukaurally, K., Bezzi, P., Santello, M., Domercq, M., Matute, C., Tonello, F., Gundersen, V., and Volterra, A. (2007). Glutamate exocytosis from astrocytes controls synaptic strength. *Nature neuroscience* 10, 331-339.

Juszczak, G.R., and Swiergiel, A.H. (2009). Properties of gap junction blockers and their behavioural, cognitive and electrophysiological effects: Animal and human studies. *Progress in Neuro-Psychopharmacology and Biological Psychiatry* 33, 181-198.

Kang, J., Jiang, L., Goldman, S., and Nedergaard, M. (1998). Astrocyte-mediated potentiation of inhibitory synaptic transmission. *Nature neuroscience* 1, 683-692.

Kepecs, A., and Fishell, G. (2014). Interneuron cell types are fit to function. *Nature* 505, 318-326.

Kettenmann, H., and Verkhratsky, A. (2008). Neuroglia: the 150 years after. *Trends Neurosci* 31, 653-659.

Khakh, B.S., and McCarthy, K.D. (2015). Astrocyte Calcium Signaling: From Observations to Functions and the Challenges Therein. *Cold Spring Harbor Perspectives in Biology* 7, a020404.

Khakh, B.S., and Sofroniew, M.V. (2015). Diversity of astrocyte functions and phenotypes in neural circuits. *Nature neuroscience* 18, 942-952.

Kimelberg, H.K. (1983). Primary astrocyte cultures—a key to astrocyte function. *Cellular and Molecular Neurobiology* 3, 1-16.

Kimelberg, H.K., Cai, Z., Rastogi, P., Charniga, C.J., Goderie, S., Dave, V., and Jalonen, T.O. (1997). Transmitter-induced calcium responses differ in astrocytes acutely isolated from rat brain and in culture. *J Neurochem* 68, 1088-1098.

Kirino, T., Tamura, A., and Sano, K. (1984). Delayed neuronal death in the rat hippocampus following transient forebrain ischemia. *Acta Neuropathologica* 64, 139-147.

Kitchen, R.R., Rozowsky, J.S., Gerstein, M.B., and Nairn, A.C. (2014). Decoding neuroproteomics: integrating the genome, transcriptome and functional anatomy. *Nature neuroscience* 17, 1491-1499.

Klausberger, T., Magill, P.J., Marton, L.F., Roberts, J.D., Cobden, P.M., Buzsaki, G., and Somogyi, P. (2003). Brain-state- and cell-type-specific firing of hippocampal interneurons in vivo. *Nature* 421, 844-848.

Kosaka, T., and Hama, K. (1986). Three-dimensional structure of astrocytes in the rat dentate gyrus. *J Comp Neurol* 249, 242-260.

Kucukdereli, H., Allen, N.J., Lee, A.T., Feng, A., Ozlu, M.I., Conatser, L.M., Chakraborty, C., Workman, G., Weaver, M., Sage, E.H., *et al.* (2011). Control of excitatory CNS synaptogenesis by astrocyte-secreted proteins Hevin and SPARC. *Proceedings of the National Academy of Sciences* *108*, E440-E449.

Kuffler, S. (1967). Neuroglial cells: physiological properties and a potassium mediated effect of neuronal activity on the glial membrane potential. *Proc R Soc Lond B Biol Sci* *168*, 1-21.

Kuffler, S.W., and Potter, D.D. (1964). GLIA IN THE LEECH CENTRAL NERVOUS SYSTEM: PHYSIOLOGICAL PROPERTIES AND NEURON-GLIA RELATIONSHIP. *Journal of neurophysiology* *27*, 290-320.

Kuleshov, M.V., Jones, M.R., Rouillard, A.D., Fernandez, N.F., Duan, Q., Wang, Z., Koplev, S., Jenkins, S.L., Jagodnik, K.M., Lachmann, A., *et al.* (2016). Enrichr: a comprehensive gene set enrichment analysis web server 2016 update. *Nucleic Acids Research* *44*, W90-W97.

Kulkarni, P.M., Barton, E., Savelonas, M., Padmanabhan, R., Lu, Y., Trett, K., Shain, W., Leasure, J.L., and Roysam, B. (2015). Quantitative 3-D analysis of GFAP labeled astrocytes from fluorescence confocal images. *J Neurosci Methods* *246*, 38-51.

Law, C.W., Chen, Y., Shi, W., and Smyth, G.K. (2014). voom: precision weights unlock linear model analysis tools for RNA-seq read counts. *Genome Biology* *15*, R29.

Lein, E.S., Hawrylycz, M.J., Ao, N., Ayres, M., Bensinger, A., Bernard, A., Boe, A.F., Boguski, M.S., Brockway, K.S., Byrnes, E.J., *et al.* (2007). Genome-wide atlas of gene expression in the adult mouse brain. *Nature* *445*, 168-176.

Li, D., Herault, K., Silm, K., Evrard, A., Wojcik, S., Oheim, M., Herzog, E., and Ropert, N. (2013). Lack of evidence for vesicular glutamate transporter expression in mouse astrocytes. *J Neurosci* *33*, 4434-4455.

Li, Y., Liu, Z., Xin, H., and Chopp, M. (2014). The role of astrocytes in mediating exogenous cell-based restorative therapy for stroke. *Glia* 62, 1-16.

Liddelw, S.A., Guttenplan, K.A., Clarke, L.E., Bennett, F.C., Bohlen, C.J., Schirmer, L., Bennett, M.L., Münch, A.E., Chung, W.-S., Peterson, T.C., *et al.* (2017). Neurotoxic reactive astrocytes are induced by activated microglia. *Nature advance online publication*.

Liu, Z., Li, Y., Cui, Y., Roberts, C., Lu, M., Wilhelmsson, U., Pekny, M., and Chopp, M. (2014). Beneficial effects of gfap/vimentin reactive astrocytes for axonal remodeling and motor behavioral recovery in mice after stroke. *Glia* 62, 2022-2033.

Lundgaard, I., Osorio, M.J., Kress, B.T., Sanggaard, S., and Nedergaard, M. (2014). White matter astrocytes in health and disease. *Neuroscience* 276, 161-173.

Madisen, L., Garner, A.R., Shimaoka, D., Chuong, A.S., Klapoetke, N.C., Li, L., van der Bourg, A., Niino, Y., Egolf, L., Monetti, C., *et al.* (2015). Transgenic mice for intersectional targeting of neural sensors and effectors with high specificity and performance. *Neuron* 85, 942-958.

Madisen, L., Zwingman, T.A., Sunkin, S.M., Oh, S.W., Zariwala, H.A., Gu, H., Ng, L.L., Palmiter, R.D., Hawrylycz, M.J., Jones, A.R., *et al.* (2010). A robust and high-throughput Cre reporting and characterization system for the whole mouse brain. *Nature neuroscience* 13, 133-140.

Malach, R., and Graybiel, A.M. (1986). Mosaic architecture of the somatic sensory-recipient sector of the cat's striatum. *The Journal of Neuroscience* 6, 3436.

Martín, R., Bajo-Grañeras, R., Moratalla, R., Perea, G., and Araque, A. (2015). Circuit-specific signaling in astrocyte-neuron networks in basal ganglia pathways. *Science* 349, 730-734.

Marvin, J.S., Borghuis, B.G., Tian, L., Cichon, J., Harnett, M.T., Akerboom, J., Gordus, A., Renninger, S.L., Chen, T.W., Bargmann, C.I., *et al.* (2013). An optimized fluorescent probe for visualizing glutamate neurotransmission. *Nat Methods* 10, 162-170.

- Melom, J.E., and Littleton, J.T. (2013). Mutation of a NCKX eliminates glial microdomain calcium oscillations and enhances seizure susceptibility. *J Neurosci* 33, 1169-1178.
- Middeldorp, J., and Hol, E.M. (2011). GFAP in health and disease. *Prog Neurobiol* 93, 421-443.
- Molofsky, A.V., and Deneen, B. (2015). Astrocyte development: A Guide for the Perplexed. *Glia* 63, 1320-1329.
- Molofsky, A.V., Glasgow, S.M., Chaboub, L.S., Tsai, H.H., Murnen, A.T., Kelley, K.W., Fancy, S.P., Yuen, T.J., Madireddy, L., Baranzini, S., *et al.* (2013). Expression profiling of Aldh1l1-precursors in the developing spinal cord reveals glial lineage-specific genes and direct Sox9-Nfe2l1 interactions. *Glia* 61, 1518-1532.
- Molofsky, A.V., Kelley, K.W., Tsai, H.H., Redmond, S.A., Chang, S.M., Madireddy, L., Chan, J.R., Baranzini, S.E., Ullian, E.M., and Rowitch, D.H. (2014). Astrocyte-encoded positional cues maintain sensorimotor circuit integrity. *Nature* 509, 189-194.
- Morris, R. (2007). Chapter 13: Theories of hippocampal function. *The Hippocampus Book* Ed Andersen, Morris, Amaral, Bliss, O'Keefe *Oxford University Press*.
- Mulkey, D.K., and Wenker, I.C. (2011). Astrocyte chemoreceptors: mechanisms of H<sup>+</sup> sensing by astrocytes in the retrotrapezoid nucleus and their possible contribution to respiratory drive. *Experimental Physiology* 96, 400-406.
- Nagy, J., Patel, D., Ochalski, P., and Stelmack, G. (1999). Connexin30 in rodent, cat and human brain: selective expression in gray matter astrocytes, co-localization with Connexin43 at gap junctions and late developmental appearance. *Neuroscience* 88, 447-468.
- Nagy, J., and Rash, J. (2000). Connexins and gap junctions of astrocytes and oligodendrocytes in the CNS. *Brain Res Brain Res Rev* 32, 29-44.

Nakai, J., Ohkura, M., and Imoto, K. (2001). A high signal-to-noise Ca(2+) probe composed of a single green fluorescent protein. *Nature biotechnology* 19, 137-141.

Nakamura, E., Nguyen, M.T., and Mackem, S. (2006). Kinetics of tamoxifen-regulated Cre activity in mice using a cartilage-specific CreER(T) to assay temporal activity windows along the proximodistal limb skeleton. *Dev Dyn* 235, 2603-2612.

Nakase, T., and Naus, C.C.G. (2004). Gap junctions and neurological disorders of the central nervous system. *Biochimica et Biophysica Acta (BBA) - Biomembranes* 1662, 149-158.

Nakase, T., Söhl, G., Theis, M., Willecke, K., and Naus, C.C.G. (2004). Increased Apoptosis and Inflammation after Focal Brain Ischemia in Mice Lacking Connexin43 in Astrocytes. *The American Journal of Pathology* 164, 2067-2075.

Navarrete, M., and Araque, A. (2008). Endocannabinoids mediate neuron-astrocyte communication. *Neuron* 57, 883-893.

Nawashiro, H., Brenner, M., Fukui, S., Shima, K., and Hallenbeck, J.M. (2000). High susceptibility to cerebral ischemia in GFAP-null mice. *Journal of Cerebral Blood Flow and Metabolism* 20, 1040-1044.

Nedergaard, M., Rodríguez, J.J., and Verkhratsky, A. (2010). Glial calcium and diseases of the nervous system. *Cell calcium* 47, 140-149.

Nett, W.J., Oloff, S.H., and McCarthy, K.D. (2002). Hippocampal astrocytes in situ exhibit calcium oscillations that occur independent of neuronal activity. *Journal of neurophysiology* 87, 528-537.

Neufeld, A.H., and Liu, B. (2003). Glaucomatous optic neuropathy: when glia misbehave. *The Neuroscientist : a review journal bringing neurobiology, neurology and psychiatry* 9, 485-495.

Nikonenko, A.G., Radenovic, L., Andjus, P.R., and Skibo, G.G. (2009). Structural features of ischemic damage in the hippocampus. *Anatomical record* 292, 1914-1921.

Niu, W., Zang, T., Zou, Y., Fang, S., Smith, D.K., Bachoo, R., and Zhang, C.L. (2013). In vivo reprogramming of astrocytes to neuroblasts in the adult brain. *Nat Cell Biol* 15, 1164-1175.

Nwaobi, S.E., Cuddapah, V.A., Patterson, K.C., Randolph, A.C., and Olsen, M.L. (2016). The role of glial-specific Kir4.1 in normal and pathological states of the CNS. *Acta Neuropathol* 132, 1-21.

Oberheim, N.A., Goldman, S.A., and Nedergaard, M. (2012). Heterogeneity of Astrocytic Form and Function. In *Astrocytes: Methods and Protocols*, R. Milner, ed. (Humana Press), pp. 23-45.

Oliveira, J.F., Sardinha, V.M., Guerra-Gomes, S., Araque, A., and Sousa, N. (2015). Do stars govern our actions? Astrocyte involvement in rodent behavior. *Trends Neurosci* 38, 535-549.

Otsu, Y., Couchman, K., Lyons, D.G., Collot, M., Agarwal, A., Mallet, J., Pfrieder, F.W., Bergles, D.E., and Charpak, S. (2014). Calcium dynamics in astrocyte processes during neurovascular coupling. *Nature neuroscience*.

Palmiter, R.D. (2008). Dopamine Signaling in the Dorsal Striatum Is Essential for Motivated Behaviors: Lessons from Dopamine-deficient Mice. *Annals of the New York Academy of Sciences* 1129, 35-46.

Panatier, A., Vallee, J., Haber, M., Murai, K.K., Lacaille, J.C., and Robitaille, R. (2011). Astrocytes are endogenous regulators of basal transmission at central synapses. *Cell* 146, 785-798.

Pang, Z.P., and Südhof, T.C. (2010). Cell biology of Ca<sup>2+</sup>-triggered exocytosis. *Curr Opin Cell Biol* 22, 496-505.

Pannasch, U., Freche, D., Dallérac, G., Ghézali, G., Escartin, C., Ezan, P., Cohen-Salmon, M., Benchenane, K., Abudara, V., Dufour, A., *et al.* (2014). Connexin 30 sets synaptic strength by controlling astroglial synapse invasion. *Nature neuroscience*.

Pannasch, U., Vargová, L., Reingruber, J., Ezan, P., Holcman, D., Giaume, C., Syková, E., and Rouach, N. (2011). Astroglial networks scale synaptic activity and plasticity. *Proceedings of the National Academy of Sciences* 108, 8467-8472.

Papp, M., and Bal, A. (1987). Separation of the motivational and motor consequences of 6-hydroxydopamine lesions of the mesolimbic or nigrostriatal system in rats. *Behavioural brain research* 23, 221-229.

Parpura, V., Basarsky, T.A., Liu, F., Jęftinija, K., Jęftinija, S., and Haydon, P.G. (1994). Glutamate-mediated astrocyte-neuron signalling. *Nature* 369, 744-747.

Pascual, O., Casper, K.B., Kubera, C., Zhang, J., Revilla-Sanchez, R., Sul, J.Y., Takano, H., Moss, S.J., McCarthy, K., and Haydon, P.G. (2005). Astrocytic purinergic signaling coordinates synaptic networks. *Science* 310, 113-116.

Pasti, L., Volterra, A., Pozzan, T., and Carmignoto, G. (1997). Intracellular calcium oscillations in astrocytes: a highly plastic, bidirectional form of communication between neurons and astrocytes in situ. *J Neurosci* 17, 7817-7830.

Paukert, M., Agarwal, A., Cha, J., Doze, V.A., Kang, J.U., and Bergles, D.E. (2014). Norepinephrine controls astroglial responsiveness to local circuit activity. *Neuron* 82, 1263-1270.

Perea, G., and Araque, A. (2007). Astrocytes potentiate transmitter release at single hippocampal synapses. *Science* 317, 1083-1086.

Pert, C.B., Kuhar, M.J., and Snyder, S.H. (1976). Opiate receptor: autoradiographic localization in rat brain. *Proceedings of the National Academy of Sciences of the United States of America* 73, 3729-3733.

Petravicz, J., Boyt, K.M., and McCarthy, K.D. (2014). Astrocyte IP3R2-dependent Ca(2+) signaling is not a major modulator of neuronal pathways governing behavior. *Frontiers in behavioral neuroscience* 8, 384.

Phatnani, H., and Maniatis, T. (2015). Astrocytes in neurodegenerative disease. *Cold Spring Harb Perspect Biol* Apr 15;7(6). pii: a020628. doi: 10.1101/cshperspect.a020628.

Pioli, E.Y., Meissner, W., Sohr, R., Gross, C.E., Bezard, E., and Bioulac, B.H. (2008). Differential behavioral effects of partial bilateral lesions of ventral tegmental area or substantia nigra pars compacta in rats. *Neuroscience* 153, 1213-1224.

Plaisier, S.B., Taschereau, R., Wong, J.A., and Graeber, T.G. (2010). Rank-rank hypergeometric overlap: identification of statistically significant overlap between gene-expression signatures. *Nucleic Acids Res* Sep;38(17):e169. doi: 10.1093/nar/gkq636. Epub 2010 Jul 21.

Polack, P.O., Friedman, J., and Golshani, P. (2013). Cellular mechanisms of brain state-dependent gain modulation in visual cortex. *Nature neuroscience* 16, 1331-1339.

Porter, J.T., and McCarthy, K.D. (1995). GFAP-positive hippocampal astrocytes in situ respond to glutamatergic neuroligands with increases in [Ca<sup>2+</sup>]<sub>i</sub>. *Glia* 13, 101-112.

Porter, J.T., and McCarthy, K.D. (1996). Hippocampal astrocytes in situ respond to glutamate released from synaptic terminals. *J Neurosci* 16, 5073-5081.

Prochiantz, A., and Mallat, M. (1988). Astrocyte Diversity. *Annals of the New York Academy of Sciences* 540, 52-63.

Pulsinelli, W.A., Brierley, J.B., and Plum, F. (1982). Temporal profile of neuronal damage in a model of transient forebrain ischemia. *Annals of Neurology* 11, 491-498.

Qureshi, A.I., Tuhim, S., Broderick, J.P., Batjer, H.H., Hondo, H., and Hanley, D.F. (2001). Spontaneous Intracerebral Hemorrhage. *N Engl J Med* 344, 1450-1460.

Ramón y Cajal, S., and DeFelipe, J. (1988). *Cajal on the Cerebral Cortex: An Annotated Translation of the Complete Writings* ( Oxford University Press).

RCoreTeam (2016). R: A language and environment for statistical computing. R Foundation for Statistical Computing, Vienna, Austria URL <https://www.R-project.org/>.

Roqué, A.L. (1966). A Modification of Cajal's Gold-Sublimate Method for Tissue Fixed in Formalin *Acta Neuropathol* 6, 88-92.

Roth, B.L. (2016). DREADDs for Neuroscientists. *Neuron* 89, 683-694.

Rovira, A., Grive, E., Rovira, A., and Alvarez-Sabin, J. (2005). Distribution territories and causative mechanisms of ischemic stroke. *European radiology* 15, 416-426.

Rungta, R.L., Bernier, L.P., Dissing-Olesen, L., Groten, C.J., LeDue, J.M., Ko, R., Drissler, S., and MacVicar, B.A. (2016). Ca<sup>2+</sup> transients in astrocyte fine processes occur via Ca<sup>2+</sup> influx in the adult mouse hippocampus. *Glia* 64, 2093-2103.

Sanz, E., Yang, L., Su, T., Morris, D.R., McKnight, G.S., and Amieux, P.S. (2009). Cell-type-specific isolation of ribosome-associated mRNA from complex tissues. *Proc Natl Acad Sci U S A* 106, 13939-13944.

Sauer, B. (1994). Site-specific recombination: developments and applications. *Curr Opin Biotechnol* 5, 521-527.

Schafer, D.P., and Stevens, B. (2015). Microglia Function in Central Nervous System Development and Plasticity. *Cold Spring Harbor Perspectives in Biology* 7.

Shigetomi, E., Bowser, D.N., Sofroniew, M.V., and Khakh, B.S. (2008). Two Forms of Astrocyte Calcium Excitability Have Distinct Effects on NMDA Receptor-Mediated Slow Inward Currents in Pyramidal Neurons. *Journal of Neuroscience* 28, 6659-6663.

Shigetomi, E., Bushong, E.A., Hausteiner, M.D., Tong, X., Jackson-Weaver, O., Kracun, S., Xu, J., Sofroniew, M.V., Ellisman, M.H., and Khakh, B.S. (2013). Imaging calcium microdomains within entire astrocyte territories and endfeet with GCaMPs expressed using adeno-associated viruses. *The Journal of general physiology* 141, 633-647.

Shigetomi, E., Kracun, S., and Khakh, B.S. (2010). Monitoring astrocyte calcium microdomains with improved membrane targeted GCaMP reporters. *Neuron Glia Biology* 6, 183-191.

Shigetomi, E., Patel, S., and Khakh, B.S. (2016). Probing the Complexities of Astrocyte Calcium Signaling. *Trends Cell Biol* 26, 300-312.

Sholl, D.A. (1953). Dendritic organization in the neurons of the visual and motor cortices of the cat. *Journal of Anatomy* 87, 387-406.381.

Singh, S.K., Stogsdill, J.A., Pulimood, N.S., Dingsdale, H., Kim, Y.H., Pilaz, L.J., Kim, I.H., Manhaes, A.C., Rodrigues, W.S., Jr., Pamukcu, A., *et al.* (2016). Astrocytes Assemble Thalamocortical Synapses by Bridging NRX1alpha and NL1 via Hevin. *Cell* 164, 183-196.

Slezak, M., Göritz, C., Niemiec, A., Frisén, J., Chambon, P., Metzger, D., and Pfrieder, F.W. (2007). Transgenic mice for conditional gene manipulation in astroglial cells. *Glia* 55, 1565-1576.

Sloan, S.A., and Barres, B.A. (2014). Looks can be deceiving: reconsidering the evidence for gliotransmission. *Neuron* 84, 1112-1115.

Sofroniew, M.V., and Vinters, H.V. (2010). Astrocytes: biology and pathology. *Acta Neuropathologica* 119, 7-35.

Soreq, L., Consortium., U.B.E., Consortium., N.A.B.E., Rose, J., Soreq, E., Hardy, J., Trabzuni, D., Cookson, M.R., Smith, C., Ryten, M., *et al.* (2017). Major Shifts in Glial Regional Identity Are a Transcriptional Hallmark of Human Brain Aging. *Cell Rep* 18, 557-570.

Sosunov, A.A., Wu, X., Tsankova, N.M., Guilfoyle, E., McKhann, G.M., 2nd, and Goldman, J.E. (2014). Phenotypic heterogeneity and plasticity of isocortical and hippocampal astrocytes in the human brain. *J Neurosci* 34, 2285-2298.

Şovrea, A.S., and Boşca, A.B. (2013). Astrocytes reassessment - an evolving concept part one: embryology, biology, morphology and reactivity. *Journal of Molecular Psychiatry* 1, eCollection 2013.

Spruston, N., and McBain, C. (2007). Chapter 5: Structural and functional properties of hippocampal neurons. *The Hippocampus Book* Ed Andersen, Morris, Amaral, Bliss, O'Keefe *Oxford University Press*.

Srinivasan, R., Huang, B.S., Venugopal, S., Johnston, A.D., Chai, H., Zeng, H., Golshani, P., and Khakh, B.S. (2015). Ca<sup>2+</sup> signaling in astrocytes from *Ip3r2(-/-)* mice in brain slices and during startle responses in vivo. *Nature neuroscience* 18, 708-717.

Srinivasan, R., Lu, T.-Y., Chai, H., Xu, J., Huang, B.S., Golshani, P., Coppola, G., and Khakh, B.S. (2016). New Transgenic Mouse Lines for Selectively Targeting Astrocytes and Studying Calcium Signals in Astrocyte Processes In Situ and In Vivo. *Neuron* 92, 1181-1195.

Stein, J.L., de la Torre-Ubieta, L., Tian, Y., Parikhshak, N.N., Hernández, I.A., Marchetto, M.C., Baker, D.K., Lu, D., Hinman, C.R., Lowe, J.K., *et al.* (2014). A quantitative framework to evaluate modeling of cortical development by neural stem cells. *Neuron* 83, 69-86.

Sternweis, P., and Robishaw, J. (1984). Isolation of two proteins with high affinity for guanine nucleotides from membranes of bovine brain. *The Journal of Biological Chemistry*, 13806-13813.

Stiene-Martin, A., Zhou, R., and Hauser, K.F. (1998). Regional, developmental, and cell cycle-dependent differences in mu, delta, and kappa-opioid receptor expression among cultured mouse astrocytes. *Glia* 22, 249-259.

Su, M., Hu, H., Lee, Y., d'Azzo, A., Messing, A., and Brenner, M. (2004). Expression specificity of GFAP transgenes. *Neurochem Res* 29, 2075-2093.

Sultan, S., Li, L., Moss, J., Petrelli, F., Casse, F., Gebara, E., Lopatar, J., Pfrieder, F.W., Bezzi, P., Bischofberger, J., *et al.* (2015). Synaptic Integration of Adult-Born Hippocampal Neurons Is Locally Controlled by Astrocytes. *Neuron* 88, 957-972.

Sun, W., McConnell, E., Pare, J.F., Xu, Q., Chen, M., Peng, W., Lovatt, D., Han, X., Smith, Y., and Nedergaard, M. (2013). Glutamate-dependent neuroglial calcium signaling differs between young and adult brain. *Science* 339, 197-200.

Sun, X.D., Li, L., Liu, F., Huang, Z.H., Bean, J.C., Jiao, H.F., Barik, A., Kim, S.M., Wu, H., Shen, C., *et al.* (2016). Lrp4 in astrocytes modulates glutamatergic transmission. *Nature neuroscience Jun 13*. doi: 10.1038/nn.4326. [Epub ahead of print].

Sung, J., Wang, Y., Chandrasekaran, S., Witten, D.M., and Price, N.D. (2012). Molecular signatures from omics data: from chaos to consensus. *Biotechnology journal* 7, 946-957.

Suzuki, S., Mori, J., and Hashizume, K. (2007). mu-crystallin, a NADPH-dependent T(3)-binding protein in cytosol. *Trends in endocrinology and metabolism: TEM* 18, 286-289.

Takano, T., He, W., Han, X., Wang, F., Xu, Q., Wang, X., Oberheim Bush, N.A., Cruz, N., Dienel, G.A., and Nedergaard, M. (2014). Rapid manifestation of reactive astrogliosis in acute hippocampal brain slices. *Glia* 62, 78-95.

Tamura, A., Yamada, N., Yaguchi, Y., Machida, Y., Mori, I., and Osanai, M. (2014). Both neurons and astrocytes exhibited tetrodotoxin-resistant metabotropic glutamate receptor-dependent spontaneous slow Ca<sup>2+</sup> oscillations in striatum. *PLoS one* 9, e85351.

Tang, W., Szokol, K., Jensen, V., Enger, R., Trivedi, C.A., Hvalby, Ø., Helm, P.J., Looger, L.L., Sprengel, R., and Nagelhus, E.A. (2015). Stimulation-evoked Ca<sup>2+</sup> signals in astrocytic processes at hippocampal CA3-CA1 synapses of adult mice are modulated by glutamate and ATP. *J Neurosci* 35, 3016-3021.

Tang, X., Taniguchi, K., and Kofuji, P. (2009). Heterogeneity of Kir4.1 channel expression in glia revealed by mouse transgenesis. *Glia* 57, 1706-1715.

Theis, M., Jauch, R., Zhuo, L., Speidel, D., Wallraff, A., Döring, B., C, F., G, S., B, T., C, E., *et al.* (2003). Accelerated hippocampal spreading depression and enhanced locomotory activity in mice with astrocyte-directed inactivation of Connexin43. *Journal of Neuroscience* 23, 766-776.

Tian, L., Hires, S.A., Mao, T., Huber, D., Chiappe, M.E., Chalasani, S.H., Petreanu, L., Akerboom, J., McKinney, S.A., Schreiter, E.R., *et al.* (2009). Imaging neural activity in worms, flies and mice with improved GCaMP calcium indicators. *Nat Methods* 6, 875-881.

Tien, A.C., Tsai, H.H., Molofsky, A.V., McMahon, M., Foo, L.C., Kaul, A., Dougherty, J.D., Heintz, N., Gutmann, D.H., Barres, B.A., *et al.* (2012). Regulated temporal-spatial astrocyte precursor cell proliferation involves BRAF signalling in mammalian spinal cord. *Development* 139, 2477-2487.

Tong, X., Ao, Y., Faas, G.C., Nwaobi, S.E., Xu, J., Hausteiner, M.D., Anderson, M.A., Mody, I., Olsen, M.L., Sofroniew, M.V., *et al.* (2014). Astrocyte Kir4.1 ion channel deficits contribute to neuronal dysfunction in Huntington's disease model mice. *Nature neuroscience* 17, 694-703.

Tong, X., Shigetomi, E., Looger, L.L., and Khakh, B.S. (2013). Genetically encoded calcium indicators and astrocyte calcium microdomains. *The Neuroscientist : a review journal bringing neurobiology, neurology and psychiatry* 19, 274-291.

Tsien, J.Z. (2016). Cre-Lox Neurogenetics: 20 Years of Versatile Applications in Brain Research and Counting.... *Front Genet Feb 19;7:19. doi: 10.3389/fgene.2016.00019. eCollection 2016.*

Tsien, R.Y. (1988). Fluorescence measurement and photochemical manipulation of cytosolic free calcium. *Trends Neurosci* 11, 419-424.

Ventura, R., and Harris, K.M. (1999). Three-dimensional relationships between hippocampal synapses and astrocytes. *J Neurosci* 19, 6897-6906.

Vitali, C., Wellington, C.L., and Calabresi, L. (2014). HDL and cholesterol handling in the brain. *Cardiovascular Research* 103, 405-413.

von Poser, C., Ichtchenko, K., Shao, X., Rizo, J., and Südhof, T.C. (1997). The evolutionary pressure to inactivate. A subclass of synaptotagmins with an amino acid substitution that abolishes Ca<sup>2+</sup> binding. *J Biol Chem* 272, 14314-14319.

Wang, X., Lou, N., Xu, Q., Tian, G.-F., Peng, W.G., Han, X., Kang, J., Takano, T., and Nedergaard, M. (2006). Astrocytic Ca<sup>2+</sup> signaling evoked by sensory stimulation in vivo. *Nature neuroscience* 9, 816-823.

Wasseff, S.K., and Scherer, S.S. (2011). Cx32 and Cx47 mediate oligodendrocyte:astrocyte and oligodendrocyte:oligodendrocyte gap junction coupling. *Neurobiology of disease* 42, 506-513.

Xie, A.X., Petravicz, J., and McCarthy, K.D. (2015). Molecular approaches for manipulating astrocytic signaling in vivo. *Front Cell Neurosci* Apr 21;9:144. doi: 10.3389/fncel.2015.00144. *eCollection 2015*.

Xu, G., Wang, W., Kimelberg, H.K., and Zhou, M. (2009). Electrical coupling of astrocytes in rat hippocampal slices under physiological and simulated ischemic conditions. *Glia* 58, 481-493.

Yang, X.W., and Gong, S. (2005). An overview on the generation of BAC transgenic mice for neuroscience research. *Curr Protoc Neurosci* May;Chapter 5:Unit 5.20.

Yang, Z., and Wang, K.K.W. (2015). Glial fibrillary acidic protein: from intermediate filament assembly and gliosis to neurobiomarker. *Trends in Neurosciences* 38, 364-374.

Zhang, L.F., Yang, J., Hong, Z., Yuan, G.G., Zhou, B.F., Zhao, L.C., Huang, Y.N., Chen, J., Wu, Y.F., and Collaborative Group of China Multicenter Study of Cardiovascular, E. (2003). Proportion of different subtypes of stroke in China. *Stroke; a journal of cerebral circulation* 34, 2091-2096.

Zhang, Y., and Barres, B.A. (2010). Astrocyte heterogeneity: an underappreciated topic in neurobiology. *Current Opinion in Neurobiology* 20, 588-594.

Zhang, Y., Chen, K., Sloan, S.A., Bennett, M.L., Scholze, A.R., O'Keeffe, S., Phatnani, H.P., Guarnieri, P., Caneda, C., Ruderisch, N., *et al.* (2014). An RNA-sequencing transcriptome and splicing database of glia, neurons, and vascular cells of the cerebral cortex. *J Neurosci* 34, 11929-11947.

Zhang, Y., Sloan, S.A., Clarke, L.E., Caneda, C., Plaza, C.A., Blumenthal, P.D., Vogel, H., Steinberg, G.K., Edwards, M.S., Li, G., *et al.* (2016). Purification and Characterization of Progenitor and Mature Human Astrocytes Reveals Transcriptional and Functional Differences with Mouse. *Neuron* 89, 37-53.

Zhu, Y., Nwabuisi-Heath, E., Dumanis, S.B., Tai, L.M., Yu, C., Rebeck, G.W., and Ladu, M.J. (2012). APOE genotype alters glial activation and loss of synaptic markers in mice. *Glia* 60, 559-569.

Zhuo, L., Sun, B., Zhang, C.-L., Fine, A., Chiu, S.-Y., and Messing, A. (1997). Live Astrocytes Visualized by Green Fluorescent Protein in Transgenic Mice. *Developmental Biology* 187, 36-42.

Zhuo, L., Theis, M., Alvarez-Maya, I., Brenner, M., Willecke, K., and Messing, A. (2001). hGFAP-cre transgenic mice for manipulation of glial and neuronal function in vivo. *Genesis* 31, 85-94.